Anne Serine Ognedal

Large-Deformation Behaviour of Thermoplastics at Various Stress States

An experimental and numerical study

Thesis for the degree of Philosophiae Doctor

Trondheim, October 2012

Norwegian University of Science and Technology
Faculty of Engineering Science and Technology
Department of Structural Engineering

NTNU – Trondheim
Norwegian University of
Science and Technology

NTNU
Norwegian University of Science and Technology

Thesis for the degree of Philosophiae Doctor

Faculty of Engineering Science and Technology
Department of Structural Engineering

ISBN 978-82-471-3913-4 (printed ver.)
ISBN 978-82-471-3914-1 (electronic ver.)
ISSN 1503-8181

Doctoral theses at NTNU, 2012:298

Printed by NTNU-trykk

ABSTRACT

The large-deformation behaviour of thermoplastics has been studied by experimental tests and numerical simulations. The work herein is a part of a larger research project concerning constitutive modelling of polymers. A constitutive model for thermoplastics with structural applications has earlier been proposed in the research project. The work presented in this thesis concerns exploration of the capability of the constitutive model to capture the large-deformation behaviour of polymers at various stress states. In addition, some deformation mechanisms are investigated. Two different thermoplastics are addressed: PVC and HDPE. The PVC is an amorphous thermoplastic filled with a volume fraction of particles of about 0.2. The HDPE is a semicrystalline thermoplastic that contains fewer particles. All test specimens are taken from 5 mm and 10 mm thick extruded plates of these two materials.

From uniaxial tension and compression tests it is found that the yield stress of the PVC is pressure sensitive while that of HDPE is not. Furthermore, the stress-strain curve of PVC, in opposite to HDPE, has a peak stress followed by stress-softening and subsequent strain hardening. Reloading of already deformed tensile specimens, does not recall this local stress maximum. This observation is interpreted as a sign of damage rather than physical aging in the material. Reloading of HDPE, on the other hand, recalls the shape of the initial stress-strain curve of the material. During plastic deformation in uniaxial tension the volume change in the PVC is notable while it in the HDPE is almost zero.

Addressing the volume change in PVC, specimens deformed in uniaxial tension are studied in a scanning electron microscope. It is found that the mineral particles have debonded from the PVC matrix and that microscopic voids are formed around the mineral particles in the deformed material. Thus, debonding and void growth are identified as two damage mechanisms in the PVC. Moreover, it is found that the volume change on the macroscale is caused by the void growth on the microscale. Results from numerical unit cell analyses, simulating the interaction between a mineral particle and surrounding polymer matrix, suggest that debonding and void growth can be the cause for the stress drop and the volume change observed in the laboratory tests.

Tensile tests of axisymmetric tensile specimens with notch are carried out on both materials to study the behaviour at presence of a triaxial stress field. Again, it is demonstrated that the yield stress of PVC is pressure dependent while the yield stress of HDPE is not, or at least very little, pressure sensitive. However, during

plastic deformation of the notched tensile bars, the volume change is significant for both materials. The dilation increases with the stress triaxiality. Fracture surfaces of fractured specimens clearly suggest that the increase of volume both in the PVC and the HDPE has its origin in void growth.

Biaxial tests are carried out on the PVC and HDPE materials to serve as a basis for validation of the constitutive model. The parameters of the model are determined from uniaxial tension and compression tests. In order to check how this model is applicable for describing other stress states, the biaxial tension tests were subject for numerical simulations. Comparison of the force-displacement curves and the strain fields from the simulations and the laboratory tests show that the model is capable of capturing the large-deformation behaviour.

The test results from the axisymmetric tensile bars with notch were also used for validation of the constitutive model. Comparison of force-displacement curves from laboratory tests and numerical simulations showed that numerical simulations overestimated the maximum force. The overestimation increased with the stress triaxiality, and it was higher for the PVC than for the HDPE. The stress triaxiality seems to enhance some damage that is not captured by the numerical model.

ACKNOWLEDGEMENTS

First of all I will thank my supervisors Professor Arild Holm Clausen and Professor Odd Sture Hopperstad. Thank you for sharing your knowledge with me, always in a patient, cheerful and encouraging way. One would have to search high and far to find better supervisors (though, I doubt better supervisors exist).

I would like to send my gratitude to Professor Thomas Seelig, and his two PhD candidates, Philip Hempel and Martin Helbig, for caring for me during my two months at Karlsruhe Institute of Technology. With your help and advice, the unit cell study in this thesis could be carried out. I would also like to thank Professor Ahmed Benallal and Bumedijen Raka for their contribution to the biaxial test series. The tests would not have been possible without your help or without the testing equipment you provided in the laboratory at LMT-Cachan. Gratitude also goes to Professor Leon Govaert at Eindhoven University of Technology for providing results from termogravimetric analyses. Silje Rodahl at SINTEF gave me an introduction to scanning electron microscopy. I would like to thank you for that.

I would like my colleagues at Department of Structural Engineering and at SIMLab for creating a pleasant working environment at a high knowledge level. Many of you have contributed to unforgettable stories. Thanks to Mario Polanco-Loria, for discussions and advices, to Terence Coudert for providing 7D support and to Torodd Berstad for his patience and good answers regarding LS-DYNA. Trond Auestad and Tore Wisth have been a great support in the laboratory work. I am very grateful for your help.

The master students Anfrid Dahlen and Aleksander Haugvik Malvik have contributed to this work through their master theses. It was a pleasure to work with you, and you carried out your work in excellent ways.

Thanks to all my dear friends who have distracted me with a great lot of fun. My life (and this thesis) would have been quite different without the breaks you have given me. Special thanks go to my family (I also, off course, regard Anders' family as mine) for your motivation and support. Thanks to mum and dad, you have cultivated my curiosity and creative urge ever since I was a little child. At last, but not least, I want to thank my boyfriend Anders. You are always there for me. Many a time when I come tired home from work, you have met my troubled mind with a kiss and a hug. After drifting my worries away by your wonderful being, you have taken me out on the most exciting adventures.

TABLE OF CONTENTS

PART I – EXPERIMENTAL STUDY

PART II – NUMERICAL STUDY

CHAPTER 1

INTRODUCTION

1.1 BACKGROUND

In a long term view, the world production of plastics has increased since 1950 [1]. A variety of processing techniques for these materials makes it possible to produce components with a complex geometry at a low cost. By addition of additives and fillers, the material properties can be modified and customized to fit both esthetical and mechanical requirements. Today thermoplastics are commonly used in a lot of products within a wide spectre of fields: Packaging, construction, transport industry, medical applications etc. In example, the weight proportion of polymer materials in the Audi A6 is almost 20% [2]. Especially the parts in the front section of the car are made of polymers. The use of polymers in such applications increases the request of numerical models that can predict the mechanical behaviour of the materials. Engineers employ finite element analysis (FEA) as a tool in the design process to reduce development time, cost and technical risk. However, reliable and precise material models implemented in the FEA-software are demanded. A material model that covers all effects in large deformations of thermoplastic polymers (e.g. necking, damage, different behaviour under compression and tension, strain rate sensitivity) is not yet available in commercial FEA-codes [3].

The work presented in this monograph is a part of a larger research project concerning constitutive modelling of polymers at SIMLab, NTNU. The polymer research group at SIMLab has earlier proposed a hyperelastic-viscoplastic constitutive model for thermoplastics [4], which is implemented as a user-defined model in the non-linear FEA-code LS-DYNA [5]. Results from numerical simulations compared with results from simple laboratory tests reveal that the constitutive model is promising in describing the mechanical response even for

large deformations [6]. However, further validation of the model at various stress states is identified as an important task by the research group.

The materials concerned in the PhD study presented in this monograph are PVC and HDPE. These two materials have been chosen by the SIMLab polymer group to serve as bench-mark materials. It is believed that studying only two well-known materials through several tests will accumulate some general knowledge that can be carried forward to other polymers at a later stage. The two materials are rather different in nature. The PVC is an amorphous thermoplastic containing a mineral filler volume fraction of about 0.2, while the HDPE is a semicrystalline thermoplastic containing minor amounts of filler. The fundamental behaviour of these materials has already been studied by the research group [6]. However, the behaviour at more complex stress states has been paid little attention to. In the long term it may be interesting to include prediction of damage and fracture in the constitutive model. It is therefore relevant to study damage mechanisms in the materials. The addressed PVC and HDPE were acquired in form as extruded plates of 10 mm and 5 mm thickness. Both materials were acquired directly from a wholesaler. All laboratory tests have been carried out on specimens from these plates. All tests are carried out at room temperature and at moderate strain rates.

It is in the objectives of this study to define test setups that capture the large-deformation behaviour of the thermoplastics at 2D and 3D stress states. Interesting properties are the stress-strain relationships, the yield stress, the pressure sensitivity and the volume change. Methods for testing the desired properties have been determined, involving various shapes of the test specimens and loading patterns. Different measurement techniques have been employed. In particular, digital image analysis techniques have been widely used in order to determine the deformation of the materials. In addition, a scanning electron microscope has been used to investigate the mechanisms behind the volume change. The experimental programme also involves some uniaxial material tests in tension and compression in order to obtain information for determination of the coefficients of the material model [4].

The numerical simulations are carried out as explicit analyses in the finite element software LS-DYNA. A numerical study of a unit cell model representing a soft polymer matrix containing stiff particles has been performed. This was done to investigate the effect of the mineral filler in the PVC. The constitutive model [4] has been validated by comparing results from numerical simulations employing the material model with results from the laboratory tests.

1.2 OBJECTIVES

This thesis concerns experimental and numerical studies on the large-deformation behaviour of polymers. The objectives of the research are:

- To define and to carry out experimental tests to serve as basis for validation of the constitutive model at various stress states.
- To explore the capabilities and limitations of the constitutive model by numerical simulations of the validation tests.
- To define and to carry out experimental tests that capture the large-deformation behaviour of thermoplastics at various stress states.
- To identify and investigate damage mechanisms.

1.3 SCOPE

- The intention of this study is to explore capabilities and the limitations of the existing constitutive model rather than to propose a new.
- The work involves two materials: PVC and HDPE.
- All tests are carried out at room temperature. No temperature effects are included.
- All tests are carried out at low strain rates.
- The experimental and numerical exploration of damage is restricted to tension stress modes.

1.4 OUTLINE OF THESIS

The monograph is divided into an experimental and a numerical part. All experimental tests and their results are described in Part I. Part II presents the numerical simulations.

First, Chapter 2 introduces and discusses some concepts that explain the behaviour of polymers.

Part I first addresses uniaxial tension tests of specimens from the 5 mm sheets of PVC and HDPE in Chapter 3. The same materials are tested in uniaxial compression in Chapter 4. The results from the tests in Chapter 3 and Chapter 4 will be used for determination of material parameters in Chapter 10. The behaviour during loading and reloading, as well as possible effects of physical aging is investigated in Chapter 5. Chapter 6 addresses the plastic dilation in the PVC. Deformed tensile specimens are observed in a scanning electron microscope, and the void growth on the microscale is compared with the volume change on the macroscale. In Chapter 7 the 5 mm sheets of PVC and HDPE are deformed in biaxial tension. These tests are primarily meant to serve as a basis for validation of the constitutive model. Chapter 8 presents tensile tests of axisymmetric tensile bars with notch. These tests will be used as validation of the constitutive model and as material tests for investigating deformation mechanisms at high stress triaxialities.

Part II concerns the numerical part of the study. First in Part II, in Chapter 9, a unit cell study is presented. This study was carried out to achieve a better understanding of the matrix-particle interaction in a mineral filled polymer. The constitutive model proposed by Polanco-Loria et al. [4] is introduced in Chapter 10 which also includes identification of the material parameters for the materials from the 5 mm thick plates of PVC and HDPE. The parameters for the 10 mm plates of both materials are already determined by Hovden [6]. Employing the material parameters, numerical simulations of the uniaxial tension and compression tests are carried out in Chapter 11. The biaxial tests are simulated in Chapter 12. Chapter 13 addresses numerical simulations of the axisymmetric notched tensile bars.

The monograph is rounded off with final discussions, conclusions and suggestions for further work in Chapter 14.

REFERENCES

[1] Plastics Europe. http://www.plasticseurope.org 08.08 (2012)

[2] ATZ Extra "Der neue Audi A6", 2011.

[3] P.A. Du Bois, S. Kolling, M. Koesters, T. Frank. Material behaviour of polymers under impact loading. *International Journal of Impact Engineering*, **32** (2006), 725-740.

[4] M. Polanco-Loria, A.H. Clausen, T. Berstad, O.S. Hopperstad. Constitutive model for thermoplastics with structural applications. *International Journal of Impact Engineering*, **37** (2010), 1207-1219.

[5] LS-DYNA. LS-DYNA Keyword User's Manual. Version 971, Livermore Software Technology Corporation (LSTC), 2007.

[6] M.T. Hovden. Test and numerical simulations of polymer components. Master thesis, Department of Structural Engineering, NTNU, (2010).

CHAPTER 2

BEHAVIOUR OF THERMOPLASTICS

This chapter introduces some of the fundamental concepts that explain the deformation mechanisms in thermoplastics.

2.1 STRUCTURE OF THERMOPLASTIC POLYMERS

The word polymer origins from the Greek 'poly', meaning many, and 'meros', meaning part [1]. The name reflects that a polymer molecule is an assembly of many monomers. One group in the polymer family is the thermoplastics. A thermoplastic molecule is a long chain of many small sub-units that are joined together. Most commonly the sub-units are linked together in such way that they form a chain with a strong continuous backbone of carbon atoms with different kinds of side groups. The carbon atoms in the backbone are connected by strong covalent bonds. Between the different polymer chains weaker van der Waals bonds or hydrogen bonds are present. These bonds are also called secondary bonds as they are a result from interaction of side atoms along the chain. Different kinds of side groups can be attached to the polymer chain. These side groups can be other atoms or groups of atoms. Other polymer chains can also be connected to the main chain, this is called chain branching. The number of different combination possibilities is vast, and so is the variety of different polymer types.

Polymer chains with high molecular regularity can be arranged into a crystal structure. The crystals are formed radially out from initial nucleation centres and form spherulitic formations with lamellar structure. Polymers with such morphology are called crystalline polymers. If there is no regular arrangement the polymer is considered as amorphous. In an amorphous polymer the polymer chains are randomly distributed in space. A result from the random distribution is that some chains tangles together. The entanglements may cause the polymer to behave

like a network. Also the crystalline polymers contain some amorphous regions [1]. They are therefore often referred to as semi-crystalline. The crystal regions are smaller than the total length of the molecule. One polymer chain is long enough to pass through both crystals and amorphous regions. In this way the crystals and the amorphous regions are woven together by long polymer chains [1]. Due to the regular packing of the chains, crystalline regions of the polymer have higher density than the amorphous.

The simplest thermoplastic polymer is polyethylene (PE). A schematic representation of the structure of PE is shown in Figure 2.1. The figure illustrates that the PE macromolecule is build up by many ethylene monomers. The number n of monomers joined together to form a molecule is typically around 10^4 but it may vary between 10^3 and 10^6. Due to the regular shape of the chain, PE can easily be arranged into crystals and is therefore regarded as a semi-crystalline material. A variety of different PE grades can be composed, e.g. by chain branching or by taking advantage of the strong covalent bonds by highly oriented fibre stretching. Most common are the low-density polyethylene (LDPE) and the high-density polyethylene (HDPE). The difference in density reflects that the molecular packing is denser, i.e. the crystallinity is higher, in HDPE than in LDPE. Depending on the molecular structure, application of PE varies from plastic bags and cling-wrap (LDPE) [2] to high performance fishing lines and ballistic protection (ultra high molecular weight polyethylene UHMWPE) [3].

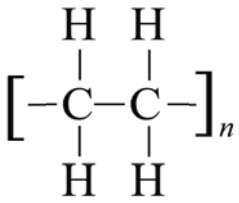

Figure 2.1 *Schematic description of polyethylene (PE).*

Figure 2.2 represents the molecular structure polyvinyl chloride (PVC). In the representation it is similar to the PE, with one of the hydrogen atoms replaced by a chloride atom. This seemingly small difference has a great impact on the mechanical behaviour of the polymer. The comparably large chloride atom prevents packing of the polymer chains into regular arrangements and hinders crystallization. The polymer may contain up to 10% crystallinity and still be considered as an amorphous polymer. Plasticizers may be added to the PVC to increase the flexibility of the polymer. About half of the produced PVC is used as rigid, unplasticized, PVC and the other half as plasticized PVC [4].

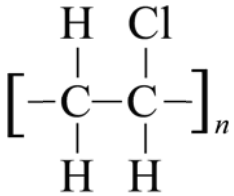

Figure 2.2 *Schematic description of polyvinyl chloride (PVC).*

2.2 DEFORMATION OF THERMOPLASTICS

Macroscopic deformation of thermoplastics is a result of movement of polymer chains, or segments of chains. Such movement can be either intermolecular, for instance by chain sliding, or intramolecular, for instance by a change in the conformation of the chain [5]. The chain segments' freedom to move arises from the ability of a chain segment to rotate about the single bonds in the structure and from the arrangement of the chain with respect to other chains [5].

The deformation is dependent on applied stress, temperature, strain rate and pressure. Thermoplastic polymers are viscoelastic materials. It can be questioned whether the concept of plasticity, in the same sense as metal plasticity, is valid for polymers. However, for modelling purposes it is convenient to divide the deformation into elastic and plastic parts. A phenomenological approach is attractive for the modelling. Examples of constitutive models that combine elasticity, viscoelasticity and viscoplasticity are proposed in the literature [6]. In the scope of this monograph the viscoelastic effects are not discussed. Only the elastic and viscoplastic deformations are considered. They are characterized as follows: Purely elastic deformations are reversible. The initial configuration of the atoms is restored when the load is removed [7]. Plastic deformations are permanent deformations that do not vanish. The relative displacement of atoms remains with removal of load [7]. The time needed for the polymer chains to move makes response viscoplastic.

2.2.1 ELASTIC DEFORMATION OF THERMOPLASTICS

Elastic deformation of thermoplastics is often regarded to consist of an energy-elastic and an entropy-elastic contribution. At small strains the energy-elastic contribution is the dominant. This response can be regarded as an intermolecular phenomenon originating from attraction and repulsive forces between atoms and rotation about the covalent bonds between the carbon atoms in the backbone of the

molecule. Turning attention to large strains, the entropy-elastic contribution becomes dominant. This is an intramolecular response involving the whole assembly of molecules. If one looks upon the polymer structure as a network of polymer chains tied together by entanglements, the intramolecular elastic contribution can be considered as network stretching. In an un-stretched state the flexible chains occur randomly coiled between the tie points. This is the state of highest entropy. According to statistical theory of rubber elasticity there is a very high number of possible configurations at this state [8]. As the chains are extended the number of possible configurations decreases, and so does the entropy. By removal of the load, the polymer chains randomly coil back to a state that maximizes the number of possible conformations and also the entropy.

2.2.2 *Plastic deformation of thermoplastics*

Plastic deformation of polymers concerns permanent relocations of macromolecules, or of segments of the macromolecules. In thermoplastics it is expected that plasticity primarily concern breaking of the van der Waal bonds, as they are much weaker than the covalent bonds in the carbon backbone [9]. On the somewhat larger scale, yielding mechanisms mentioned in the literature are cleavage of crystallites, lamellar slip, and amorphous mobility [5]. Plastic deformation may impose drastic reorganization at the morphological level where the structure may change from a spherulitic to a fibrillar type [5]. According to several authors [1, 10, 11] yielding is caused either by crazing or by shear yielding. Crazes are highly localized zones of plastic dilational deformation that appear like small crack-shaped regions. They mostly occur in the deformation of amorphous polymers. In many cases crazes can be observed as stress whitening of the material. Shear yielding, or shear banding, occurs without any volume change in the material. It can be considered as irreversible slip of molecular chains. In semi-crystalline polymers the plastic deformation involves both the crystalline and the amorphous phases. Galeski [10] discusses plastic deformation in crystalline polymer systems in terms of crystalline plasticity. The theory involves crystallographic slips controlled by the generation and propagation of crystallographic dislocations. Deformation of the amorphous phase between the crystallites occurs in form of intralamellar slip, lamellar separation or rotation of stacks of lamellae [10].

A required condition for obtaining large plastic deformations is the possibility of molecular motions on a time scale similar to the deformation rate [10]. This explains why polymers have a strain rate dependent, i.e. viscoplastic, behaviour. Moreover, the plasticity in polymers is temperature dependent: An increase in

temperature leads to an increase in chain mobility. It should be kept in mind that yielding is a dissipative process that leads to adiabatic heating. Self heating of a tensile specimen may affect its tensile behaviour at large deformation.

Detailed knowledge about the molecular mechanisms of plasticity in polymers are at time being not very well established because of the complex microstructure [9]. However, from an engineering point of view the yield stress can be regarded as the minimum stress that produces permanent deformation when the stress is subsequently removed. The case is then reduced to a matter of choice. There are various ways to define the yield stress. However, all methods are related to a change in slope in the stress-strain curve. For polymers it is common to choose the yield stress as the first local stress maximum. If no such maximum exists, the use of an offset strain, e.g. at 0.2%, and the Considère construction [1] are typical methods to define the yield stress.

2.3 NECKING AND COLD DRAWING

Necking is a type of deformation where strain localizes in a region of the material. The location for onset of necking may be determined by a local increase in temperature, or by a structural or material imperfection. A necessary, but not sufficient, condition for necking is the existence of a local maximum point on the nominal stress-strain curve [12]. This is equivalent with a local maximum of the force-displacement curve. The condition necessary for necking can for uniaxial tension be described as [1]

$$\frac{\mathrm{d}\sigma_n}{\mathrm{d}\lambda} = 0 \tag{2.1}$$

where σ_n is the nominal stress and λ is the stretch defined as the change of the length of a small line segment L, $\lambda = L / L_0$. By assuming deformation at constant volume, the condition above can be expressed in terms of Cauchy stress σ as [1]

$$\frac{\mathrm{d}\sigma}{\mathrm{d}\lambda} = \frac{\sigma}{\lambda} \tag{2.2}$$

Equation (2.2) is also called the Considère construction [1] . It can be employed to determine onset of necking and it can be used as a definition of yield stress. However, the Considère construction requires deformation at a constant volume. This is an assumption that is not always valid for polymers.

With further deformation after onset of necking, the neck in some cases stabilizes and begins to extend by drawing fresh material from the surrounding regions into the neck. This is often referred to as cold drawing. Figure 2.3 schematically describes this process. As illustrated in the figure, drawing of the material in the neck may impose high degree of orientation of the polymer chains.

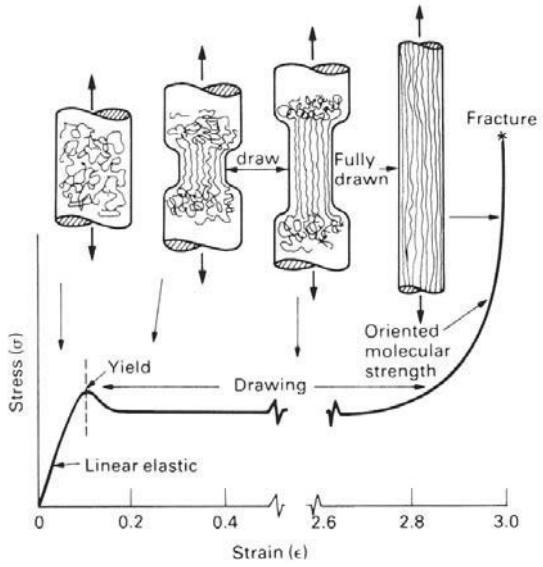

Figure 2.3 *Schematic figure of the drawing of a polymer [13].*

2.4 PHYSICAL AGING

It is observed that storage at constant temperature and at zero stress affects the properties of polymer materials. This phenomenon is called aging. Aging referring to changes in properties that are reversible and without any permanent modification of the structure is often called physical aging. The term "physical" is commonly used to distinguish the phenomenon from irreversible types of aging, like chemical or biological aging. It follows that it is possible to reduce or remove this aging effect by some suitable treatment of the material.

Physical aging takes place in both amorphous and crystalline polymers. For both polymer types the potential for aging is created from a small decrease in the specific volume during cooling [1]. Within this context, physical aging can be related to the concept of free volume. The free volume is the volume of the vacant

sites in the material that is not occupied by molecules [11]. When the material is rapidly cooled down, i.e. quenched, without being able to contract sufficiently, it ends up in a non-equilibrium state. After quenching, the molecular mobility is not zero. Because of the molecular mobility, there will be a slow and gradual evolution towards equilibrium during time [14], see Figure 2.4. This slow change of the thermodynamic state is referred to as structural recovery [15]. It occurs at temperatures T between the glass transition temperature T_g and a secondary transition temperature T_β [14].

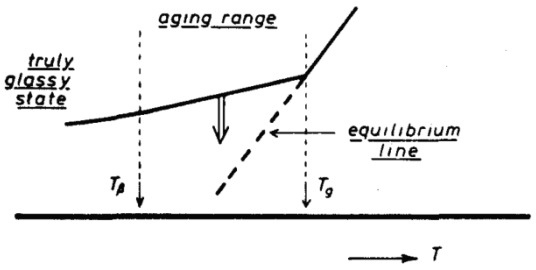

Figure 2.4 *The origin of aging in amorphous polymers. The specific volume is plotted against temperature T . Between T_g and T_β there is an internal movement towards the equilibrium [14].*

Thus, physical aging can be regarded as a process where the polymer contracts towards its equilibrium state. It is an internal process that affects the macroscopic properties of the material. A typical effect of physical aging on the stress-strain curve is an increase in yield stress followed by stress softening [16-18], see Figure 2.5 a). The physical aging can be "erased" by rejuvenation of the material, see Figure 2.5 b). The purpose of rejuvenation is to bring the material back to its freshly quenched state. It can be done by heat treatment [14], i.e. by heating the material above the glass transition temperature followed by rapid cooling. It can also be done mechanically [18] by deforming the material by e.g. twisting or rolling. The material is then mechanically pushed back to its original state. The difference between thermal and mechanical rejuvenation is discussed in the literature [15, 16, 18]. Even though the rejuvenation immediately brings the material to its original state, physical aging will re-occur with time. It should be noted that, as illustrated by Figure 2.5, physical aging has no effect in the large strain domain [16].

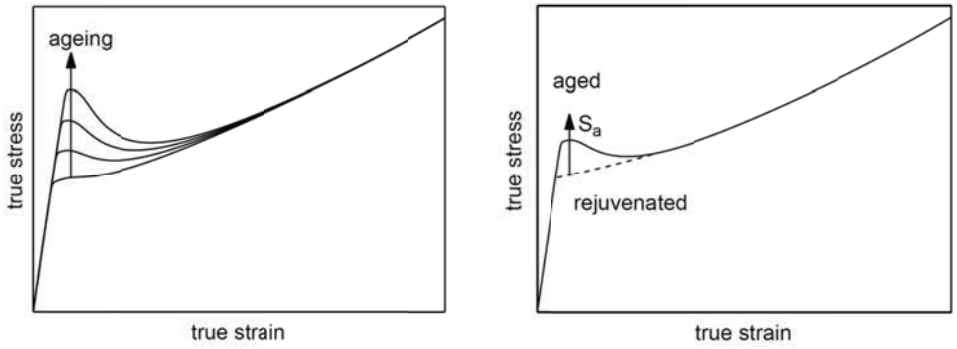

a) b)

Figure 2.5 *Schematic representation of a) increase in yield stress as a consequence of aging and b) the effect of rejuvenation and aging [16].*

2.5 MINERAL FILLERS

The properties of polymers can easily be modified by adding fillers of different kinds. Such fillers are small-sized particles added to the material. Many of the plastics we refer to in the everyday language are in fact different kinds of polymer-particle composites. Each type of polymer-particle composite has its own properties that are influenced by volume fraction, mechanical properties, particle size, shape and surface treatment of the filler.

Concerning the type of fillers, rubber and mineral particles are common since they are both known to have a toughening effect [19-21]. A difference between the two is that the soft rubber particles decrease Young's modulus of the bulk material while the relatively stiff mineral particles have the opposite effect [19, 20, 22-24]. Mineral particles are also cheaper than those of rubber, and may therefore also decrease the cost of the polymer. They are also known to improve flame retardance, and to reduce thermal expansion and heat conductivity amongst other properties. Therefore they are often called "functional fillers" by the polymer industry. Calcium carbonate ($CaCO_3$) is by far the most common filler for polymers [25, 26], while titanium dioxide (TiO_2) is the second most applied one [26]. This section will focus on mineral fillers.

Fillers with proper adhesion to the matrix stay bonded to the polymer matrix at low deformation levels. Stiff particles then act as reinforcement, and the bulk material behaves like a composite. When reaching a certain level of stress the particles debond from the matrix. Thus the load bearing cross section of the material is reduced, resulting in a softening effect on the stress-strain curve. At the same time,

the debonding process results in formation of voids which is the main feature in the toughening process. The voids are smaller than what a human eye can observe. However, at a macroscopic scale the voids can be observed as stress whitening. The reason for the white appearance is that small voids reflect the light due to refractive index differences between the components. This is known as the Fresnel effect [26].

It has already been mentioned that stiff particles work as reinforcement, i.e. the elastic modulus of the polymer increases with addition of $CaCO_3$ particles [19, 20, 22-24]. On the other hand, several authors report that addition of such particles also decreases the plastic resistance [20, 27]. This observation, however, depend on how well the particles are bonded to the matrix material [23]. The matrix-particle bonding strength can be altered by surface treatment of the particles [25, 28]. Stearic acid ($CH_3(CH_2)_{16}CO_2H$) is typically used for this purpose [25]. Surface treatment improves also the dispersion of the filler. Any type of particles added to the polymer should be well dispersed through the material. With poor dispersion there will be less uniform zones of matrix between the particles. The thinnest matrix zones between closely located particles may then act as a weakest link and initiate fracture.

The size of the particles affects the interfacial interaction between the matrix and the particle. For a given particle volume fraction, the total surface area of smaller sized particles will be larger than the surface area of larger particles. Small particles therefore tend to have a better adhesion to the polymer matrix [28, 29]. Addition of small sized mineral particles can improve the impact strength and fracture toughness [22, 25, 28, 29]. The strains are reported to have a more favourable distribution at low filler concentrations and with fine particle size because the stress field around smaller particles is more uniform than around larger ones [26]. The argument for this is that the matrix must stretch over the entire surface of large particles, while smaller particles more easily move with an elongating matrix [26]. Moreover, larger particles are more irregular than smaller particles and may thus prevent a uniform strain pattern [26]. It follows that larger particles may act as a material defect. This also regards particles with a high aspect ratio, where the longer dimension is much larger than the shorter dimension. Particles made of $CaCO_3$ have a rather nodular shape with a low aspect ratio.

The toughening effect of rubber and mineral particles can be explained by initiation of void growth, and therefore reduction of the plastic resistance [20]. In this way brittle behaviour is avoided. Indeed, Argon and Cohen [21] argue that the most effective way to avoid a ductile to brittle transition is to lower the plastic resistance. For polymers, the easiest way to do this is by the addition of particles that can cavitate or debond and, as Argon and Cohen say, “convert the polymer in

to a cellular solid" [21]. Socrate and Boyce [30] showed in a numerical study that the presence of voids in polycarbonate (PC) gives stress fields that favour shear yielding over brittle fracture mechanisms even for triaxial stress states. The toughening effect is reported for both semi-crystalline and amorphous polymers, and even for epoxies [31], containing any kind of voids. The voids can be present in form of pre-existing voids, self-cavitating rubber particles or debonding stiff mineral particles. Also the processes of debonding and void growth promote dissipation of energy and distribution of strain throughout the material so the deformation takes place over a larger volume.

Wu [32] studied the effect of adding rubber particles to a nylon. It was found that a sharp brittle-to-tough transition occurs when the average thickness of the matrix ligament between the particles is reduced below a critical value. He claimed that this critical interparticle distance is a material property of the matrix material. This means, according to Wu [32], that it is not the particle size or volume fraction that controls the toughening effect. Bartczak et al. [20] support this observation. They found that the source of toughness is a result of plastic extensibility of the matrix material [19, 20]. Thus, they further suggest that the properties of the filler are of little relevance. They demonstrate this by investigation of HDPE filled with stiff and soft particles [19, 20] and it was found true under the requirement that the particles debond from the matrix and initiate voids.

The explanation of the effect of the interparticle distance on the toughening of semicrystalline polymers is that the presence of particles alters the microstructural morphology. Addegio et al. [24] report that $CaCO_3$ particles reduce the crystallinity of HDPE, while Bartczak et al. [20] report that such particles affect the orientation of the crystals in the same material. The same effect is observed for rubber particles [19]. Interparticle ligaments of thickness below the critical distance possess a structure of highly ordered lamellar crystallites having reduced plastic resistance in certain directions [20]. The local anisotropy at microscale reduces the overall plastic resistance of the blend [20] and increases plastic yielding leading to a tougher response of the polymer [32]. It should be noted that these considerations regard the morphology of semicrystalline polymers.

For obtaining the best result by adding mineral filler, the particles should be well dispersed in the polymer matrix. Moreover, the matrix-particle interface strength should be strong enough to stay attached during the initial deformation and weak enough to debond for larger strains. If these requirements are fulfilled, it can be concluded that the particles have the following effects on the polymer:

- Young's modulus increases because the particles have a reinforcing effect.

- Debonding of particles reduces stiffness and gives rise to void growth. The void growth is required to obtain the desired toughening effect.
- The overall yield stress is reduced leading to a tougher response of the polymer.

2.6 THE PRINCIPLE OF DELESSE

The methods relating 3D quantities to 2D images can be referred to as stereology. Thus, stereological methods can be used to say something about the 3D morphology of a material or tissue just by looking at a 2D section of it. One of the basic principles of stereology was formulated in 1847 by the French geologist A. Delesse [33]. He stated that the *area fraction of a rock component in a random cross section of a rock is equal to the volume fraction of the component in the whole rock.* This principle is now called the principle of Delesse and it applies for all materials containing objects of any size or shape, connected or separated, isotropic or anisotropic [33, 34]. The "random cross section" statement implies that the principle even holds for an arbitrary cutting direction. The sectioning angle will affect both the profile area of the anisotropic objects and the surrounding object in a proportional way [33]. The only requirements are that the cross section is typical and that it is selected at random.

The area fraction ω_A of some component in a cross section of a body represents the ratio of the area covered by the component A_{comp} to the total cross sectional area A

$$\omega_A = \frac{A_{comp}}{A} \tag{2.3}$$

In the same manner, the component volume fraction ω_V is the volume of a certain component V_{comp} in an object divided by the total volume V of the object

$$\omega_V = \frac{V_{comp}}{V} \tag{2.4}$$

If we slice a body in thin slices with area a and take an image of each slice we expect to find about the same area fraction of the component a_{comp} in each image. By giving each slice an infinitesimal thickness dy the volume of the slice v becomes

$$v = a \cdot dy \tag{2.5}$$

The volume of the component v_{comp} in the slice is

$$v_{comp} = a_{comp} \cdot dy \tag{2.6}$$

If we sum up the volume of the component and divide it by the total volume of the object at hand we get the

$$\frac{\sum v_{comp}}{\sum v} = \frac{\sum a_{comp} \cdot dy}{\sum a \cdot dy} \tag{2.7}$$

The thickness dy cancels out and we get [33]

$$\frac{V_{comp}}{V} = \frac{A_{comp}}{A} \tag{2.8}$$

This gives that the volume fraction equals the area fraction.

$$\omega_V = \omega_A \tag{2.9}$$

The principle of Delesse can also be proved more rigorously by geometrical probability theory [35].

A version of the Delesse principle for two dimensions was some years later suggested by A. Rosiwal, who also was a geologist. He proposed a way to estimate the area fraction ω_A by "linear integration" [33]. The procedure is to lay out a test line onto the section of the body and to measure the fractional length ω_L of the line intersecting the components of the body. The ratio between the length of the line section cutting through the component L_{comp} and the total length L of the line is

$$\omega_L = \frac{L_{comp}}{L} \tag{2.10}$$

The procedure can be justified in similar manner as the principle of Delesse: To measure the plane area of an object, it can be divided in to thin strips, or test lines, each with a small thickness dy. The component area fraction a_{comp} of each strip can be estimated from the fractional length ω_L of the test line multiplied by its thickness dy. By summing up the strips, the area fraction ω_A for the whole area can be found. According to Rosiwal we get

$$\omega_A = \omega_L \tag{2.11}$$

A consequence of these principles is that if you follow any path through the specimen, the relative partition of a component you meet will be the same.

As geologists, Delesse and Rosiwal were interested in the fraction of a certain component in a rock sample. However, the principle of Delesse is also valid for quantification of the fraction of voids in a solid material. It has also been used on polymers [24]. It should be noted that principle of Delesse can only give an estimate of the fraction of a component. To pose assumptions on shape, distribution, orientation or density of the considered component, other stereological approaches are needed.

In a cut through an object containing oblong voids, the relative area of voids will remain the same, independent of the cutting angle. This can be demonstrated as follows. Figure 2.6 a) shows a micrograph of mineral filled PVC stretched in the vertical direction. The image is taken from the test PVC-8 from the Chapter 6. It shows the grey PVC matrix containing particles and oblong voids. The areas containing voids or particles are identified and marked black in Figure 2.6 b), while the remaining parts of the object, i.e. the matrix, are represented in white. Digital image analysis performed with the software ImageJ [36] reveals that the area in black covers 32% of the total surface area, i.e. $\omega_A = 0.32$.

Figure 2.7 displays horizontal blue and vertical red test lines intersecting the black regions at arbitrary locations. It can be seen from Figure 2.7 that the horizontal lines intercept smaller black areas rather frequently, while the vertical lines cut through fewer and larger black areas. Beside each line the fractional length ω_L is given, addressing the black region fraction cut through by the line at hand. The average value of the five blue horizontal length fractions is $\omega_L = 0.32$ and the average value of the five red vertical length fractions is $\omega_L = 0.30$.

Hereafter the volume fraction ω_V will be referred to as ω.

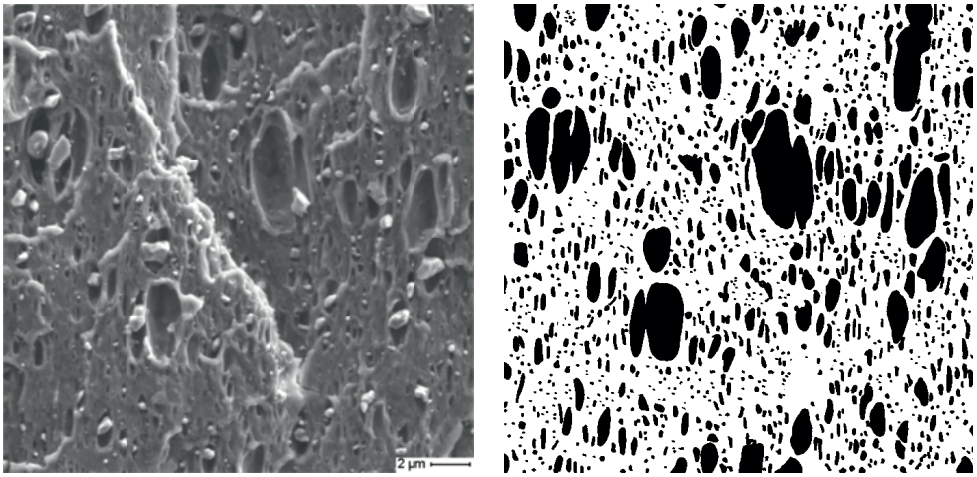

a) b)

Figure 2.6 *a) SEM micrograph of deformed PVC containing mineral particles and voids. b) Particles and voids are identified and marked black. The area fraction of the black component is* $\omega_A = 0.32$.

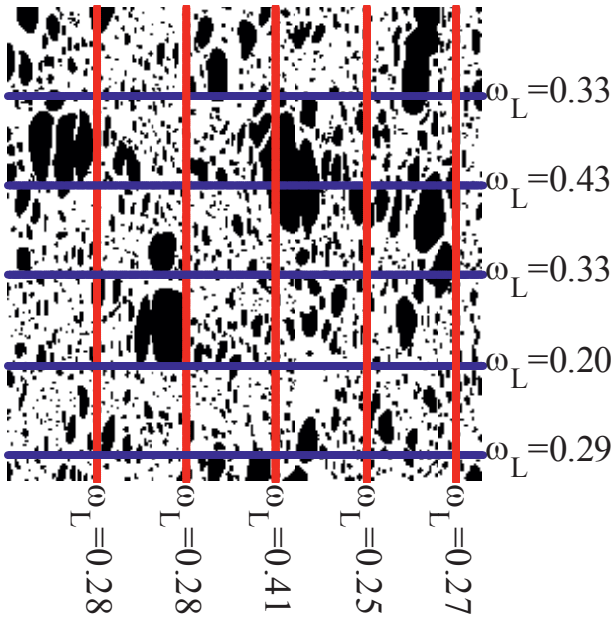

Figure 2.7 *Length fractions* ω_L *of the black component estimated from horizontal and vertical test lines located at arbitrary positions.*

2.7 DAMAGE BY VOID GROWTH

The void growth rate $\dot{\omega}$ in a material can be decomposed into a term for growth of existing voids $\dot{\omega}_g$ and a term for nucleation of new voids $\dot{\omega}_n$ [37]

$$\dot{\omega} = \dot{\omega}_g + \dot{\omega}_n \tag{2.12}$$

Assuming an incompressible matrix, the expression for void growth $\dot{\omega}_g$ can be formulated in terms of the plastic rate-of-deformation-tensor $\mathbf{D}^p$ [37]

$$\dot{\omega}_g = (1-\omega)\,\mathrm{tr}(\mathbf{D}^p) \tag{2.13}$$

It can alternatively be expressed as [8]

$$\dot{\omega}_g = (1-\omega)\frac{\dot{J}^p}{J^p} \tag{2.14}$$

where the plastic part of the Jacobian J^p is the determinant of the plastic part of the deformation gradient $\mathbf{F}^p$, $J^p = \det \mathbf{F}^p$. In some cases the nucleation of voids can be neglected, while in other cases this is considered as unrealistic. A material containing particles which debond after certain deformation is one case where the nucleation term should be considered. Different formulations describing the nucleation process, driven either by stress or by strain, are suggested in the literature [38, 39].

Formation of voids is a damage process that causes a reduction of strength. This is due to a reduction of the load carrying cross section. The area of the real load carrying cross section is called the effective area A_{eff}. It is equal to the matrix cross section between the voids and it is, obviously, smaller than the total area A of the cross section. The total area is then referred to as the total cross section area observed macroscopically. The effective area can therefore be expressed as the difference between the total area A and the voided area A_v

$$A_{eff} = A - A_v \tag{2.15}$$

Since the void area fraction is equal to the void volume fraction, i.e. $\omega_A = \omega$, as explained by the principle of Delesse in Chapter 2.6, the voided area A_v is

$$A_v = \omega A \tag{2.16}$$

Thus the effective area can be expressed in terms of the void volume fraction

$$A_{eff} = A(1-\omega) \tag{2.17}$$

An estimate of the effective stress in the polymer matrix σ_{eff} can be found as the applied load F divided by the effective area A_{eff}, i.e. the solid ligaments between the voids [40]

$$\sigma_{eff} = \frac{F}{A_{eff}} \tag{2.18}$$

With Cauchy stress defined as the applied load F divided by the total area A of the cross section

$$\sigma = \frac{F}{A} \tag{2.19}$$

the effective stress can be expressed as

$$\sigma_{eff} = \frac{\sigma}{(1-\omega)} \tag{2.20}$$

2.8 THE MATERIALS IN THIS STUDY

The study presented in this monograph is a part of a larger research project about constitutive modelling of the mechanical behaviour of thermoplastics. It involves material testing and validation of the constitutive model in terms of benchmark tests. In this context, 5 mm and 10 mm thick extruded sheets of PVC and HDPE were bought from the supplier SIMONA. The in-plane dimensions of the sheets were 2·1 m^2. According to SIMONA, the 5 mm and the 10 mm plates consist of the same materials. The intention by the choice of these particular materials was to cover two different types of thermoplastics: The PVC is amorphous and the HDPE is semicrystalline. The fundamental behaviour of the materials has earlier been investigated [41, 42]. All tests in this monograph have been performed on these materials.

2.8.1 PVC

The PVC is by the supplier denoted SIMONA®PVC-TF [43]. SIMONA reports that it has excellent formability, high weather ability, high rigidity, increased impact strength and a low coefficient of thermal expansion. Typical material data provided by SIMONA is listed in Table 2.1.

Table 2.1 *Material data for SIMONA®PVC-TF as provided by SIMONA [43].*

Density [kg/m^3]	Yield stress [MPa]	E-modulus [MPa]	Elongation at break [%]	Application temperature range [°C]	Thermal coefficient of elongation [K^{-1}]
1430	53	3000	20	–10 to +60	$0.8 \cdot 10^{-4}$

Moura et al. [41] found that there were some minor direction dependency in the 10 mm thick extruded plates of PVC. This was done by employing tensile tests machined out at 0°, 45°, and 90° to the extrusion direction, and compression tests from the in-plane and the out-of-plane directions. For modelling purposes however, the material has been treated as isotropic, with good results [42]. Moreover, transverse isotropy has been confirmed to be a good assumption regarding the strain in the width- and thickness-direction [41].

Hovden [42] carried out an experimental test programme involving tension and compression tests of the 10 mm thick extruded plates of PVC. Stress-strain curves and evolution of volume strain from these tests are presented in Figure 2.8 and Figure 2.9. The figures include results from different strain rates. All specimens were taken from the extrusion direction of the plate, except from the compression specimen deformed at a nominal strain rate 10^{-2} s^{-1} which was taken from the out-of-plane direction. The strains in the tension tests and the compression tests deformed at nominal strain rate 10^{-2} s^{-1} were determined by digital image correlation (DIC). The strains in the other compression tests were determined from diameter and height measurements.

According to Figure 2.8 the response of the PVC is linear elastic before a local stress maximum is reached. The local maximum on is interpreted as the yield stress [42]. Stress softening follows after the peak stress before strain re-hardening sets in when the strain gets larger. It is seen that the yield stress increases with increasing strain rate. Moreover, the yield stress is higher in compression than in tension. Addressing the volume strains in Figure 2.9, it is interesting to see that the volume

increases for plastic deformation in uniaxial tension. The volume strains in compression remain close to zero.

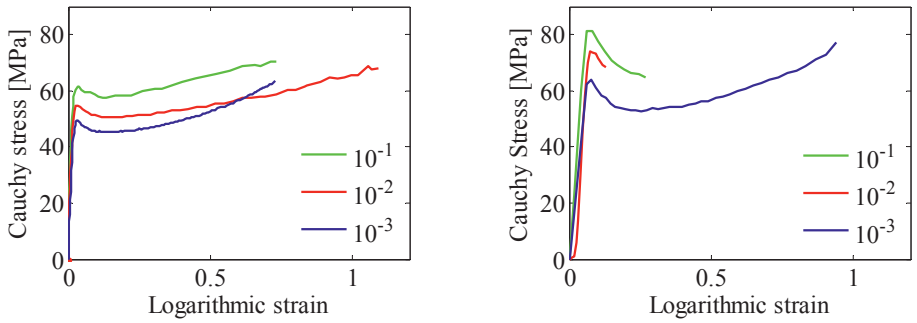

Figure 2.8 *Stress-strain curves for material from the 10 mm thick plates of mineral filled PVC at three different nominal strain rates. a) Uniaxial tension. b) Uniaxial compression. The data is taken from Hovden [42].*

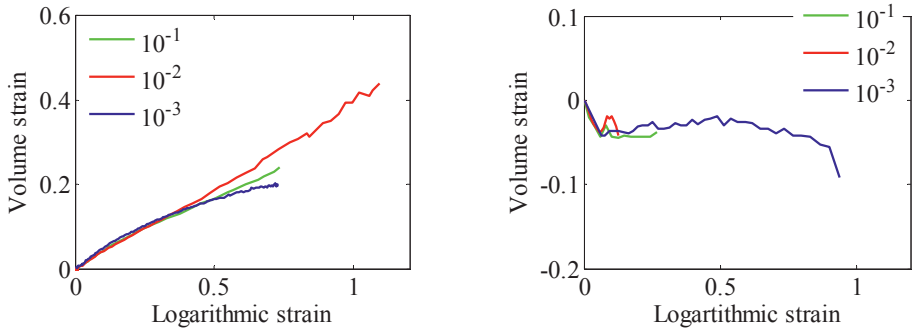

Figure 2.9 *Logarithmic volume strain plotted against logarithmic longitudinal strain for material from the 10 mm thick plates of mineral filled PVC at three different nominal strain rates. a) Uniaxial tension. b) Uniaxial compression. The data is taken from Hovden [42].*

In the technical data sheet provided by SIMONA it was not found information about any filler added to the PVC. However, investigation of the material from a 10 mm plate in a scanning electron microscope (SEM) revealed that it contained some particles, as seen in Figure 2.10. The 5 mm plate appeared similarly in the SEM.

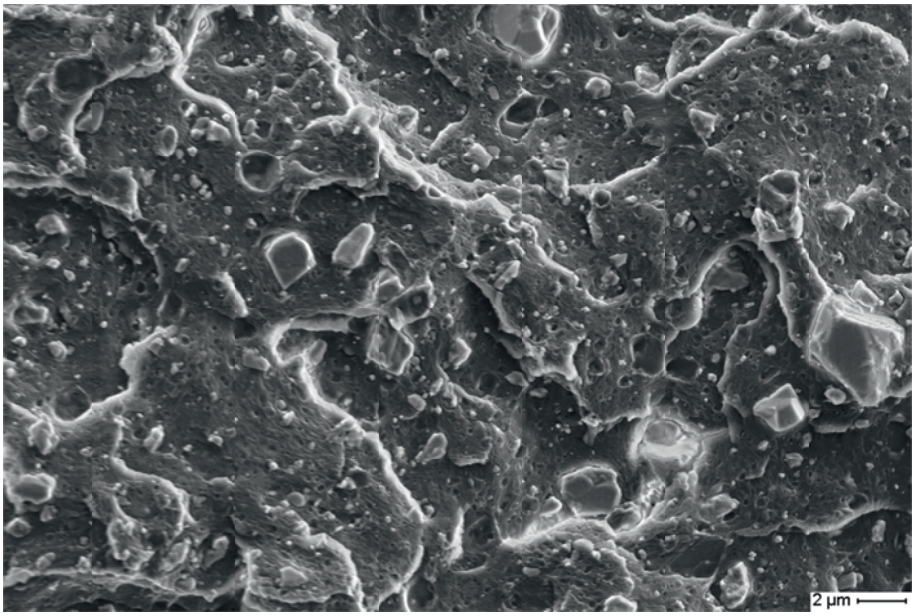

a)

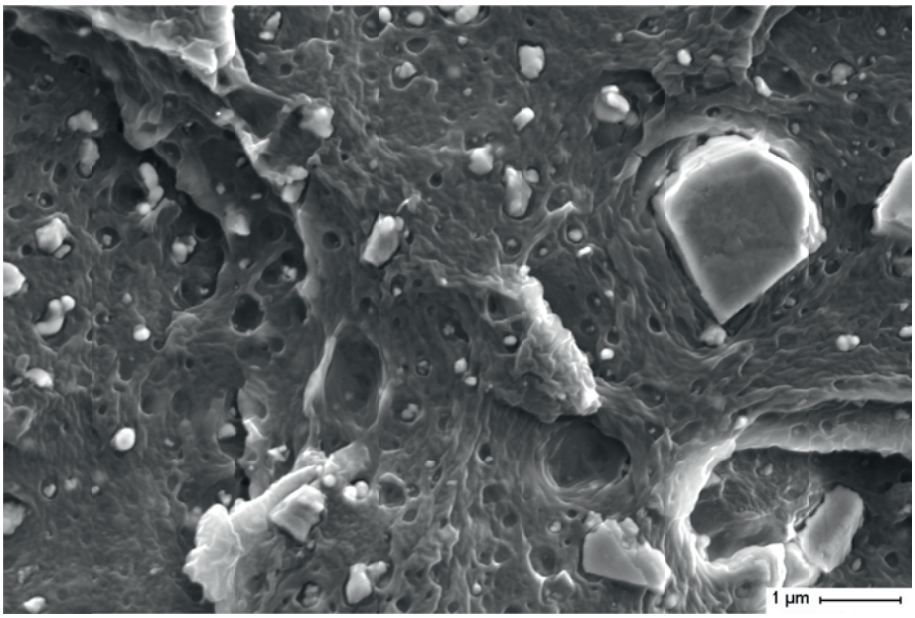

b)

Figure 2.10 *SEM micrograph of a cryogenic fracture surface of 10 mm thick sheet of the mineral filled PVC at a) moderate and b) high magnification.*

Prior to the SEM investigations, the material was stored in liquid nitrogen for 30 minutes before it was split in two. This was done to obtain brittle fracture, without introducing any plastic deformation. The fracture surface was prepared by carbon sputtering before it was investigated in the SEM. SEM micrographs of deformed PVC revealed voids had formed around the particles. This will be further discussed in Chapter 6.

By identifying the area covered by particles in Figure 2.10 a) and employing the principle of Delesse, the particle volume fraction ω was estimated to be around 0.2. The particle identification process will be presented in Chapter 6.

One of the larger particles in Figure 2.10 was analysed by energy dispersive spectroscopy (EDS), which is a built-in tool of the SEM. The EDS resulted in the spectrogram presented in Figure 2.11 a). Both Ca and Ti have numerous counts, suggesting particles made out of calcium carbonate ($CaCO_3$), which is the most common filler in PVC [25], and titanium dioxide (TiO_2), the second most common filler. A high peak for Cl is also observed. The EDS does not provide information from exactly one point, it also includes some information from the surrounding matrix, thereby hitting some Cl atoms. A spectrogram presenting the contents of the matrix is shown in Figure 2.11 b). From the results of EDS spectroscopy we can expect that the particles have a rather stiff mechanical response compared to the PVC matrix.

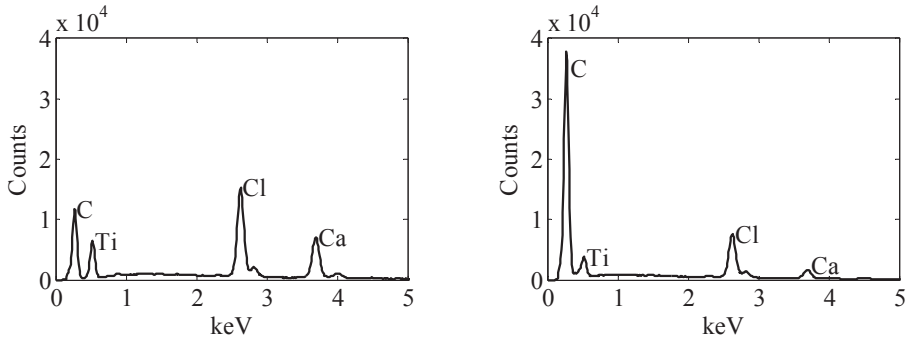

Figure 2.11 *EDS spectrums of a) a 2μm particle and b) the matrix material.*

Results from a termograviometric analysis (TGA) performed at Eindhoven University of Technology state that the PVC contains around 45 wt% solid filler.

2.8.2 HDPE

The HDPE employed in this study is denoted SIMONA®PE-HWU by the supplier [44]. It is reported to be very tough even at low temperatures and to have good sliding properties and good processing and machining characteristics. In addition, the black polymer has a high UV-protection. The crystalline melting range for the polymer is 126-130 °C. Additional data for the material is listed in Table 2.2.

Table 2.2 *Material data for SIMONA®PE-HWU as provided by SIMONA [44].*

Density	Yield stress	E-modulus	Elongation at tear	Application temperature range	Thermal coefficient of elongation
[kg/m^3]	[MPa]	[MPa]	[%]	[°C]	[K^{-1}]
950	22	800	300	–50 to +70	$1.8 \cdot 10^{-4}$

According to Moura et al. [41], tests performed on specimens the 10 mm thick plates of HDPE cut out at 0°, 45°, and 90° to the extrusion direction revealed almost no direction dependency of the material. They also showed that there was no difference between the transverse strains, and therefore concluded that transverse deformation isotropy was a sound assumption also for this material.

Figure 2.12 and Figure 2.13 show the response of specimens cut from the 10 mm thick plates of HDPE in tension and compression. The data is collected from Hovden [42]. All specimens were taken from the extrusion direction of the material. DIC was employed to collect the strains in the tension tests, while the strains in the compression tests were calculated from height and diameter measurements.

In Figure 2.12 it is seen that after yielding, progressive strain hardening is present. There is no stress softening, thus no peak stress. Also, the yield stress increases with increasing strain rate. There seems to be no difference in the yield stress in tension and compression. The volume strains plotted in Figure 2.13 reveal that there is hardly any volume change when the HDPE is deformed at moderate strain rates. However, from the figure, it appears as if the volume change increases with increasing strain rate. It is uncertain whether this can be an artefact from poor test data.

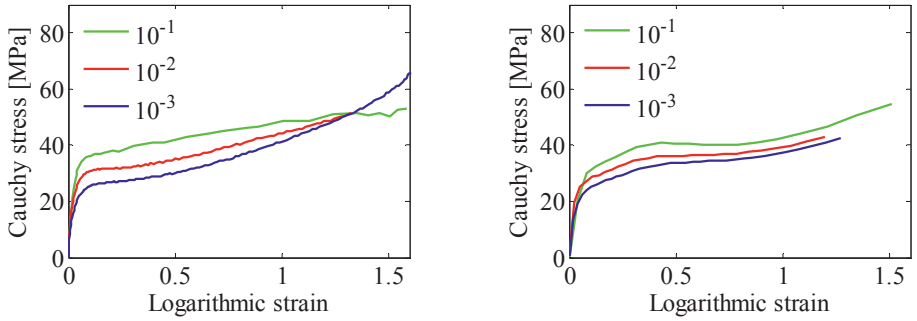

Figure 2.12 *Stress strain curves for material from the 10 mm thick plates of HDPE at three different nominal strain rates. a) Uniaxial tension. b) Uniaxial compression. The data is taken from Hovden [42].*

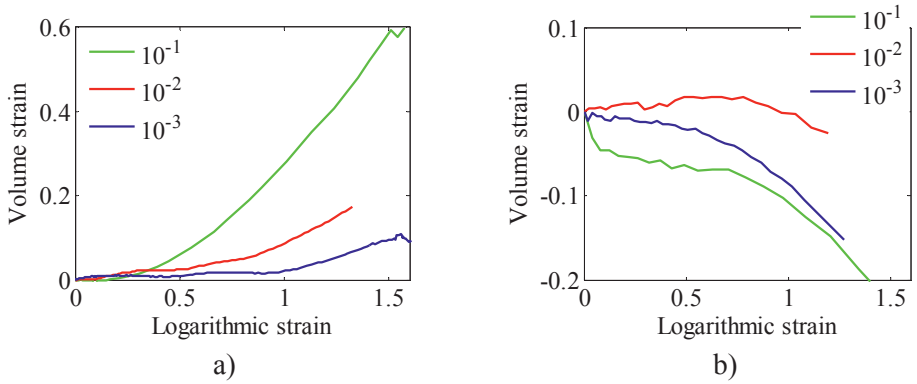

Figure 2.13 *Logarithmic volume strain plotted against logarithmic longitudinal strain for material from the 10 mm thick plates of HDPE at three different nominal strain rates. a) Uniaxial tension. b) Uniaxial compression. The data is taken from Hovden [42].*

Scanning electron micrographs of a fracture surface of the 10 mm thick sheet of HDPE is shown in Figure 2.14. The 5 mm sheet appeared similarly in the SEM. The fracture was imposed after storing the polymer in liquid nitrogen for 30 minutes. The fracture surface has been coated by carbon dust. It can be seen that some particles have been added also to this material. However, they were too small for characterization by EDS.

TGA measurements performed at Eindhoven University of technology state that the weight percent of solid filler in the HDPE is around 10 wt%.

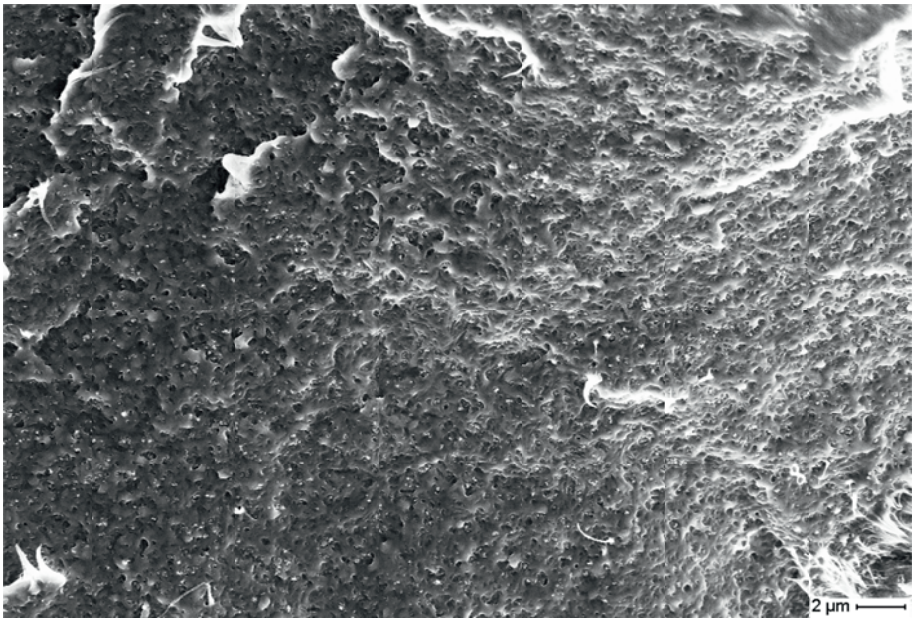

a)

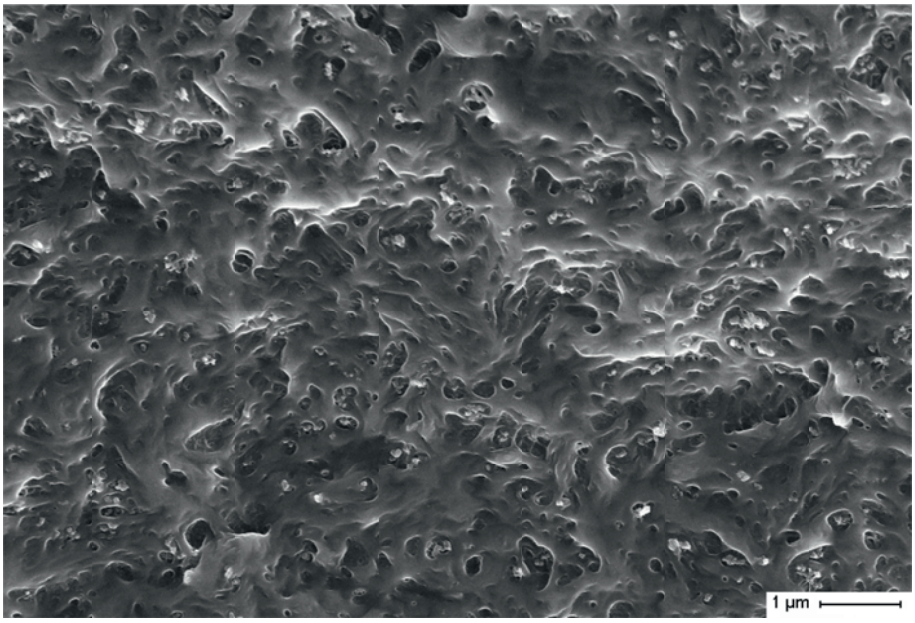

b)

Figure 2.14 *SEM micrograph of a cryogenic fracture surface of 5mm thick sheet of HDPE at a) moderate and b) high magnification.*

2.9 SUMMARY

Typical observations found in the literature for the macroscopic deformation of some thermoplastic polymer materials are:

- Macroscopic pressure sensitivity, i.e. a higher yield stress in compression than in tension.
- Stress softening.
- Plastic dilation.
- Void growth.
- Crazing.
- Strain rate sensitivity.
- Temperature sensitivity.

The four first bullet points will be further discussed in the following chapters.

Turning attention to the PVC and the HDPE materials addressed in this monograph, typical characteristics are:

The PVC:

- Amorphous thermoplastic.
- Contains a volume fraction of about 0.2 of mineral filler, primarily $CaCO_3$.
- Exhibits a higher yield stress in compression than tension.
- Dilation in plastic deformation.
- Stress softening.
- Void growth.

The HDPE:

- Semicrystalline thermoplastic.
- Contains minor amounts of solid filler.
- The yield stress is not pressure sensitive.
- Hardly any plastic dilation in uniaxial tension (at a strain rate of $10^{-3}\ s^{-1}$)
- No stress softening.

REFERENCES

[1] N.G. McCrum, C.B. Bucknall, C.P. Buckley. *Principles of polymer engineering.* Oxford University Press, Oxford (1997).

[2] Glad. www.glad.com.au/about-glad/for-students 27.06 (2012)

[3] M.J.N. Jacobs, J.L.J. Van Dingenen. Ballistic protection mechanisms in personal armour. *Journal of Materials Science*, **36** (2001), 3137-3142.

[4] H.-G. Elias. *An introduction to plastics.* Wiley-VCH, Weinheim (2003).

[5] I.M. Ward, J. Sweeney. *An introduction to the mechanical properties of solid polymers.* John Wiley and sons, Ltd, Chichester (2004).

[6] F. Zerilli, R. Armstrong. A constitutive equation for the dynamic deformation behavior of polymers. *Journal of Materials Science*, **42** (2007), 4562-4574.

[7] J. Lemaitre, J.-L. Chaboche. *Mechanics of solid materials.* Cambridge University Press, Cambridge (1990).

[8] G.A. Holzapfel. *Nonlinear solid mechanics. A continuum approach for engineering.*, John Wiley and sons, Ltd, (2001).

[9] N.J. Mills. Plastics - Microstructure and Applications (3rd Edition), Elsevier, 2005.

[10] A.A. Galeski. Strength and toughness of crystalline polymer systems. *Progress in Polymer Science*, **28** (2003), 1643-1699.

[11] G.W. Ehrenstein. *Polymeric materials: structure, properties, applications.* Hanser, Munich (2001).

[12] P. Chandran, S. Jabarin. Biaxial Orientation of Poly(ethylene Terephtalate). Part I: Nature of the Stress-Strain Curves. *Advances in Polymer Technology*, **12** (1993), 119-132.

[13] D.R.H. Jones, M. Ashby. *Engineering Materials, Volume 2: An Introduction to Microstructures, Processing and Design (2nd Edition).* Elsevier Butterworth-Heinemann, (1998).

[14] L.C.E. Struik. Physical aging in plastics and other glassy materials. *Polymer Engineering & Science*, **17** (1977), 165-173.

[15] G.B. McKenna. Mechanical rejuvenation in polymer glasses: fact or fallacy? *Journal of Physics-Condensed Matter*, **15** (2003), S737-S763.

[16] H.E.H. Meijer, L.E. Govaert. Mechanical performance of polymer systems: The relation between structure and properties. *Progress in Polymer Science*, **30** (2005), 915-938.

[17] O.A. Hasan, M.C. Boyce. Energy storage during inelastic deformation of glassy polymers. *Polymer*, **34** (1993), 5085-5092.

[18] L.E. Govaert, H.G.H. van Melick, H.E.H. Meijer. Temporary toughening of polystyrene through mechanical pre-conditioning. *Polymer*, **42** (2001), 1271-1274.

[19] Z. Bartczak, A.S. Argon, R.E. Cohen, M. Weinberg. Toughness mechanism in semi-crystalline polymer blends: I. High-density polyethylene toughened with rubbers. *Polymer*, **40** (1999), 2331-2346.

[20] Z. Bartczak, A.S. Argon, R.E. Cohen, M. Weinberg. Toughness mechanism in semi-crystalline polymer blends: II. High-density polyethylene toughened with calcium carbonate filler particles. *Polymer*, **40** (1999), 2347-2365.

[21] A.S. Argon, R.E. Cohen. Toughenability of polymers. *Polymer*, **44** (2003), 6013-6032.

[22] I. Kemal, A. Whittle, R. Burford, T. Vodenitcharova, M. Hoffman. Toughening of unmodified polyvinylchloride through the addition of nanoparticulate calcium carbonate. *Polymer*, **50** (2009), 4066-4079.

[23] S. Mishra, G.B. Perumal, J.B. Naik. Studies on Mechanical Properties of Polyvinyl Chloride Composites. *Polymer-Plastics Technology and Engineering*, **36** (1997), 489-500.

[24] F. Addiego, J.D. Martino, D. Ruch, A. Dahoun, O. Godard, S. Patlazhan. Quantification of Cavitation in Neat and Calcium Carbonate-Filled High-Density Polyethylene Subjected to Tension. *Journal of Engineering Materials and Technology*, **133** (2011), 030904.

[25] R.F. Grossman. *Handbook of vinyl formulating.* Wiley-Interscience, Hoboken, N.J. (2008).

[26] H.S. Katz, J.V. Milewski. *Handbook of fillers for plastics.* Van Nostrand Reinhold Co., New York (1987).

[27] Y. Nakamura, S. Okabe, N. Yoshimoto, T. Iida. Effect of particle shape on the mechanical properties of particle-filled PVC. *Polymers & Polymer Composites*, **6** (1998), 407-414.

[28] S. Sun, C. Li, L. Zhang, H.L. Du, J.S. Burnell-Gray. Interfacial structures and mechanical properties of PVC composites reinforced by CaCO3 with different particle sizes and surface treatments. *Polymer International*, **55** (2006), 158-164.

[29] N. Chen, C. Wan, Y. Zhang, Y. Zhang. Effect of nano-CaCO3 on mechanical properties of PVC and PVC/Blendex blend. *Polymer Testing*, **23** (2004), 169-174.

[30] S. Socrate, M.C. Boyce. Micromechanics of toughened polycarbonate. *Journal of the Mechanics and Physics of Solids*, **48** (2000), 233-273.

[31] R. Bagheri, R.A. Pearson. The use of microvoids to toughen polymers. *Polymer*, **36** (1995), 4883-4885.

[32] S. Wu. Phase structure and adhesion in polymer blends: A criterion for rubber toughening. *Polymer*, **26** (1985), 1855-1863.

[33] E.R. Weibel. *Stereological methods - Practical Methods for Biological Morphometry.* Academic Press, London (1979).

[34] J. Ohser, F. Mücklich. *Statistical analysis of microstructures in materials science.* John Wiley, New York (2000).

[35] E.R. Weibel. *Stereological methods - Theoretical foundations.* Academic Press, London (1980).

[36] ImageJ - Image Processing and Analysis in Java, 2012.

[37] T. Belytschko, W.K. Liu, B. Moran. *Nonlinear finite elements for continua and structures.* Wiley, Chichester (2000).

[38] C.C. Chu, A. Needleman. Void Nucleation effects in Biaxially Stretched Sheets. *Journal of Engineering Materials and Technology*, **102** (1980), 249-256.

[39] H.-Y. Jeong. A new yield function and a hydrostatic stress-controlled void nucleation model for porous solids with pressure-sensitive matrices. *International Journal of Solids and Structures*, **39** (2002), 1385-1403.

[40] J. Lemaitre, R. Desmorat. *Engineering Damage Mechanics: Ductile, Creep, Fatigue and Brittle Failures.* Springer-Verlag Berlin Heidelberg, Berlin, Heidelberg (2005).

[41] R.T. Moura, A.H. Clausen, E. Fagerholt, M. Alves, M. Langseth. Impact on HDPE and PVC plates - Experimental tests and numerical simulations. *International Journal of Impact Engineering*, **37** (2010), 580-598.

[42] M.T. Hovden. Test and numerical simulations of polymer components. Master thesis, Department of Structural Engineering, NTNU, (2010).

[43] SIMONA. Product Information PVC-TF, SIMONA.

[44] SIMONA. Product Information PE-HWU / PE-HWST, SIMONA.

PART I

EXPERIMENTAL STUDY

CHAPTER 3

UNIAXIAL TENSION

Uniaxial tensile tests were carried out to achieve basic information about the behaviour of the 5 mm plates of PVC and HDPE.

3.1 INTRODUCTION

The uniaxial tensile test is probably the most common material test. From laboratory tests on a simple standard "dog bone" shaped test specimen, as the one in Figure 3.1, basic information about the material behaviour is disclosed. This study addresses the mechanical response of a mineral filled PVC and HDPE from extruded plates of 5 mm thickness. As mentioned in Chapter 2, similar tests have earlier been performed by Hovden [1] on the same material types, but from extruded plates of 10 mm thickness. It has turned out that although the 5 mm and 10 mm plates, according to the producer, are made of the same materials their mechanical responses are somewhat different. Results from tension tests from the 10 mm plates of these materials are also reported by Moura et al. [2]. However, Moura et al. used tensile specimen with a small pre-machined imperfection. In our study it was chosen to employ specimens without any imperfection to avoid any undesirable effects. Results from the tests in this chapter will later, in Chapter 10, be used in identification of parameters for the material model of Polanco-Loria et al. [3].

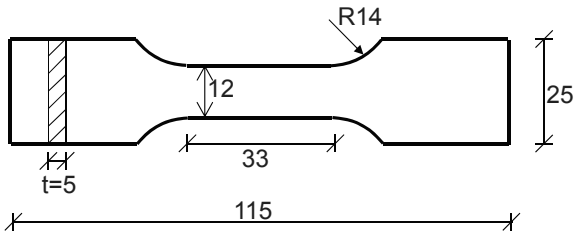

Figure 3.1 *Geometry of tensile test specimen. Measures are given in mm.*

3.2 TEST SETUP

Test specimens according to Figure 3.1 were cut from larger plates of 5 mm thickness both parallel and normal to the extrusion direction. Two materials were addressed. The first material was a mineral filled PVC. The particle volume fraction ω was assumed to be equal to that in the 10 mm thick PVC plates, i.e. ω ~ 0.2. The second material was a HDPE. It also contains some fillers, but in a much less amount. Both materials are further described in Chapter 2.8.

A servo-hydraulic Dartec machine with a 20 kN load cell connected to an Instron controller was employed to carry out the tests. The specimens were clamped at both ends. One end was fixed while the other was displaced at a pre-defined velocity of 0.033 mm/s, which corresponds to a nominal strain rate $\dot{\varepsilon}_{nom} = 10^{-3}$ s^{-1}. The deformation was monitored by a charge-coupled device (CCD) camera. The CCD camera captured images of the deformation at 0.1 Hz. It has earlier been shown that transverse isotropy is a good approximation for these materials [1, 2]. Therefore the in-plane stress field was adequate for establishing stress-strain curves so only one camera was employed in the tests. Also, any stress triaxiality caused by necking was neglected. All tests were carried out in room temperature.

The width and thickness of all specimens were measured with a sliding calliper prior to the testing. In general, two parallel tests were performed for specimens of each material and machining direction, and the force-displacement curves were compared to ensure repeatability of the results. The scatter between the replicates was small.

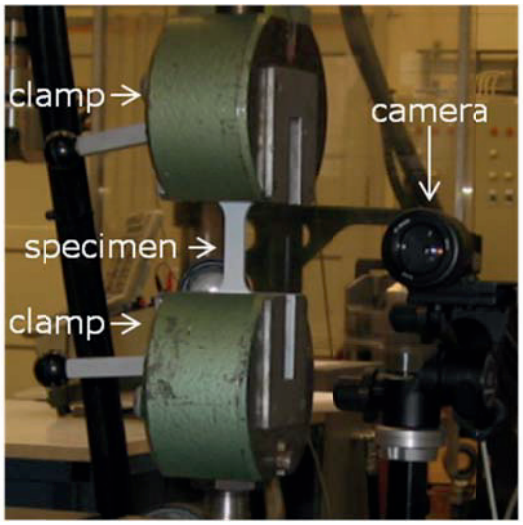

Figure 3.2 *Test setup for uniaxial tensile test. The specimens were clamped at both ends. A CCD-camera was used to monitor the deformation.*

3.3 STRAIN MEASUREMENT

The digital image correlation (DIC) software 7D [4] was used after the tests to obtain the in-plane principal logarithmic strain fields from the images captured by the CCD camera during testing. Before testing a random black and white speckle pattern was applied to each specimen. After the test, the images captured by the CCD camera were loaded into 7D. The displacement field is determined by using grey level correlation of each image with the initial reference image. Prior to this process a grid is defined with a certain number of grid elements. Each grid element refers to the same material point during the entire deformation. The software also provides the option to trace displacements by comparing two and two subsequent images. However, this option was not employed in this study.

From the displacement of each node in the grid element, the software calculates the deformation gradient $\mathbf{F}$. The deformation gradient can be decomposed into pure rotation and pure stretch by polar decomposition [5]

$$\mathbf{F} = \mathbf{R} \cdot \mathbf{U} \tag{3.1}$$

The rotation is represented by the rotation tensor $\mathbf{R}$. The right stretch tensor $\mathbf{U}$ expresses the stretch. The eigenvalues of the stretch tensor are called the principal stretches $\lambda_i, i = 1,2,3$. The principal stretches found from $\mathbf{U}$ represent the ratio

between the deformed length L and the undeformed length L_0 of a material line element in the principal directions of $\mathbf{U}$, $\lambda_i = L_i / L_{i0}$.

The Green-Lagrange strain tensor, or Green strain tensor, $\mathbf{E}$ is calculated from

$$\mathbf{E} = \frac{1}{2}\left(\mathbf{F}^{\mathbf{T}}\mathbf{F} - \mathbf{I}\right) \tag{3.2}$$

Applying the principal stretches, the Green strains in the principal directions are

$$E_i = \frac{1}{2}\left(\lambda_i^2 - 1\right) \tag{3.3}$$

The logarithmic strain tensor is defined as

$$\boldsymbol{\varepsilon} = \ln\left(\mathbf{U}\right) \tag{3.4}$$

The principal logarithmic strains can also be found directly from the principal stretches

$$\varepsilon_i = \ln\left(\lambda_i\right) = \ln\left(\frac{L_i}{L_{i0}}\right) \tag{3.5}$$

In this study the major and minor logarithmic strain fields were exported from 7D to MATLAB where the rest of the test post processing was carried out.

In the following, it is assumed that the direction of the major principal strain is aligned with the longitudinal direction of the specimen. This means that the major principal strain is taken as the longitudinal strain and the minor principal strain is taken as the transverse strain. The validity of this assumption will be discussed later.

Further, the stress and strain calculations in the following are based on the major principal strain ε_1 and the minor principal strain ε_2 from the cross section first experiencing necking, i.e. where strain localization was first observed. Figure 3.3 shows an example of the major logarithmic strain field in a uniaxial tensile test of PVC during onset of strain localization. The black square indicates the element used for extracting strains in this chapter. When the representative grid element was chosen, the entire strain history was taken from this grid element.

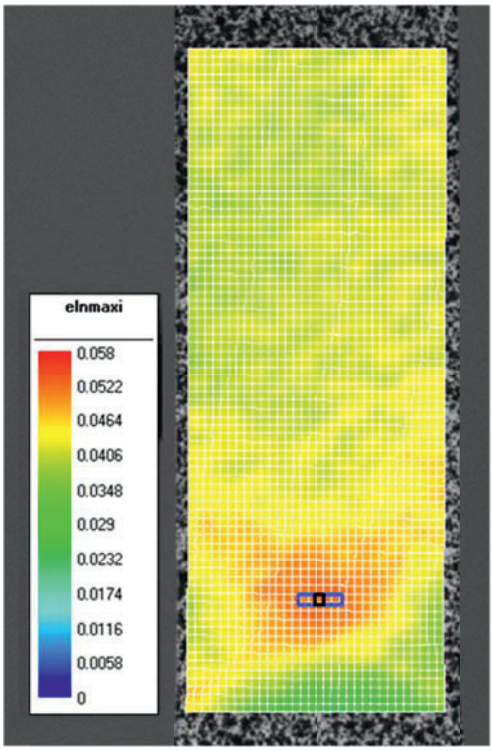

Figure 3.3 *Example of strain localization in the major principal logarithmic strain field in a uniaxial PVC tensile test.*

Similar to other measurement techniques also DIC involves some degree of measurement noise. This can be seen as variation in the strain field in Figure 3.3. The noise originates from noise in the grey level images captured by the camera. It appears as high frequent spatial noise in the displacement field. The relationship between strain and displacement is obtained by numerical differentiation. When the strains are computed, the numerical differentiation can amplify the noise in the displacement field [6]. Also, a poor speckle pattern with low contrast can reduce the quality of the DIC results. A solution for post processing of tests with measurement noise is to average the strains from some grid elements over the cross section as indicated by the blue rectangle in Figure 3.3.

3.4 STRESS AND STRAIN CALCULATIONS

The applied force F was recorded by the Instron controller. In this chapter, the strains are taken from one grid element from the DIC process of PVC and HDPE.

The strains in this grid element, see Figure 3.3, are assumed to be representative for the strain through the cross section of the specimen. This means that the strain field is assumed to be homogenous through the cross section. By assuming transverse isotropy [1, 2] , i.e. that the two transverse strains ε_2 and ε_3 are equal

$$\varepsilon_2 = \varepsilon_3 \tag{3.6}$$

the Cauchy stress σ can be determined.

The width w of the test specimen during the deformation is

$$w = w_0 \exp(\varepsilon_2) \tag{3.7}$$

and the thickness t of the specimen is

$$t = t_0 \exp(\varepsilon_2) \tag{3.8}$$

where w_0 and t_0 are the width and thickness measured on the sample before the test.

This gives the current cross section area A

$$A = t \cdot w = w_0 t_0 \exp\left(2\varepsilon_2\right) \tag{3.9}$$

and the Cauchy stress

$$\sigma = \frac{F}{A} \tag{3.10}$$

Still assuming transverse isotropy, we get the volume strain ε_v

$$\varepsilon_v = \varepsilon_1 + 2\varepsilon_2 \tag{3.11}$$

3.5 RESULTS

Typical force-displacement relationships for two representative specimens of PVC are shown in Figure 3.4. One of the specimens was cut out parallel, 0°, to the extrusion direction while the other was cut out normal, 90°, to the extrusion direction. The test data reveal some anisotropy of the material. There is about 6% difference in the maximum force level obtained from the two directions.

At maximum force it was observed that the PVC specimens gradually started to whiten. As the deformation continued, the stress whitening became clearer. Also a neck started to form at the same location as onset of stress whitening. The stress whitening zone and the neck propagated through the parallel section of the specimen during the deformation. Inspection of a test specimen from an interrupted test indicated that the stress whitening zone is somewhat longer than the necked zone with reduced cross section area. This suggests that the stress whitening zone has propagated slightly in front of the neck. When the neck covered the total parallel section, the specimens in the two tests addressed in Figure 3.4 fractured.

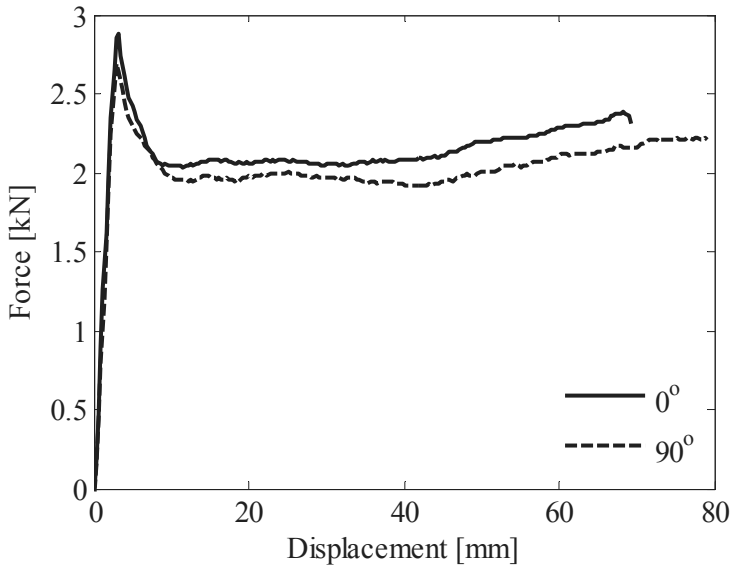

Figure 3.4 *Force-displacement curves for PVC specimens in uniaxial tension. The solid line represents specimens taken out at 0° to the extrusion direction of the plates. The dashed line represents specimen taken out at 90° to the extrusion direction of the plates.*

Figure 3.5 shows typical force-displacement relationships for HDPE specimens. In a similar way as in Figure 3.4, results from one specimen cut out parallel, 0°, to the extrusion direction and one cut out normal, 90°, to the extrusion direction are included in the figure. The difference in maximum force between the two samples is less than 1 %.

Also in the HDPE specimens necking occurred. However, no stress whitening was observed in any of these samples. Moreover, the HDPE specimens appeared rather ductile. All tests were aborted after some deformation because the maximum stroke length of the testing machine was 100 mm, which was insufficient to fracture the HDPE samples. Therefore none of these specimens were deformed until fracture.

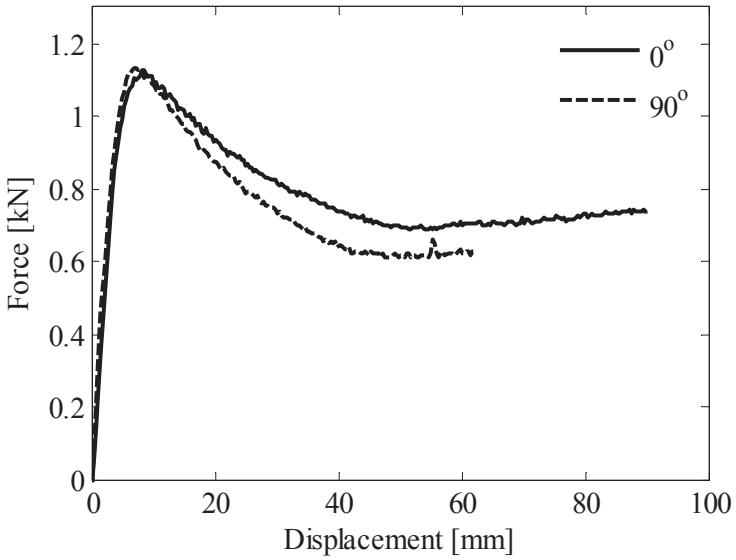

Figure 3.5 *Force-displacement curves for HDPE specimens in uniaxial tension. The solid lines represent specimens taken out at 0° to the extrusion direction of the plates. The dashed lines represent specimen taken out at 90° to the extrusion direction of the plates.*

From this point the specimens cut in the extrusion direction, i.e. 0°, will be regarded. These data will later be used as basis for determination of parameters for the material model proposed by Polanco-Loria et al. [3].

The grid used by the DIC software to obtain the strain fields in the representative PVC specimen is shown in Figure 3.6 a). The field of major principal logarithmic strain for the PVC specimen at different deformation levels is shown in Figure 3.6 b) to f). It is seen that after a certain deformation, the strain localizes and a neck is formed. With further deformation the neck propagates through the parallel section of the specimen.

The grid used by the DIC software to obtain the strain fields in the HDPE specimen is shown in Figure 3.7 a). Sub-figures b) to f) show the major principal logarithmic strain at different strain levels. Although not as distinct as in PVC, the strain also localizes in HDPE. A neck is formed, and it propagates through the parallel section of the specimen when further deformation is applied.

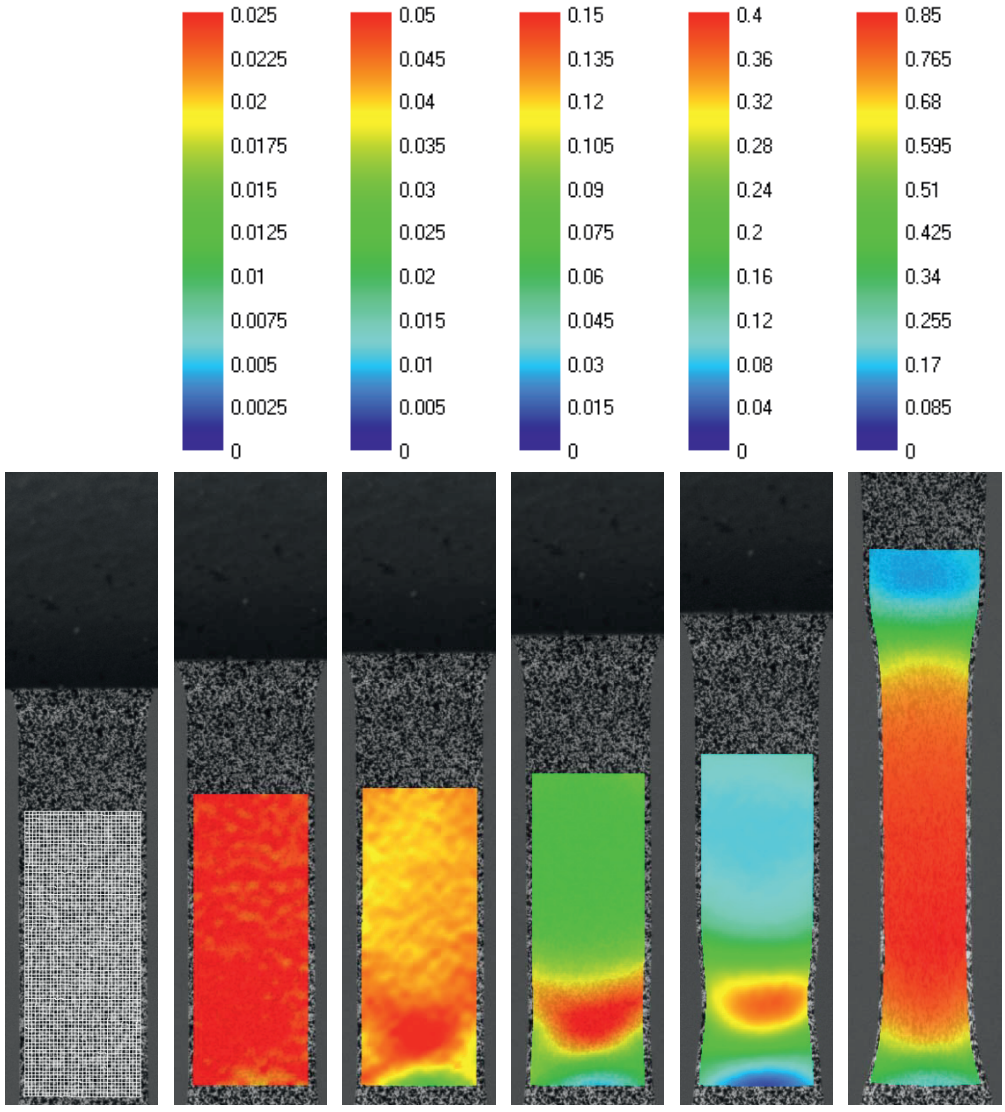

Figure 3.6 *Major principal logarithmic strain field in PVC at different strain levels. a) The grid employed by the DIC software to calculate the strains. b) Elastic regime. c) Peak stress. d) Local stress minimum. e) The state of highest strain rate in the minimum cross section. f) With propagated neck.*

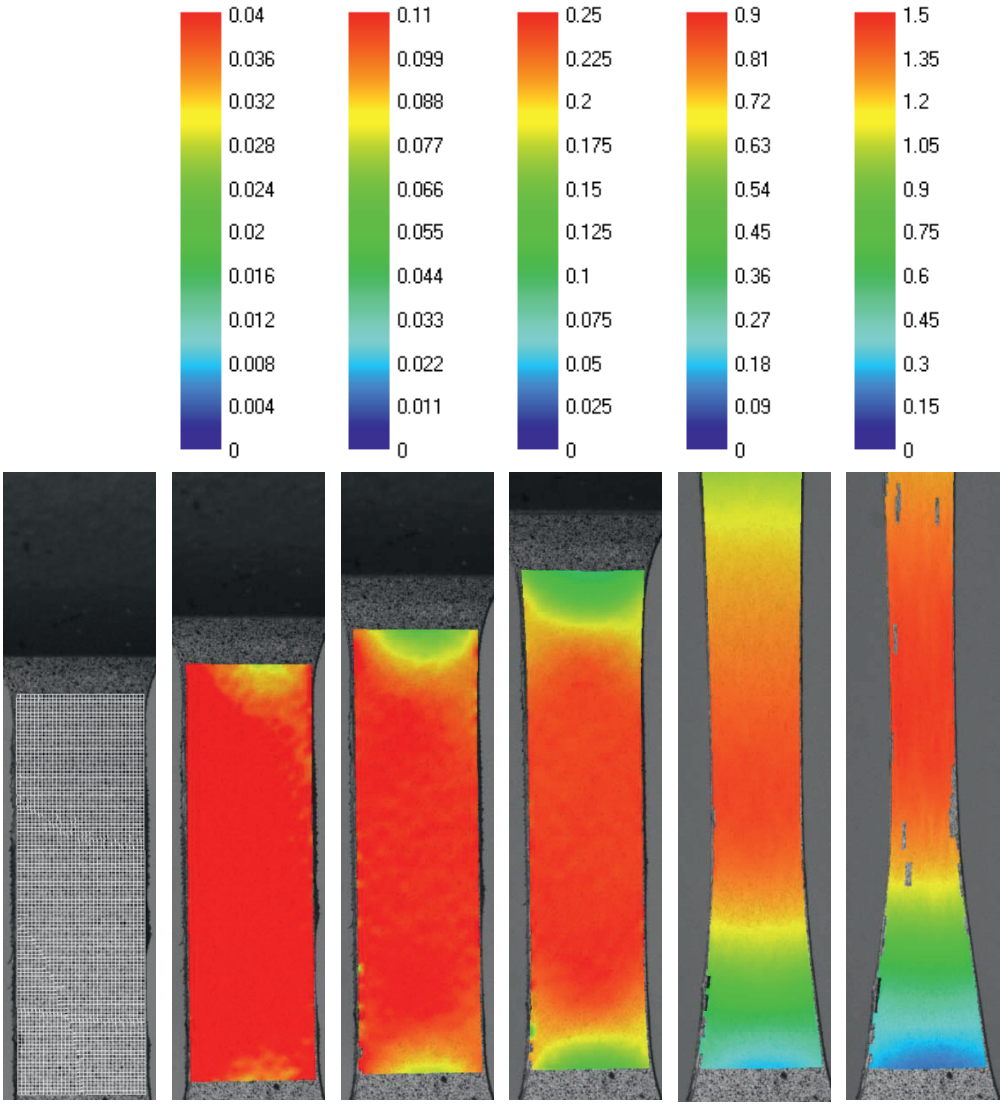

Figure 3.7 *Major principal logarithmic strain field in HDPE at different strain levels. a) The grid employed by the DIC software to calculate the strains. b) Elastic regime. c) Close to onset of yielding. d) Close to onset of strain hardening. e) During strain rehardening. f) With propagated neck.*

The stress-strain curve for the PVC is presented in Figure 3.8. In the figure, the Cauchy stress is plotted against logarithmic strain in the longitudinal direction, i.e. the major principal strain ε_1. Unless other is specified, the term logarithmic strain will in the following refer to logarithmic strain in the longitudinal direction. The

stress-strain curve in Figure 3.8 shows a linear response before peak stress, i.e. a local stress maximum, is reached. The local stress maximum coincides with the local force maximum seen in Figure 3.4, and also with the visually observed onset of stress whitening. After the local stress maximum some stress softening sets in before the stress level increases again. This subsequent rise in stress may be elastic, caused by stretching of the polymer chain network. Nevertheless, the phenomenon will be denoted strain rehardening hereafter. It is seen that strain rehardening dominates until the end of the curve. Due to distortion of the speckle pattern the DIC software could not follow the deformation until fracture.

The strain field in the PVC specimen is rather uniform in the elastic domain. This is seen in Figure 3.6 b), displaying the field of major principal logarithmic strain at $\varepsilon_1 = 0.025$. The strain field at peak stress, i.e. $\varepsilon_1 = 0.048$, is seen in Figure 3.6 c). At this strain level it is possible to see that the strain starts to localize. From Figure 3.6 d) it is seen that the strain localization is even stronger in the strain field at the state of the stress minimum, at $\varepsilon_1 = 0.14$. In sub-figure e), at $\varepsilon_1 = 0.36$ it is possible to see the neck as a local contraction of the width of the specimen. With further deformation, the neck has propagated as seen in Figure 3.6 f) showing the major principal strain field at $\varepsilon_1 = 0.85$.

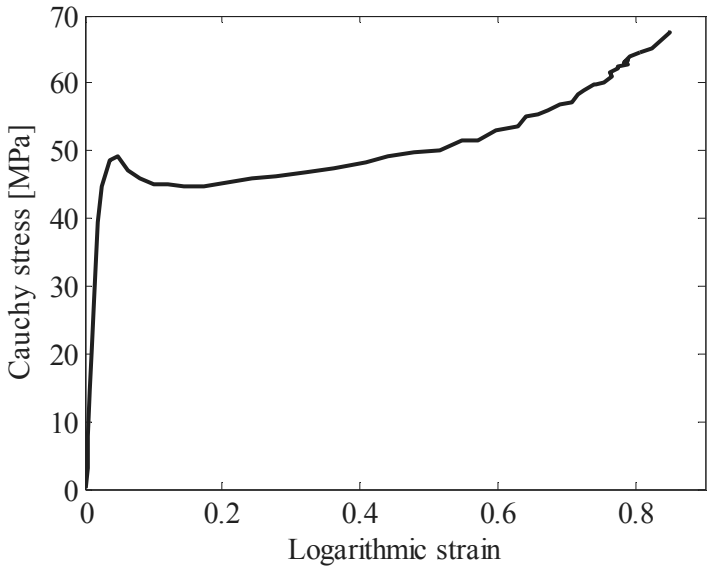

Figure 3.8 *Cauchy stress vs. logarithmic strain in a PVC specimen machined out in the extrusion direction and deformed at a nominal strain rate of* $10^{-3}s^{-1}$.

The stress-strain curve from HDPE is displayed in Figure 3.9. The response is initially linear before it bends off to a lower slope at longitudinal strain around $\varepsilon_1 =$ 0.1. Thereafter the stress increases progressively with strain. Although this behaviour may origin from an elastic contribution, the stress increase is hereafter denoted strain hardening. Since the HPDE test was aborted before fracture, the last logging point in Figure 3.9 does not represent the fracture strain.

The major logarithmic strain field in HDPE at different strain levels was displayed in Figure 3.7. Figure 3.7 b) shows the strain field in the elastic domain of Figure 3.9, at $\varepsilon_1 = 0.040$. The strain field at the strain level $\varepsilon_1 = 0.10$, where the stress-strain curve bends off, is depicted in Figure 3.7 c). Sub figures d), e) and f) represent in turn strain levels of $\varepsilon_1 = 0.24$, $\varepsilon_1 = 0.86$ and $\varepsilon_1 = 1.46$. These are all addressing the strain hardening part of the deformation, as seen in the stress – strain curve in Figure 3.9.

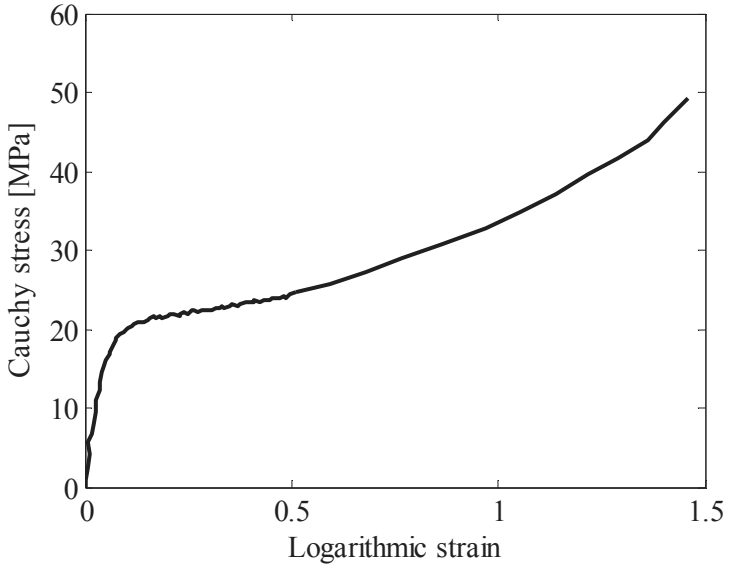

Figure 3.9 *Cauchy stress vs. logarithmic strain in a HDPE specimen machined out in the extrusion direction and deformed at a nominal strain rate of 10^{-3} s^{-1}.*

Figure 3.10 and Figure 3.11 display the longitudinal and the transverse strain, ε_1 and ε_2, in the PVC and the HDPE tests plotted against time. In particular, the strain rate increases at the onset of yielding.

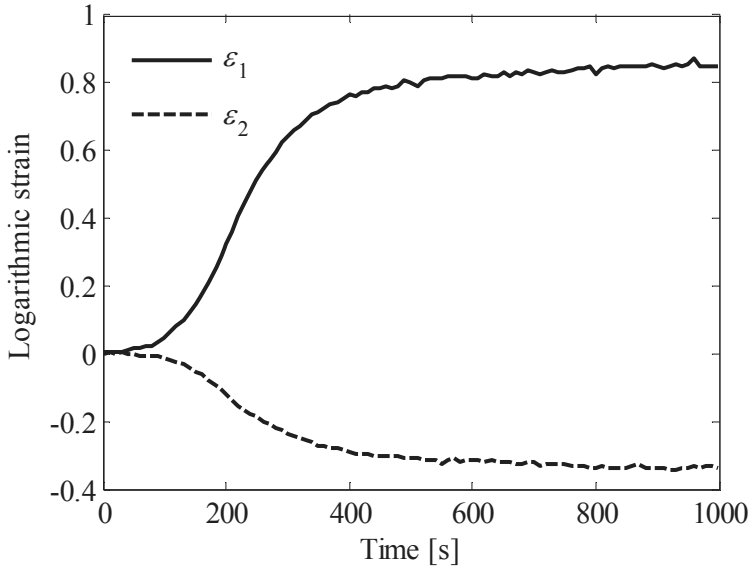

Figure 3.10 *Longitudinal and transverse strain, both taken from a grid element in the cross section first experiencing strain localization, plotted against time for the PVC.*

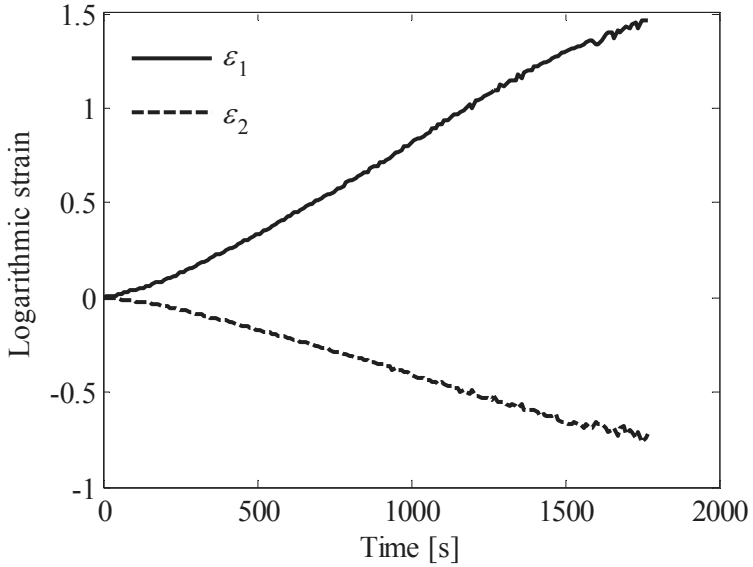

Figure 3.11 *Longitudinal and transverse strain, both taken from a grid element the cross section first experiencing strain localization, plotted against time for the HDPE.*

The slope of the curves in Figure 3.10 and Figure 3.11 represent the strain rate. Therefore the strain rate could be found by numerical differentiation. The strain rates $\mathrm{d}\varepsilon_1 / \mathrm{d}t$ and $\mathrm{d}\varepsilon_2 / \mathrm{d}t$ are plotted against longitudinal strain for PVC in Figure 3.12 and for HDPE in Figure 3.13. Differentiation of data with a moderate noise level give results with large fluctuations. Therefore the strain-time curves were smoothed before the differentiation.

Although the applied deformation rate from the Instron testing machine was constant, the cross section used for extracting strains did not experience a constant strain rate. It is seen that the strain rate in the cross section varies during the deformation. As the strain localizes and a neck is formed, the strain rate in the actual cross section is increasing. When the neck propagates, and the shoulder of the neck moves away from the cross section, the strain rate decreases. The maximum strain rate in PVC, both in longitudinal and transverse direction, occurs at a longitudinal strain of $\varepsilon_1 = 0.36$. This corresponds to a point in the strain rehardening region of the stress-strain curve in Figure 3.8 and to the strain level displayed in Figure 3.6 e). The maximum strain rate is in HDPE at a longitudinal strain of $\varepsilon_1 = 0.86$. This is the deformation stage addressed in Figure 3.7 e). Also this strain corresponds to a point in the strain hardening region, as seen in Figure 3.9.

The volume strains ε_v found from Equation (3.11) for PVC and HDPE are plotted in Figure 3.14 and Figure 3.15. It is clearly seen that PVC dilates during plastic deformation while the volume in HDPE remains almost constant. The variations we see in the volume strain for HDPE is, except at high deformation levels where the precision of the DIC measurements is reduced, within ±0.005, and can most likely be regarded as measurement noise.

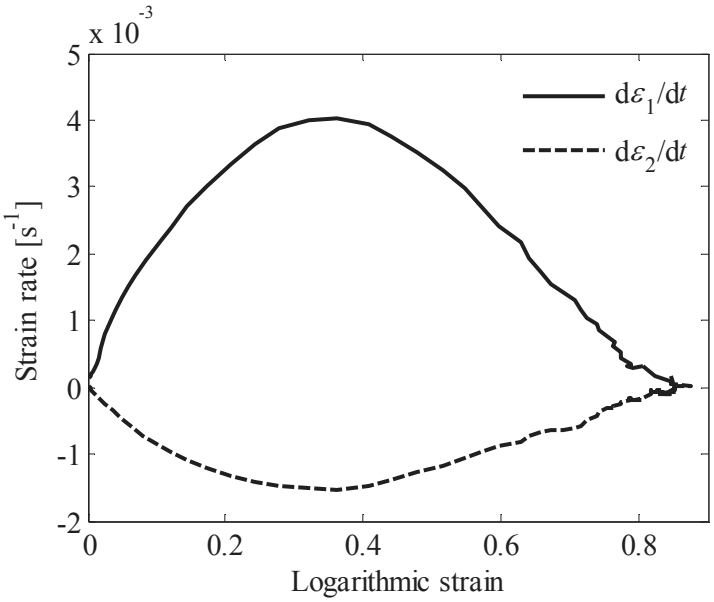

Figure 3.12 *Logarithmic strain rate plotted against longitudinal logarithmic strain for the PVC.*

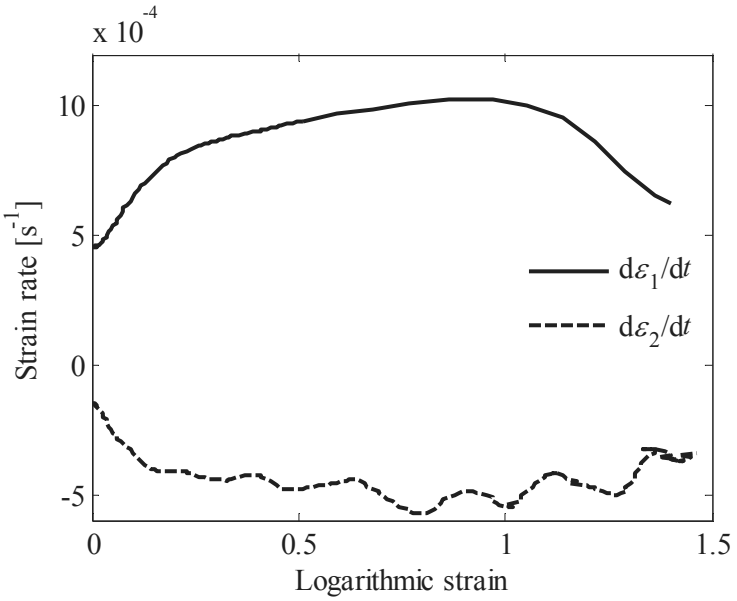

Figure 3.13 *Logarithmic strain rate plotted against longitudinal logarithmic strain for the HDPE.*

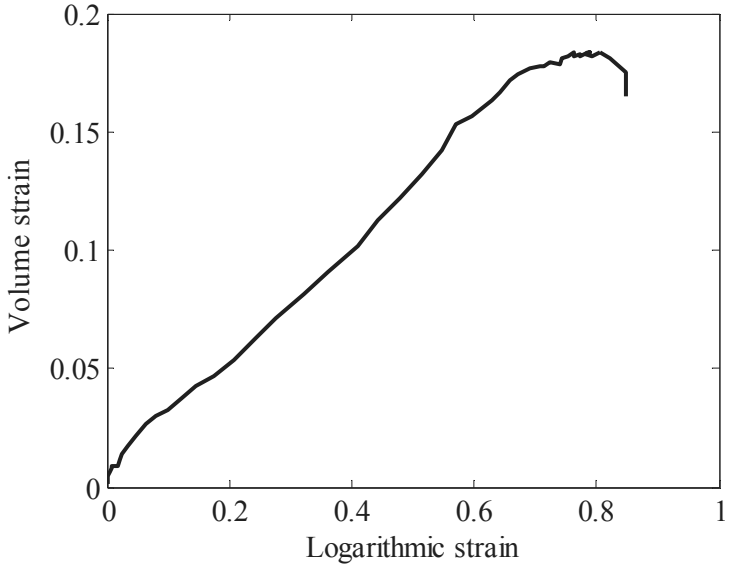

Figure 3.14 *Logarithmic volume strain in the PVC.*

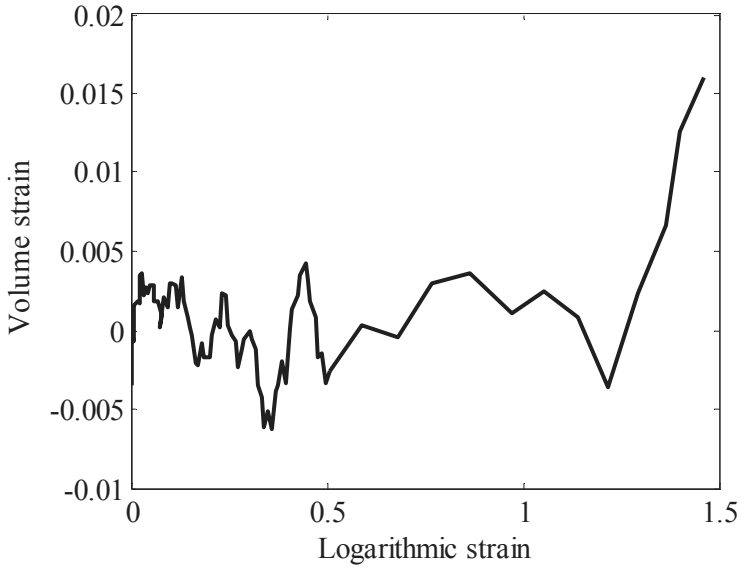

Figure 3.15 *Logarithmic volume strain in the HDPE.*

3.6 DISCUSSION

Uniaxial tension tests were used to acquire basic information of the deformation behaviour of a mineral filled PVC and HDPE. The specimens were cut out from extruded plates of 5 mm thickness both in and normal to the extrusion direction. Little difference was seen between the force-displacement relationships in the two directions, shown in Figure 3.4 and Figure 3.5. Therefore it was decided to treat both materials as isotropic. This has also been regarded as a good approximation by others [1, 2]. During machining of the specimens no reduction of the thickness direction was performed. Therefore possible effects of skin layers originating from the extrusion process are included in the responses reported in this study. This might be a feasible explanation why the behaviour of the 5 mm sheets of PVC and HDPE appears somewhat different from the behaviour of the 10 mm sheets [1] as reported in Chapter 2.8.

The 7D software can provide information of the strain fields in terms of Green strain or logarithmic strain. The logarithmic strains are provided in the principal directions only. The Green strains, however, are provided both in the direction defined by the coordinate axes as well as in the principal directions. In the beginning of this chapter, it was assumed that direction of the major principal strain is aligned with the longitudinal direction of the specimen, i.e. that the principal directions are equal to the directions defined by the coordinate axes. To check the validity of this assumption, the Green strains in the principal directions and in the directions of the coordinate axes were plotted in Figure 3.16 for the PVC test and in Figure 3.17 for the HDPE test. It is seen that the two strain measurements give the same results. Thus, it is reasonable to conclude that the major and minor logarithmic strains, ε_1 and ε_2, can be employed as longitudinal and transverse strains.

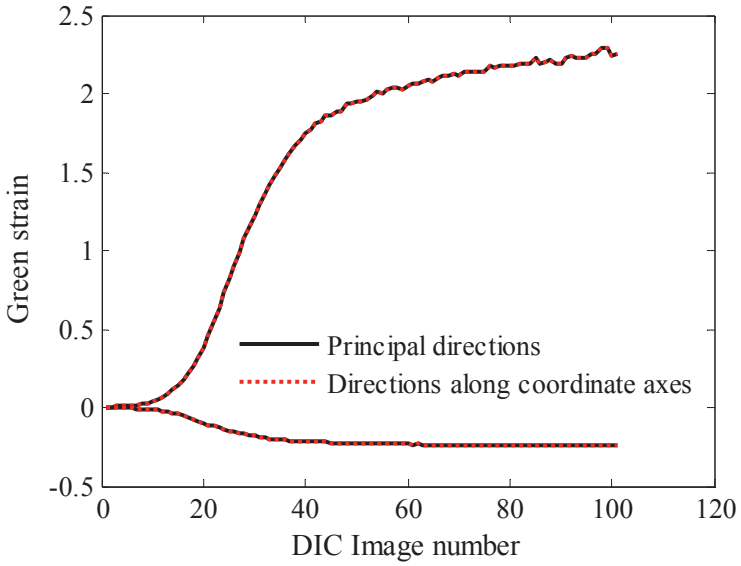

Figure 3.16 *Green strains in the principal directions and along the directions defined by the coordinate axes, i.e. the longitudinal and the transverse direction of the specimen. The data is taken from the PVC test.*

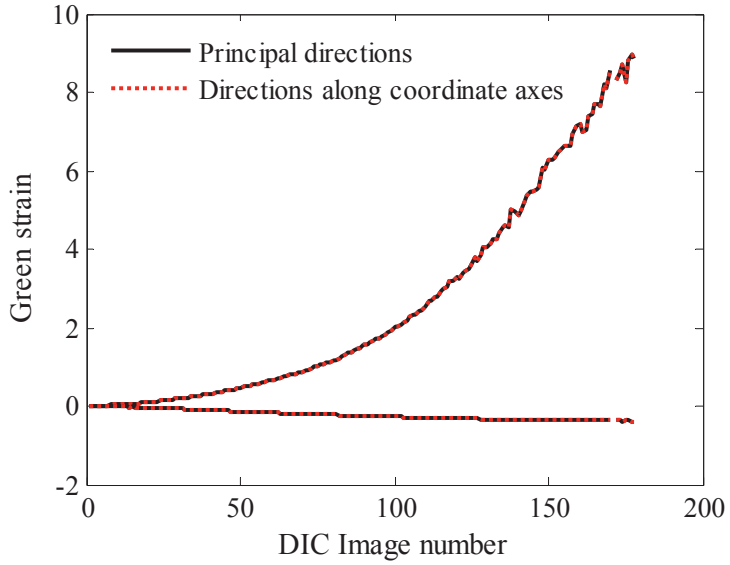

Figure 3.17 *Green strains in the principal directions and along the directions defined by the coordinate axes, i.e. the longitudinal and the transverse direction of the specimen. The data is taken from the HDPE test.*

By DIC it was possible to acquire the in-plane principal logarithmic strain fields even though the strains were rather large and inhomogeneous as seen in Figure 3.6 and Figure 3.7. The geometry of the specimen in the neck produces transverse components of the stress tensor [7]. Therefore, the stress state changes from a uniaxial state to a triaxial state at necking. After the neck has propagated away from this location and the stress state is again uniaxial. The effect of the neck is neglected in this study.

The mineral filled PVC started to stress whiten when reaching the maximum force and the peak stress around $\varepsilon_1 = 0.048$. After this point material experienced plastic volume change, even though it was in the plastic regime. However, in the HDPE, no stress whitening and almost no volume change in the plastic regime was observed.

Figure 3.12 and Figure 3.13 show the longitudinal and the transverse strain rate in the sections where the strains for the stress and strain computations are collected. Even though the specimens were deformed by a constant rate, it can be seen that the local strain rate varies throughout the deformation. Strain localization and neck formation lead to an increase in strain rate. When the neck propagates the strain rate decreases. Comparing the strain rate of PVC with that of HDPE, it is seen that the strain rate is somewhat more constant in HDPE than in PVC. From the strain fields of the two materials in Figure 3.6 and Figure 3.7, it also appears that there is a stronger localization in the PVC specimens before the neck propagates. The strong localization of strain in the PVC specimen may be related to the softening behaviour of the material. Propagation of the neck, indicated by a decrease in the strain rate, can be linked to the strain rehardening effect of the material. HDPE, having no stress softening and a weaker strain hardening, shows less variation in strain rate during the deformation. In other words, the PVC seems to be more exposed to strain localization than HDPE. On the other hand, the PVC also seems to redistribute the strain, and therefore propagate the neck, better due to more pronounced strain rehardening.

The increase in strain rate may lead to an increase in temperature. However, unpublished temperature measurements of similar mineral filled PVC and HDPE materials deformed at room temperature at the same strain rate reveals that the temperature increase in the specimens was about 5°C. The temperature effect is therefore not regarded as important for the tension test results reported in this section.

With the test setup and post processing method employed in this study, it is not possible to obtain stress-strain curves at a constant strain rate. G'Sell et al. [8] have developed a video-controlled tensile testing method allowing for continuous adjustment of the deformation velocity based on real time strain computations. The strain measurement in the method is based on the displacement between seven ink markers printed on the surface of a specimen with a pre-machined imperfection. With such a system the local strain rate can be kept constant during the test. The method employed in this study and the method of G'Sell et al. produce similar results for the stress – strain curve at quasi-static strain rate [9]. Lauro et al. [10] developed the $SE\dot{E}$ technique that employs results from DIC to construct a surface in a 3D space spanned by stress, strain and strain rate. By cutting this surface at one strain rate, they obtained a stress – strain curve for a constant strain rate.

Only one strain rate was tested in this work. For test results at other strain rates, and a more comprehensive test programme in general, the reader is referred to Hovden [1] or Moura et al. [2].

3.7 CONCLUDING REMARKS

- The behaviour of the 5 mm sheets of PVC and HDPE is somewhat different from the behaviour of the 10 mm sheets. This may be related to skin-layer effects.

- The 5 mm extruded plates of PVC and HDPE can be regarded as isotropic in tension.

- The stress-strain curve from the mineral filled PVC shows a peak stress, stress softening and subsequent strain rehardening. Stress whitening sets in at peak stress. Moreover, dilation during plastic deformation was found. The specimen was deformed until fracture.

- The stress-strain curve of the HDPE has no stress peak. Strain hardening is dominant in the material at large strains. The HDPE has a nearly isochoric plastic deformation. Due to ductile behaviour, the test was aborted before fracture occurred in the specimen.

REFERENCES

[1] M.T. Hovden. Test and numerical simulations of polymer components. Master thesis, Department of Structural Engineering, NTNU, (2010).

[2] R.T. Moura, A.H. Clausen, E. Fagerholt, M. Alves, M. Langseth. Impact on HDPE and PVC plates - Experimental tests and numerical simulations. *International Journal of Impact Engineering*, **37** (2010), 580-598.

[3] M. Polanco-Loria, A.H. Clausen, T. Berstad, O.S. Hopperstad. Constitutive model for thermoplastics with structural applications. *International Journal of Impact Engineering*, **37** (2010), 1207-1219.

[4] P. Vacher, S. Dumoulin, F. Morestin, S. Mguil-Touchal. Bidimensional strain measurement using digital images. *Proceedings of the Institution of Mechanical Engineers Part C-Journal of Mechanical Engineering Science*, **213** (1999), 811-817.

[5] G.A. Holzapfel. *Nonlinear solid mechanics. A continuum approach for engineering.* Wiley, (2001).

[6] B. Pan, K. Qian, H. Xie, A. Asundi. Two-dimensional digital image correlation for in-plane displacement and strain measurement: a review. *Measurement Science and Technology*, **20** (2009), 062001.

[7] C. G'Sell, N.A. Aly-Helal, J.J. Jonas. Effect of stress triaxiality on neck propagation during the tensile stretching of solid polymers. *Journal of Materials Science*, **18** (1983), 1731-1742.

[8] C. G'Sell, J.M. Hiver, A. Dahoun. Experimental characterization of deformation damage in solid polymers under tension, and its interrelation with necking. *International Journal of Solids and Structures*, **39** (2002), 3857-3872.

[9] V. Delhaye. Behaviour and modelling of polymers for crash applications. Doctoral thesis, Department of Structural Engineering, NTNU, (2010).

[10] F. Lauro, B. Bennani, D. Morin, A.F. Epee. The SEĖ method for determination of behaviour laws for strain rate dependent material: Application to polymer material. *International Journal of Impact Engineering*, **37** (2010), 715-722.

CHAPTER 4

UNIAXIAL COMPRESSION

Uniaxial compression tests of specimens from the 5 mm extruded plates of PVC and HDPE were carried out to study the pressure sensitivity of the two materials.

4.1 INTRODUCTION

The basic response of the 5 mm thick extruded sheets of PVC and HDPE in uniaxial tension was disclosed in Chapter 3. However, it is well known that the mechanical response of polymers is sensitive to pressure. Therefore, also testing of these materials' compressive behaviour is of great interest. In this chapter compression tests on cylindrical specimens as outlined in Figure 4.1 are presented. Results from these test will be used in calibration of the material model of Polanco-Loria et al. [1] in Chapter 10.

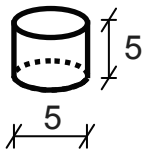

Figure 4.1 *Geometry of compression test specimen. Measures are given in mm.*

4.2 TEST SETUP

The compressive test coupons were machined with nominal dimensions according to Figure 4.1. They were cut out from 5 mm thick extruded plates of mineral filled PVC and HDPE. These were the same plates that were used in the uniaxial tensile test in Chapter 2. Specimens were cut with three different orientations: The longitudinal axis in the extrusion direction, 0°, in the in-plane transverse direction, 90°, and in the out-of-plane direction of the sheets. Two tests of each material and machining direction were carried out in order to check the repeatability which turned out to be good.

The tests were carried out under displacement control in a servo-hydraulic Dartec machine with a 20 kN load cell connected to an Instron controller. The loading rate was kept constant at 0.005 mm/s, corresponding to a nominal strain rate of 10^{-3} s^{-1}. The friction between the sample and the steel platen of the test machine was minimized by applying a lubricant to the contact surfaces. The deformation of the specimens was monitored by a charge-coupled device (CCD) camera taking digital images at a frequency of 0.2 Hz. The initial diameter and height of each sample were measured before the tests.

4.3 DEFORMATION MEASUREMENT

The CCD camera monitoring the deformation had its focus at the edge of the test specimens. After testing, the diameter d of the mid cross section as well as the height h of the cylinder was measured on the images as illustrated in Figure 4.2. This data were used for the calculation of Cauchy stress and logarithmic strain. The strains were assumed to be homogenously distributed in the test coupon.

a) b)

Figure 4.2 *A PVC compression specimen. After the test the measurements shown were measured on the images. a) The coupon before deformation showing the initial measurements. b) The specimen after some deformation.*

4.4 STRESS AND STRAIN CALCULATIONS

The Cauchy stress was defined as the applied force F divided by the actual cross section area

$$\sigma = \frac{F}{\pi / 4 \cdot d^2} \tag{4.1}$$

The longitudinal logarithmic strain ε_z was computed from the current height h of the specimen and the initial height h_0

$$\varepsilon_z = \ln\left(\frac{h}{h_0}\right) \tag{4.2}$$

The radial strain was found from the current diameter d and the initial diameter d_0

$$\varepsilon_r = \ln\left(\frac{d}{d_0}\right) \tag{4.3}$$

Transverse isotropy was assumed, implying that any ovalization of the cross section was not taken into account. Thus, ε_r represents the strain in both the radial and the circumferential directions of the sample. This assumption is supported by earlier investigations. [2, 3]. Hence, the volume strain was expressed as

$$\varepsilon_v = \varepsilon_z + 2\varepsilon_r \tag{4.4}$$

4.5 RESULTS

Representative force-displacement relationships for compression coupons of PVC from the different directions of the plate are plotted in Figure 4.3. The difference in the peak force is 12% between the out-of-plane specimen and the specimen cut in the extrusion direction, 0^o. It is also observed that the peak force differs with less than 4% between the samples in the 0° and 90° directions. These differences are regarded as small enough to consider the material as isotropic. Similarly Figure 4.4 shows representative force-displacement curves for HDPE. Also this material is regarded as isotropic. Transverse isotropy has earlier been demonstrated for similar materials [2, 3]. From this point onwards, only results from representative specimens machined in the extrusion direction will be treated.

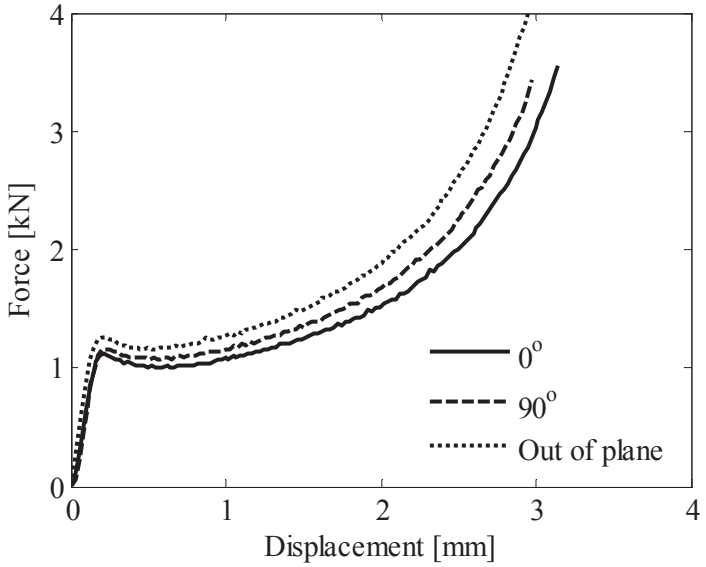

Figure 4.3 *Force-displacement curves measured during compression of the PVC coupons.*

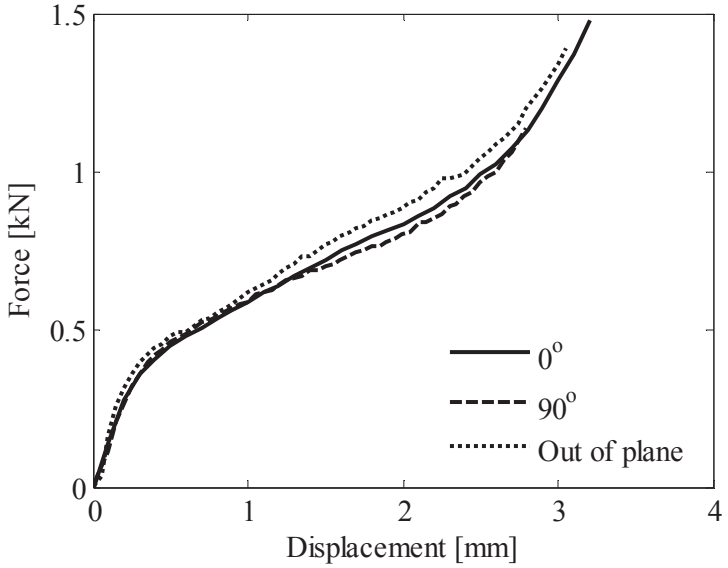

Figure 4.4 *Force-displacement curves measured during compression of the HDPE coupons.*

Figure 4.5 and Figure 4.6 show photos of test specimens of PVC and HDPE at different stages during compression. From the figure it can be seen that bulging, or "barrelling", started after some deformation. This was probably due to friction between the steel platens and the top and bottom surfaces of the test coupons.

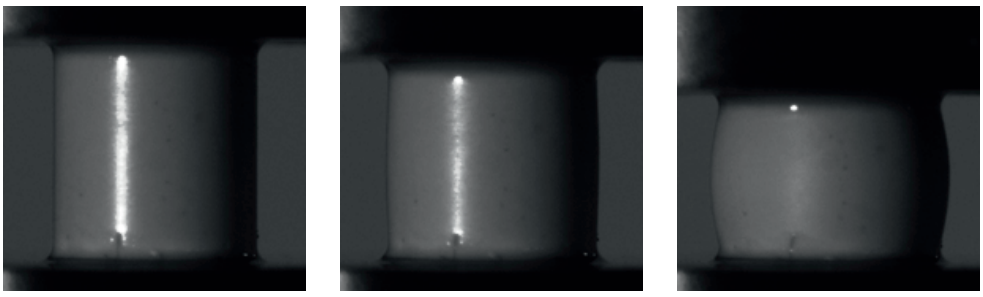

a) b) c)

Figure 4.5 *Compression coupon of PVC a) before deformation b) at onset of barrelling and c) at the last logging point used for stress and strain calculations.*

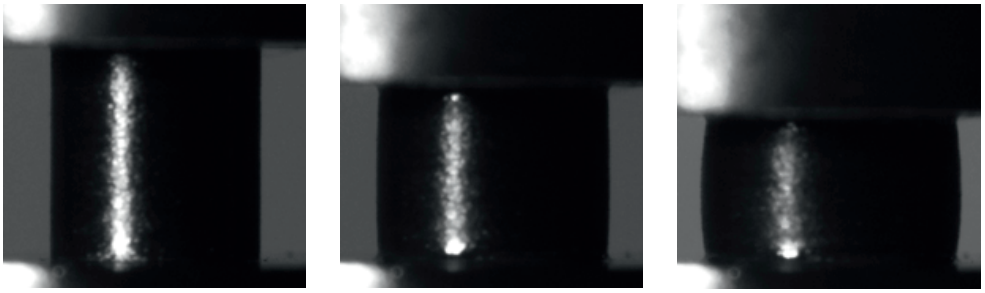

a) b) c)

Figure 4.6 *Compression coupon of HDPE a) before deformation b) at onset of barrelling and c) at the last logging point used for stress and strain calculations.*

Applying Equations (4.1) and (4.2), the Cauchy stress – logarithmic strain curve from a representative compressive test of mineral filled PVC was found. It is shown in Figure 4.7. The response is linear up to a local stress maximum. Thereafter, the stress-strain curve drops markedly. The stress-strain curve before barrelling of the test coupon is plotted with a solid line. Onset of barrelling is marked with a circle. After this point the stress state is no longer uniaxial, and the curve therefrom has to be considered with less confidence. The following response is therefore represented by a dashed line. The onset of barrelling is somewhat unclear. However, the first clear sign of barrelling was observed after the peak stress was reached.

Figure 4.8 displays the Cauchy stress against logarithmic strain for the representative HDPE compression test. Also here, barrelling is marked with a circle, and the subsequent response is represented by a dashed line.

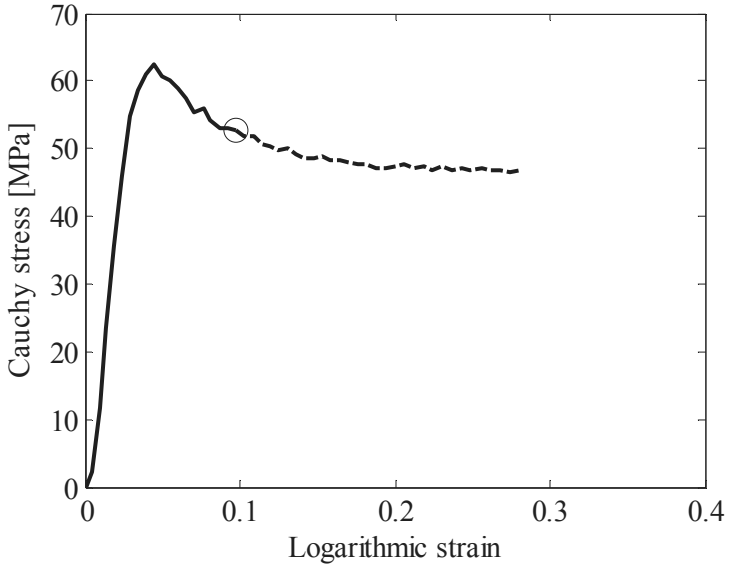

Figure 4.7 *Cauchy stress vs. logarithmic strain curve for PVC in uniaxial compression. The circle represents onset of barrelling, and the dashed line represent the stress-strain curve after barrelling.*

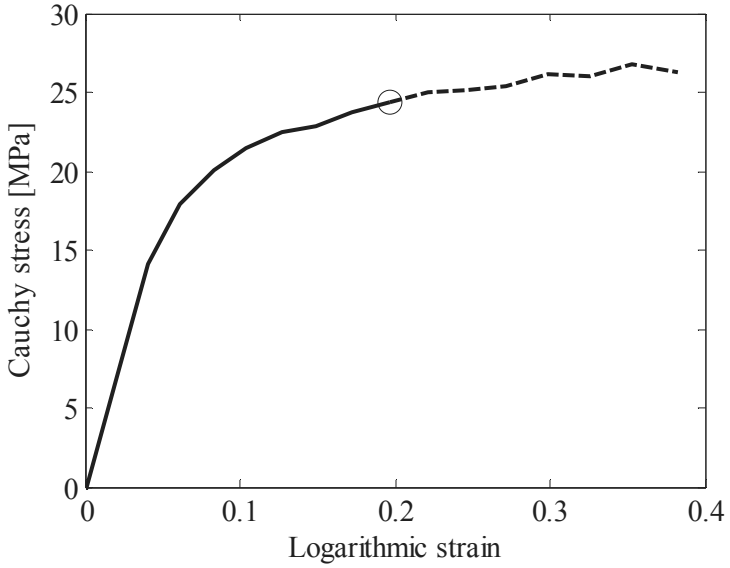

Figure 4.8 *Cauchy stress vs. logarithmic strain curve for HDPE in uniaxial compression. The circle represents onset of barrelling, and the dashed line represent the stress-strain curve after barrelling.*

The volume strains, found from Equation (4.4), are for the two materials presented in Figure 4.9 and Figure 4.10. Also here onset of barrelling is marked by a circle and the response thereafter by dashed lines. It is seen that the volume diminishes during elastic loading. In PVC it seems that the volume increases after reaching plasticity. However, it is again emphasised that the results must be regarded with care after onset of barrelling. Barrelling of the test coupon exaggerate the transverse expansion and leads to overestimation of the radial strain and also the volumetric strain. In HDPE the volume remains about constant for large deformation. Some small increase in volume strain is observed, but this may also be related to barrelling of the specimen.

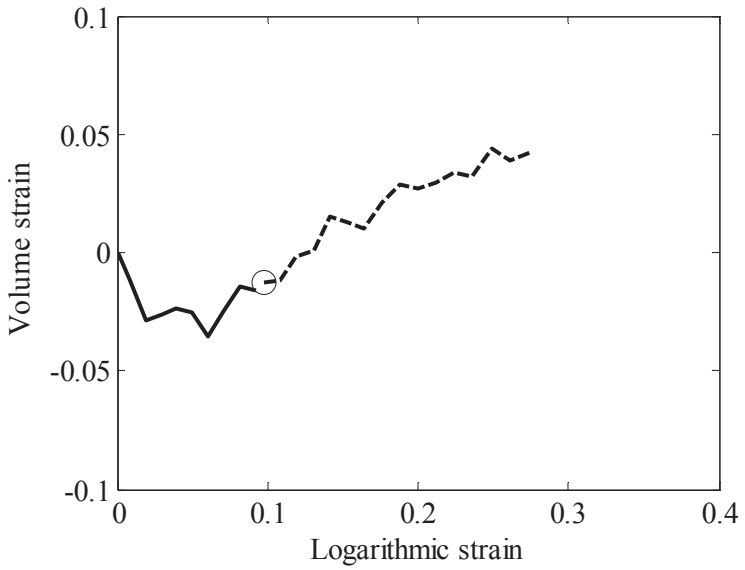

Figure 4.9 *Logarithmic volume strain in PVC in compression. The circle represents onset of barrelling, and the dashed line represent the volume strain after barrelling.*

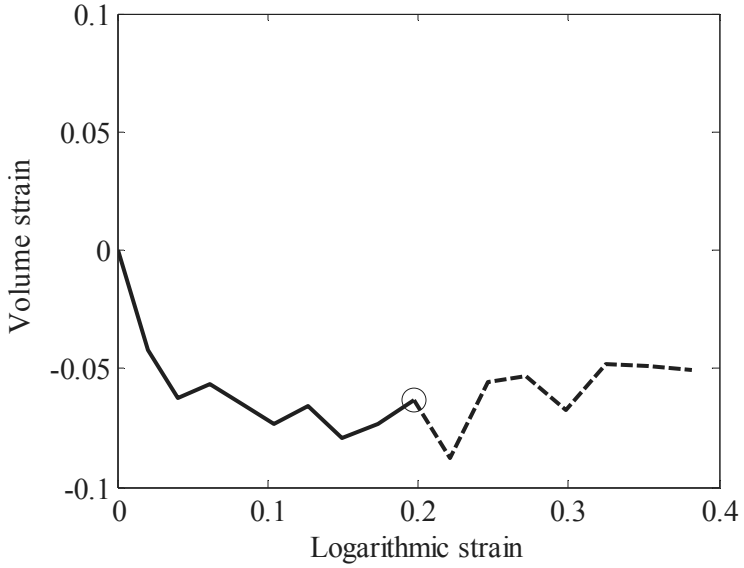

Figure 4.10 *Logarithmic volume strain in HDPE in compression. The circle represents onset of barrelling, and the dashed line represent the volume strain after barrelling.*

4.6 DISCUSSION

Small cylinders of mineral filled PVC and HDPE were tested in uniaxial compression. The strains were determined from measurements of the height and the diameter of the cylinder during deformation. By combining this data with the force recorded by the tensile machine the stress-strain relationships presented in Figure 4.7 and Figure 4.8 were established. After some deformation the test coupon started to bulge, or "barrel". The onset of barrelling was somewhat unclear since it appeared gradually. Nevertheless, the first clear visual evidence of barrelling is marked with a circle. To indicate that the results may be inadequate after this point the response is plotted by dashed lines in Figure 4.7 and Figure 4.8.

In Figure 4.11 the stress-strain curves from the compression tests are plotted together with those found from uniaxial tension in Chapter 2. For PVC the peak stress in compression is about 1.3 times higher than that in uniaxial tension. It is interesting that not only in tension but also in compression the peak stress in PVC is followed by stress softening. Moreover, the stress

softening appears even stronger in compression. The stress-strain response of HDPE in uniaxial compression is very similar to that in tension, see Chapter 2.

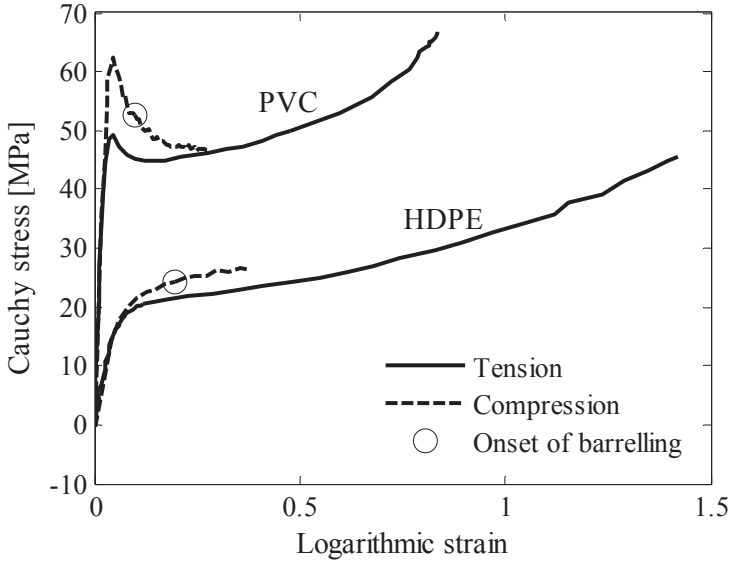

Figure 4.11 *Stress-strain curves for PVC and HDPE in tension and compression.*

The Cauchy stress was computed by employing the mid section of the compression coupons. This is where the cross area is at its largest after barrelling. The difference between the maximum (mid) cross section diameter and the minimum (upper and lower) cross section diameter was about 4% in the compression coupons at the stage defined as onset of barrelling, see Figure 4.5 b) and Figure 4.6 b). It means that the barrelling actually started at some earlier stage. This leads to an underestimation of Cauchy stress already at the point marked with a circle in Figure 4.7 and Figure 4.8. Further deformation of the specimen, and therefore more barrelling, increases the error.

The volume change in the two materials is presented in Figure 4.9 and Figure 4.10. Initial elastic deformation of both materials leads to compaction of the test coupon. When the PVC reaches peak stress, a volume

increase can be observed in Figure 4.9. However, most of the dilation emerges after onset of barrelling. The computed volume strain includes the radial strain as according to Equation (4.4). The radial strain was found from measurement of the mid cross section of the specimen, i.e. the cross section with the largest diameter after barrelling as seen in Figure 4.5 c). The result is an overestimation of the radial strain and therefore also volume strain. The data provided by these tests are not sufficient for drawing conclusions about the volume change of mineral filled PVC and HDPE in compression. In order to do this, new and better compression tests are needed. Some improvements for future compression tests are suggested in the following.

Better quality of the images can improve the measurement of the evolution of the diameter. As seen in Figure 4.5 and Figure 4.6 the images used in the post processing in this study are somewhat unclear. By increasing the contrast between the test coupon and the background, the diameter measurement can be done by an automatic script. Such a script could also be coded to trace the boundary of the specimen and compute the total volume of the specimen in each image by for instance solving a disk integral. Moreover, one should also take care to focus at the edge of the specimen in order to get a sharp contour. To reduce measurement noise, the specimen should cover a sufficient part of the photograph. If the specimen is represented by too few pixels in the picture, measurement noise in the order of just one pixel can have a great impact on the strain results.

Lubricant was added to the top and bottom surfaces of the test coupon. Yet, the barrelling of the specimens indicates that some friction is present between the specimen and the compression platens. This friction should be reduced further. Van Melick et al. [4] reduced the friction by using a PTFE film and soap water. By this procedure, they reported true strains up to -1.5 without observing any bulging or buckling of the sample.

The strains could also have been measured by digital image correlation (DIC). Moura et al. [3] and Delhaye [5] report results from compression test on cubical specimens. The advantage of cubical test coupons is that 2D-DIC can be used to measure the full in-plane strain field on one of the flat sides. The disadvantage is undesirable effects produced by the corners of the specimen, causing a non-homonegeous strain field in a transverse section of the sample. 3D-DIC has been performed on test coupons of cylindrical

shape by Hovden [2]. The results from 3D-DIC were compared with results from employing measurement of the diameter expansion. Even though the 3D-DIC produced a high level of noise in the measurement, the main results were similar.

Even though some of the test results from this study are regarded as inadequate, the main objective was to acquire data for determination of the material parameters for the constitutive model by Polanco-Loria et al. [1]. The results herein are considered suitable for this purpose because only the compression yield stress is involved in the parameter identification procedure.

4.7 CONCLUDING REMARKS

- The 5 mm thick extruded plates of PVC and HDPE can be regarded as isotropic in compression.

- The PVC has a higher yield stress in compression than in tension. Moreover, the stress softening is more pronounced in compression than in tension.

- The stress-strain curve of the HDPE in compression is similar to that in tension. The yield stress of the material is regarded as insensitive to pressure.

- Plastic dilation is observed in compression of PVC. However, it is suspected that this is an effect from undesired friction between the test specimen and the compression platens. New and better tests results are needed.

REFERENCES

[1] M. Polanco-Loria, A.H. Clausen, T. Berstad, O.S. Hopperstad. Constitutive model for thermoplastics with structural applications. *International Journal of Impact Engineering*, **37** (2010), 1207-1219.

[2] M.T. Hovden. Test and numerical simulations of polymer components. Master thesis, Department of Structural Engineering, NTNU, (2010).

[3] R.T. Moura, A.H. Clausen, E. Fagerholt, M. Alves, M. Langseth. Impact on HDPE and PVC plates - Experimental tests and numerical simulations. *International Journal of Impact Engineering*, **37** (2010), 580-598.

[4] H.G.H. van Melick, L.E. Govaert, H.E.H. Meijer. On the origin of strain hardening in glassy polymers. *Polymer*, **44** (2003), 2493-2502.

[5] V. Delhaye. Behaviour and modelling of polymers for crash applications. Doctoral thesis, Department of Structural Engineering, NTNU, (2010).

CHAPTER 5

LOADING, STORAGE AND RELOADING

Tensile specimens of mineral filled PVC and HDPE were loaded to different elongations and unloaded to zero force. The specimens were then stored for different periods of time before they were reloaded. The purpose of these tests is to study whether physical aging, as an effect of storage, affect the mechanical response of the polymers. In particular, it is paid attention to whether the peak stress in the mineral filled PVC could be recalled by storage.

5.1 INTRODUCTION

The shape of the stress-strain curves presented in Chapter 2.8 and in Chapter 3 generated curiosity regarding the characteristics of the behaviour of the mineral filled PVC and the HDPE. The PVC showed a stress peak followed by softening before subsequent rehardening, while the stress of the HDPE increased during the whole test. It is generally known that time affects polymer materials in terms of physical aging, as discussed in Chapter 2.4. A shape of the stress-strain curve similar to that of the PVC is familiar also for physically aged polymers [1]. Rolling of polystyrene tensile specimens was shown by Govaert et al. [2] to rejuvenate the material by decreasing both the maximum stress and the subsequent stress softening. The effect was temporary, after 20 minutes a clear recovery of the softening was observed and after 30 minutes the effect from the rejuvenation had vanished.

It was of interest to see how storage time affects the mechanical response of the two materials in this study. This was done by first applying a loading cycle to tensile specimens. Thereafter, the specimens were stored for a certain time before they were reloaded.

5.2 TEST SETUP

Fifteen uniaxial tensile test specimens were machined from 10 mm thick extruded sheets of mineral filled PVC and HDPE according to Figure 5.1. The thickness was reduced to 4 mm by removing material from both sides of the plates. The specimens were divided into three groups to create three test series denoted I, II, and III from both materials. Each test series represented one loading cycle consisting of loading until a particular elongation level followed by unloading. The test series and associated elongation levels are listed in Table 5.1 and Table 5.2 for specimens of mineral filled PVC and HDPE in turn. On the first test day all specimens were subjected to the first load cycle particular for the respective test series. The five specimens belonging to each series were then stored for five different periods of time and reloaded according to the same loading cycle. In total 15 different tests from each material were carried out with this test setup.

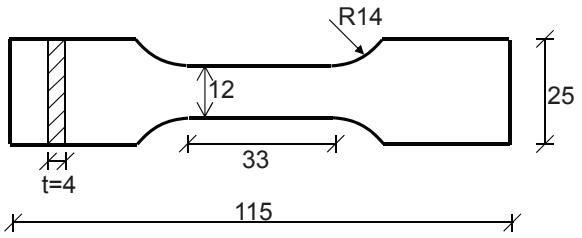

Figure 5.1 *The geometry of the tensile test specimens. Measures are given in mm.*

A speckle pattern was painted on the surface of the specimens, and the deformation was monitored by a CCD camera during the test with an image frequency of 0.5 Hz. DIC was subsequently used to find the strain fields as in Chapter 3. Stress and strain calculations were also carried as described in Chapter 3.The strains were taken as an average from five grid elements to reduce noise, see Figure 3.3. To ensure that all specimens were unloaded at the same deformation level, an MTS 634.31F-25 extensometer with 30 mm gauge length was clamped to the specimens to measure the elongation of the parallel area. When the elongation had reached a certain level, as listed in Table 5.1 and Table 5.2, the testing machine was programmed to start the unloading stage. To avoid compression of the specimens the unloading was carefully stopped when the testing machine measured zero force. Both the loading and the unloading processes were displacement controlled with a deformation speed of 0.033 mm/s.

Table 5.1 *Test programme for loading, storage and reloading of PVC specimens.*

Test number	Test series	Elongation level (extensometer)	Storage time before reloading
1	I	1 mm	5 min
2	I	1 mm	24 hours
3	I	1 mm	9 days
4	I	1 mm	80 days
5	I	1 mm	33 weeks
6	II	1.5 mm	5 min
7	II	1.5 mm	24 hours
8	II	1.5 mm	9 days
9	II	1.5 mm	80 days
10	II	1.5 mm	33 weeks
11	III	2 mm	5 min
12	III	2 mm	24 hours
13	III	2 mm	9 days
14	III	2 mm	80 days
15	III	2 mm	33 weeks

Table 5.2 *Test programme for loading, storage and reloading of HDPE specimens.*

Test number	Test series	Elongation level (extensometer)	Storage time before reloading
16	I	1.5 mm	5 min
17	I	1.5 mm	24 hours
18	I	1.5 mm	9 days
19	I	1.5 mm	80 days
20	I	1.5 mm	33 weeks
21	II	2.5 mm	5 min
22	II	2.5 mm	24 hours
23	II	2.5 mm	9 days
24	II	2.5 mm	80 days
25	II	2.5 mm	33 weeks
26	III	4 mm	5 min
27	III	4 mm	24 hours
28	III	4 mm	9 days
29	III	4 mm	80 days
30	III	4 mm	33 weeks

5.3 RESULTS

The loading paths for all tests can be seen in Figure 5.2 in terms of load-extensometer displacement curves. The dotted lines represent the first load cycle and the continuous lines represent the reloading cycle of the same specimens after different storage times.

Separating the results into the three series I, II and III, Figure 5.3 and Figure 5.4 display stress-strain curves and volume strain plots. The stress-strain curves of the first load cycles are plotted as dashed lines. The stress-strain curves of the reloading, after storage for different periods of time, are plotted as solid lines. Colours are used to distinguish the different test specimens. Note that the scales for the *x*-axes are changing between the test series, while the *y*-axes remain the same for each material.

The response from the first loading cycle is initially linear elastic with local stress maxima followed by stress softening. This is similar to the response the material from 10 mm sheets reported in Chapter 2.8 and also to that of 5mm sheets addressed in Chapter 3. The PVC-I-test specimens, see Figure 5.3 a), were unloaded at the local stress maximum, while the PVC-II- and PVC-III-test specimens, see Figure 5.3 c) and e), were unloaded at two different stages of the softening process. The test results reveal that the second loading cycle has a response quite different from the first. The slope of the stress-strain curve during reloading is gradually decaying. The stress is at its maximum at the end of the reloading stage, no stress softening is observed for any of the reloading cycles. The stress level during the reloading cycle is approaching the response of the first loading cycle at the end of the softening regime. This applies also for the specimens stored for the longest period. However, these specimens, stored for 33 weeks before reloading, reach slightly higher values of stress than the other specimens when reloaded.

The volume strain observed in the PVC specimens during the experiment is plotted in Figure 5.3 b), d) and f). Both for the first and the second loading cycles the volume strain increases during the entire loading stage.

In contrast to the PVC specimens, the HDPE specimens show the same stress-strain relationship in the first and the second load cycles. It is seen in Figure 5.4 a), c) and e) that the response of the second loading cycle is equal to that of the first loading cycle. This behaviour does not seem to change with storage time.

Hardly any volume change is observed for the HDPE specimens. The volume strains during both load cycles is around zero in Figure 5.4 b), d) and f).

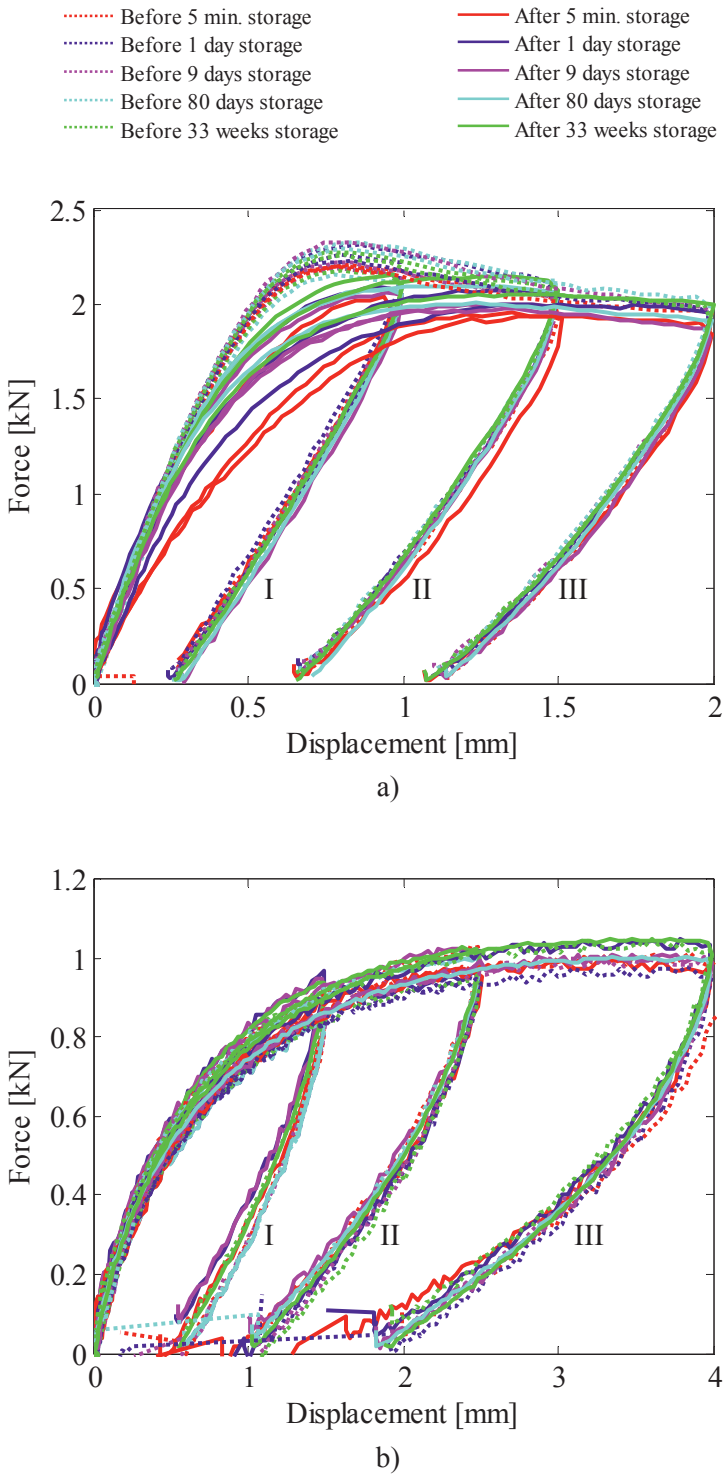

Figure 5.2 *Force – extensometer displacement measured for all tests of a) PVC and b) HDPE.*

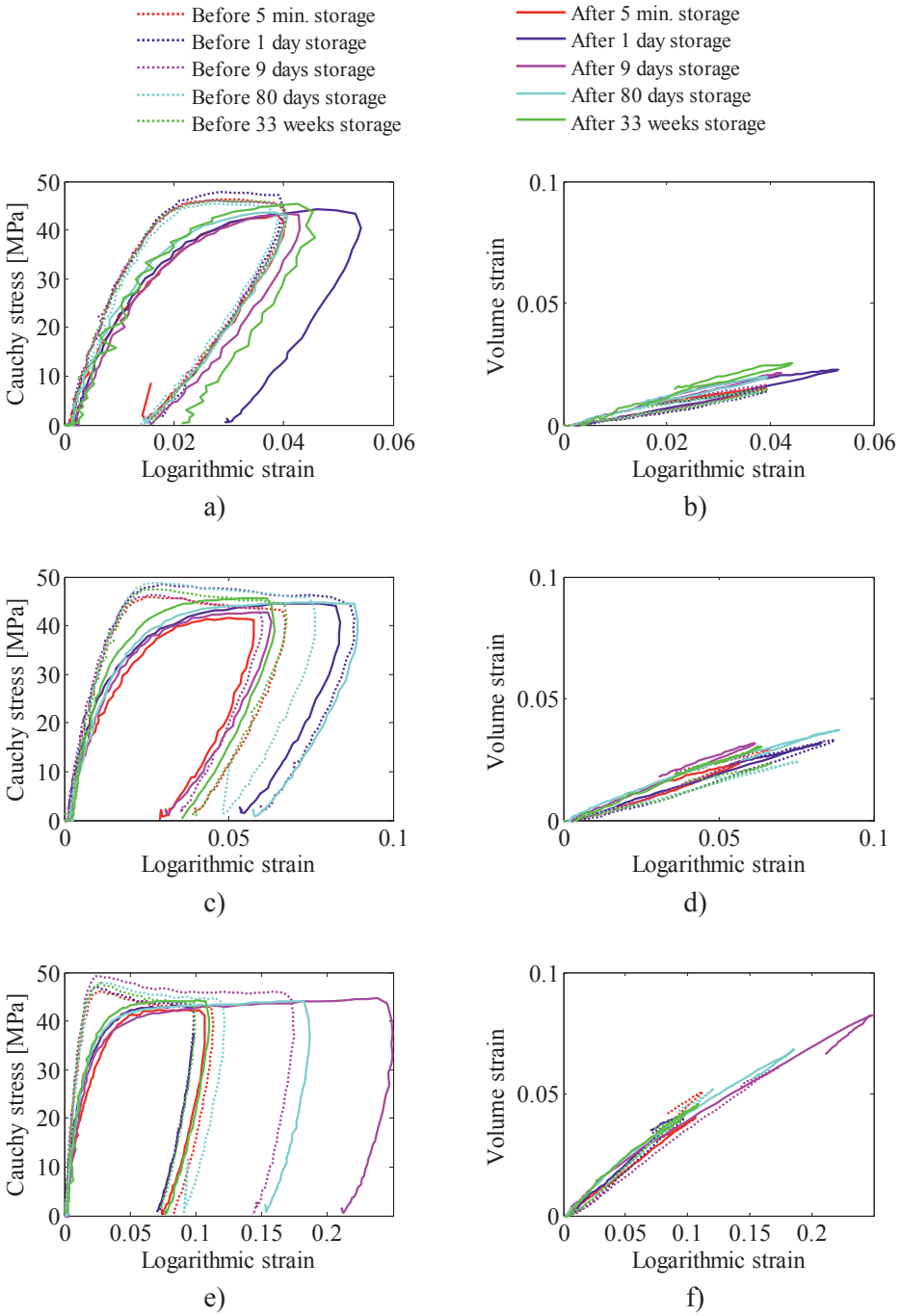

Figure 5.3 *Cauchy stress – logarithmic strain curves and logarithmic volume strain plotted against logarithmic longitudinal strain from tensile tests of PVC. a) and b): I-series. c) and d): II-series. e) and f): III-series.*

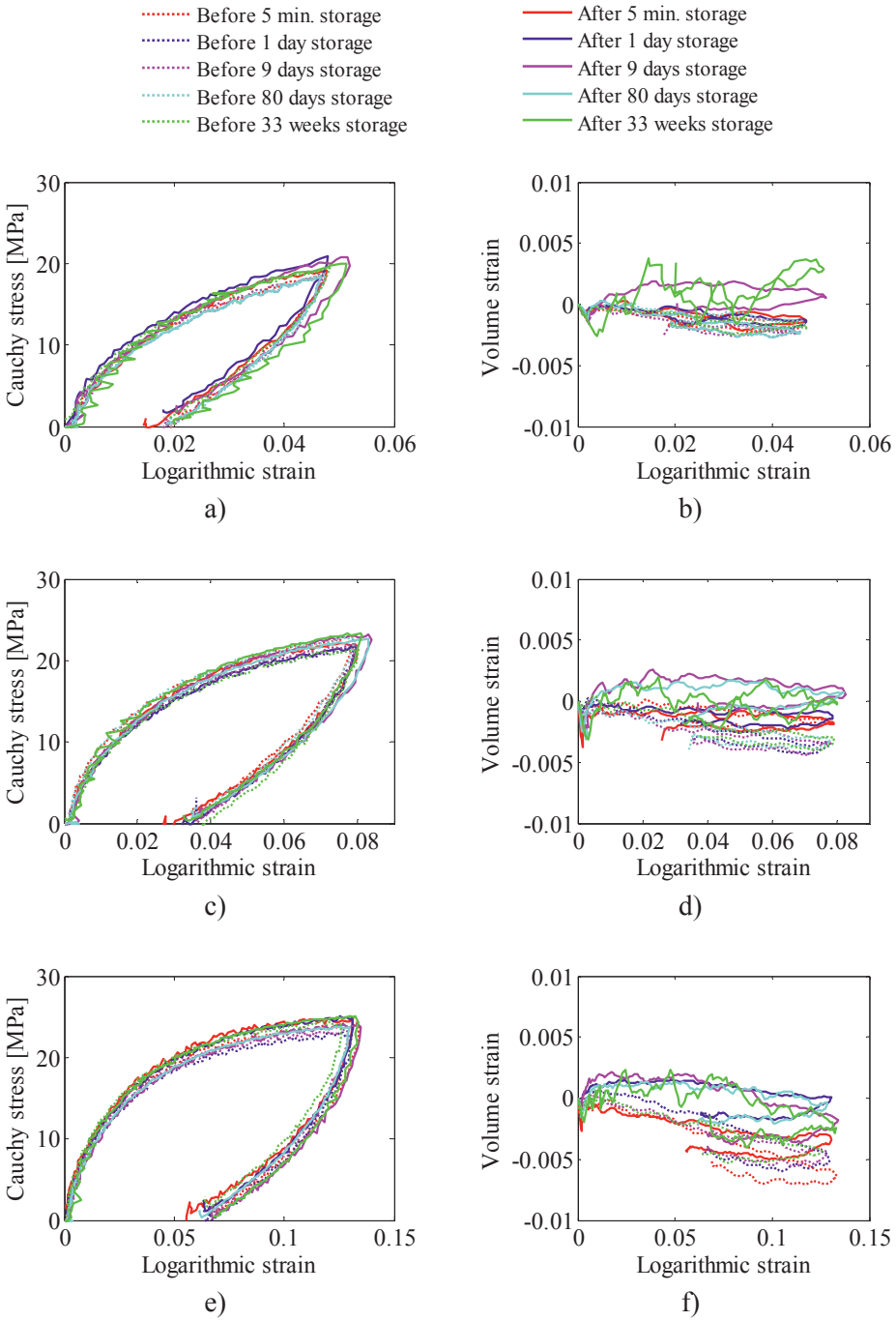

Figure 5.4 *Cauchy stress – logarithmic strain curves and logarithmic volume strain plotted against logarithmic longitudinal strain from tensile tests of HDPE. a) and b): I-series. c) and d): II-series. e) and f): III-series.*

5.4 DISCUSSION

There is a pronounced difference in the stress-strain curves of the first and the second load cycle for all specimens of the mineral filled PVC. This is clearly seen in Figure 5.3 a), c) and e) where the first load cycle is plotted as dashed lines and the reloading cycle as solid lines. While the specimens during the first load cycle show a linear elastic response up to a local stress maximum followed by a stress drop, the stress drop is absent in the second load cycle. The peak stress followed by stress softening did not reappear. Moreover, the reloading response is initially softer. Storage within the time scale of this study did not seem to give any dramatic change in the reloading response of this particular PVC. Therefore it seems reasonable to suspect that other irreversible mechanisms such as damage occur during the first load cycle. However, it should be noted that the specimens with the longest storage time before reloading reached a slightly higher stress level than the other specimens. This can be an indication of some physical aging.

For the specimens made of HDPE no significant difference was observed in the stress-strain relationships from the first to the second loading cycle, see Figure 5.4 a), c) and e). The response also seemed to be insensitive to storage time.

In these tests, an extensometer was used to control that every specimen in all of the test series was deformed to the pre-defined elongation level. However, the extensometer was so loosely attached that it slipped from the surfaces of some of the specimens. As a result, these specimens were elongated to a higher level than intended. This explains the high strain levels for some of the curves in Figure 5.3 and Figure 5.4. This could have been avoided by using the cross-head displacement, rather than an extensometer, to control the elongation level. Even so, since the strains were rendered from DIC and not from the extensometer, the stress-strain curves are still correct.

5.5 CONCLUDING REMARKS

- The mineral filled PVC in these tests shows different stress-strain relationships during the first and the second load cycle: during the second load cycle the response is softer and without the characteristic peak stress and stress softening. This characteristic behaviour in the PVC is not recalled by storage. It is therefore suspected that some damage mechanisms occurred in the material during the first load cycle.

- Some minor indication of physical aging can be observed for the mineral filled PVC specimens with the longest storage time.
- The HDPE material in these tests does not show any signs of damage or aging.
- Storage does not alter the evolution of volume strain. In the mineral filled PVC the volume increases with the deformation during both loading cycles. In the HDPE the volume change is approximately zero.

REFERENCES

[1] H.E.H. Meijer, L.E. Govaert. Mechanical performance of polymer systems: The relation between structure and properties. *Progress in Polymer Science*, **30** (2005), 915-938.

[2] L.E. Govaert, H.G.H. van Melick, H.E.H. Meijer. Temporary toughening of polystyrene through mechanical pre-conditioning. *Polymer*, **42** (2001), 1271-1274.

CHAPTER 6

VOID GROWTH IN PVC

Tensile test specimens of mineral filled PVC were deformed in tension to different elongations and then unloaded. The specimens were thereafter split in two and investigated in a scanning electron microscope. The void growth on the microscale was then compared with the dilation of the material on the microscale. The intention of the study is to investigate the mechanisms behind the plastic dilation observed in experimental tests.

6.1 INTRODUCTION

Stress whitening and volume change during plastic deformation were observed in uniaxial tension of mineral filled PVC as reported in Chapter 2.8 and Chapter 3. Plastic dilation in polymers can be assumed to be related to damage. Such damage can be voids that grow from local irregularities of the molecular packing [1], from cavitation of rubber particles or from debonding of particles made of rubbers or minerals [2, 3] as discussed in Chapter 2.5. By the use of a scanning electron microscope (SEM), the voids in the damaged material can be investigated. It this study, SEM micrographs have been used to quantify the void growth on the microscopic scale. These results were subsequently compared it with the volume change on the macroscopic scale.

6.2 TEST SETUP

The polymer-particle composite material investigated in this study is taken from the 10 mm thick extruded PVC plates produced by SIMONA. Ten tensile test specimens with geometry according to Figure 6.1 were machined from the

extrusion direction of the plates. The thickness was reduced to 4 mm by removing 3 mm material from each side of the plates.

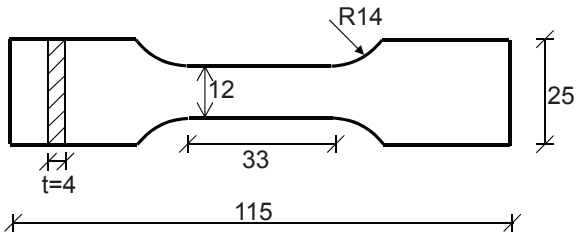

Figure 6.1 *The geometry of the tensile test specimens. Measures are given in mm.*

The loading of the specimens was displacement controlled with a deformation rate of 0.033 mm/s, giving an initial nominal strain rate $\dot{\varepsilon}_{nom} = 10^{-3}\text{s}^{-1}$. Each specimen was loaded until a certain deformation was achieved. The specimens were then unloaded to zero force at a load rate corresponding to the deformation rate. Load control was chosen for the unloading to avoid that any compression occurred in the specimens.

The tests were instrumented with a CCD camera acquiring digital pictures at a frequency of 0.5 Hz. The specimens were left in the testing machine for 10 minutes after unloading. At the end of this period, a new digital image was taken and added to the subset of images from the test. This was done to capture any possible stress relaxation causing volume change. The strain history from the start of the test until the end of the 10 min relaxation period could then be found by using digital image correlation (DIC) as described in Chapter 3. The width and the thickness of the specimens were again measured by a sliding calliper about a week after testing. No further shrinkage was then found. By using the results from strain measurements and assuming transverse isotropic deformation, the Cauchy stresses were found as described in Chapter 3.

6.3 TENSION TEST RESULTS

The force-displacement curves for all eight samples addressed in this study are shown in Figure 6.2. In addition, two tensile specimens were deformed until fracture, but they are not reported herein.

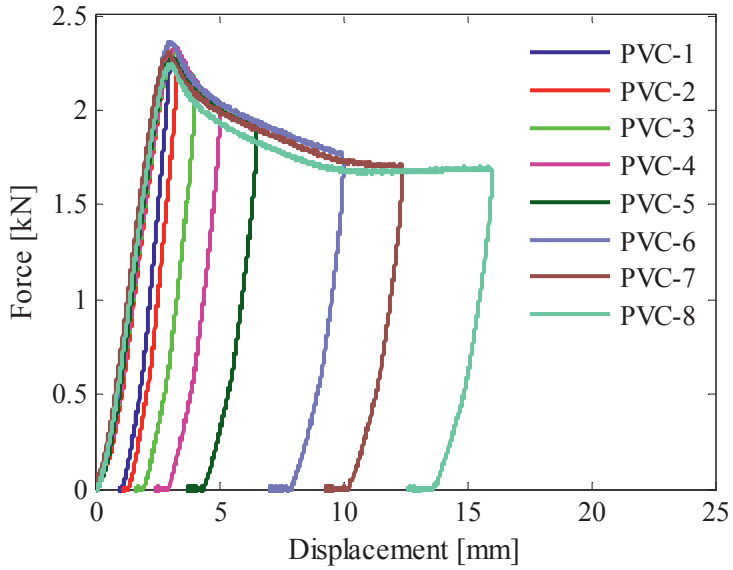

Figure 6.2 *Force-displacement curves for 8 PVC tension test samples with unloading at different deformation levels.*

The Cauchy stress – logarithmic strain curves for all eight specimens are shown Figure 6.3. The results are in accordance with the observations reported earlier in this thesis: All stress-strain curves show a linear elastic response up to a local stress maximum. The peak stress is followed by a load drop and subsequent strain rehardening. Defining the local stress maximum as the yield stress, plasticity sets in at 48-50 MPa, with little variation between the tests. This corresponds to a longitudinal logarithmic strain around 0.035. After onset of yielding a gradual increase of stress whitening could be observed visually during the test.

The logarithmic volume strains are plotted against logarithmic strains in the longitudinal direction in Figure 6.4. There is some variation between the curves in the figure. However, plastic dilation is clearly characterized in the tests. From the figure it can be seen that the volume strain does not increase linearly with the longitudinal strain. The curves have a slight convex shape.

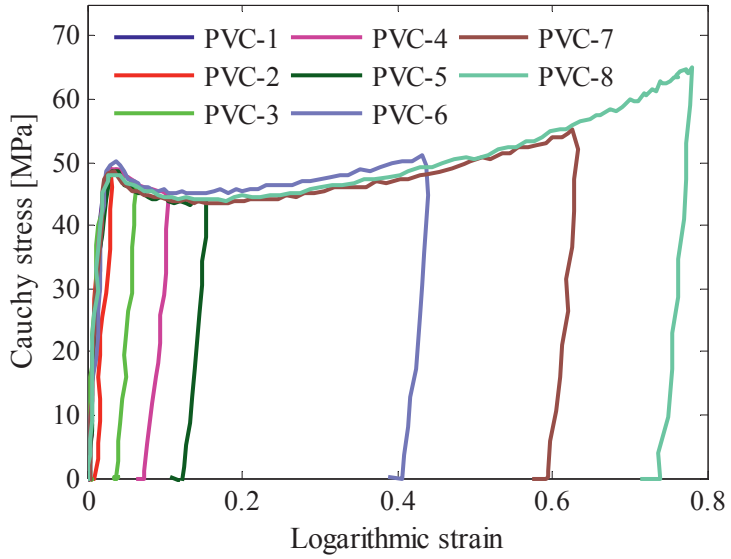

Figure 6.3 *Cauchy stress vs. logarithmic strain for all tests. The plot includes the loading and unloading stages as well as the relaxation after the test.*

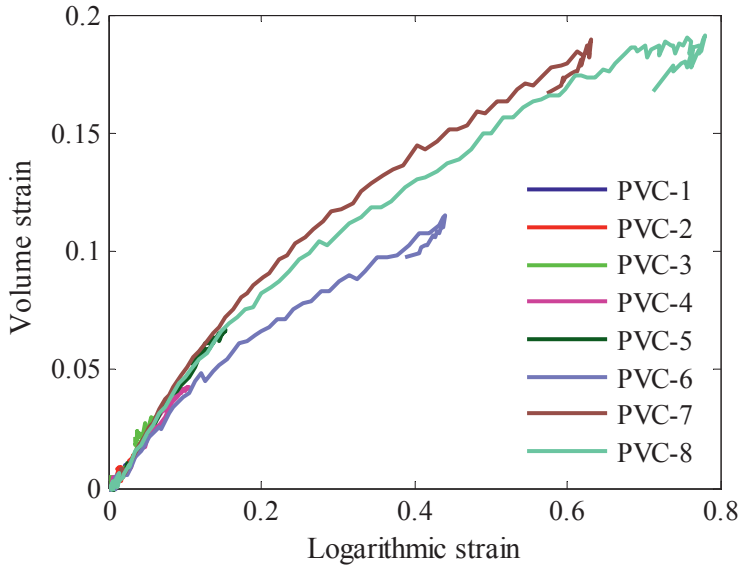

Figure 6.4 *Logarithmic volume strain plotted against logarithmic longitudinal strain for all tests. The plot includes the loading and unloading stages as well as the relaxation after the test.*

The nonlinearity in the dilation becomes clearer when looking at Figure 6.5, representing the retraction ratio defined as $\rho = -\varepsilon_2 / \varepsilon_1$, i.e. the ratio of transverse strain to longitudinal strain, plotted against plastic longitudinal strain. The retraction ratio in Figure 6.5 can be regarded as a kind of a Poisson's ratio during the plastic deformation, and describes the trend in the dilation. Since noise in the strain measurements causes fluctuations in the retraction ratio, the smoothing function in Matlab was used to obtain a better representation. It is seen that the retraction ratio has a minimum at a plastic strain of 0.04-0.06, corresponding to longitudinal strain of ε_1 = 0.07-0.095. The retraction ratio increases, i.e. the increase in dilation decays, when the longitudinal strain exceeds about 0.1. At unloading, there is a difference in the evolution of the retraction ratio between the different tests. The retraction ratio remains almost constant, or exhibits a slight increase, during unloading of the highly stretched specimens, i.e. PVC-6 to PVC-8, while it has a significant decrease while unloading of the other specimens.

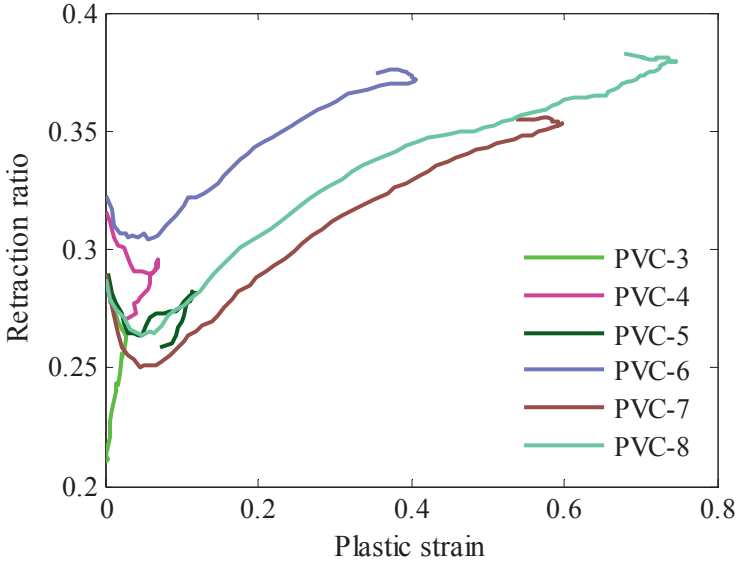

Figure 6.5 *Retraction ratio plotted against plastic logarithmic longitudinal strain. The plot includes the loading and unloading stages as well as the relaxation after the test.*

In Figure 6.6, the Cauchy stress-logarithmic strain curve is plotted together with the retraction ratio for the first part of test PVC-8. Here, no smoothing function is used for the retraction ratio. Therefore the initial fluctuations due to measurement noise are easy noticeable. It is seen that peak stress is reached before the retraction ratio approaches its lowest value. The minimum value of the retraction ratio is reached when the stress-strain curve flattens out.

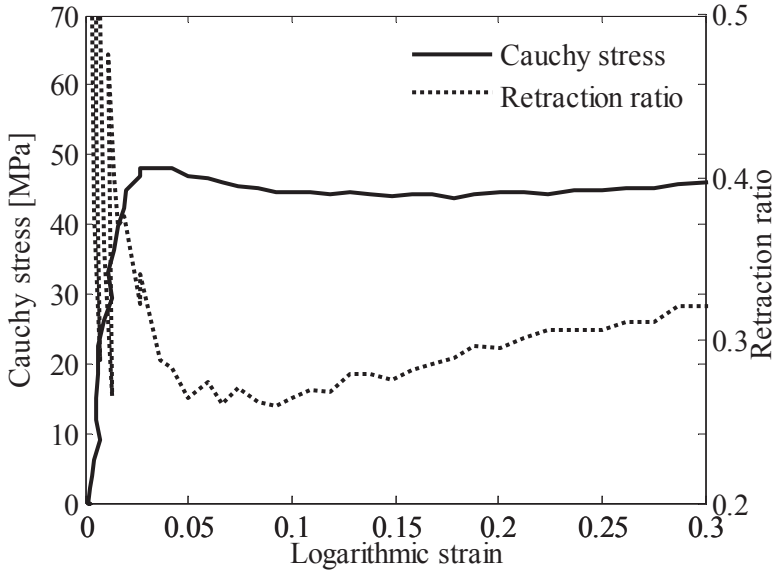

Figure 6.6 *Stress and retraction ratio plotted against strain for the first part of test PVC-8.*

Two additional tests specimens were deformed until fracture. Before onset of fracture they reached logarithmic strains of 0.80 and 0.56, respectively. This was at stress levels of 68.8 MPa and 51.8 MPa, and at logarithmic volume strains of 0.17 and 0.14. The latter of these two specimens fractured at a considerably lower deformation than any of the other specimens in this study.

6.4 SPECIMEN PREPARATION FOR SEM

The cross sections where the strains were extracted by DIC for stress and strain computations, i.e. the location for the first occurrence of necking, were marked on the test specimens. Small pieces containing these cross sections were thereafter cut out, see Figure 6.7. After storing these pieces in liquid nitrogen at –196°C for 30 minutes, they were split in two in the longitudinal direction. This created two longitudinal sections as seen in Figure 6.7. The fracture surface of one section from each test specimen was chosen for microscopic examination.

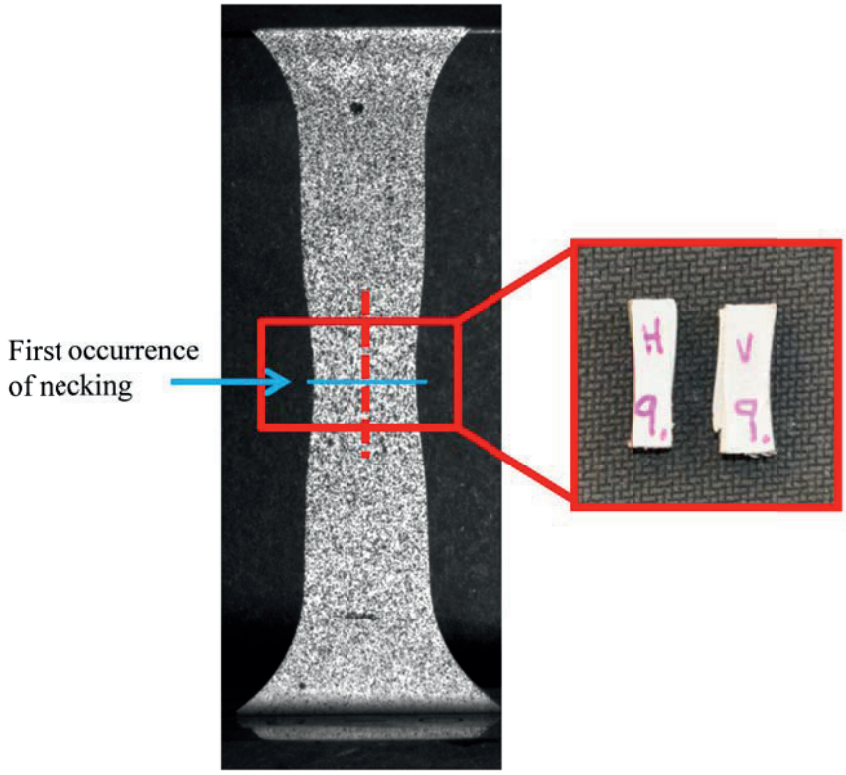

Figure 6.7 *Picture of a specimen after deformation. The red square shows the region cut out from the sample. The red dashed line indicates the longitudinal section investigated in the SEM.*

Prior to the SEM investigation the fracture surface of one of the split longitudinal sections from each specimen was coated with carbon dust by an Agar Turbo Carbon Coater. Then the location for onset of necking was investigated in a Zeiss

Supra 55VP SEM, as described in Chapter 2.8. The contents of one of the larger particles were identified by energy dispersive spectroscopy (EDS), which is a built-in tool of the SEM.

The contours of the areas containing particles and voids in the SEM micrographs were traced manually. It was in many cases hard to distinguish particles from voids. Moreover, it was impossible to determine whether a void used to contain a particle before the specimen was split in two. Therefore, particles and voids, together, were identified as one object type. The area fraction of particles and voids ω_A was determined from the manually traced boundaries by using the open-source image processing and analyzing program ImageJ [4]. The principle of Delesse, stating that the area fraction ω_A of a component in a random cross section is equal to the volume fraction ω of the component in the entire material, was then used. The principle is described closer in Chapter 2.6. The particle content of the material was found in following way. It was assumed that the undeformed PVC contained no voids, only particles. The fraction of objects observed in the SEM of the undeformed material, ω_0, was therefore interpreted as the particle content of the material. To ensure representative results, two micrographs from each test specimen were investigated, each covering an area of $38.6\mu m \cdot 26.0\mu m$.

6.5 SEM RESULTS

A section from a scanning electron micrograph of undeformed PVC is displayed in Figure 6.8. As always, it was cooled in liquid nitrogen before it was split in two to ensure that undesired deformations did not occur during the fracture process. Image analysis suggests that the material contains particle volume fraction ω_0 around 0.24. Judged from their visual appearance, two kinds of particles might be present. There are some rather spherical particles that are comparatively small, having diameter around 0.2-0.4 μm, and some larger particles having a more irregular shape. The dispersion of particles in the matrix material appears to be good. Both kinds of particles exhibit a distribution of size. The smallest particles were hard to observe in the SEM, so no exact size distribution can be determined. Still, some general reflections can be made. Although not present in Figure 6.8, particles up to 18 μm were found, but they were very few. Most of the particles were considerably smaller. A common particle size appeared to be from 2 μm and smaller with a higher incidence of particles sized 0.5 μm and smaller. The smallest particle observed at the magnification level used in the SEM was 0.06 μm. Smaller particles might exist even though they were not discovered.

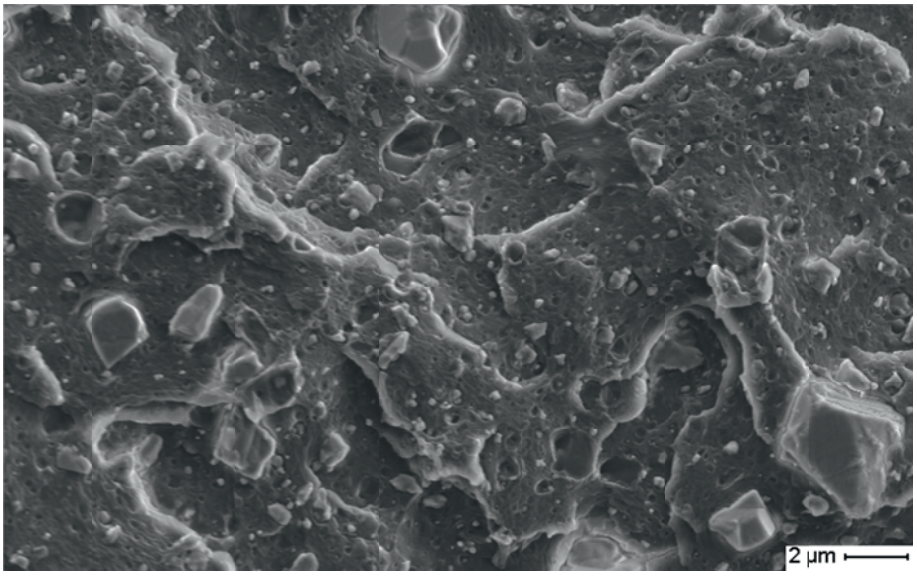

Figure 6.8 *SEM micrograph of cryo-fractured undeformed mineral filled PVC.*

The smallest spherical particle type was too small for energy dispersive spectroscopy. As presented in Chapter 2.8 EDS on the larger irregular particles suggest that the filler is made of calcium carbonate ($CaCO_3$). We can therefore expect that the particles have a rather stiff mechanical response compared to the PVC matrix.

Representative micrographs for all deformed test specimens are presented in Figure 6.9 to Figure 6.12. The vertical direction represents the tensile direction in all cases. The micrographs were recorded from the cross sections where necking was initiated. It was clearly seen in the SEM that the region for onset of necking contained more voids than the surrounding regions.

Figure 6.9 shows the two least deformed specimens. Sample PVC-1 was only deformed elastically while PVC-2 was unloaded at peak stress, in other words at onset of yielding from a macroscopic point of view. Still, some plastic deformation might have occurred locally in the PVC matrix. No voids are observed around any of the particles in Figure 6.9. Nevertheless, the particles might have debonded from the matrix. If debonding takes place before the material yields, the void growth is elastic and the void might just enclose the particle during unloading. Also in the micrograph of PVC-3, in Figure 6.10 a), no clear sign of void growth can be seen. In the micrograph of PVC-4 in Figure 6.10 b) we can vaguely see the first evidence of particle-matrix separation causing formation of voids around some particles. The debonding seems to occur around the large particles first. However, the voids are

not very clear at this stage. Between the tests PVC-4 in Figure 6.10 b) and PVC-5 Figure 6.11 a) there is a markedly difference in the appearance of the voids, even though the difference in strain level, see Figure 6.3, between these two tests is moderate. In PVC-5 many of the particles have clearly debonded from the matrix, and it is apparent that the void size has increased around the particles. Also in the micrographs of specimen PVC-6 in Figure 6.11 b) we can clearly see how the voids have grown around the particles. In the two most deformed specimens, PVC-7 and PVC-8, shown in Figure 6.12, a larger amount of the particles has debonded from the matrix and the voids are considerably larger than in the other micrographs.

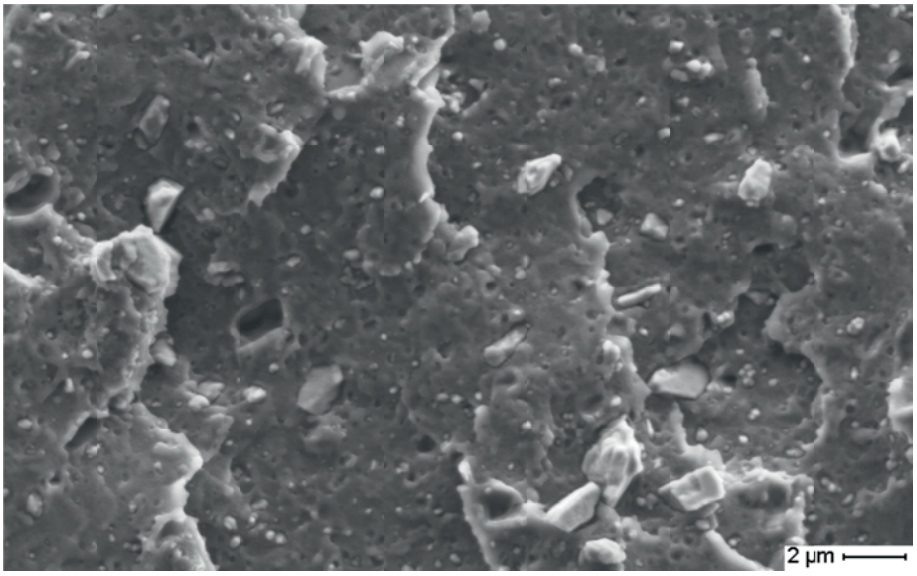

a)

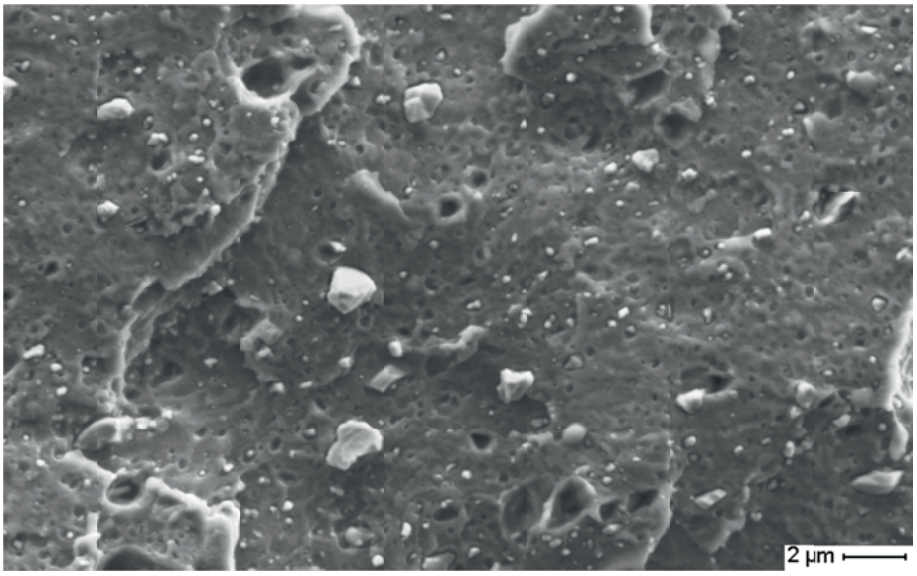

b)

Figure 6.9 *SEM micrograph of deformed samples a) PVC-1 and b) PVC-2. The specimens were loaded in the vertical direction.*

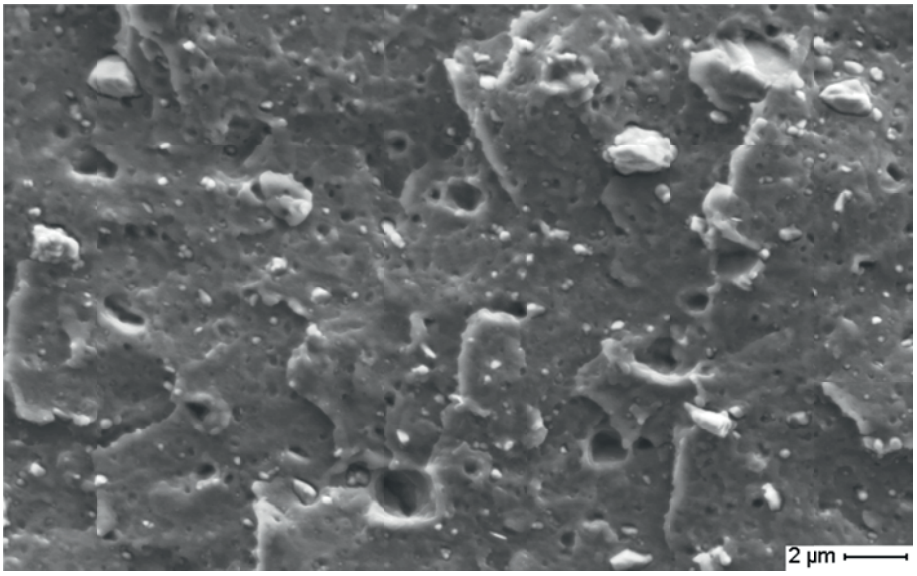

a)

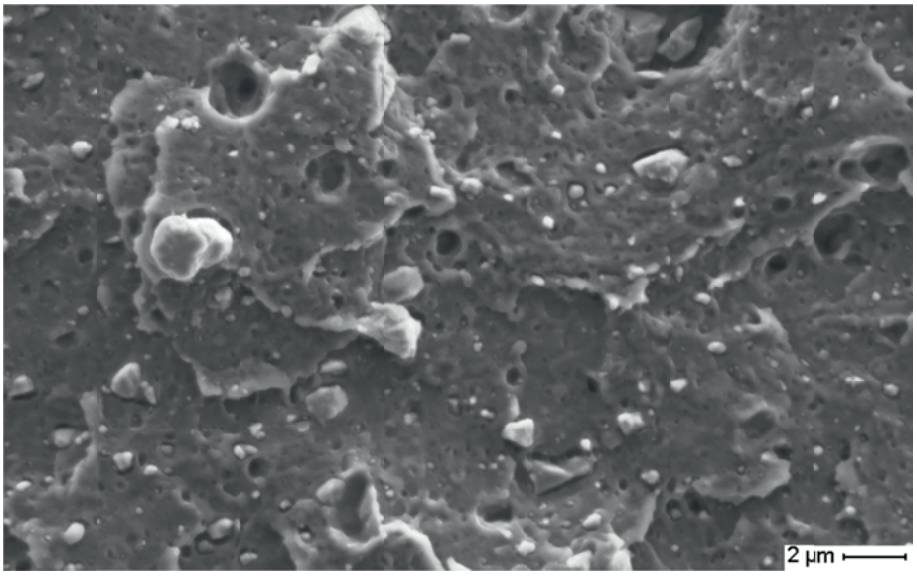

b)

Figure 6.10 *SEM micrograph of deformed samples a) PVC-3 and b) PVC-4. The specimens were loaded in the vertical direction.*

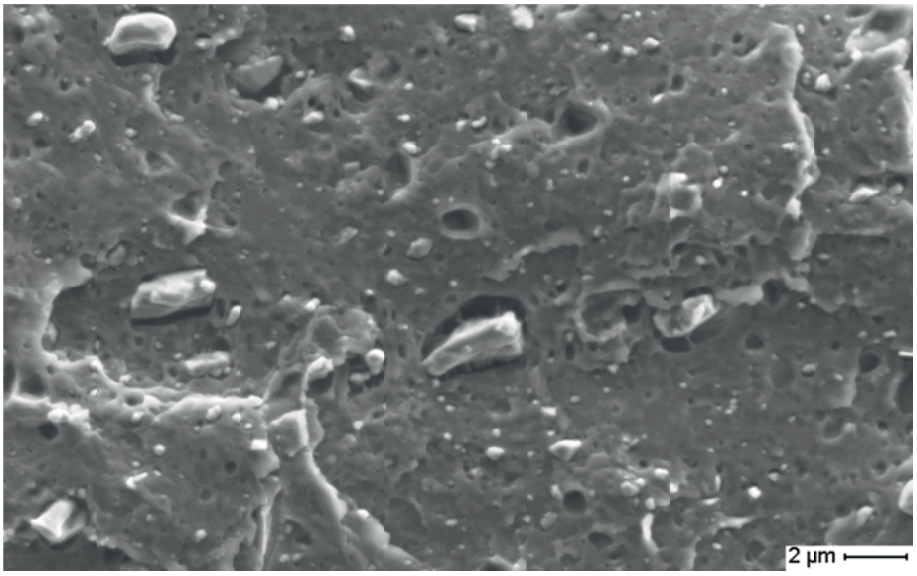

a)

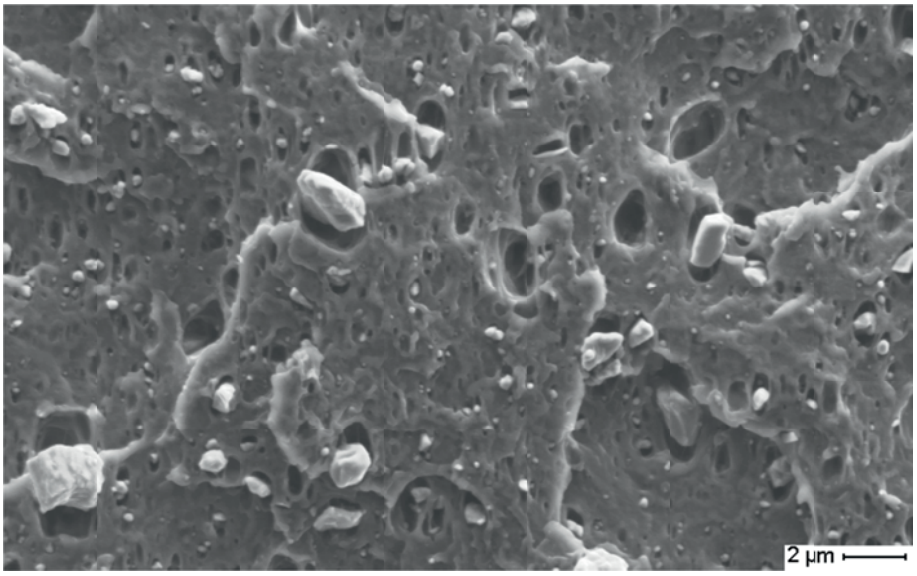

b)

Figure 6.11 *SEM micrograph of deformed samples a) PVC-5 and b) PVC-6. The specimens were loaded in the vertical direction.*

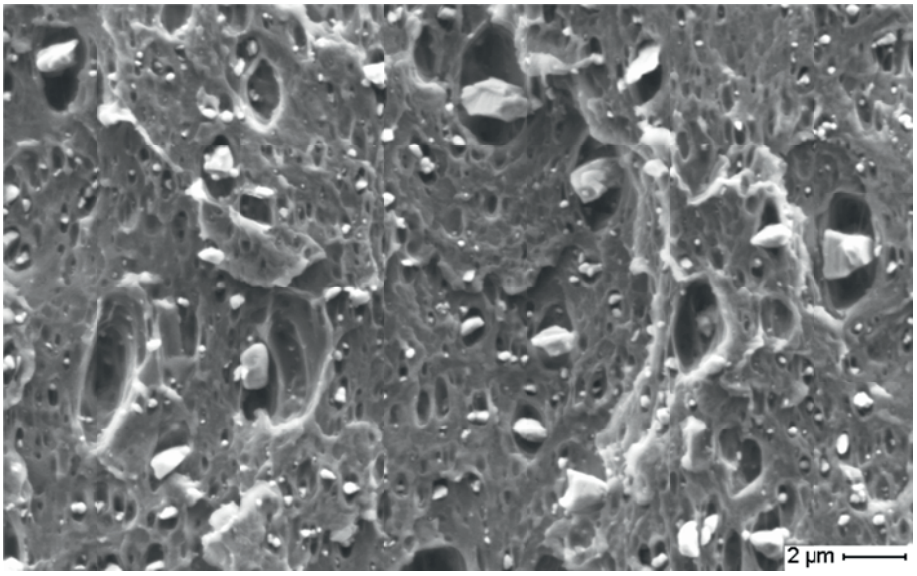

a)

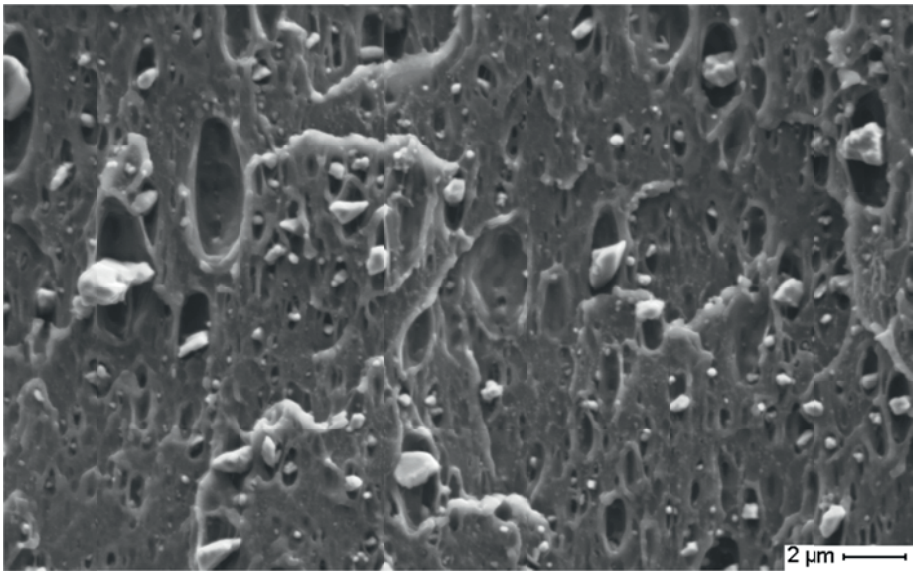

b)

Figure 6.12 *SEM micrograph of deformed samples a) PVC-7 and b) PVC-8. The specimens were loaded in the vertical direction.*

Large particles, and cavities obviously formed by large particles that fell out during the splitting process, could be observed in some of the micrographs. One example is shown in Figure 6.13. This micrograph is recorded from specimen PVC-4, which is a specimen without particularly large deformations. Still it can be seen that the presence of one large particle causes local deformations so large that many smaller particles in the vicinity debond from the matrix. Very few such large cavities and particles were observed during the microscopic examination, indicating that the amount of such large particles is limited in this particular PVC.

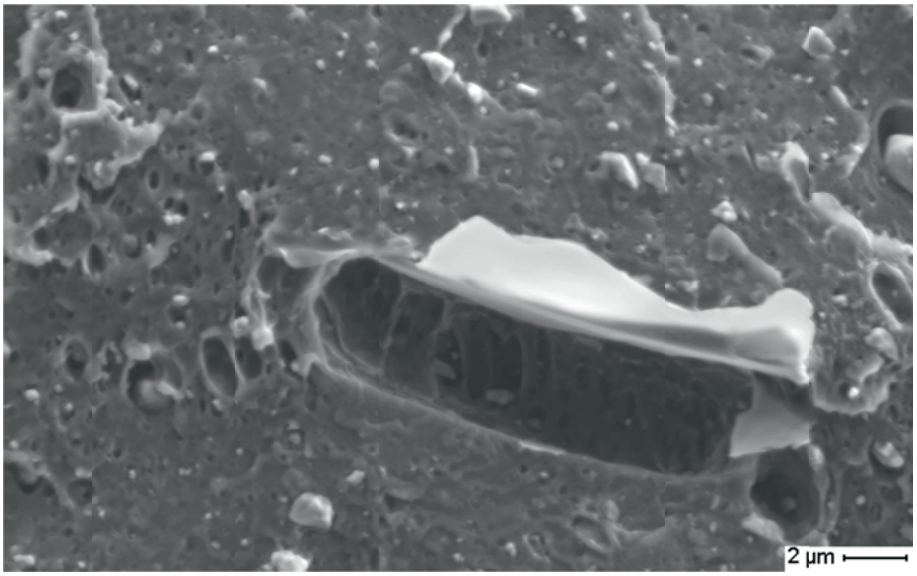

Figure 6.13 *SEM micrograph of specimen PVC-4 showing a cavity, probably after a large particle of high aspect ratio. The particle is assumed to have fallen out during splitting of the specimen. It can be seen that some smaller particles near the large cavity have debonded from the matrix material. The specimen was loaded in the vertical direction.*

6.6 ESTIMATION OF VOID VOLUME FRACTIONS

The contours of the particles and voids were traced manually before their volume fraction ω, which was assumed to be equal to the area fraction ω_A, was determined in the software ImageJ. An example image displaying a micrograph with the traced contours is shown for specimen PVC-8 in Figure 6.14. Particle and

void volume fractions ω were estimated from exploring two such micrographs from each of the eight tests.

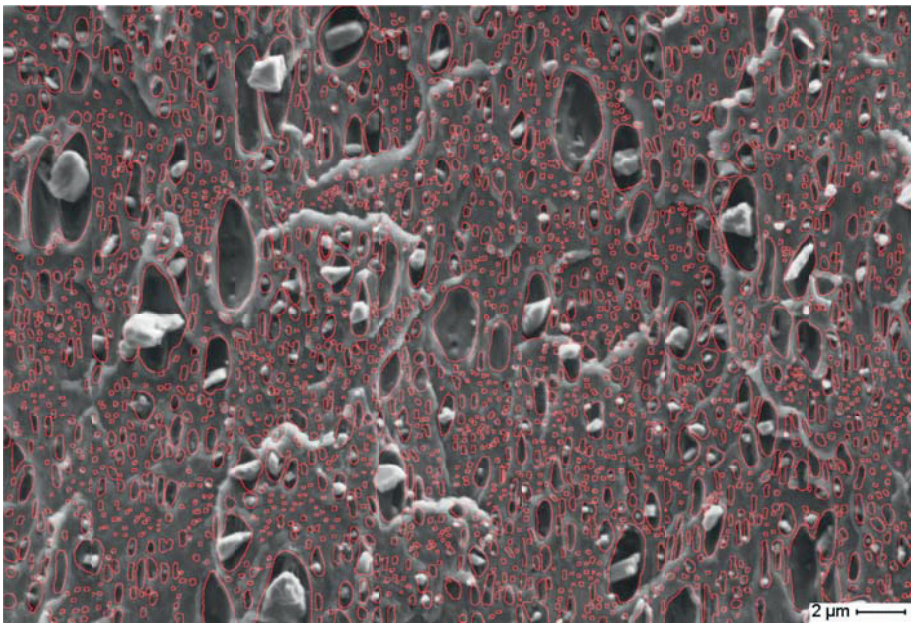

Figure 6.14 *SEM micrograph of PVC-8. The outlines of areas containing particles and voids are marked in red. The specimen was deformed in the vertical direction.*

The particle and void volume fractions ω are plotted against the plastic strain at the end of the respective test in Figure 6.15. It clearly seen that ω increases with the plastic strain. Each colour in the plot represents the results from one test, and the colours correspond to those used for the different tests earlier in this section, see Figure 6.2 to Figure 6.4.

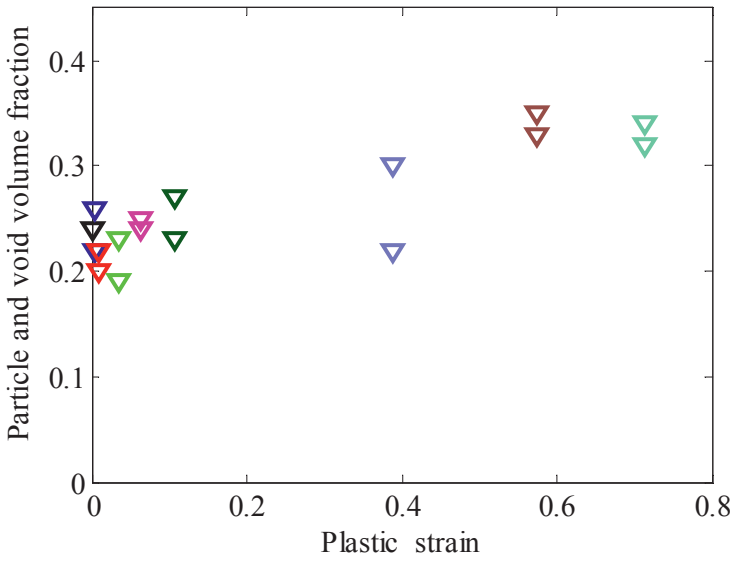

Figure 6.15 *Particle and void volume fractions ω estimated from scanning electron micrographs. Two micrographs were considered for each test. The colour used for each test corresponds with the colour in the previous plots.*

It can be assumed that particle debonding is the only source of void nucleation, meaning that all void growth happens around the already present particles. Ignoring other sources of nucleation, the evolution of the particle and void volume fraction $\dot{\omega}$ can be written

$$\dot{\omega} = \dot{\omega}_g \tag{6.1}$$

where $\dot{\omega}_g$ is the growth of particle and void volume fraction.

The evolution in the particle and void volume fraction $\dot{\omega}_g$ can, as described in Chapter 2.7, be expressed through the plastic part of the Jacobian J^p

$$\dot{\omega}_g = (1-\omega)\frac{\dot{J}^p}{J^p} \tag{6.2}$$

By integrating this differential equation and using that $\varepsilon_v^p = \ln(J^p)$, we can describe the plastic volume strain in terms of ω

$$\varepsilon_v^p = \ln\left(\frac{1-\omega_0}{1-\omega}\right) \tag{6.3}$$

From a micrograph of an undeformed sample, the initial void and particle fraction ω_0 was found to be 0.24. Equation (6.3) was used to calculate values of ε_v^p from the estimates of ω. The results are plotted with triangles in Figure 6.16. In the same figure, the volume strains measured by DIC at the end of 10 minutes of relaxation after the test are plotted with crosses. Each of the colours represents the results from one test. Moreover, two straight lines were fitted to the two data sets to better show the results. It is seen that the volume strains predicted by the SEM data, i.e. the estimated values of ω and Equation (6.3), are rather close to the volume strains measured by DIC. In particular, it is noted that the slopes of the two lines are almost identical. The deviation may be related to some inaccuracies in the SEM data, especially for the undeformed sample. It is estimated that the undeformed sample has a higher value of ω than some of the deformed specimens. Thus, some faulty negative volume strains are predicted from the SEM data.

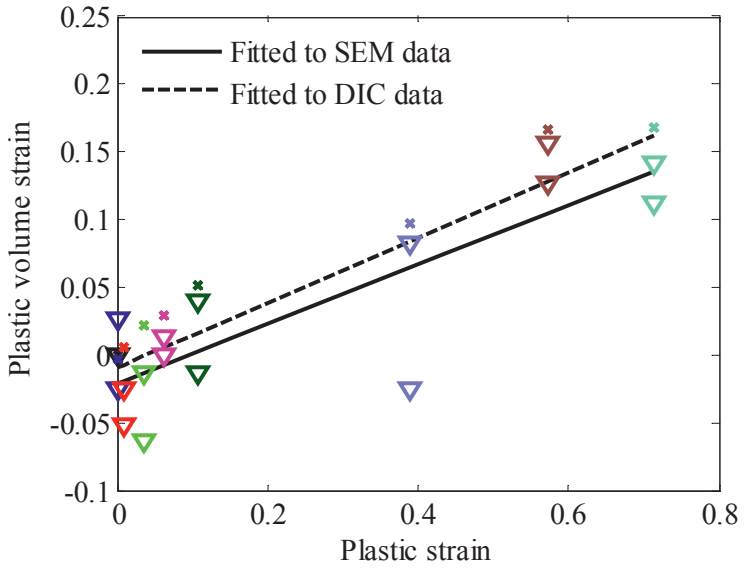

Figure 6.16 *Plastic logarithmic volume strain plotted against plastic longitudinal strain. The triangles represent plastic volume strain estimated from SEM and the crosses refer to plastic volume strain at the end of the test measured by DIC. The colour used for each test corresponds with the colour in the previous plots.*

6.7 ESTIMATION OF EFFECTIVE STRESS

To investigate the damage effect in terms of loss of strength of the composite material, it is interesting to establish an expression for the void volume fraction. In that context we first denote the volume fraction of what is considered as damaged material as ω_D . This parameter represents the volume fraction of debonded particles and the voids around them. In other words, the volume occupied by a debonded particle is included in ω_D . Volume occupied by particles that are still attached to the matrix is not included in ω_D since these particles still carry load. Since the particles seem to have a good initial bonding to the matrix, the initial volume fraction of damaged material can be regarded to be $\omega_D = 0$. We then assume that when a critical stress is reached the particles act as nucleation sites for voids, and ω_D rapidly starts to increase. The volume fraction of material that is damaged by nucleated voids is denoted $\omega_{D,n}$. If we assume that all particles are debonded after a certain deformation, and that particle debonding is the only nucleation process, we get an upper limit of $\omega_{D,n}$ that is determined by the particle content of the material. In addition to the nucleation, the already nucleated voids grow. This gives rise to another contribution to the damage volume fraction that is denoted $\omega_{D,g}$. The total increase of void volume fraction ω_D is then therefore sum of two contributions

$$\dot{\omega}_D = \dot{\omega}_{D,n} + \dot{\omega}_{D,g} \tag{6.4}$$

During the tests, it was visually observed that stress whitening gradually started at peak stress. This indicates that the particle debonding also is initiated at this stage. We therefore assume that nucleation of voids occurs between plastic strains of $\varepsilon^p = 0$ and $\varepsilon^p \approx 0.1$. Thus, the following simple model for volume fraction of nucleated voids can be formulated

$$\omega_{D,n} = \omega_0 \left[1 - \exp\left(-50 \cdot \varepsilon^p \right) \right] \tag{6.5}$$

The particles volume fraction $\omega_0 = 0.24$ is considered as the upper limit for the void nucleation process. The factor 50 is has no other interpretation than to control the termination of the nucleation process at around $\varepsilon^p = 0.1$. Differentiating Equation (6.5) gives the following expression for void nucleation on rate form

$$\dot{\omega}_{D,n} = 50\omega_0 \exp(-50\varepsilon^p)\dot{\varepsilon}^p \tag{6.6}$$

The expression for void growth is, similar to Equation (6.2),

$$\dot{\omega}_{D,g} = (1-\omega_v)\frac{\dot{J}^p}{J^p} \tag{6.7}$$

Employing Equation (6.4) with Equations (6.6) and (6.7) on test data from specimen PVC-8, we obtain the evolution of void volume fraction ω_D presented in Figure 6.17 a). As described in Equation (6.6), the nucleation process ceases at a strain around 0.1. The contribution from the void growth term increases continuously during the test.

Debonding and void growth can be interpreted as damage since the section occupied by voids and debonded particles does not carry load. Reaching the deformation that initiates particle-matrix separation will cause a sudden reduction of the load bearing cross section even though no such sudden volume change can be observed macroscopically. b). An estimation of the effective stress σ_{eff} , regarded as the average stress in the ligaments between the debonded particles and the voids [5], can be expressed as

$$\sigma_{eff} = \frac{\sigma}{(1-\omega_D)} \tag{6.8}$$

By using the test PVC-8 as an example, the effective stress-strain curve is represented in Figure 6.17 b). The dashed line in the figure represents the effective stress of the damaged composite, i.e. the stress carried by the matrix between the voids as the particles gradually separate from the matrix. It is seen that there is no stress drop in the effective stress. The solid line in Figure 6.17 b) represents the stress-strain curve from the test without taking damage into account.

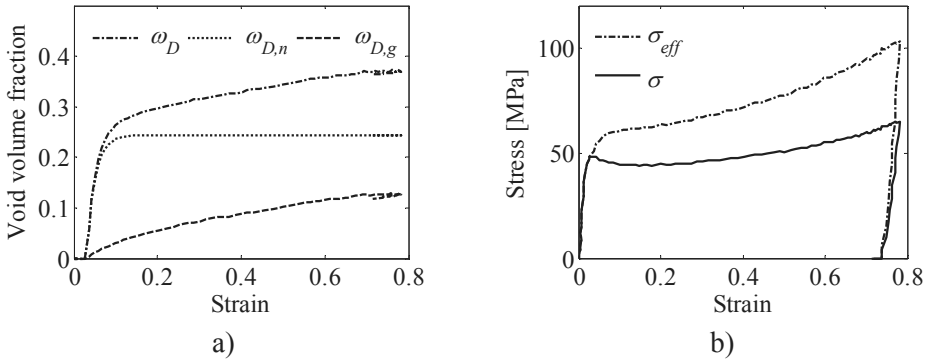

Figure 6.17 *a) Estimation of the evolution of void volume fraction of debonded particles and the voids around them for test PVC-8. b) Estimation of effective stress in the matrix ligaments between the voids.*

6.8 DISCUSSION

Eight uniaxial tensile specimens of $CaCO_3$ filled PVC were loaded to different elongations and thereafter unloaded. The most deformed zones of the specimens were investigated in SEM after testing to study how the morphology of the composite change with the deformation. Initially the $CaCO_3$ particles appear to be well bonded to the PVC matrix. The material then acts like a composite where the particles serve as reinforcement. At larger deformations it is clearly seen that the particles debond from the matrix. The particles act as nucleation sites for voids that continue growing as the material deforms, causing a volume change.

Volume fractions of particles and voids ω, found from analyzing two micrographs from each test specimen, were employed to produce an estimation of plastic volume strain. The plastic volume strain estimated from the microscopic measurements is, according to Figure 6.16, in good agreement with the volume increase at the macroscopic scale measured by DIC. It is therefore reasonable to conclude that the macroscopic dilation is caused by void growth on the microscopic scale. The difference between the two data sets may be related to viscous effects, poor quality of SEM micrographs or by inaccurate estimation of particle and void area fractions from the micrographs.

The volume strains plotted in Figure 6.4 and the retraction ratio plotted in Figure 6.5 show that the dilation changes during the deformation. Initially, when the particles are well attached to the matrix, the retraction ratio of the composite is determined by the Poisson's ratio of each of the components. When debonding sets in, growth of voids causes dilation at the macroscale, observed as a reduction in the retraction ratio. The retraction ratio has the lowest value at longitudinal strain of ε_1 = 0.07-0.095. Figure 6.6 shows both the Cauchy stress and the retraction ratio plotted against logarithmic strain for the specimen PVC-8. It is interesting to note that the minimum value of the retraction ratio occurs after peak stress. This means that the volume change is at its largest somewhat after onset of plasticity. It could be an indication of a sudden debonding process at this stage. Subsequently, in the large strain regime, the retraction ratio increases. In other words the increase of dilation decays. This might be related to that the void growth is limited when the strain hardening in the matrix material around the voids sets in. Additional aspects, such as molecular packing caused by orientation of amorphous chain segments [6] or nucleation of new voids in lesser dense packed areas [1], might affect the volume change. These are assumed to be minor effects and will not be further discussed here.

In Figure 6.11 it can be seen that particles lying close to each other tend to impose some linkage of void growth in, or with a small angle to, the transverse direction. This might be an indication of formation of dilational bands, similar to what is observed in rubber toughened polymers [7, 8]. From the micrographs, the dilational bands seem to form where the particles are located close to each other or where a large particle is present as in Figure 6.13. According to Chapter 2.5 small particles follow the flow of the matrix material. Larger particles, with less mobility, separate from the matrix. The random position of the smaller and larger particles determines how the dilation bands spread through the material. The dilational band formation is in general not very clear in these tests. In the micrographs of more deformed specimens in Figure 6.12, there is no indication of such dilational bands at all. This is might be related to the strain hardening property of the matrix, the stretched material between the voids exhibits higher stiffness than the surrounding matrix material due to network stretching and molecular orientation. Therefore, the deformation is subsequently redistributed to the surrounding, and more deformable, material. In this way the deformation is stabilized. Moreover, the stretched fibrils between the voids may hinder coalescence of voids. No coalescence is observed in any of the micrographs even though some of the specimens were deformed close to the fracture strain.

Particle debonding and void growth can be regarded as damage mechanisms. When a particle debonds from the matrix, the load bearing cross section of the specimen is reduced. Simple expressions for particle debonding and void growth were used to estimate an effective stress in the damaged material. This was done to check whether the stress drop can be explained by damage. Figure 6.17 b) shows that the macroscopic stress softening disappeared when the void nucleation and growth was taken into account. However, in Chapter 2.5 and Chapter 4 it was reported that such a stress drop also occurs in compression. The reason for this is still left to explain. It could mean that the stress drop has other causes than debonding and void growth.

A consequence from the principle of Delesse, discussed in Chapter 2.6, is that the cross section area reduction due to the voids is independent of the cutting direction. This also holds for anisotropic voids. The damage, in terms of area reduction, is therefore assumed to be isotropic. Nevertheless, the oblong voids bring along geometrical and material anisotropy that is not taken into account in this study. The elliptic voids cause local stress concentrations in the material that vary with the direction of the applied load. This is referred to as geometrical anisotropy. The material anisotropy refers to fibril stretching and orientation of polymer chains in the PVC matrix in the ligaments between the voids.

The initial particle volume fraction was only determined from one SEM micrograph. It was estimated to be $\omega = 0.24$. This might be a too high estimate since it is higher than particle and void volume fractions estimated for the somewhat more deformed specimens. A volume fraction of $\omega \sim 0.2$ is assumed to be more realistic.

There are several possible sources of error in the particle and void identification process. The micrographs were recorded some time after the experimental test. The specimens might have contracted due to relaxation in this time period, even though new measurements done a week after the testing did not indicate so. Another source of error is that the regions investigated in the SEM may contain more particles than the other regions of the test specimen. It is reasonable to believe that a local high density of particles is the reason for the onset of a neck. Thus, the investigated section might contain a local high density of particles. For the less deformed specimens, PVC-1 and PVC-2, where no neck had occurred yet, the choice of what section to observe was more or less arbitrary. This would lead to a lower estimate of particle and void fractions ω for these two tests. Further, the splitting of the specimens does not create an entirely plane surface. The fracture imposed during splitting follows the "easiest way" through the specimen. The surface investigated in the SEM may therefore have contained a higher density of voids than what is representative for the whole specimen. Moreover, splitting of the specimens during the SEM preparation might have caused a stress release of residual stress around the voids and in next turn a change of the geometry of the void.

A relatively low accelerating voltage, 5 keV, was used in the SEM to limit the penetration depth of the electron beam. Still, some penetration should be accounted for. This may lead to overestimation of the particle content. The quality of the SEM micrographs is another source of error. With a poor focus, fewer particles are visible at the micrograph. If too much time was used to focus at one point, the material was heated and cracked. Therefore, the SEM process had to be performed rather quickly. The applied zooming level might cause the smallest particles not to appear in the micrographs. Moreover, the considered micrographs had to be sufficiently large in order to depict a realistic area fraction of particles and voids. As an extreme, Figure 6.13 would produce an unrealistic high estimate of the particle content. This micrograph was therefore not included in the estimation of volume fraction ω. Two micrographs were considered for each specimen during the counting process. These might not have been recorded at an area that was representative, or they might not have been located exactly at the root of the notch.

It was challenging to determine from the micrographs whether the observed objects were particles, voids or just material irregularities. Different automatic techniques

to trace the outlines of the particles and the voids were evaluated [9]. Comparison of the outlines found by the various techniques demonstrated that manual identification was the most accurate one. An alternative method for determination of the void volume fraction could have been to use X-ray tomography [10].

6.9 CONCLUDING REMARKS

- The investigated material is a composite of a PVC matrix containing comparably stiff mineral particles, mainly $CaCO_3$.
- Debonding of the mineral particles seems to initiate when a certain stress is reached. After this, void growth is a dominating mechanism on the microscale.
- The observed plastic dilation on the macroscale is in good agreement with the estimated void growth on the microscale. Void growth is therefore assumed to be the reason for the plastic dilation.
- Particle debonding and void growth are two damage mechanisms. Thus, the damage cannot be estimated from the volume change alone. The volume occupied by particles that have debonded should be taken into account when estimating the damage.
- The stress drop on the Cauchy stress – logarithmic strain curve of the mineral filled PVC may be related to debonding and void growth.

REFERENCES

[1] A.A. Galeski. Strength and toughness of crystalline polymer systems. *Progress in Polymer Science*, **28** (2003), 1643-1699.

[2] H.S. Katz, J.V. Milewski. *Handbook of fillers for plastics.* Van Nostrand Reinhold Co., New York (1987).

[3] V. Delhaye, A.H. Clausen, F. Moussy, O.S. Hopperstad, R. Othman. Mechanical response and microstructure investigation of a mineral and rubber modified polypropylene. *Polymer Testing*, **29** (2010), 793-802.

[4] ImageJ - Image Processing and Analysis in Java, 2012.

[5] J. Mohanraj, D.C. Barton, I.M. Ward, A. Dahoun, J.M. Hiver, C. G'Sell. Plastic deformation and damage of polyoxymethylene in the large strain range at elevated temperatures. *Polymer*, **47** (2006), 5852-5861.

[6] L. Cangemi, S. Elkoun, C. G'Sell, Y. Meimon. Volume strain changes of plasticized poly(vinylidene fluoride) during tensile and creep tests. *Journal of Applied Polymer Science*, **91** (2004), 1784-1791.

[7] A. Lazzeri, C.B. Bucknall. Dilatational bands in rubber-toughened polymers. *Journal of Materials Science*, **28** (1993), 6799-6808.

[8] D.M. Laura, H. Keskkula, J.W. Barlow, D.R. Paul. Effect of rubber particle size and rubber type on the mechanical properties of glass fiber reinforced, rubber-toughened nylon 6. *Polymer*, **44** (2003), 3347-3361.

[9] A.H. Malvik. Void growth in calciumcarbonate filled PVC. Master thesis, Department of Structural Engineering, NTNU, (2011).

[10] L. Laiarinandrasana, T.F. Morgeneyer, H. Proudhon, C. Regrain. Damage of semicrystalline polyamide 6 assessed by 3D X-ray tomography: From microstructural evolution to constitutive modeling. *Journal of Polymer Science Part B: Polymer Physics*, **48** (2010), 1516-1525.

CHAPTER 7

BIAXIAL TENSION

This chapter presents and discusses a set of biaxial tests performed on specimens from the 5 mm plates of PVC and HDPE. Addressing the pressure sensitivity of the yield stress, it is interesting to investigate the mechanical response at more complex stress states than uniaxial tension and compression. The main purpose of these tests is to serve as a basis for validation of a constitutive model that will be presented in Chapter 10.

7.1 INTRODUCTION

Tensile biaxial load cases occur in several practical applications of thin-walled polymer components. It is therefore important that the material model represents such stress states properly. Within this context, it is relevant to evaluate the capability of the Raghava yield function to describe large deformations in a biaxial loading mode. This chapter presents and discusses a set of laboratory tests for this purpose.

Some investigations on the mechanical response of different polymers in biaxial deformation have been reported in the literature [1-8]. The studies on biaxial deformation found in the literature often concern manufacturing conditions involving high strain rates and high temperatures or the behaviour of polymer films. Paying attention to validation of material models, Chevalier and co-workers [9, 10] have shown that by using a multiaxial testing machine, a charge-coupled device (CCD) camera and digital image correlation (DIC) software, biaxial displacement and strain fields from such tests can be evaluated for rubber-like materials. By assuming incompressibility they derived the stress evolution in the test specimen during deformation and compared this with the stress calculated by different rubber material models.

7.2 TEST SETUP

Cross-shaped test specimens, see Figure 7.1, were cut out from the 5 mm thick extruded PVC and HDPE plates. At the centre of the samples, the thickness was gradually reduced to 1 mm. This was done to control the location of the initial strain localization.

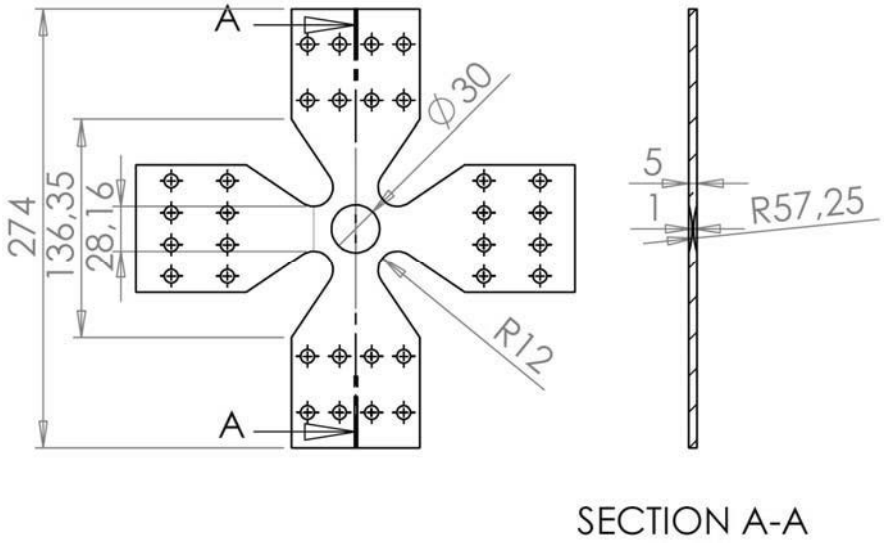

Figure 7.1 *Sketch of the biaxial test specimen including some relevant measures (in mm).*

All experiments were performed in the Astree triaxial testing machine [9, 11] at LMT-Cachan in France. Two of the three axes of this machine were employed using displacement controlled loading. The software LabView was used for computer control of the test and data acquisition. Each test specimen was mounted in the testing machine, according to Figure 7.2, with the extrusion direction parallel to the horizontal *x*-axis and the transverse direction parallel to the vertical *y*-axis. The deformation was surveyed by a CCD-camera taking pictures at frequencies according to Table 7.1. All specimens were painted with a speckled pattern before testing, facilitating post-test analysis with the DIC program 7D [12] to find the in-plane Green strain fields E_x, E_y and E_{xy} at the surface of the biaxial test samples.

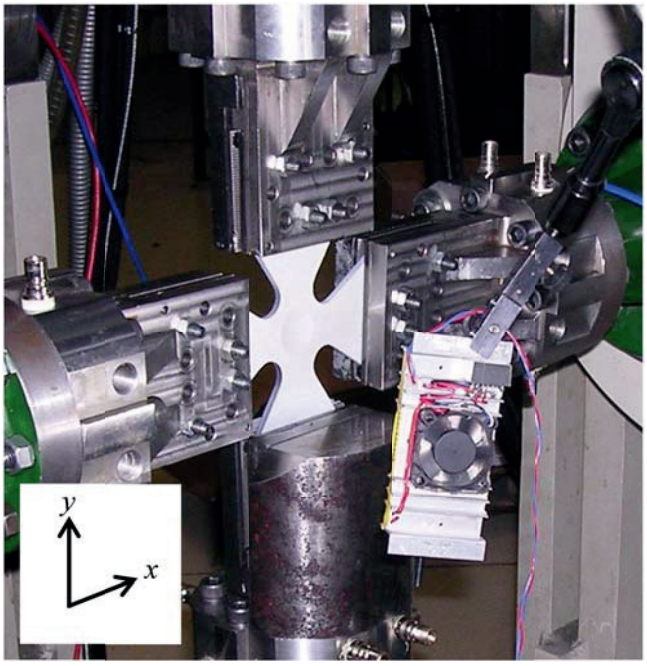

Figure 7.2 *A biaxial tension specimen in the Astree testing machine.*

In order to obtain different states of biaxial loading, three biaxial load cases with different ratios were investigated for each material, see Table 7.1. The biaxial extension ratio $B = v_y / v_x$, i.e. the ratio between the cross-head velocities v_y and v_x in the *y*- and *x*-directions, respectively, was equal to ¼, ½ and 1. To obtain this, v_y varied between the different tests while v_x was fixed. During each test, however, v_x and v_y were constant. The displacement in the two directions started and stopped simultaneously. As a special case, one biaxial sample of both materials was tested in uniaxial tension, applying a servo-hydraulic MTS testing machine. For these tests the two transverse arms of the specimen were unconstrained and free to move in the *y*-direction.

According to Table 7.1, the strain rate was set relatively low, ensuring that plastic dissipation of the samples did not cause any large increase of temperature. Further, an inspection of the clamped areas after the tests revealed no signs of sliding in the fixtures. All tests were carried out at room temperature.

Table 7.1 *Biaxial test programme.*

Material	B	v_x [mm/s]	v_y [mm/s]	Initial strain rate [s^{-1}]	Sequence	CCD-camera frequency [s^{-1}]
PVC	–	0.05		$4.1 \cdot 10^{-4}$	Uniaxial	0.50
PVC	¼	0.035	0.0086	$2.3 \cdot 10^{-4}$	Biaxial	0.90
PVC	½	0.035	0.017	$2.3 \cdot 10^{-4}$	Biaxial	0.90
PVC	1	0.035	0.035	$2.3 \cdot 10^{-4}$	Equibiaxial	0.90
HDPE	–	0.05		$4.1 \cdot 10^{-4}$	Uniaxial	0.50
HDPE	¼	0.045	0.011	$3.7 \cdot 10^{-4}$	Biaxial	0.23
HDPE	½	0.045	0.022	$3.7 \cdot 10^{-4}$	Biaxial	0.23
HDPE	1	0.045	0.045	$3.7 \cdot 10^{-4}$	Equibiaxial	0.23

7.3 RESULTS

Figure 7.3 shows the force-displacement curves for PVC for the four different extension ratios. With the exception of the specimen loaded in the *x*-direction only, see Figure 7.3 a), results from both directions *x* and *y* are included. All PVC load curves show a rather linear behaviour up to maximum load, corresponding to the onset of yielding. After the point of maximum load a softening effect can be observed before cold-drawing and failure. All samples of PVC were deformed until failure.

Also Figure 7.4 represents force-displacement relationships for the biaxial PVC specimens. In this figure, only the response in the *x*-direction is included. This means that the figure expresses how the response in the *x*-direction is affected by the deformation in *y*-direction. It is seen that yielding starts at the same force level in the tests loaded in uniaxial and the equibiaxial tension. The two tests with extension ratios $B = ½$ and $B = ¼$ reach the same force at yielding, at a higher level than the other tests.

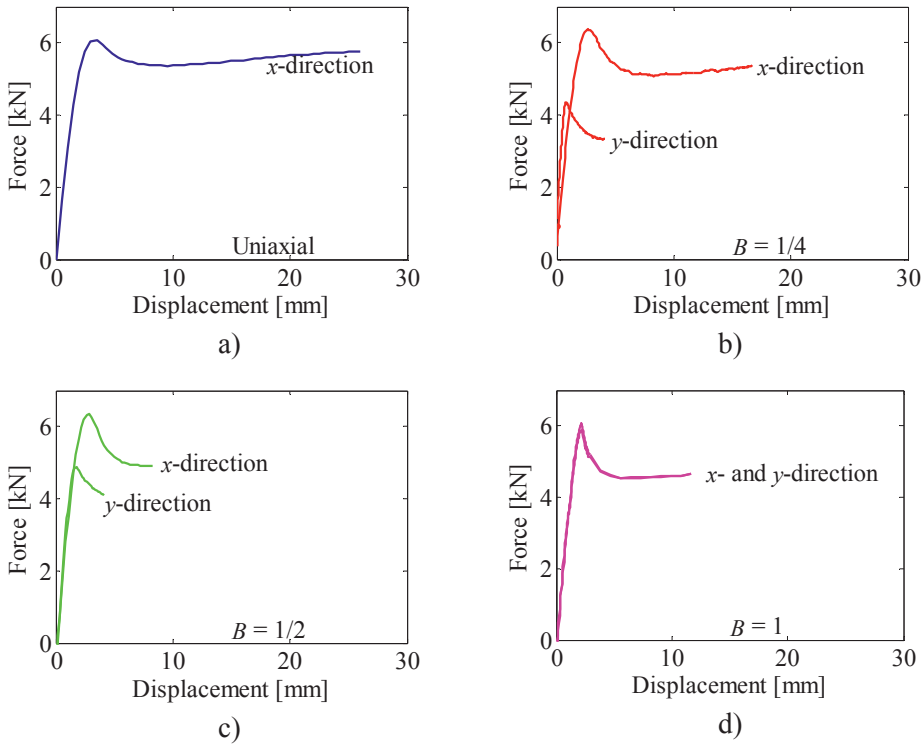

Figure 7.3 *Force-displacement curves for PVC. a) Uniaxial test on biaxial sample. The biaxial tests b) B = ¼ , c) B = ½ and d) B =1.*

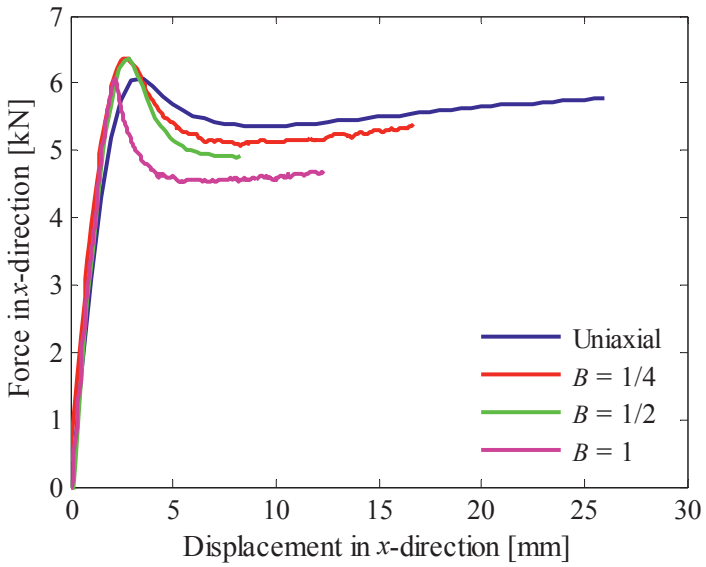

Figure 7.4 *Force-displacement curves in x-direction for biaxial samples of PVC loaded at various extension ratios.*

Figure 7.5 shows force-displacement curves for the HDPE specimens deformed at the different biaxial extension ratios. Also the HDPE samples experienced a load drop after reaching the maximum force. Holes started to grow in the centre of all HDPE specimens deformed in biaxial tension. The first appearances of the holes are marked with a circle in the figure. With further deformation the holes kept on growing larger. Due to the ductile behaviour of the material, these holes continued to grow, without causing cracking and global failure of the test specimens, until the test was aborted.

The responses of the HDPE specimens in the *x*-direction are presented in Figure 7.6. The force level reached in the uniaxial test is about the same as in the equibiaxial test. The tests deformed at $B = ½$ and $B = ¼$ reach higher force values.

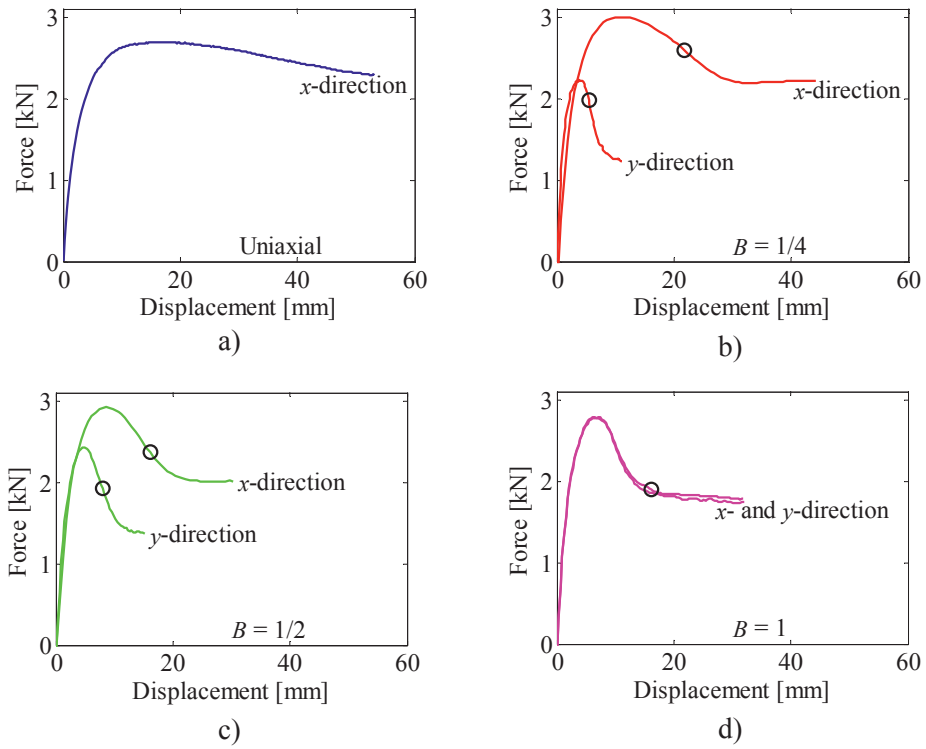

Figure 7.5 *Force-displacement curves for HDPE. a) Uniaxial test on biaxial sample. The biaxial tests b) B = ¼ , c) B = ½ and d) B =1.*

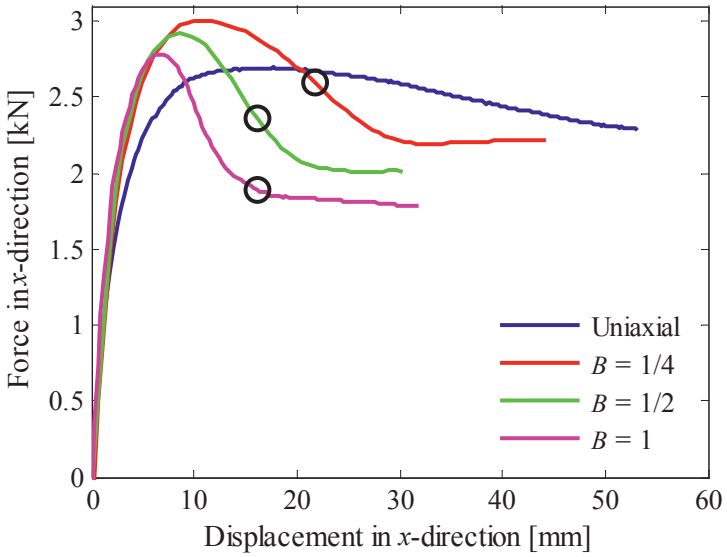

Figure 7.6 *Force-displacement curves in x-direction for biaxial samples of HDPE loaded at various extension ratios.*

Figure 7.7 shows photos of the PVC specimens at certain deformation stages. The displacement in the *x*-direction is addressed under each picture. The first row displays the specimen deformed uniaxially in the MTS testing machine. The three next rows show the specimens deformed in biaxial tension in the Astree testing machine. For all specimens sub-figure a) shows the specimens at peak force. In some of the images, stress whitening can be seen at centre of the specimen at this stage. The next column of pictures, see sub-figure b), is captured during the load drop. It is now seen that the stress whitening zone has evolved to an X-shape. At this stage, an X-shaped neck was also present in this region. The three first rows of sub-figure c) show the specimen after fracture. Also the equibiaxial specimen fractured in similar manner, however, it was not captured by the CCD-camera.

Figure 7.8 displays the deformed HDPE specimens at different deformation stages. Also here, the specimen subjected to uniaxial deformation is displayed in the first row and the biaxial tests are shown in the three subsequent rows. Sub-figure a) shows the specimens at peak force. A hole appeared at the centre point of each of the biaxially loaded HDPE specimens after some deformation. Sub-figure b) displays the last images captured before the hole was observed. The holes kept on growing during the deformation until the test was aborted. Distinct X-shaped necks had evolved in the centre region of all specimens at the deformation stage in sub-figure b). Sub-figure c) shows the specimens towards the end of the deformation.

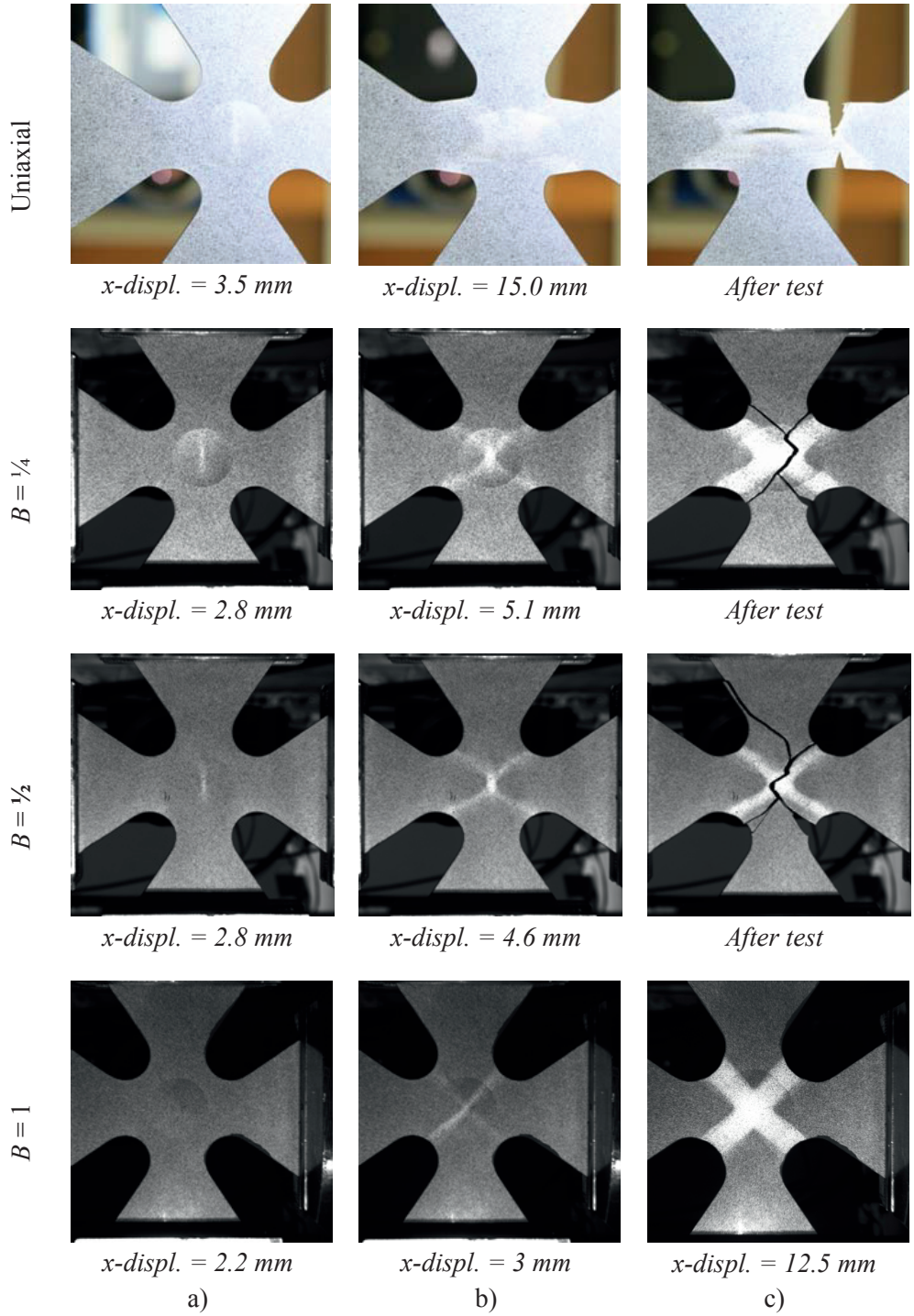

Figure 7.7 *Biaxial test specimens of PVC. The images are taken a) at peak force b) during deformation c) after fracture, or the last image before fracture.*

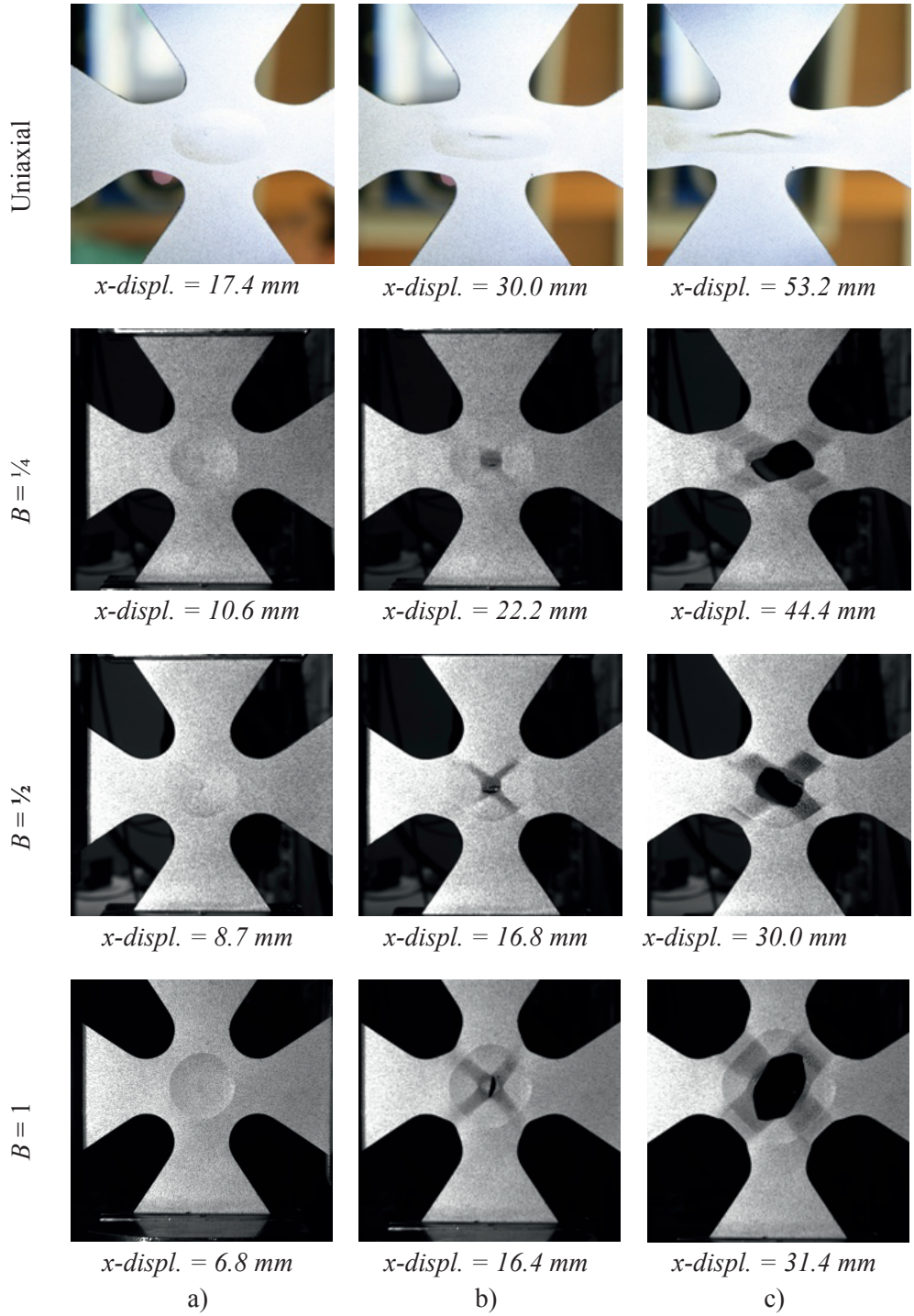

Figure 7.8 *Biaxial test specimens of HDPE. The images are taken a) at peak force b) during deformation c) towards the end of test.*

After the tests, all digital pictures were processed with the DIC software 7D. The Green strain fields E_x and E_y from the PVC specimen deformed at B = ½ are shown in Figure 7.9. The Green shear strain field E_{xy} from the same specimen, but applying a different colour bar, is shown in Figure 7.10. Sub-figure a) in Figure 7.9 and Figure 7.10 represents the strain state at maximum force. Strain localization can be seen in the E_x strain field. In sub-figure b) the strain localization becomes clearer. This can be seen for all three strain components. The strain localization is even stronger in sub-figure c). The same X-shape as earlier observed for the neck and the stress whitening zone can be recognized. In the last sub-figure, c), some information is missing in the strain field. At this stage, the speckle pattern used for correlation was so distorted in the centre point that the DIC software could not follow the deformation here. There are some fluctuations in the strain level. This is due to measurement noise. Also, close to the edge there is some noise from the correlation process.

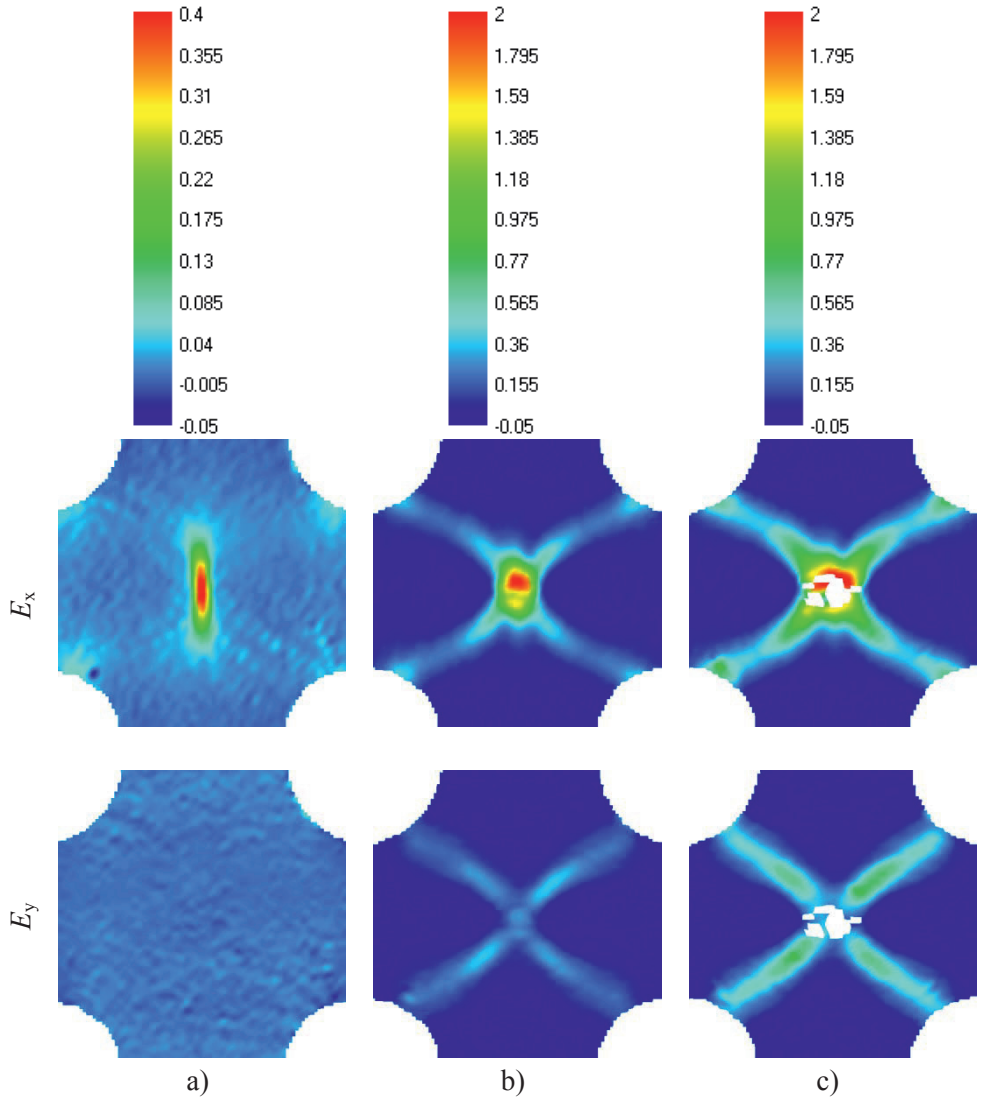

Figure 7.9 *Green strain fields E_x and E_y in the centre region of the PVC specimen deformed at B = ½ , at a) 2.8 mm b) 5.9 mm and c) 8.3 mm deformation in the x-direction .*

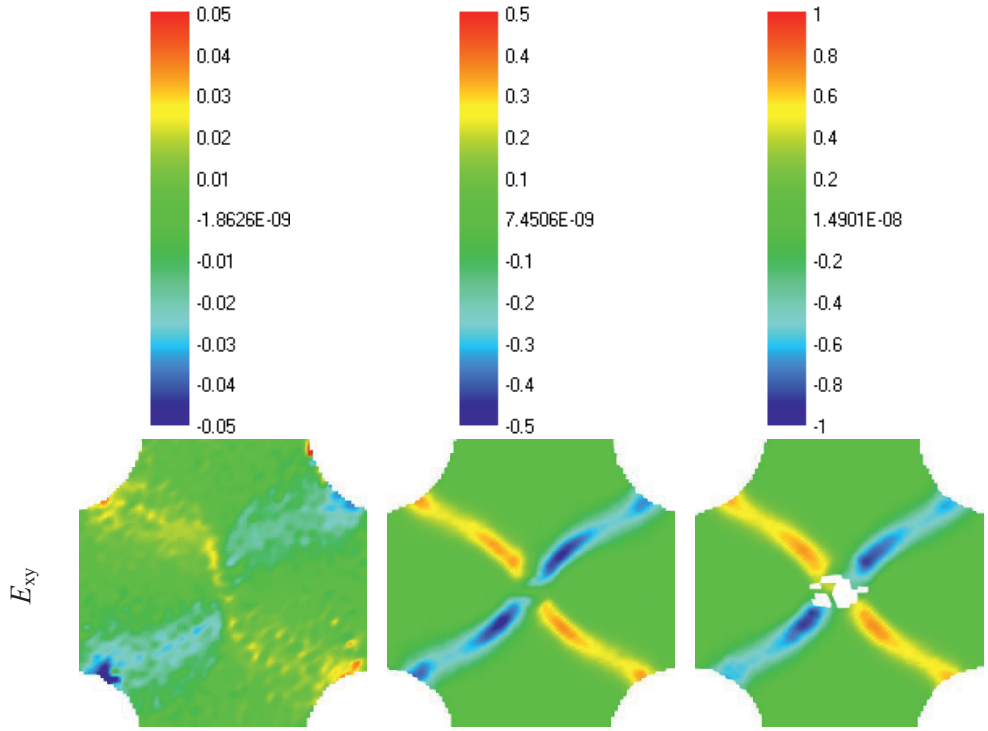

Figure 7.10 *Green shear strain field* E_{xy} *in the centre region of the PVC specimen deformed at* $B = ½$ *, at a) 2.8 mm b) 5.9 mm and c) 8.3 mm deformation in the x-direction .*

The Green strain fields E_x and E_y from the HDPE specimen deformed at $B = ½$ are shown in Figure 7.11. The Green shear strain field E_{xy} is presented in Figure 7.12. It is seen that in sub-figure a) of Figure 7.11 and Figure 7.12, representing the specimen at peak force, there is some strain localization. The strain localization becomes stronger as the specimen is deformed. The earlier observed characteristic X-shape can be recognized as the zone with the largest strains. This is seen in sub-figure b) and c). In the last sub-figures some information about the strain is missing. This is a result of distortion and cracking of the speckle pattern due to large deformations in this region. It can be assumed that the missing values exceed the maximum value indicated by the corresponding colour bars.

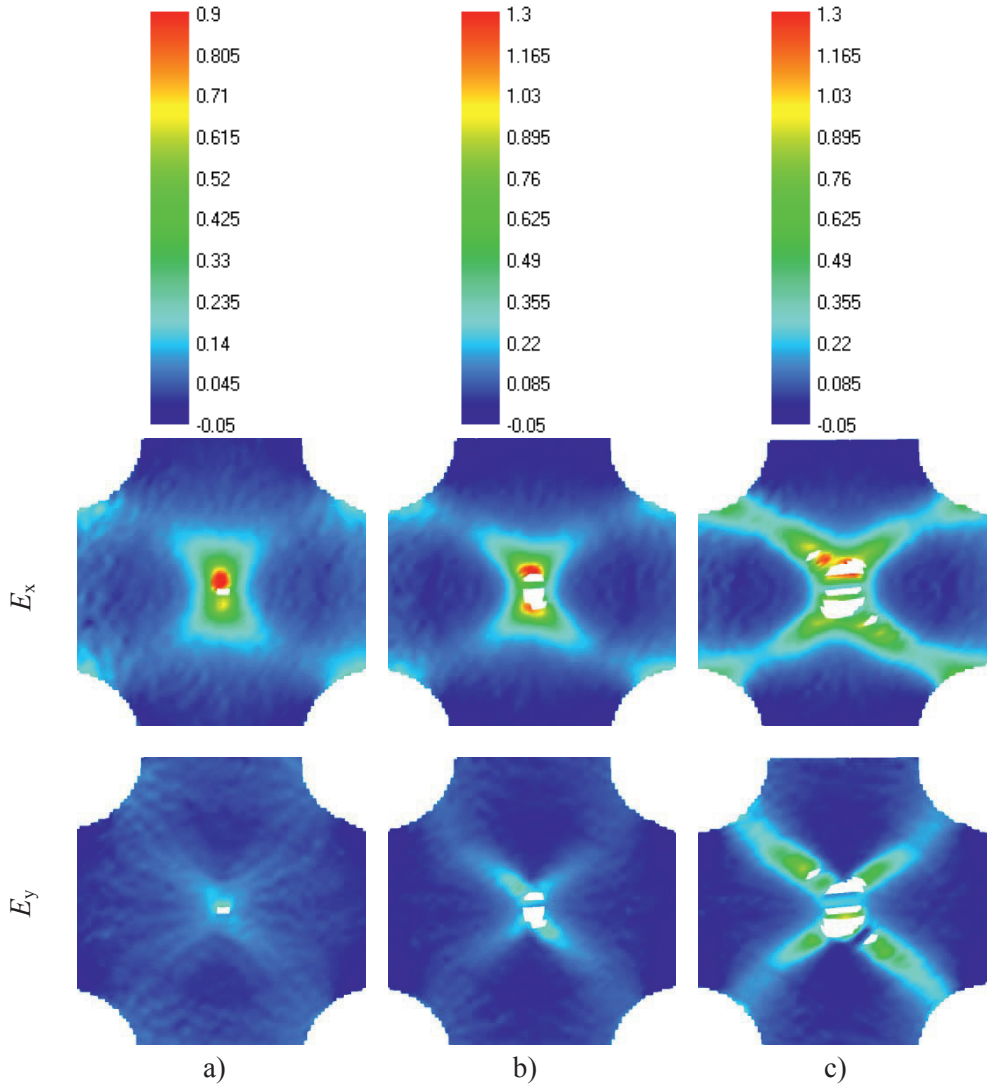

Figure 7.11 *Green strain fields E_x and E_y in the centre region of the HDPE specimen deformed at B = ½, at a) 8.7 mm b) 10.8 mm and c) 13.6 mm deformation in the x -direction .*

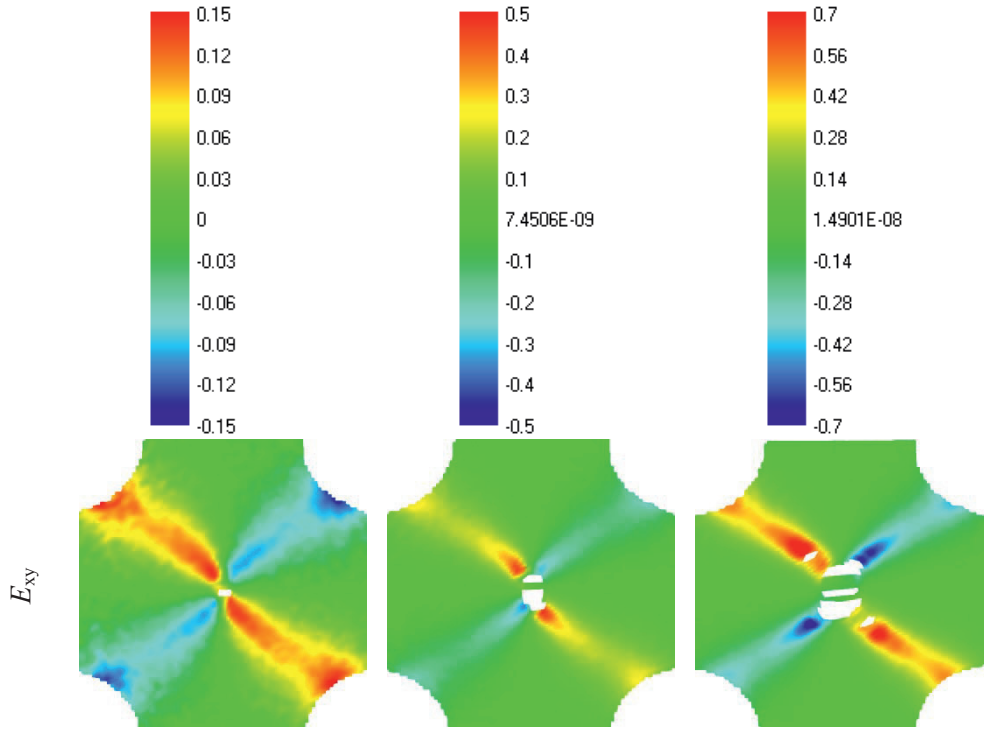

Figure 7.12 *Green shear strain field E_{xy} in the centre region of the HDPE specimen deformed at B = ½, at a) 8.7 mm b) 10.8 mm and c) 13.6 mm deformation in the x -direction .*

The strain fields are inhomogeneous for all tests. Therefore only the centre point is chosen to show how the extension ratio B affects the evolution of the strains with increasing deformation. The strain components E_x and E_y at this location are plotted in Figure 7.13 and Figure 7.14 for PVC. Figure 7.15 and Figure 7.16 show the same for HDPE. As seen from Figure 7.10 and Figure 7.12, the shear strains are small at this location and are therefore not included in the figures. The large deformations at the centre point caused distortion of the speckle pattern, so it was not possible to follow the strains towards the end of the experiments. Therefore, the plots of the curves are aborted when the DIC software was unable to determine the strain.

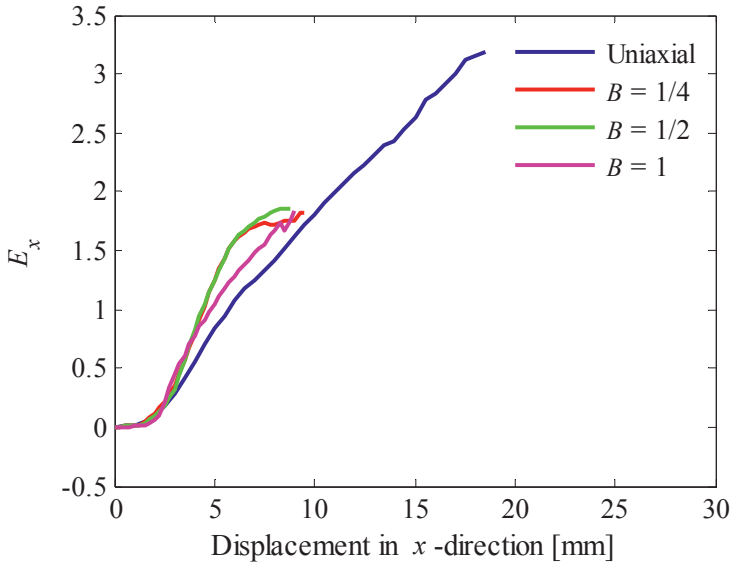

Figure 7.13 *Green strain E_x at the centre point of all PVC tests plotted against displacement in the x-direction.*

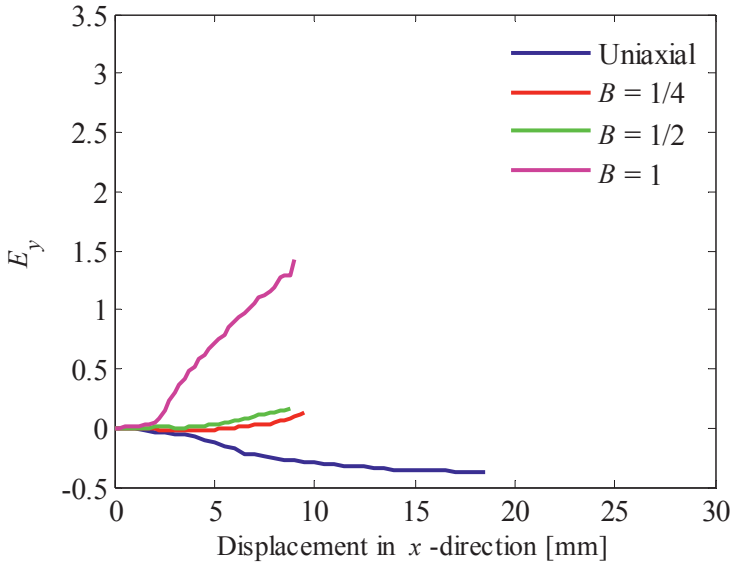

Figure 7.14 *Green strain E_y at the centre point of all PVC tests plotted against displacement in the x-direction.*

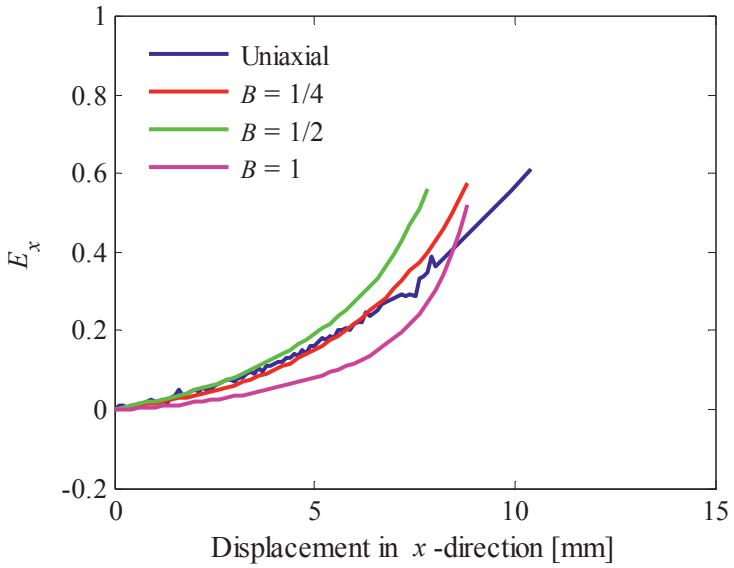

Figure 7.15 *Green strain E_x at the centre point of all HDPE tests plotted against deformation in the x-direction.*

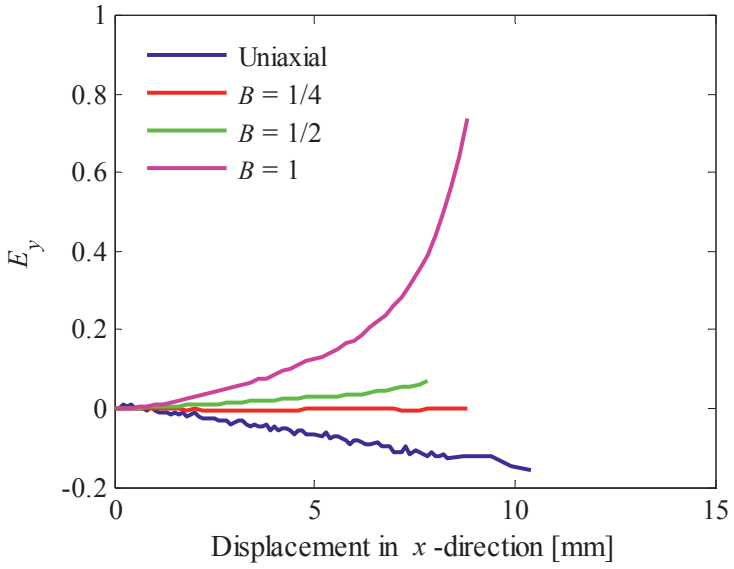

Figure 7.16 *Green strain E_y at the centre point of all HDPE tests plotted against displacement in the x-direction.*

From Figure 7.14 and Figure 7.16 it is seen that uniaxial tension of the cross-formed specimen produces negative E_y , indicating compression, for both materials. The Poisson effect causes the upper and lower free parts to move closer in the *y*-direction when the left and right parts are pulled away from each other in the *x*-direction. Therefore a state of compression is created. Towards the end of the deformation of these specimens, the centre region started to buckle, as a consequence of the contraction. With respect to the strains in the biaxial specimens, it can be seen that the higher the biaxial extension ratio B is, the larger is the strain component E_y .

7.4 DISCUSSION

The biaxial tension specimens were machined from 5 mm thick extruded plates of mineral filled PVC and HDPE. Except from some thinning of the centre region, no reduction of the thickness was done during the machining process. This means that eventual skin layers from the extruding process are left in the specimens, and will affect the test results.

For the specimens deformed at $B = ½$ and $B = ¼$, there is a difference between the two materials. For PVC, the tests at $B = ½$ and $B = ¼$ reach about the same force level. For HDPE, the test at $B = ¼$ reaches a somewhat higher level. From uniaxial tension and compression tests in Chapter 3 and Chapter 4 it was observed that the yield stress of the PVC is sensitive to pressure while that of the HDPE is not. The peak force in this study is also linked to the yield stress. The observations regarding the maximum force levels may therefore be related to differences in pressure sensitivity in PVC and HDPE.

The strain field plots in Figure 7.9 to Figure 7.12 indicate that strain localisation occurs at an earlier deformation stage in PVC than in HDPE. However in both materials strain localization sets in when maximum force is obtained. Further deformation lead to X-shaped necks in the centre region of the specimens. In the HDPE specimens, extensive drawing of the necked region made the centre region very thin. When the cross section thickness decreases, less material is left to restrict the deformation, and a softer response is observed. This geometrical effect might explain why the load drop seems to increase slightly with the biaxial extension ratio B . The thinning in the X-shaped neck in the centre of the test specimens was more pronounced for the HDPE specimens than for the PVC specimens. The drawing of the centre region in the three biaxial samples of HDPE resulted in creation of holes. Due to the ductile behaviour of the material, these holes

continued to grow, without causing cracking and global failure of the test specimens, until the tests were aborted. All PVC specimens were deformed until fracture.

During uniaxial tension of the cross-shaped test specimens the left and right parts are pulled away from each other in the *x*-axis direction causing the upper and lower free parts to move closer in the *y* direction. This Poisson effect is clearly visible in the centre region of the specimen. By examination of the strain curves for the uniaxial test in Figure 7.13 and Figure 7.14 for PVC, and in Figure 7.15 and Figure 7.16 for HDPE, it can be seen that E_y becomes negative. This indicates that some compression is present. In PVC the ratio E_x / E_y in the centre of the specimen at 10 mm deformation can roughly be estimated to –6.3. In HDPE the ratio E_x / E_y at the same deformation is around –3.8. After applying some additional deformation, buckling could also be observed at the centre of the specimen. Due to the comprehensive thinning of this section, the load-bearing capacity might be reduced so much that the global response of the specimen is not affected by the transverse compression in the same manner as in the case of PVC.

With respect to the strains, it can be seen that the higher the biaxial extension ratio B, the larger the strain component E_y. However, due to the geometry of the cross-shaped test specimen, the ratio E_x / E_y in the specimens is not directly linked to the extension ratio B. Moreover, it is not obtained one single deformation state in the specimen as seen from the inhomogeneous strain fields in Figure 7.9 to Figure 7.12. This means that these laboratory tests are not suitable for material tests with the purpose to test the material response at one specific stress state. Also, with the employed test setup employing only one CCD camera only the in-plane strains could be determined. This means that the volume strains are unknown. Therefore, such tests alone are not very well suited for investigation of mechanisms of biaxial deformation. However, since these laboratory tests involve various strain states as biaxial tension, compression and shear, they are considered as suitable for constitutive model validation. Such validation is performed in Chapter 12. Different other tests are present to test the biaxial behaviour, for instance formability tests. An advantage of the test setup presented in this chapter is that it allows for testing under controlled deformation without any unwanted effects from contact and friction.

7.5 CONCLUDING REMARKS

- From the biaxial tension tests, it can be observed that there is some difference in the pressure sensitivity of the yield stress of the tested PVC and HDPE.

- All the PVC specimens fractured during testing. The HDPE specimens showed a ductile behaviour. A hole appeared in the centre of all HDPE specimens tested in biaxial tension. The hole grew larger throughout the test without causing global failure of the specimens.

- The specimen geometry applied in this study produces inhomogeneous strain fields and are therefore not suitable as material tests where the purpose is to investigate the material response at one specific stress state.

- The tests results presented in this chapter are regarded as a good basis for validation of a constitutive model for polymers.

REFERENCES

[1] A.M. Adams, C.P. Buckley, D.P. Jones. Biaxial hot drawing of poly(ethylene terephthalate): measurements and modelling of strain-stiffening. *Polymer*, **41** (2000), 771-786.

[2] C.P. Buckley, D.C. Jones, D.P. Jones. Hot-drawing of poly(ethylene terephthalate) under biaxial stress: Application of a three-dimensional glass-rubber constitutive model. *Polymer*, **37** (1996), 2403-2414.

[3] P. Chandran, S. Jabarin. Biaxial Orientation of Poly(ethylene Terephtalate). Part I: Nature of the Stress-Strain Curves. *Advances in Polymer Technology*, **12** (1993), 119-132.

[4] P. Chandran, S. Jabarin. Biaxial Orientation of Poly(ethylene Terephtalate). Part II: The Strain-Hardening Parameter. *Advances in Polymer Technology*, **12** (1993), 133-151.

[5] P. Chandran, S. Jabarin. Biaxial Orientation of Poly(ethylene-Terephthalate). Part III:Comparative structure and property changes resulting from simultaneous and sequentioal orientation. *Advances in Polymer Technology*, **12** (1993), 153-165.

[6] J. Sweeney, I.M. Ward. Rate dependent and network phenomena in the multiaxial drawing of poly(vinyl chloride). *Polymer*, **36** (1995), 299-308.

[7] F.F. Zeng, P. Le Grognec, M.F. Lacrampe, P. Krawczak. A constitutive model for semi-crystalline polymers at high temperature and finite plastic strain: Application to PA6 and PE biaxial stretching. *Mechanics of Materials*, **42** (2010), 686-697.

[8] L. Chevalier, Y. Marco. Identification of a strain induced crystallisation model for PET under uni- and bi-axial loading: Influence of temperature dispersion. *Mechanics of Materials*, **39** (2007), 596-609.

[9] L. Chevalier, S. Calloch, F. Hild, Y. Marco. Digital image correlation used to analyze the multiaxial behavior of rubber-like materials. *European Journal of Mechanics A/Solids*, **20** (2001), 169-187.

[10] L. Chevalier, Y. Marco. Tools for multiaxial validation of behavior laws chosen for modeling hyper-elasticity of rubber-like materials. *Polymer Engineering & Science*, **42** (2002), 280-298.

[11] Y. Marco, L. Chevalier, M. Chaouche. WAXD study of induced crystallization and orientation in poly(ethylene terephthalate) during biaxial elongation. *Polymer*, **43** (2002), 6569-6574.

[12] P. Vacher, S. Dumoulin, F. Morestin, S. Mguil-Touchal. Bidimensional strain measurement using digital images. *Proceedings of the Institution of Mechanical Engineers Part C-Journal of Mechanical Engineering Science*, **213** (1999), 811-817.

CHAPTER 8

AXISYMMETRIC TENSILE BARS WITH NOTCH

Tensile tests of axisymmetric bars with notch were carried out on specimens of mineral filled PVC and HDPE. The effect of stress triaxiality on the yield stress and the volume change is studied in particular.

8.1 INTRODUCTION

The geometry of axisymmetric tensile bars with notch is known to induce transverse components to the stress tensor and thereby create a triaxial stress state in the minimum cross section of the specimen. The relationship between the curvature and the stress triaxiality in necked metal specimens with circular cross section has been expressed by Bridgman [1]. Bridgman's formulas involve the relationship between the smallest cross section radius a and the neck radius R. They enable estimation of the average axial yield stress by compensating for transverse stresses produced by the geometry of the neck. In his work, Bridgman made some assumptions with respect to geometry, namely that the contour of the neck could be approximated by the arc of a circle with radius R and that the minimum cross section of the neck remained circular during the test [2]. Further, he assumed the strains to be constant over the cross section of the neck [2]. And, at last, he assumed J_2 flow theory.

The theory derived by Bridgman has been criticized in the literature [3] especially for its lack of ability to handle large strains. Nevertheless, it is still the most often used theory for treating the effect of stress triaxiality in a neck. Even though the work was derived for smooth axisymmetric specimens [3], the formulas of Bridgman have later widely been employed to describe the stress state in axisymmetric tensile metal bars with a pre-machined notch [4-6].

During experimental testing of metallic samples it is common to work under the assumption of isochoric plastic deformations. In the case of metallic axisymmetric specimens it is therefore adequate to measure the contraction of the minimum cross section of the notch to determine the axial strain. In polymers with plastic dilation another test setup is needed because measurements of both the volume change and the axial strain are required. A new test setup was applied in this study to measure the deformation of the notch as the specimen is extended.

Experiments on notched circular tensile bars made of polymers are found in the literature [7-10]. Castagnet and Deburck [7] measure the actual cross section area by employing a DCC camera followed by image analyses. By plotting the radial strain against axial strain of the gauge length for specimens with different radii, they showed that the change of the diameter (radial strain) was lower for higher triaxialities. Measurement of the reduction of the minimum diameter of polymer specimens has also been performed by applying a strain gage at the root of the notch [8-10]. To express how the volume change was affected by stress triaxiality, also Boisot et al. [8] plotted radial strain against axial strain. Moreover, Boisot et al. [8] used a scanning electron microscope (SEM) to observe test specimens from interrupted tests and to determine the porosity of the deformed material in the notch. They used the data to calibrate parameters in a modified Gurson-Tvergaard-Needleman material model. They compared numerical results from finite element simulations with the predictions from the Bridgman theory and found that the Bridgman theory over-predicted the yield stress. They addressed this discrepancy to viscous effects and volume change effects [8]. Still, they consider the approach to be relevant for describing distribution of stress. As a support to this consideration, they showed by the SEM investigation and also with finite element analyses that the void growth was greatest in the specimen centre.

Even though the assumptions for the Bridgman framework are questionable for polymers it is considered as reasonable to expect that the stress triaxiality in the polymeric test specimens increases with decreasing notch radius. This is in accordance with the Bridgman theory.

8.2 STRESS TRIAXIALITY AND BRIDGMAN'S EXPRESSIONS

The stress triaxiality is often represented as the dimensionless stress triaxiality ratio σ^*. It is defined as [11]

$$\sigma^* = \frac{\frac{I_1}{3}}{\sqrt{3J_2}} \tag{8.1}$$

The definition involves the first principal stress invariant, $I_1 = \mathrm{tr}(\boldsymbol{\sigma})$, and the second deviatoric stress invariant, $J_2 = \frac{1}{2}(\boldsymbol{\sigma}^{dev} : \boldsymbol{\sigma}^{dev})$. The deviatoric stress tensor is $\boldsymbol{\sigma}^{dev} = \boldsymbol{\sigma} - \frac{1}{3}\mathrm{tr}(\boldsymbol{\sigma})\mathbf{I}$.

According to the above definition a uniaxial stress state in tension gives $\sigma^* = 1/3$ while a pure hydrostatic stress state gives an infinitely high, or low, stress triaxiality ratio.

The stress state in the cross section of the notched samples is inhomogeneous. The average axial stress $\bar{\sigma}_z$ can be defined as the applied force F over the cross section A:

$$\bar{\sigma}_z = \frac{F}{A} \tag{8.2}$$

For an axisymmetric specimen with notch radius R and minimum cross section radius a, Bridgman expressed the axial stress σ_z normalized by the yield stress Y at the distance r from the centre axis as follows [3]

$$\frac{\sigma_z}{Y} = 1 + \ln\left(1 + \frac{a^2 - r^2}{2aR}\right) \tag{8.3}$$

Integration over the minimum cross section area gives the total applied force. By using that $r \in [0, a]$, where a is the current minimum radius, we get

$$\frac{F}{Y} = \pi a^2 \left(1 + \frac{2R}{a}\right) \ln\left(1 + \frac{a}{2R}\right) \tag{8.4}$$

The current area of the minimum cross section is $A = \pi a^2$. Equation (8.4) can therefore be expressed in terms of the averaged normalized axial stress $\bar{\sigma}_z$

$$\frac{\bar{\sigma}_z}{Y} = \left(1 + 2\frac{R}{a}\right)\ln\left(1 + \frac{a}{2R}\right) \tag{8.5}$$

An advantage with this expression is that it is measurable in experimental tests.

Bridgman's analysis assumes that the value of the yield stress Y is constant in the minimum cross section. Moreover, no strain hardening, strain rate effects, pressure sensitivity or plastic dilation is taken into account.

8.3 TEST SETUP

The axisymmetric tensile bars were prepared by using a lathe. The material was taken from 10 mm thick extruded plates of PVC and HDPE. The samples were machined with their longitudinal direction in the extrusion direction. Figure 8.1 a) shows the geometry of the notched specimens. Four different notch radii R_0 were 20 mm, 5 mm, 2 mm and 0.8 mm were employed. In addition some smooth specimens were machined according to Figure 8.1 b). Both ends of the specimens were prepared by M10 threads for mounting in the tensile machine.

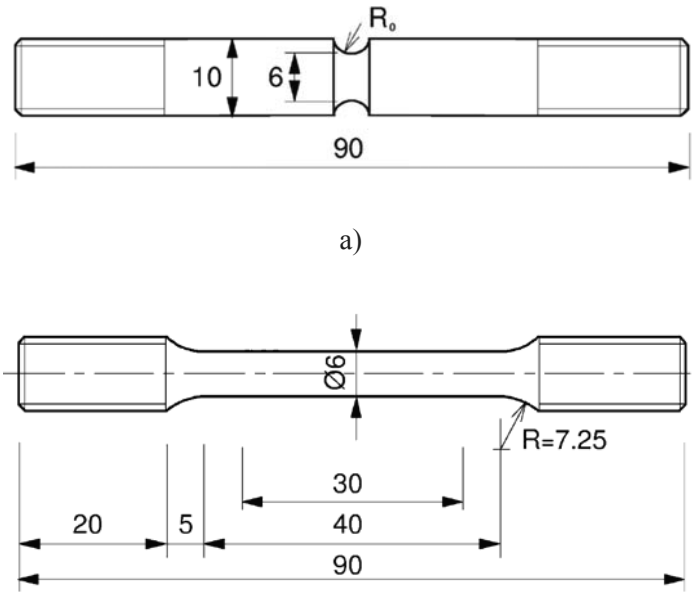

Figure 8.1 *Specimen geometry of a) notched axisymmetric tensile bar and b) smooth axisymmetric tensile bar [5]. Measures are given in mm.*

The different test specimens will be denoted by the material and the initial notch radius R_0, e.g. PVC-08 and HDPE-20. All specimens were deformed by the same cross-head speed of v = 0.04 mm/s. The deformation of the notch was surveyed by a CCD-camera.

Each test was carried out with three replicates. The reproducibility of the force-displacement response turned out to be good. For each geometry and material, the test having the highest image quality from the CCD-camera was chosen to represent all replicates. All specimens made of PVC were deformed until fracture. Regarding the specimens of HDPE, only the samples with the smallest initial notch radii R_0, i.e. HDPE-2 and HDPE-08, fractured during testing.

8.4 STRAIN MEASUREMENTS

Prior to the tests all specimens were marked with small spots on each side of the root of the notch, see Figure 8.2 a). The distance between the marks was initially $L_0 \sim 2$ mm. During the tests the deformation of the specimens was monitored by a CCD-camera. The marks were captured by the camera, facilitating an optical extensometer so that the longitudinal deformation could be followed, see Figure 8.2 b). The specimens were placed in front of a background in a contrasting colour and the focus of the camera was at the outer edge of the notch so that the contour clearly was depicted in the images. This was important in order to obtain good measurements of the local notch radius R and the specimen radius a by image processing after the test.

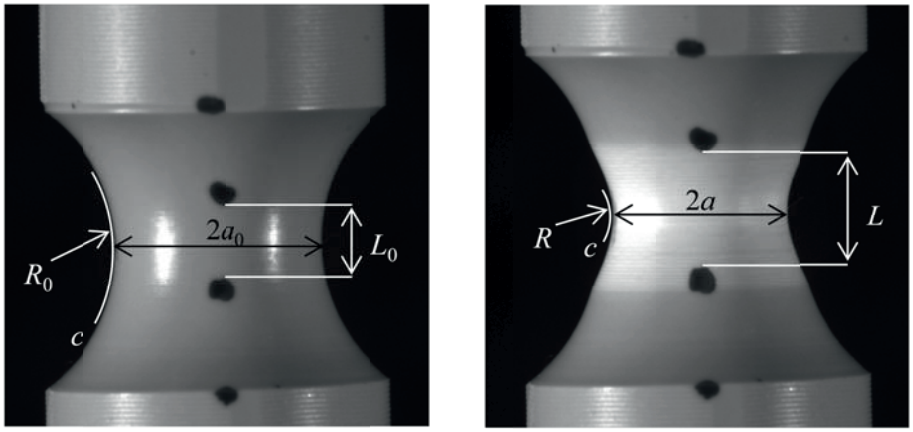

a) b)

Figure 8.2 *A test specimen with notch radius R_0 =5 mm. The black dots were applied to the specimen before the test to serve as an optical extensometer. After the test the different measurement quantities were determined by image processing. a) The specimen before deformation showing the initial measures. b) The specimen after some deformation.*

By the use of a MATLAB script that was created by Dahlen [12] for the purpose, the following data was found for each image taken during the test, see Figure 8.2:

- The minimum specimen radius a
- The local notch radius R
- The distance L between the optical extensometer marks

In addition, the local contour c in the root of the notch was used as an auxiliary measurement for finding a and R. The contour was used to locate the narrowest section of the specimen. The smallest diameter of the specimen, $2a$, was measured at this location. In order to find the notch radius R locally in the notch, the least squares method was used to fit a circle to the contour. The radius of the fitted circle was used as the local notch radius R.The curvature of the specimen changed during deformation. After some deformation a local neck could appear inside the notch, see Figure 8.2 b). In order to obtain a measure of the radius R in the local neck only a short part of the contour c lying at the root of the notch was used for the circle fitting. The length of c was determined by the value of the notch radius from the previous image R_p; $c = (\pi / 3)R_p$. After cold-drawing, the curvature of the neck changed character, then a maximum limit of c was set to 2 mm. The

MATLAB code also traced the distance L between the two extensometer marks closest to the root of the notch. Subsequently the volume V between the two extensometer marks was found from revolving a curve describing the left contour around the specimen axis and thereafter calculating the volume of the solid of revolution by disk integration.

From Figure 8.2 was seen that the cross section of the specimen varies over the distance L . Also the strains are not homogenous distributed over L.The average axial strain $\bar{\varepsilon}_z$ over the notch was computed as

$$\bar{\varepsilon}_z = \ln\left(\frac{L}{L_0}\right) \tag{8.6}$$

The average radial strain $\bar{\varepsilon}_r$ was calculated from the change of the radius a

$$\bar{\varepsilon}_r = \ln\left(\frac{a}{a_0}\right) \tag{8.7}$$

The averaged axial stress was found by dividing the applied force F by the current minimum cross section area A , recall Equation (8.2).

The average volume strain $\bar{\varepsilon}_v$ between the two marks was be expressed as

$$\bar{\varepsilon}_v = \ln\left(\frac{V}{V_0}\right) \tag{8.8}$$

where V_0 is the volume between the two marks for the undeformed sample.

8.5 RESULTS

Force-displacement plots for all specimen geometries are shown in Figure 8.3 and Figure 8.4 for PVC and HDPE. Black open circles are used to indicate the peak of the force-displacement curve. The state of maximum force will be addressed similarly in the following figures in this section.

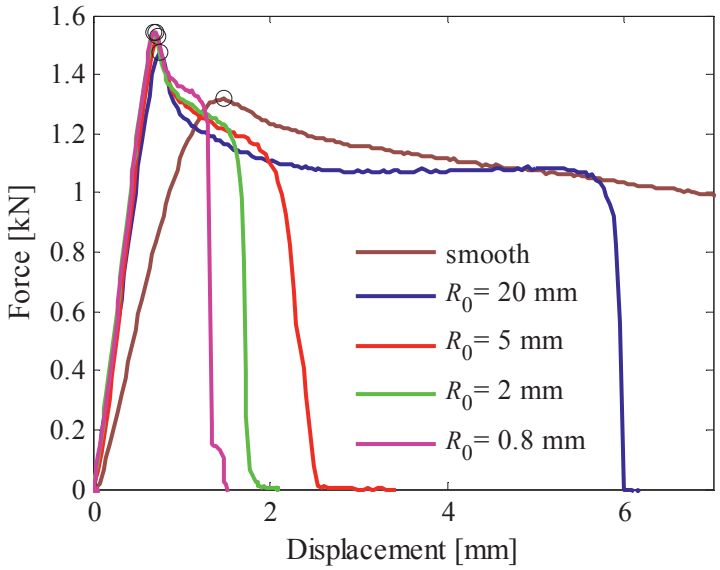

Figure 8.3 *Force-displacement curves for representative PVC specimens. The circles indicate the maximum force.*

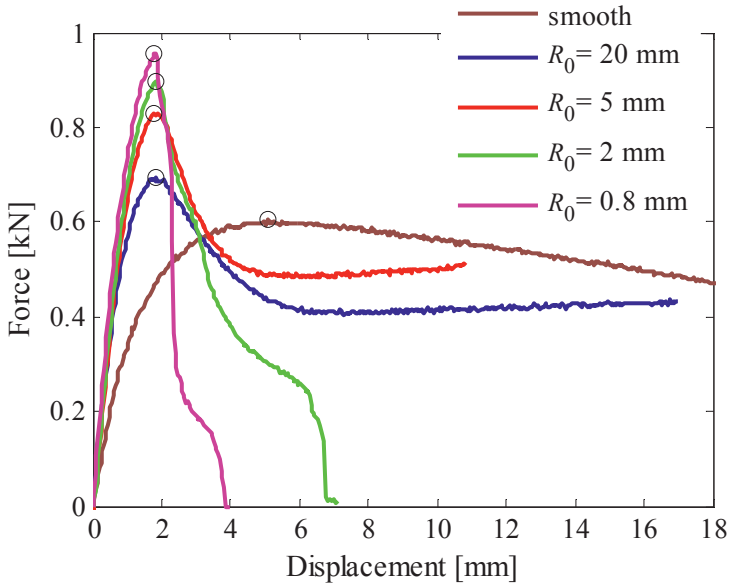

Figure 8.4 *Force-displacement curves for representative HDPE specimens. The circles indicate the maximum force.*

Paying attention to the pre-notched samples, photos of the PVC specimens at certain deformations are shown in Figure 8.5. The upper row shows specimen PVC-20, the second row PVC-5, the third row PVC-2 and the last and fourth row PVC-08. Each of the four columns represents a sub-figure and a deformation state. The undeformed specimens are depicted in sub-figure a). Sub-figure b) shows the specimens at the instant where maximum force is reached, i.e. at the state marked with an open circle in the previous figures. At this state stress whitening gradually sets in. In sub-figure c) the specimens are at a local stress minimum. Now, the stress whitening is more distinct. At this point, it is also possible to see that small necks have been formed in the pre-machined notch of the specimens PVC-20 and PVC-5. The last sub-figure d) shows the last image before fracture, i.e. the specimens at their most deformed state. It is seen that PVC-20 experienced cold-drawing towards the end of the deformation.

The notched HDPE specimens are depicted during testing in Figure 8.6. Also here, the four rows from the top show the specimens in the order: HDPE-20, HDPE-5, HDPE-2 and HDPE-08. The four columns are divided in four different sub-figures and represent four different deformation states. Sub-figure a) shows un-deformed specimens and sub-figure b) displays the specimens when the maximum force is reached. After some deformation a local neck forms inside the pre-machined notch. It appears as a change in the curvature of the notch resulting in a reduction of the notch radius R. It is particular distinct for HDPE-20 and HDPE-5. Further deformation leads to cold drawing of the material observed as an increase of R. Sub-figure c) depicts the specimens when the notch radius starts to increase. The last sub-figure, d), shows the specimens at the last sampled points in the graphs. For HDPE-2 and HDPE-08, sub-figure d) is the last captured photo of the specimen before fracture. Cold-drawing can be seen in sub-figure d) for all HDPE specimens.

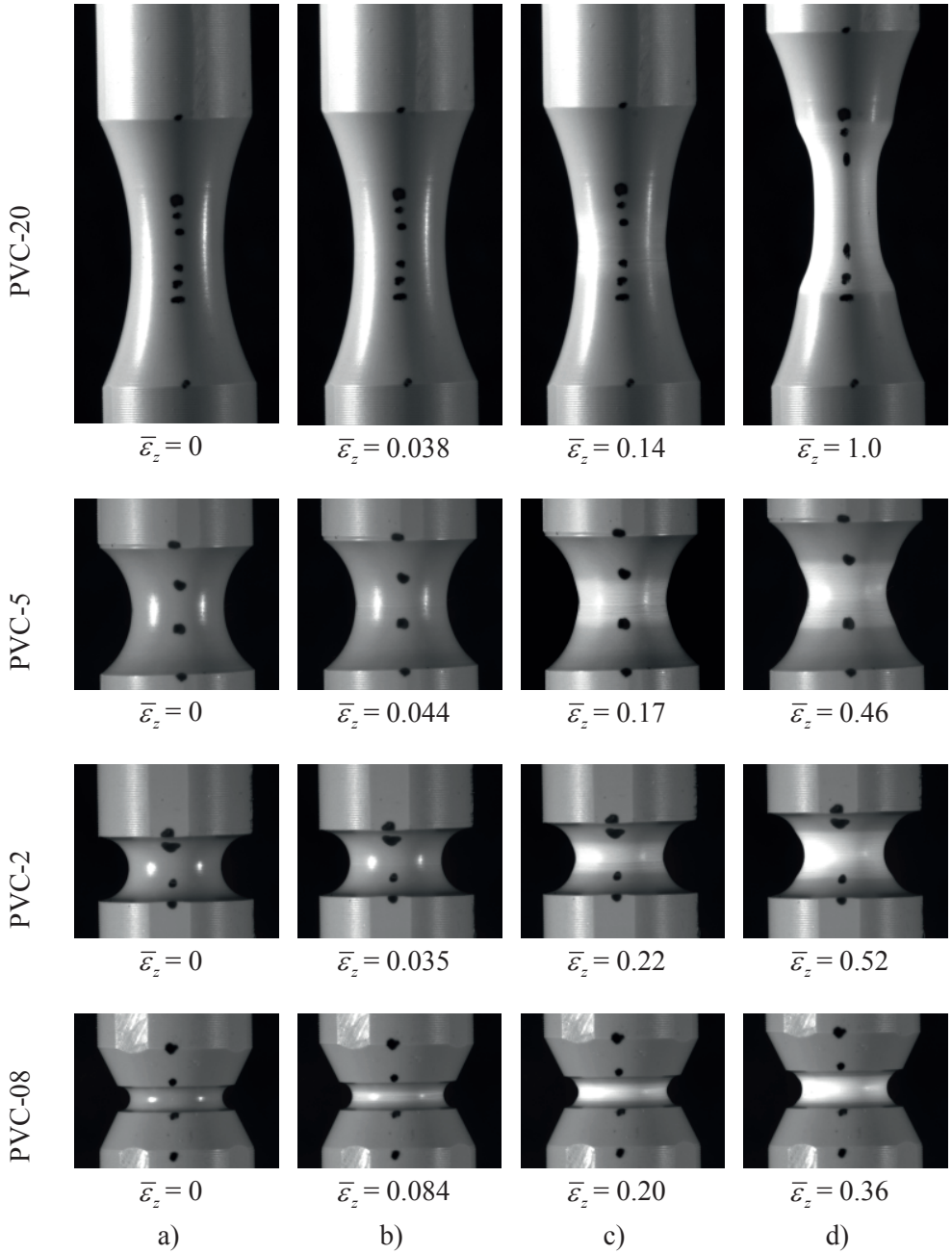

Figure 8.5 *Photos of PVC specimens at different stages of deformation. The first row from the top shows PVC-20, the second row PVC-5, the third row PVC-2 and the bottom row PVC-08. The photos were captured a) before deformation, b) at maximum force, c) at local minimum of average axial stress – average axial strain curve and d) just before fracture.*

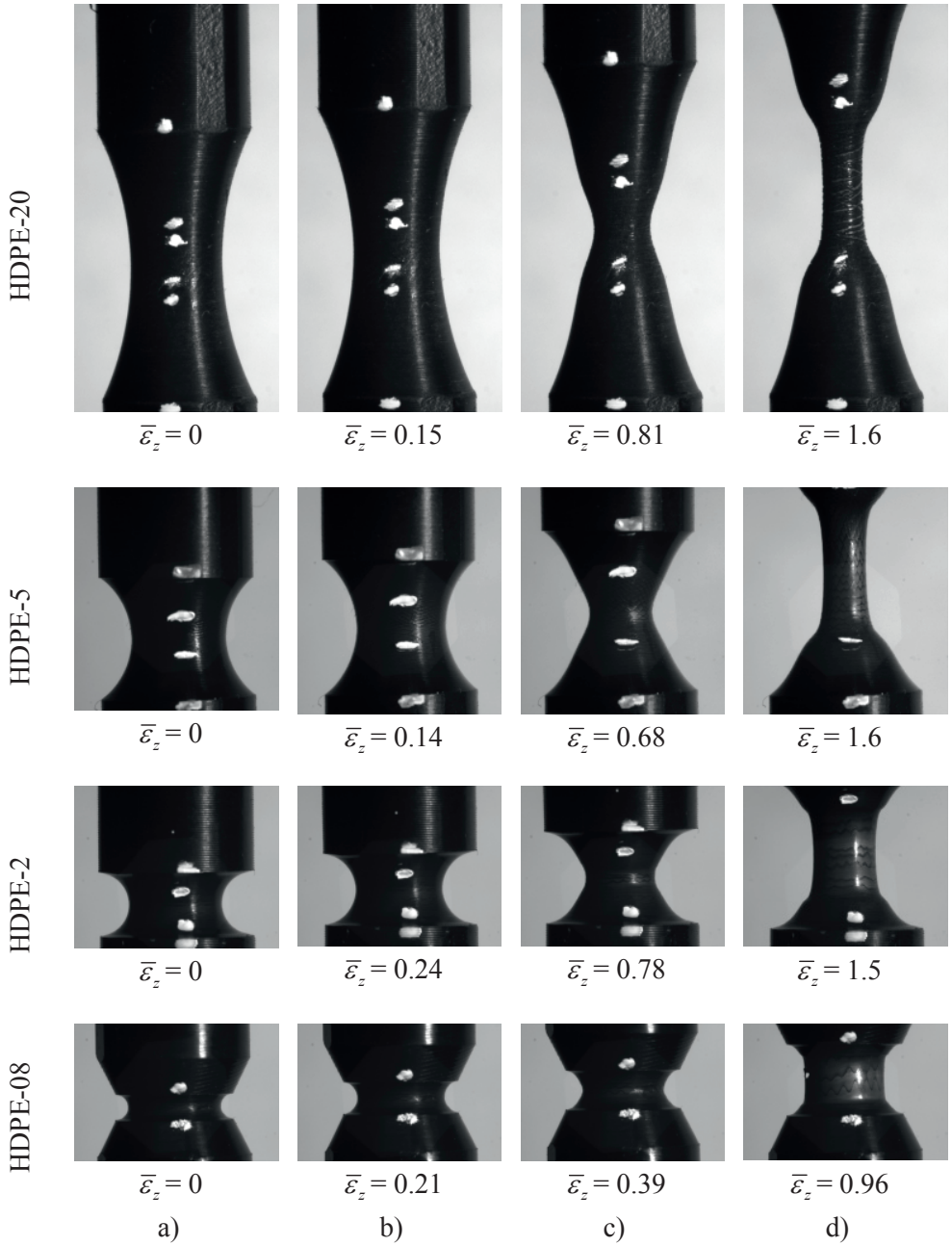

Figure 8.6 *Photos of HDPE specimens at different stages of deformation. The first row show HDPE-20, the second row HDPE-5, the third row HDPE-2 and the fourth row HDPE-08. The photos were captured a) before deformation, b) at maximum force, c) when the notch radius starts to increase and d) just before fracture or as the last photo that was captured.*

The averaged axial stress $\bar{\sigma}_z = F / A$ is plotted against averaged axial strain $\bar{\varepsilon}_z = \ln(L / L_0)$ in Figure 8.7 for the PVC specimens and in Figure 8.8 for the HDPE specimens. Also results from the smooth specimens are included to serve as a reference. Again, black open circles are used to mark the state where maximum force is reached, see Figure 8.3 and Figure 8.4.

All stress-strain curves for the PVC specimens, plotted in Figure 8.7, have a familiar response including a local stress maximum before softening followed by strain re-hardening. The position of the black open circles demonstrates that the peak stress coincides with the peak of the force-displacement curve. Further, it is seen that the notched specimens obtain a higher stress maximum than the smooth specimen.

As seen in Figure 8.8, the two HDPE specimens with the smallest notch radius, i.e. HDPE-2 and HDPE-08, have a softening behaviour after a peak stress is reached. These specimens also fractured during testing. The other HDPE specimens strain-harden monotonically throughout the deformation and the tests were aborted before fracture. The black open circle coincides with peak stress for the HDPE-08 specimen.

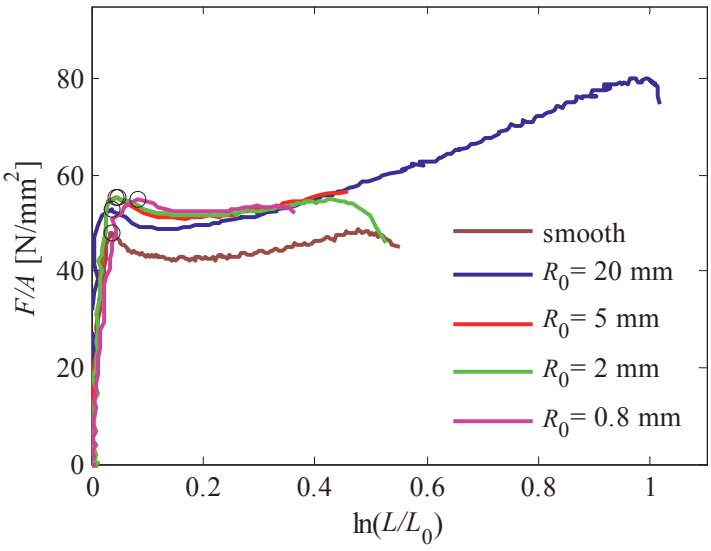

Figure 8.7 *Averaged axial stress plotted against averaged axial strain for representative PVC specimens. The circles indicate the state at maximum force.*

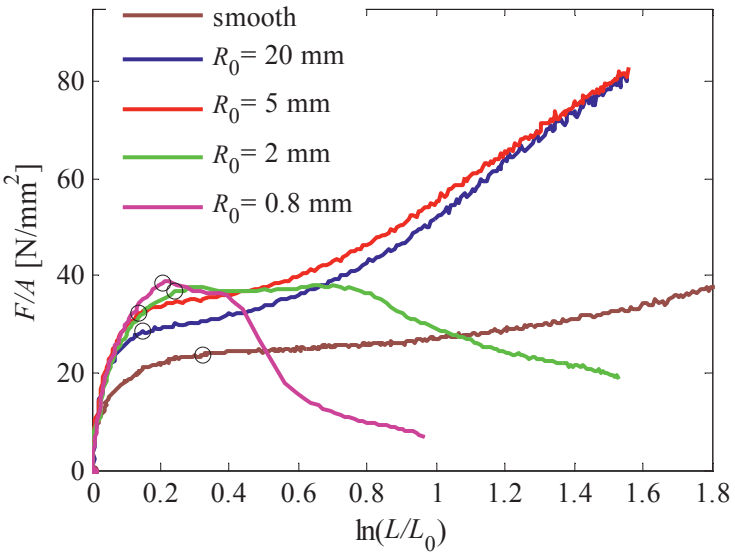

Figure 8.8 *Averaged axial stress plotted against averaged axial strain for representative HDPE specimens. The circles indicate the state at maximum force.*

The average axial strain is plotted against time in Figure 8.9 and Figure 8.10 for the first part of the deformation. The state of maximum force is again marked with open circles. Results from the smooth specimens are plotted for reference also in these plots. In the figures it is seen that after some deformation, there is an increase in the slope of the curves, representing the rate of the axial strain averaged over the notch. It can be noted that this average strain rate, from a time of 20 s onwards, is higher for the notched specimens than for the smooth one. This difference is more evident for PVC than for HDPE. Further, it is seen that between the notched specimens, there is no large variation in strain rate. The rates of average strain, i.e. the slopes of the curves, at maximum force are listed in Table 8.1 and Table 8.2.

Table 8.1 *Rate of average axial strain at maximum force in the PVC specimens.*

	PVC smooth	PVC-20	PVC-5	PVC-2	PVC-08
$\dot{\bar{\varepsilon}}_Z$ [s^{-1}]	0.0015	0.012	0.018	0.018	0.021

Table 8.2 *Rate of average axial strain at maximum force in the HDPE specimens.*

	HDPE smooth	HDPE-20	HDPE-5	HDPE-2	HDPE-08
$\dot{\varepsilon}_Z$ $[s^{-1}]$	0.0024	0.0059	0.0070	0.012	0.013

The test and post-processing method used in this study was found suitable for the notched bars, where the onset of necking is given by the specimen geometry. However, the method produced poor results for the smooth specimens since onset of necking could not be controlled to occur exactly between two optical extensometer markings. The smooth specimens will not be included in the results hereafter.

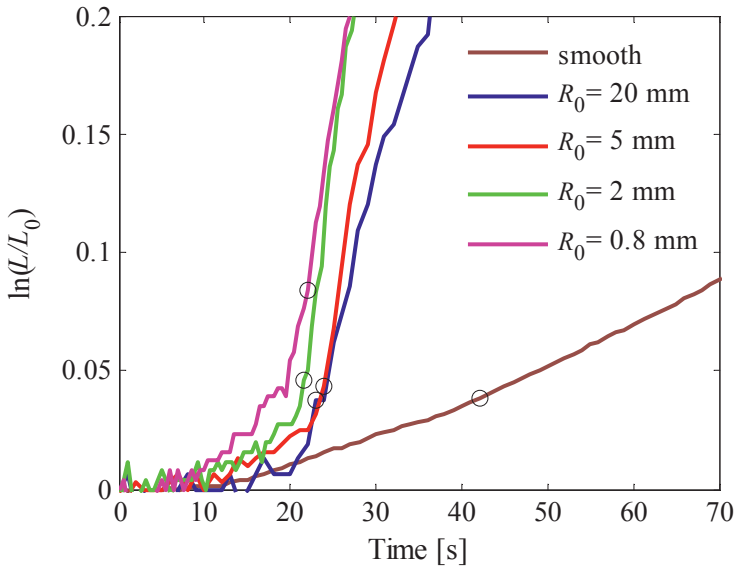

Figure 8.9 *Average axial strain plotted against time for representative PVC specimens. The circles indicate the state at maximum force.*

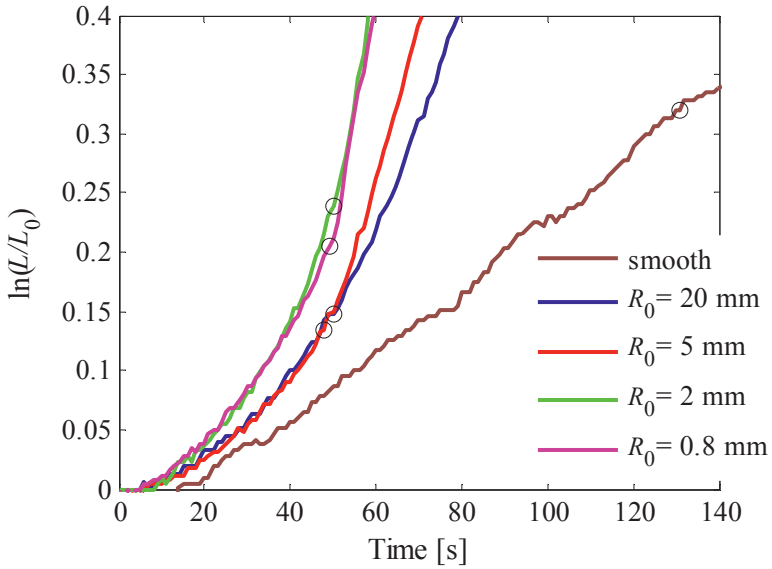

Figure 8.10 *Average axial strain plotted against time for representative HDPE specimens. The circles indicate the state at maximum force.*

The evolution of the notch radii R during the experiments are plotted for all specimens in Figure 8.11 and Figure 8.12, addressing respectively PVC and HDPE. In similar way as in the previous figures, the black open circles indicate the notch radius at maximum force. Thereafter the notch radius R remains nearly constant. During the test, the deformation localizes and a neck forms inside the pre-machined notch. This can be seen as a decrease of R. It is more distinct for the specimens with a large notch. For some of the tests this neck stabilizes and cold drawing sets in. These are the tests where an increase in R can be observed towards the end of the test; PVC-20 and all HDPE tests. This was in fact already seen in Figure 8.5 d) and in Figure 8.6 d). When the radius of the notch increases, the noise in the data also increases due to the fitting of the circle to find R in the image post processing. Therefore the parts of the curves in Figure 8.11 and Figure 8.12 with increasing R are smoothed by a MATLAB function.

Assuming that the notch radius R affects the stress state in the specimen, it can be interpreted from Figure 8.11 and Figure 8.12 that the stress state changes quite radically during deformation. Following Bridgman, a decrease of the notch radius R is expected to lead to an increase of the hydrostatic stress in the notch.

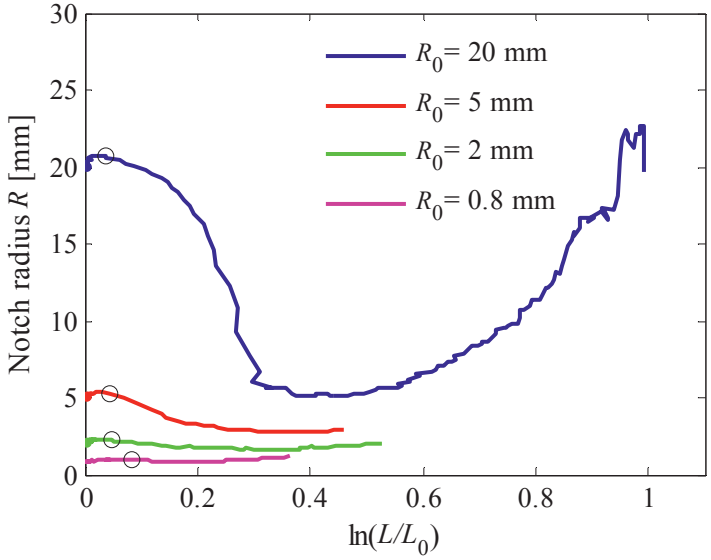

Figure 8.11 *The notch radius R against average axial strain for representative PVC specimens. The circles indicate the state at maximum force.*

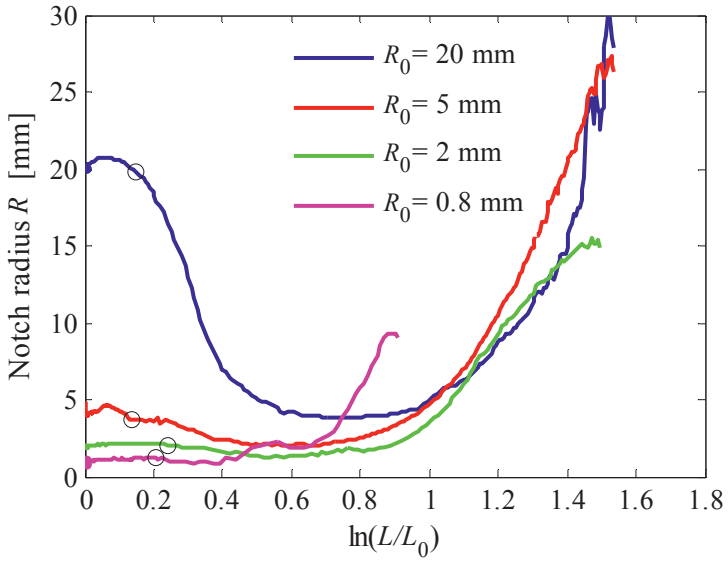

Figure 8.12 *The notch radius R against average axial strain for representative HDPE specimens. The circles indicate the state at maximum force.*

The net volume strains $\bar{\varepsilon}_v = \ln(V / V_0)$, as defined in Equation (8.8), are plotted in Figure 8.13 and Figure 8.14 for PVC and HDPE respectively. Also here, the states of maximum force are marked by black open circles. The general observation is that the volume change is larger for the specimens with sharper initial notch radius R_0. Assuming that a small notch radius produces a high triaxial stress state, the volume change can be observed to increase quite radically with the stress triaxiality.

Plastic dilation in the PVC was already reported in Chapter 2.8. Hardly any volume change has been observed in the HDPE during plastic deformation in uniaxial tension at moderate strain rates, see Chapter 2.8. However, Figure 8.14 reveals that the HDPE experiences a significant increase of volume when subjected to a triaxial stress state. Indeed, the net volume strain is only slightly lower than for PVC at equal levels of average axial strain $\bar{\varepsilon}_z = \ln(L / L_0)$.

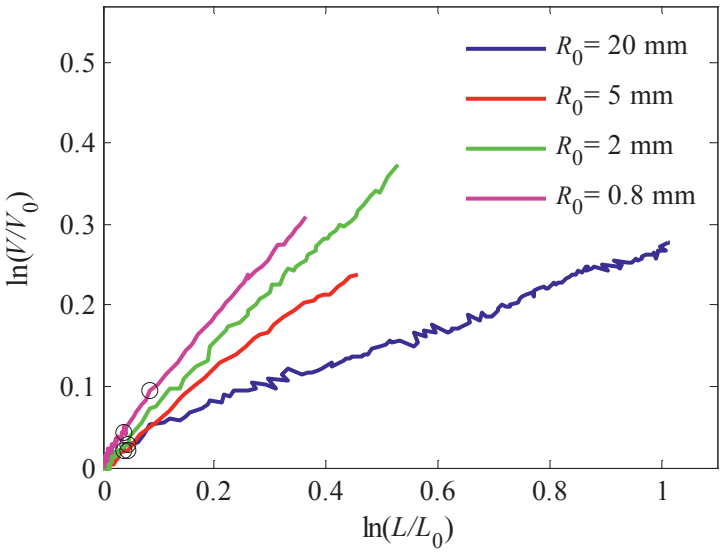

Figure 8.13 *Volume strain in the PVC specimens, calculated from the change of the volume in the notch between the two extensometer markings, plotted against average axial strain. The circles indicate the state at maximum force.*

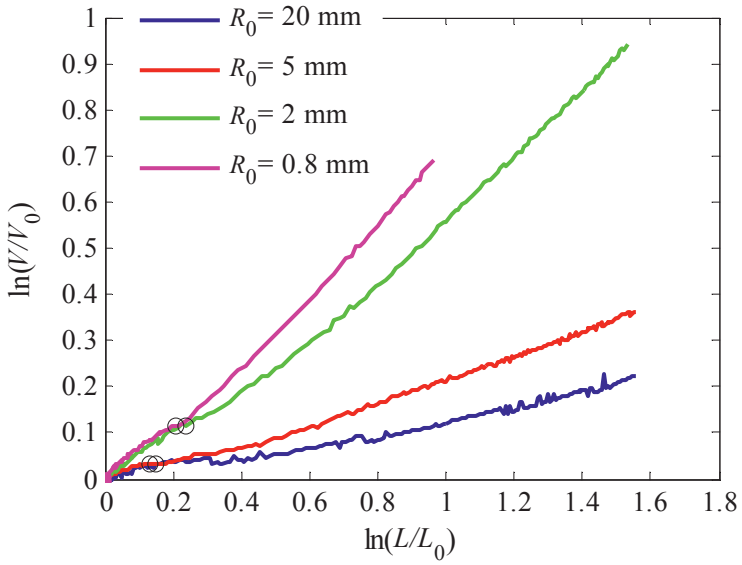

Figure 8.14 *Volume strain in the HDPE specimens, calculated from the change of the volume in the notch between the two extensometer markings, plotted against average axial strain. The circles indicate the state at maximum force.*

The plots of average radial strain $\bar{\varepsilon}_r = \ln(a / a_0)$ in Figure 8.15 and Figure 8.16 once again demonstrate the increase in volume strain with decrease of R. The results show that a sharp initial notch radius R_0 causes less contraction of the specimen than a large initial notch radius does. Reduced contraction can be interpreted as higher dilation.

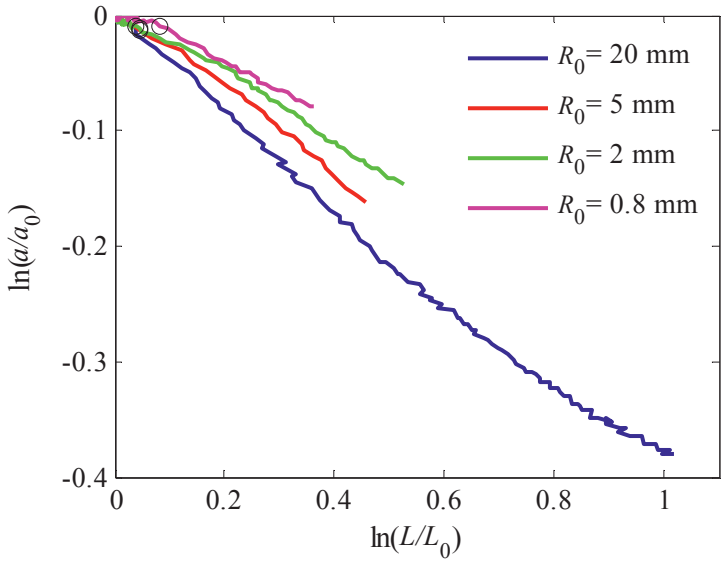

Figure 8.15 *Average radial strain plotted against average axial strain for all PVC specimens. The circles indicate the state at maximum force.*

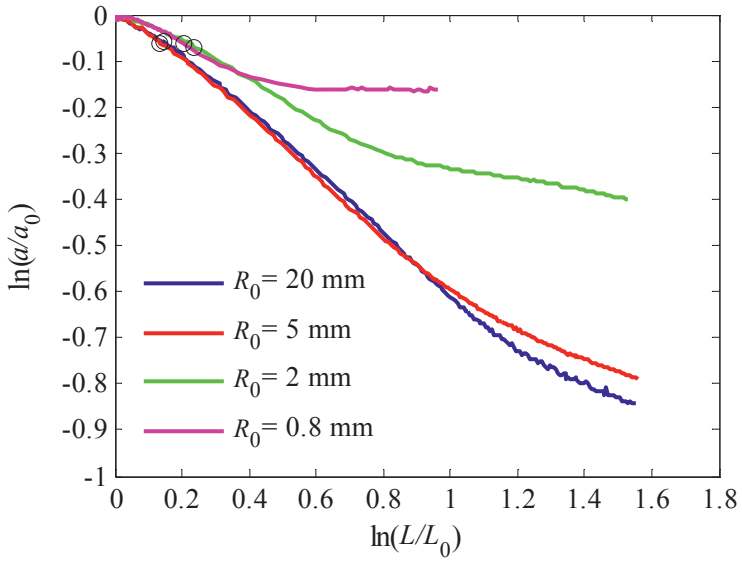

Figure 8.16 *Average radial strain plotted against average axial strain for all HDPE specimens. The circles indicate the state at maximum force.*

In order to show how the specimen geometry and thereby the stress triaxiality affects the yield stress, the averaged axial stress at maximum force is plotted against the notch radius R in Figure 8.17. The stresses are normalized by the stress Y, which is the stress in the smooth test specimens at maximum force.

According to the Bridgman theory, the axial yield stress increases with increasing triaxiality. Figure 8.17 includes a plot of the Bridgman prediction expressed by Equation (8.5). The fixed value of the Bridgman curve represents an estimate of the relationship between the normalized averaged yield stress and the notch radius for test specimens of a perfect plastic material at small strains without any pressure sensitivity, dilational or viscous effects. It shows that in such a material the average axial yield stress is higher when the notch radius is smaller. This means that higher stress triaxialities increase the average axial peak stress.

For the PVC specimens there is a clear mismatch with the Bridgman prediction. Higher stress triaxialities do not increase the axial net peak stress of the PVC. This was also observed in the stress-strain curves in Figure 8.7. For HDPE the general trend is similar to that of the Bridgman prediction; smaller R leads to higher normalized average axial stress $(F / A)_{\max}$ at maximum force.

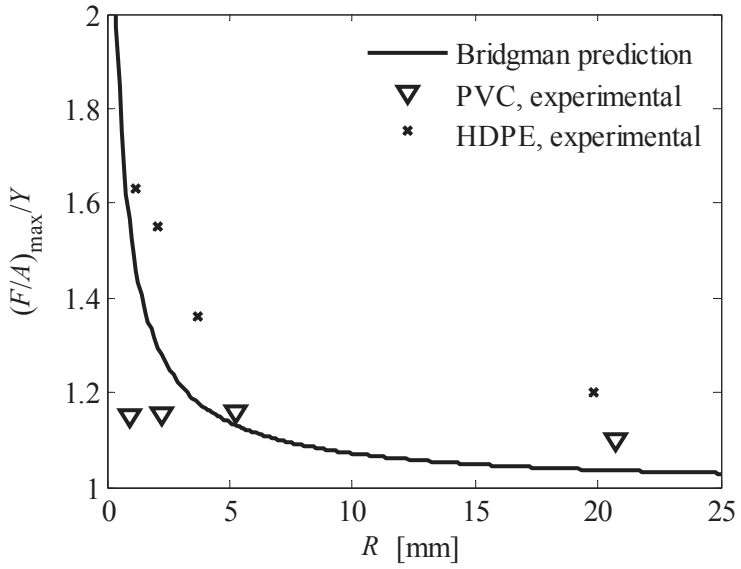

Figure 8.17 *Variation in normalized average stress at peak force with the notch radius R.*

8.6 NUMERICAL STUDY OF STRESS TRIAXIALITY

This chapter is based on the assumption that the geometrical conditions from the notch produce a triaxial stress field in the minimum cross section of the axisymmetric test specimen. However, we do not know the value of the stress triaxiality ratio. To investigate this, finite element simulations were used to provide an estimate of the stress triaxiality in the elastic regime, before onset of yielding. Axisymmetric meshes representing the geometries of the different tensile specimens were used in the analyses. The meshes will be further introduced in Chapter 8, addressing finite element analyses of the notched tensile specimens. The simulations were carried out employing elastic material models with Young's modulus and Poisson's ratios for the two materials; E = 3000 MPa and ν = 0.3 for PVC, and E = 800 MPa and ν = 0.4 for HDPE [13]. The results were taken out from 20 elements that define the minimum cross sections of the axisymmetric mesh. The axial stress in the element in the minimum cross section located closest to the centre axis, at $r \approx 0$ mm, is used as a reference for the stress state. The results from each simulation are normalized by the axial stress of this centre element. Figure 8.18 to Figure 8.20 represent the axial, radial and hoop stress normalized with respect to the axial stress at the centre axis. All the figures are plotted as radial distributions i.e. from $r = 0$ to $r = a_0 = 3$ mm.

The radial distribution of the normalized axial stress in the minimum cross section is plotted in Figure 8.18. Because the stress at the centre axis of the specimen is selected as reference stress and therefore equal to 1 all normalized stresses are equal to 1 at r = 0 mm. For larger r, towards the root of the notch, the axial stress increases. The increase depends on the specimen geometry. In particular, is seen that the specimens with the smallest notch radius, R_0 = 0.8 mm, has a less homogenous stress distribution than the other specimens. The normalized axial stress is almost constant in the sample with the highest notch radius of R_0 = 20 mm.

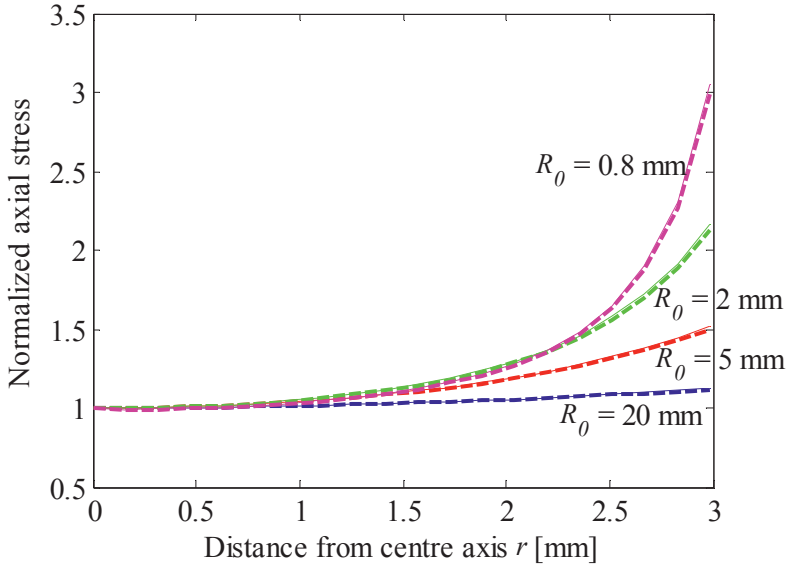

Figure 8.18 *Variation of axial stress in the minimum cross section of the test specimens from the FE simulations of elastic deformation. The stresses are normalized by the axial stress in the element closest to the centre axis. Solid lines are applied for PVC and dashed lines for HDPE.*

Figure 8.19 shows the radial distribution of normalized radial stress in the minimum cross section for elastic deformation. Again, the curves are determined from the elastic numerical simulations of PVC and HDPE specimens. Also here the stress is normalized by the axial stress in the element closest to the centre axis. It is seen that the smaller the notch radius is the higher is the stress component in the radial direction. For specimens with $R_0 = 0.8$ mm the maximum value is about 40-50% of the reference axial stress while it in specimens with $R_0 = 20$ mm is less than 10% of the reference axial stress.

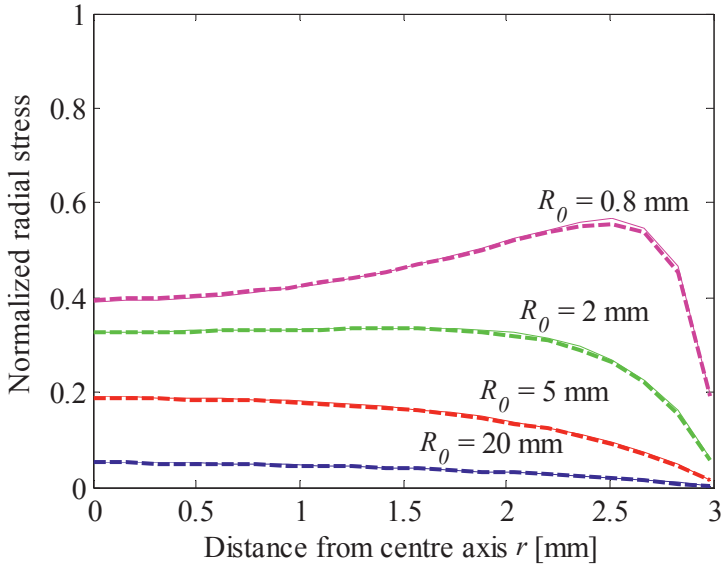

Figure 8.19 *Variation of radial stress in the minimum cross section of the test specimens from the FE simulations of elastic deformation. The stresses are normalized by the axial stress in the element closest to the centre axis. Solid lines are applied for PVC and dashed lines for HDPE.*

The radial distribution of the hoop stress is plotted in Figure 8.20. As in the two previous figures, it is normalized by the axial stress in the centre element for each of the specimens. Also for this case, the stress is higher in the specimens with lower R_0. Like the other stress components, the homogeneity of the stress field reduces with decreasing R_0. For the specimens with $R_0 = 0.8$ mm, the normalized hoop stress varies from about 0.4 to 1.

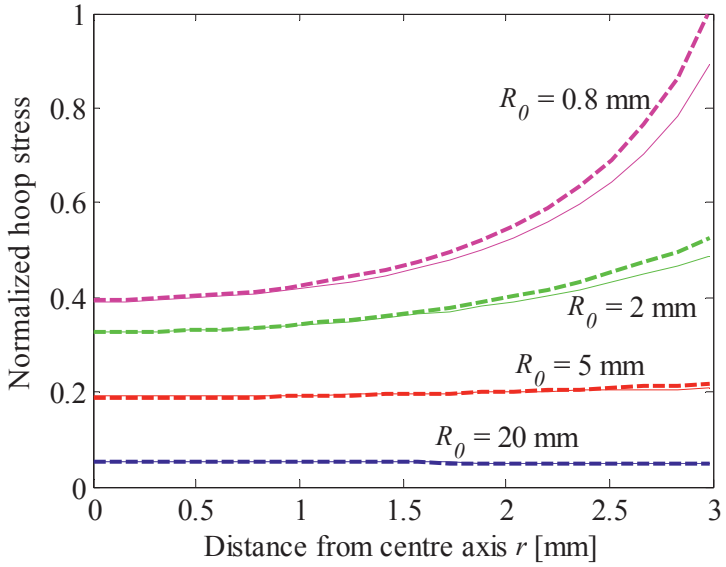

Figure 8.20 *Variation of hoop stress in the minimum cross section of the test specimens from the FE simulations of elastic deformation. The stresses are normalized by the axial stress in the element closest to the centre axis. Solid lines are applied for PVC and dashed lines for HDPE.*

By combining the three stress components, the stress triaxiality ratio σ^* defined in Equation (8.1) are found for each of the numerical models. Their radial distributions are plotted in Figure 8.21. It is seen that the smaller the notch radius R_0 is, the higher is the stress triaxiality and so is the variation in the radial distribution.

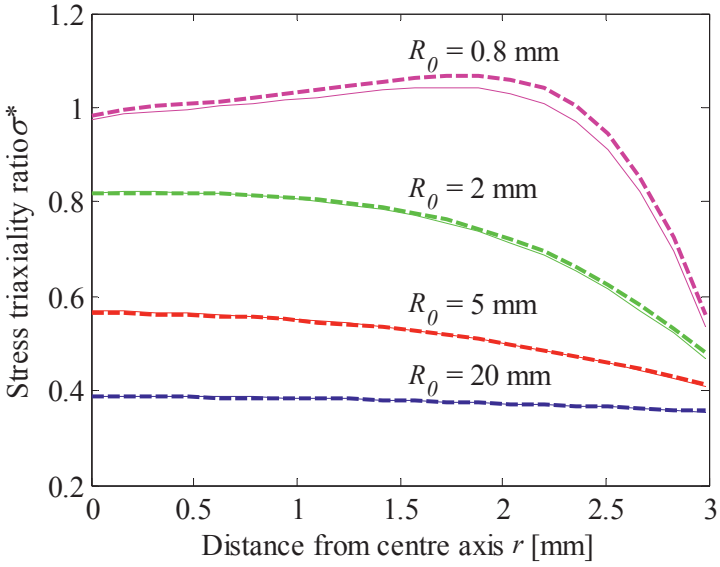

Figure 8.21 *Variation of the stress triaxiality ratio, σ^*, stress in the minimum cross section of the test specimens from the FE simulations of elastic deformation.. Solid lines are applied for PVC and dashed lines for HDPE.*

In order to get a better impression of the stress state in the specimens just before yielding, the stress states from the numerical simulations of the elastic deformation of both PVC and HDPE are plotted in a stress invariant space in Figure 8.22, applying the hydrostatic stress invariant $I_1/3$ and the deviatoric stress invariant $\sqrt{3J_2}$ as axes. This is done to show how the two invariants are present in the different test specimens before onset of plasticity. Figure 8.22 applies sectors to show the variation of stress states that occur in each of the specimen geometries. Moreover, the stress states of the PVC specimens lie within the solid lines and stress states for the HDPE specimens lie within the dashed lines. The specimens with the largest notch ($R_0 = 20$ mm), see sub-figure a), have a quite narrow sector in the $I_1/3 - \sqrt{3J_2}$ stress space. As seen in Figure 8.18 - Figure 8.20, there is little variation in the radial distribution of stress in these specimens. The sector in sub-figure b) representing the stress state in the specimens with $R_0 = 5$ mm is somewhat wider. The stress states in the specimens with $R_0 = 2$ mm and $R_0 = 0.8$ mm are displayed by sectors in sub-figures c) and d). Again, it is seen that the variation in stress state in the specimens with low R_0 is larger than for the other specimens.

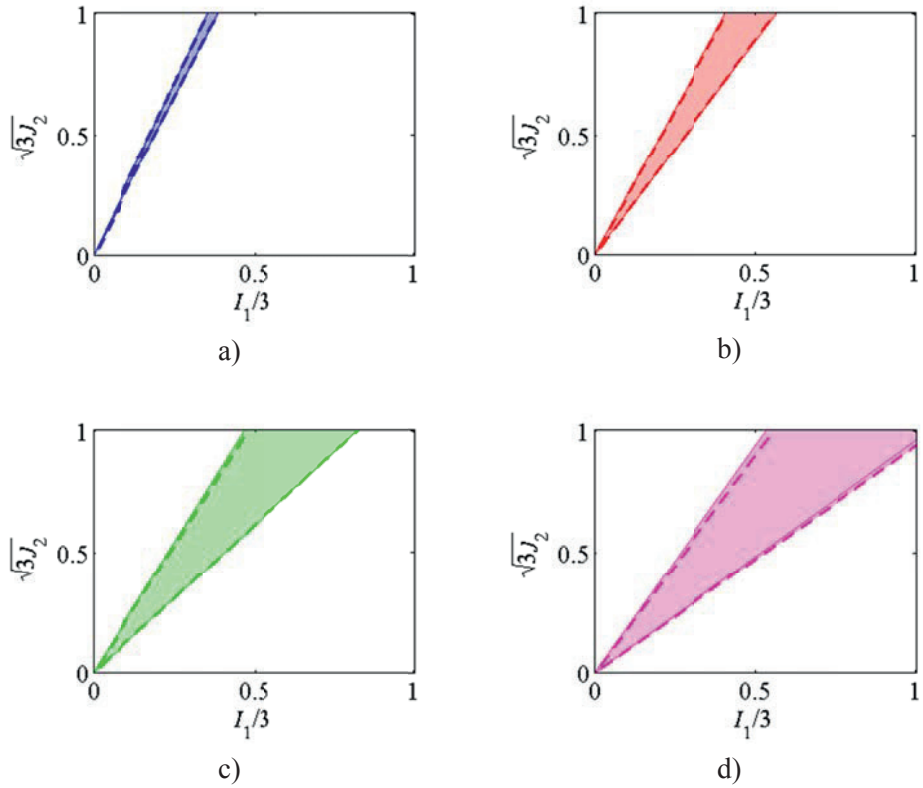

Figure 8.22 *Sectors representing the stress states present in the minimum cross section of each specimen before yielding: a)* $R_0 = 20$ *mm, b)* $R_0 = 5$ *mm, c)* $R_0 = 2$ *m and d)* $R_0 = 0.8$ *mm. Solid lines are applied for PVC and dashed lines for HDPE.*

8.7 FRACTURE

All PVC specimens fractured during testing. Fracture surfaces of representative samples of each of the specimen geometries are displayed in Figure 8.23 to Figure 8.26. Only the two HDPE specimens with lowest R_0 ruptured in the tests. Their fracture surfaces are presented in Figure 8.27 and Figure 8.28. All fracture surfaces indicate that the failure is dominated by void growth: Small holes can be seen at the PVC fracture surface and traces after large voids are present at the HDPE fracture surfaces. For both materials, and especially for the HDPE, a fibrillar structure oriented radially out from the voids is observed.

Visual observation of the fracture surfaces of the PVC specimens reveals a rough topography. An impression from comparing the different PVC specimens is that a higher R_0 caused a rougher fracture surface. Moreover, the fracture surfaces of PVC in general appear more uneven than the fracture surfaces of HDPE.

Comparison of the fracture surfaces of HDPE-2 and HDPE-08, see Figure 8.27 and Figure 8.28 respectively, reveals that the void size is largest in the first case. The fracture surfaces of the other two specimens of the same material and geometry indicate the same. Assuming that the voids initially were small and of equal size in the two specimens, and taking into account that the HDPE-2 specimen fractured at a larger strain than HDPE-08, this observation indicates that the voids coalesce during deformation. HDPE-2 is deformed more than HDPE-08, therefore more of the voids have coalesced. The voids located close to, but not at, the rim of the fracture surface of HDPE-08 also appear somewhat larger than those in the centre and those at the rim. The comparatively large voids are thus in the region of highest triaxiality in the elastic domain, as reported in Figure 8.27. Comparing the strains at fracture, the fracture strains are much lower for PVC than for HDPE.

It was also noted that some kind of a thin skin layer was formed around the fracture surface of the HDPE specimens. Whether this was a structural or damage effect, or if it originated from changes in the surface material during machining of the specimens is not known.

a) b)

Figure 8.23 *Fracture surface of a PVC-20 specimen. a) Upper part. b) Lower part.*

a) b)

Figure 8.24 *Fracture surface of a PVC-5 specimen. a) Upper part. b) Lower part.*

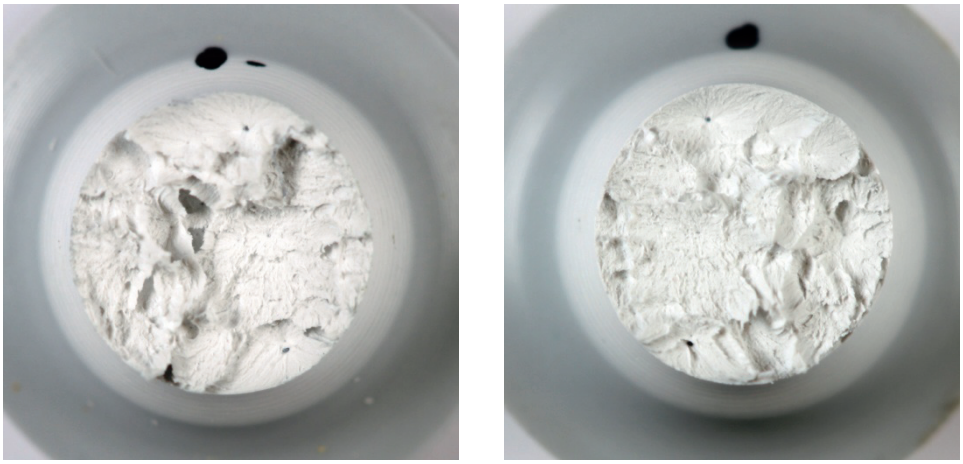

a) b)

Figure 8.25 *Fracture surface of a PVC-2 specimen. a) Upper part. b) Lower part.*

a) b)

Figure 8.26 *Fracture surface of a PVC-08 specimen. a) Upper part. b) Lower part.*

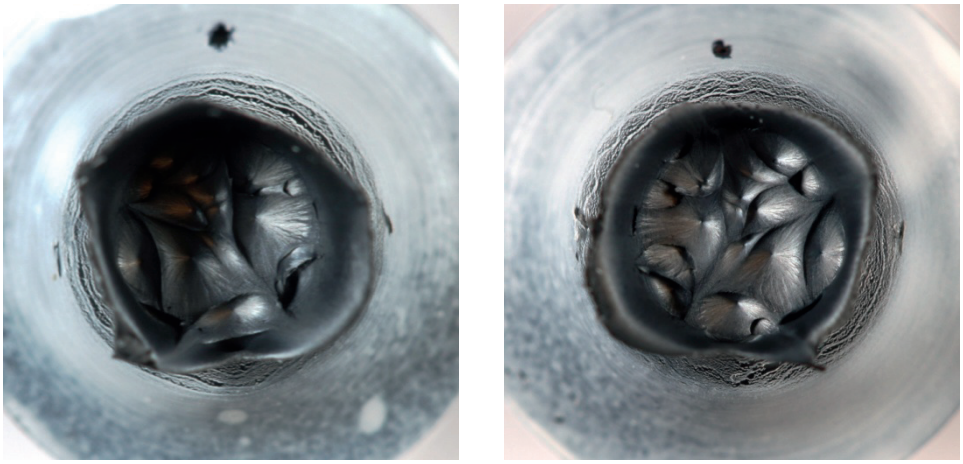

a) b)

Figure 8.27 *Fracture surface of a HDPE-2 specimen. a) Upper part. b) Lower part.*

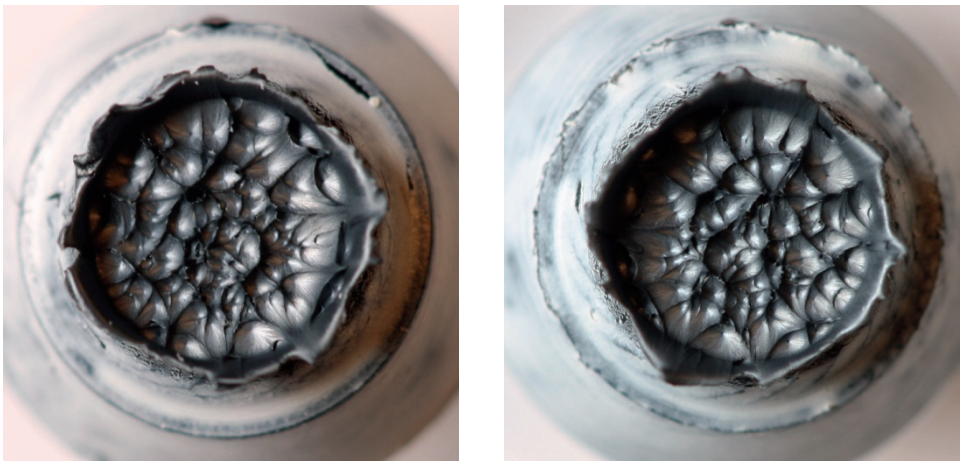

a) b)

Figure 8.28 *Fracture surface of a HDPE-08 specimen. a) Upper part. b) Lower part.*

8.8 DISCUSSION

Axisymmetric tensile bars with and without notch were machined from the extruded plates of mineral filled PVC and HDPE. Different notch radii were employed to create different stress triaxialities. In this work it is assumed that smaller notch radii produce higher stress triaxialities, in accordance with Bridgman [1]. The assumption is supported by results from the numerical simulations of elastic deformation of notched axisymmetric tensile bars presented in Figure 8.21.

Each of the test specimens was marked with small spots prior to the test and the specimens were deformed in front of a contrast background as seen in Figure 8.2. The deformation was surveyed by a CCD camera so that the curvature of the specimen and the distance between the marks could be traced after testing by a image post-processing code made in MATLAB [12]. This method allowed for measurement of the minimum radius a, notch radius R, optical extensometer length L, and volume V for the entire deformation process. This test data created a comprehensive basis for studying the effect of the changes in stress triaxiality on the mechanical response of the two materials.

All force-displacement curves in Figure 8.3 and Figure 8.4 reach a peak in terms of a maximum force followed by a drop in the force level. The averaged axial stress-strain curves plotted in Figure 8.7 and Figure 8.8 account for reduction of the minimum cross section due to necking by defining the net stress as the applied force divided by the current minimum cross section area in accordance with Equation (8.2). Yet, a local maximum followed by a drop can also be observed in the stress-strain curves for all PVC specimens and for HDPE-2 and HDPE-08. These peaks may be related to internal damage: If void growth sets in at this stage, the effective load bearing cross section is reduced. The area reduction from an increasing void volume fraction cannot be measured by the test setup employed here. By interrupting the deformation and splitting the specimens, as done for uniaxial tensile specimens in Chapter 6 and by Boisot et al. [8] for axisymmetric specimens with notch, estimates of the void volume fraction could have been found by using SEM. X-ray tomography is an alternative method that also could have been applied [14, 15].

In Chapter 6 it was shown that void growth on the microscale can be linked to volume strain on the macroscale. The change of volume in the notch can be presented in terms of volume strain, as in Figure 8.13 and Figure 8.14, or in terms of radial strain [7, 8], see Figure 8.15 and Figure 8.16. One major difference between the two measures is that the volume strain is calculated for a larger zone, while the radial strain is measured in the minimum cross section where the strain is localized. However, the same trend is seen in the two ways of presenting volume

change: The dilation increases with decreasing R_0. Comparing with the volume strains in uniaxial tension in Chapter 2.8, the volume changes are quite dramatic when the materials are subjected to a triaxial stress field. Especially for the HDPE, behaving almost isochoric in uniaxial tension, the difference is significant. It is reasonable to assume that the volume change, both in PVC and HDPE, is linked to void growth. Voids in the PVC specimens can be observed in terms of stress whitening in Figure 8.5. No stress whitening is observed for the HDPE. Still, the volume change evident from Figure 8.14 suggests that growth of voids occurs. The presence of voids, in both materials, is further confirmed by examining the fracture surfaces as demonstrated in Figure 8.23 to Figure 8.27.

The average stress-strain responses of the PVC specimens are plotted in Figure 8.7. It is seen that all the notched specimens have a higher yield stress than the smooth specimen. Further, it is seen that there is little variation between the responses of the notched PVC specimens. Figure 8.9 and Table 8.1 reveal that there is some difference in the strain rate in the smooth and the notched specimens, while the difference in the strain rate between the notched specimens is less. The average stress-strain curves from the HDPE specimens are plotted in Figure 8.8. The figure shows that also for HDPE there is a difference in the responses between the smooth and the notched specimens. Moreover, the stress-strain curves differ for HDPE samples with different notch radii. Between the HDPE specimens, there are no considerable differences in the strain rates. According to the slopes of the curves in Figure 8.10 and the data in Table 8.2 the rates of average strain of HDPE is less influenced by R_0 than they are for PVC.

For a material without pressure sensitivity, the axial net stress which the material can sustain before yielding is higher when a stress component of hydrostatic tension is present. This means that the presence of a notch producing a triaxial stress field increases the observed averaged axial yield stress in testing of such materials. This is in accordance with the theory of Bridgman and the relationship is plotted by a solid line in Figure 8.17. In a pressure sensitive material, like many polymers, also the hydrostatic stress component contributes to reach the onset of yielding. This is seen in Figure 8.17 where the axial net stress is plotted against the notch radius, both taken at maximum force, for the experimental test results. Since PVC does not obey the Bridgman prediction, it is suggested that the yield stress of PVC is pressure sensitive. HDPE followed the Bridgman prediction better, and is therefore likely to be less pressure sensitive. This is in accordance to what is observed in the tension and compression of PVC and HDPE, see Chapter 2.8. The discrepancy from the Bridgman prediction might to some degree relate to the viscous effects seen in Figure 8.9 and Figure 8.10. However, Table 8.1 reveals that the rate of average axial strain in PVC-20 is 8 times the rate in the smooth

PVC specimen while it from Table 8.2 is seen that the rate of average axial strain in HDPE-20 is 2.5 times the rate in the smooth HDPE specimen. Moreover, as will be seen in Chapter 10, the magnitude of strain rate dependency C is higher for PVC than for HDPE. Therefore one should expect that the PVC-20 should deviate more from the Bridgman prediction than HDPE-20. It is not so. Another point worth noticing in this relation is that the Bridgman prediction should regard the yield stress of the two materials. Here, the axial average stress is determined at maximum force, and this may not be a proper way to consider the yield stress for HDPE.

In order to gain information of the stress triaxiality σ^* in the different test specimens in this study, a numerical study of the elastic deformation of the two materials was carried out for the different specimen geometries. The stress components found from the numerical simulations are plotted in Figure 8.18 to Figure 8.20. It is seen that the stress components vary a lot over the cross section. In general, the normalized value of each of the stress components seem to increase with decreasing R_0. Consequently, a large variation occurs in the stress triaxiality ratio, see Figure 8.21. The range of stress triaxialities are plotted in the $I_1 / 3 - \sqrt{3J_2}$ principal stress space in Figure 8.22. Again the variation in the stress field is demonstrated. From Figure 8.18 to Figure 8.22 it is obvious that one test specimen does not evaluate a single stress state, but a combination of stress states. Without knowing the yield criterion, we do not know when plasticity sets in.

The radial distribution of stress triaxiality in the numerical simulation of elastic deformation of specimens with $R_0 = 0.8$ mm in Figure 8.21 reveals that the stress triaxiality is not at its maximum in the centre of the specimen, but at a location closer to the root of the notch. The increased void size at positions approaching the boundary of the fracture surface of HDPE-08, see Figure 8.28, indicates that void growth and coalescence have been more pronounced in this zone. For a similar test specimen, also with a low value of $R_0 / 2a$, Laiarinandrasana et al. [15] identified the same zone as the location of maximum damage. This was done for polyamide 6 both by finite element modelling and by experimental tests employing X-ray tomography. If the minimum diameter $2a$ is considerably larger than R, the stress triaxiality does not increase monotonically towards the specimen centre.

In addition to HDPE-2 and HDPE-08 all PVC specimens fractured during testing. The fracture surfaces, depicted in Figure 8.23 to Figure 8.28, suggest that the fractures were induced by void growth. The surfaces of the PVC specimens have a rather rough topography. An impression from comparing the different PVC specimens is that a higher R_0 caused a rougher fracture surface. This fits with the

observation from Figure 8.5 that the stress whitened zone of these specimens ranges over a larger extent in the longitudinal direction than for the specimens with a lower R_0. It may indicate coalescence of voids in longitudinal and lateral directions in PVC for the largest R_0. The fracture surfaces of the two HDPE specimens are more planar, oriented transverse to the loading direction. A possible interpretation is that the void growth of the HDPE occurs on a more local level and that the voids coalesce in the transverse direction. The shape of the stress-strain curves in Chapter 2.8 suggests that the strain hardening is less in HDPE than in PVC. Thus the ability to redistribute strain is less in HDPE. The voids are able to coalesce and form fracture in the transverse direction. It is also worth noticing that the two HDPE specimens that did fracture, HDPE-2 and HDPE-08, have a noticeable dilation compared to HDPE-20 and HDPE-5. This is clearly seen in Figure 8.14 and Figure 8.16.

Laiarinandrasana et al. [10] discussed the effect of strain rate, temperature and stress triaxiality on the fracture surface on polyvinylidene fluoride. They showed that more ductile fracture surfaces were present for circular notched tensile specimens with larger notch radii, i.e. lower triaxialities. They also showed that higher strain rate and high stress triaxialities gave more brittle fracture. This is in accordance with the experience from our study. The HDPE specimens with large R_0 were too ductile to fracture, while the specimens with lower R_0 fractured.

It should be emphasized that several of the entities presented in the results are averaged over a length, an area or a volume. Except the cross section radius a, the deformations are not measured locally. Local values of axial strain in the minimum cross section is probably higher in the averaged axial strain $\ln(L/L_0)$. Also the local strain rate in the minimum cross section is likely to be higher in the minimum cross section than what we have measured. The rates of average axial strain are represented by the slopes of the curves in Figure 8.9 and Figure 8.10. Since PVC and HDPE are viscoplastic materials, this may have affected the maximum force level more than what first appears. As an effect of this also the temperature might have been higher in the notched specimens.

The comparatively small radial strains $\ln(a/a_o)$ in Figure 8.15 and Figure 8.16 are a sign of little contraction of the minimum cross section and therefore much dilation. The slopes of HDPE-20 and HDPE-5 in Figure 8.15 are steeper than –0.5. This is an effect of $\ln(a/a_0)$ being a measure over the localized zone while $\ln(L/L_0)$ is not. None of the PVC specimens have a slope close to –0.5.

An approach to get the local strains, instead of net strains, could be to use DIC. In fact, some introductory tests on axisymmetric notched tensile bars were carried out using 3D DIC employing two CCD-cameras. The small size of the notch combined with the large local deformations and the double-curved surface caused difficulties with the image quality and also so much noise that the test results were poor. Therefore, the simple test setup described in this section, involving one camera focusing on the rim of the test specimen so that its curvature could be traced, was chosen. To obtain reliable results with the test setup in general, the image resolution for the images taken by the CCD-camera should be good. If the resolution is poor, the relative size of one pixel is large. Thus, inaccuracy or noise from one pixel can have a large influence on the result.

8.9 CONCLUDING REMARKS

- The yield stress of mineral the filled PVC does not follow the formulas of Bridgman and is therefore likely to be is sensitive to stress triaxiality. Also the plastic dilation of the material is sensitive to stress triaxiality: higher stress triaxialities leads to more volume increase in the PVC.

- The yield stress of the HDPE does hardly show any sensitivity to stress triaxiality. However, the change of volume at higher stress triaxialities is evident: higher stress triaxialities leads to more volume increase in the HDPE.

- Void growth is assumed to be the reason for the plastic dilation in both materials. Also the fracture of both materials is assumed to be related to voids.

- From the numerical simulations it is observed that the geometry of the axisymmetric specimens with notch creates a stress field with that increasing triaxiality with decreasing notch radius R.

- When the notch radius R is small relative to the minimum diameter $2a$, the value of maximum triaxiality is not located in the specimen centre, but closer to the root of the notch. The photos of the fractured surfaces of the two HDPE samples with the smallest R_0 support this prediction.

REFERENCES

[1] P.W. Bridgman. *Studies in large plastic flow and fracture.* Harvard University Press, (1952).

[2] G.E. Dieter. *Mechanical Metallurgy.* McGraw-Hill Book Company, (1988).

[3] M. Gromada, G. Mishuris, A. Öchsner. *Correction formulae for the Stress Distribution in Round Tensile Specimens at Neck Presence.* Springer, (2011).

[4] A.H. Clausen, T. Børvik, O.S. Hopperstad, A. Benallal. Flow and fracture characteristics of aluminium alloy AA5083-H116 as function of strain rate, temperature and triaxiality. *Materials Science & Engineering*, **364** (2004), 260-272.

[5] T. Børvik, O.S. Hopperstad, T. Berstad, M. Langseth. A computational model of viscoplasticity and ductile damage for impact and penetration. *European Journal of Mechanics A/Solids*, **20** (2001), 685-712.

[6] J.S. Olsen, Z.L. Zhang, H. Lu, C. van der Eijk. Fracture of notched round-bar NiTi-specimens. *Engineering Fracture Mechanics*, **84** (2012), 1-14.

[7] S. Castagnet, Y. Deburck. Relative influence of microstructure and macroscopic triaxiality on cavitation damage in a semi-crystalline polymer. *Materials Science and Engineering: A*, **448** (2007), 56-66.

[8] G. Boisot, L. Laiarinandrasana, J. Besson, C. Fond, G. Hochstetter. Experimental investigations and modeling of volume change induced by void growth in polyamide 11. *International Journal of Solids and Structures*, **48** (2011), 2642-2654.

[9] M. Challier, J. Besson, L. Laiarinandrasana, R. Piques. Damage and fracture of polyvinylidene fluoride (PVDF) at 20 degrees C: Experiments and modelling. *Engineering Fracture Mechanics*, **73** (2006), 79-90.

[10] L. Laiarinandrasana, J. Besson, M. Lafarge, G. Hochstetter. Temperature dependent mechanical behaviour of PVDF: Experiments and numerical modelling. *International Journal of Plasticity*, **25** (2009), 1301-1324.

[11] J.W. Hancock, A.C. Mackenzie. Mechanisms of ductile failure in high-strength steels subjected to multi-axial stress states. *Journal of the Mechanics and Physics of Solids*, **24** (1976), 147-169.

[12] A. Dahlen. Plastic deformation and fracture of polymer materials. Master thesis, Department of Structural Engineering, NTNU, (2011).

[13] M.T. Hovden. Test and numerical simulations of polymer components. Master thesis, Department of Structural Engineering, NTNU, (2010).

[14] L. Laiarinandrasana, T.F. Morgeneyer, H. Proudhon, C. Regrain. Damage of semicrystalline polyamide 6 assessed by 3D X-ray tomography: From microstructural evolution to constitutive modeling. *Journal of Polymer Science Part B: Polymer Physics*, **48** (2010), 1516-1525.

[15] L. Laiarinandrasana, H.A. Cayzac, T.F. Morgeneyer, H. Prudhorn. Modelling of damage distribution and orientation assessed by X-ray tomography technique on semi-crystalline polymers. 15th International Conference on Deformation, Yield and Fracture of Polymers, Rolduc Abbey, Kerkrade, The Netherlands, 1-5 April, (2012).

PART II

NUMERICAL STUDY

CHAPTER 9

UNIT CELL MODEL

This chapter deals with a numerical study of the matrix-particle interaction in a composite material subjected to uniaxial tension. The study employs unit cell models representing soft polymer matrix containing stiff particles with idealized arrangements and geometries. The study was carried out to achieve a better understanding of the effect of the filler on the PVC. In particular, the macroscopic response of the unit cell in terms of stress-strain relationship and volume change is investigated.

9.1 INTRODUCTION

Finite element analysis on simplified micromechanical models have been used by many researchers [1-8] to achieve a better understanding of the macromechanical response of polymer materials containing second phase particles. It is challenging to reconstruct the complex microstructure of a polymer-particle composite exact in a finite element mesh. Also, to run simulations on a "geometrical perfect" model would be rather computationally expensive. It is therefore attractive to represent the real microstructure by geometrically simpler structures in terms of unit cell models. Real particles might have rather irregular shapes. The particle size might also be quite diverse. In unit cell models it is common to idealize the particle shapes as perfect spheres of identical size. Their arrangement is often idealized as well. Real particles are normally distributed randomly in the matrix. A unit cell model, on the other hand, usually contains particles of equal size in periodic patterns. Such simplifications can affect the results. The arrangement of the particles influences how the matrix flows between them. Also, a stress field around one particle may overlap the stress field of its neighbour. Socrate and Boyce [1] report that if the interparticle distance approaches the average particle diameter, such interactions between particles become important. In that case a more advanced micromechanical model as a 'representative volume elements' (RVE)

can be used. In such a model particles can be organized in a more irregular pattern with a larger variety of particle sizes than possible in a simple unit cell model [2]. Still, some homogenization assumptions are required also for these models.

Many of the micromechanical unit cell models found in the literature concern self-cavitation of rubber particles and void growth. These phenomena are often modelled simply by a matrix material containing initial voids [1, 3, 4]. In some cases actual rubber particles are modelled with a proper constitutive model [2, 5, 6]. Some studies are also performed on polymers containing stiff particles [5, 7-9]. Van Dommelen et al. [9] present a study of a two dimensional (plane strain) as well as an axisymmetric RVE representing a semicrystalline polymer containing both soft and stiff particles with different particle-matrix interface strengths. Their models included local anisotropy of the matrix material around the particles and their work is mainly focused on the effect of this. Kemal et al. [8] have studied the toughening of PVC through the addition of $CaCO_3$ nano-particles. They presented a unit cell model of spherical particles in a stacked array with weak bonding between the particle and the matrix [8]. Another two dimensional unit cell model representing polypropylene (PP) containing stiff mineral particles in a periodic stacked array and plane strain condition was developed by Delhaye [5]. In this model, the matrix-particle interface was modelled without any bonding. The effect of different matrix-particle interface strengths was investigated by Hempel et al. [7]. They created a three dimensional unit cell model representing a PP matrix containing platelet-like talc particles.

The unit cell models in this study represent the microstructure as a periodic distribution of rather stiff linear elastic particles surrounded by a soft elastic-plastic matrix of PVC. Four parameters have been varied. They are the:

- particle volume fraction ω
- particle shape
- particle arrangement
- particle-matrix interface strength

Two particle volume fractions, $\omega = 0.1$ and $\omega = 0.2$, are represented in the models. Meshes with both cubical and spherical particles were created to study the effect of the particle shape. The particles are organized in both a stacked and a staggered array. The four combinations of shape and arrangement of particles are illustrated in Figure 9.1. Particle-matrix debonding was modelled by using a contact algorithm that allows for failure when a critical stress criterion is met. This is similar to what is done in the study of Hempel et al. [7]. By setting different critical stresses, the effect of the particle-matrix interface strength is investigated. Although only these four parameters have been varied one should keep in mind

that any change of these parameters has influence on other parameters such as the distance between particles and the area of the matrix-particle interface.

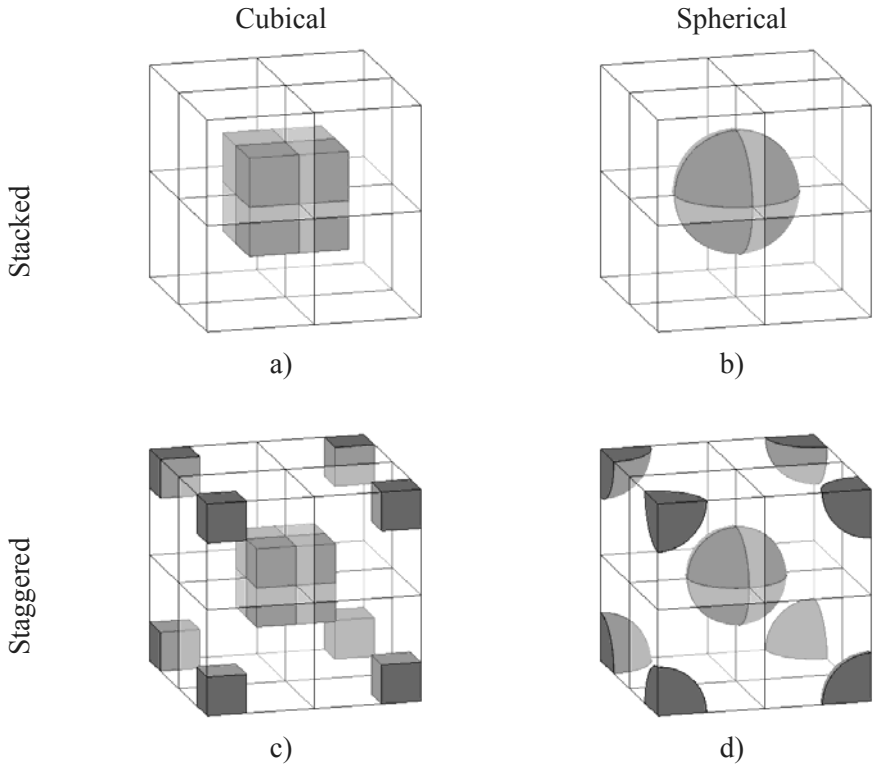

Figure 9.1 *Sketches of eight unit cell models assembled into a) stacked array of cubical particles, b) stacked array of spherical particles, c) staggered array of cubical particles and d) staggered array of spherical particles. These unit cell models contain a particle volume fraction of* $\omega = 0.1$.

9.2 MESH

Eight different unit cell meshes were defined. Each unit cell has a total volume of 1 and it contains the particle volume fraction ω. Meshes of unit cells containing cubical and spherical particles organized in stacked and staggered arrays were constructed as explained in the following. Eight node solid elements with reduced integration were used in all meshes. Stiffness based hourglass control was employed to avoid nonphysical hourglass modes. Rather extensive mass scaling, by a factor of 10^8, was employed to make the simulations run faster. Also, additional simulations with less mass scaling were carried out on a test mesh of a unit cell

model with cubical particles. They showed that the mass scaling did not alter the numerical results. After the simulations it was controlled that the kinetic, the sliding and the hourglass energy did not exceed 1% of the total energy in the simulations.

9.2.1 STACKED ARRAY OF CUBICAL PARTICLES

The arrangement of cubical particles in a stacked array is shown in Figure 9.1 a). Figure 9.2 a) shows the mesh used in the simulations. It contains a total of 28^3 equally sized cubical elements whereof 13^3 are modelled as particles. This give a particle volume fraction of $\omega = 0.1$. The mesh in Figure 9.2 b) consists of 24^3 equally sized elements whereof 14^3 are modelled as particles. This gives a volume of particles equal to $\omega = 0.19$, a number that is regarded as adequate for representing a material with a particle volume fraction of $\omega = 0.2$.

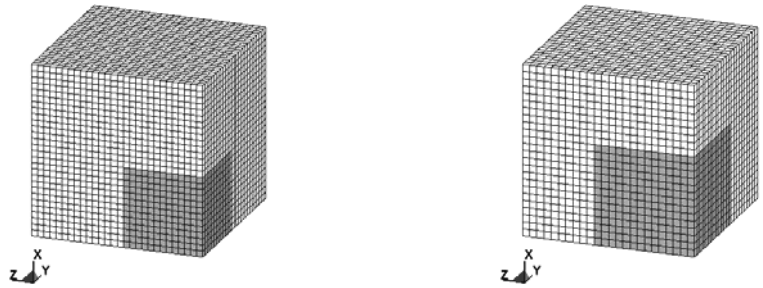

a) b)

Figure 9.2 *Unit cell models representing a stacked array of cubical particles with particle volume fractions of a) $\omega = 0.1$ and b) $\omega = 0.2$.*

9.2.2 STAGGERED ARRAY OF CUBICAL PARTICLES

Figure 9.1 c) shows cubical particles organized in a staggered BCC-array. The mesh containing particle volume fraction $\omega = 0.1$, see Figure 9.3 a), was made as a model of 19^3 equally sized cubical elements whereof $2 \cdot 7^3$ were modelled as particles. This means that 10% of the volume is occupied by particles. The mesh with $\omega = 0.2$ was modelled with 28^3 equal-sized elements whereof $2 \cdot 13^3$ were modelled as particles. It is displayed in Figure 9.3 b).

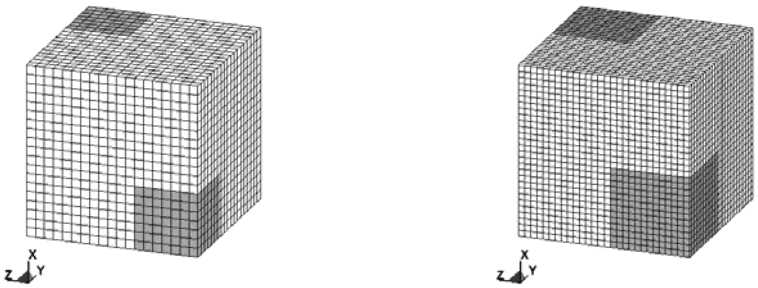

a) b)

Figure 9.3 *Unit cell models representing a staggered array of cubical particles with particle volume fractions of a) $\omega = 0.1$ and b) $\omega = 0.2$.*

9.2.3 STACKED ARRAY OF SPHERICAL PARTICLES

The total volume of the unit cell is still 1, the volume fraction is ω and the radius of the particles is r. The volume of an entire spherical particle is $(4/3)\pi r^3$. A unit cell model contains 1/8 of a spherical particle. It is placed in one corner of the unit cell as shown in Figure 9.1 b). The particle volume fraction is then

$$\omega = \frac{1}{8} \cdot \left(\frac{4}{3} \pi r^3 \right) \tag{9.1}$$

which gives the radius

$$r = \sqrt[3]{\frac{6\omega}{\pi}} \tag{9.2}$$

Particle volume fractions of $\omega = 0.1$ and $\omega = 0.2$ results in $r = 0.576$ and $r = 0.726$, shown in Figure 9.4 a) and b), respectively.

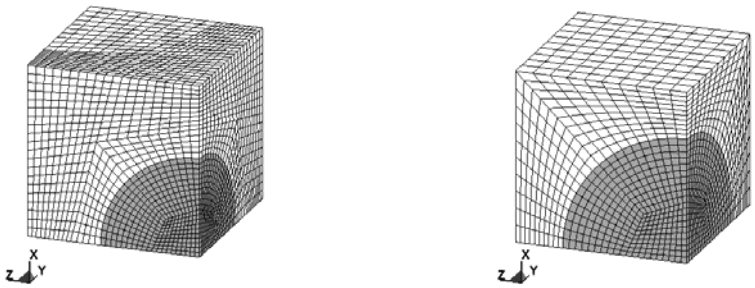

a) b)

Figure 9.4 *Unit cell models representing a stacked array of spherical particles with particle volume fractions of a) $\omega = 0.1$ and b) $\omega = 0.2$.*

9.2.4 STAGGERED ARRAY OF SPHERICAL PARTICLES

The staggered BCC array of spherical particles is shown in Figure 9.1 d). One such unit cell contains two times an 1/8 part of a spherical particle placed in opposite corners. The particle volume fraction is

$$\omega = \frac{2}{8} \cdot \left(\frac{4}{3} \pi r^3 \right) \tag{9.3}$$

Solved for the radius r

$$r = \sqrt[3]{\frac{3\omega}{\pi}} \tag{9.4}$$

This gives $r = 0.457$ and $r = 0.576$ for $\omega = 0.1$ and $\omega = 0.2$. The meshes created for these unit cells are shown in Figure 9.5 a) and b).

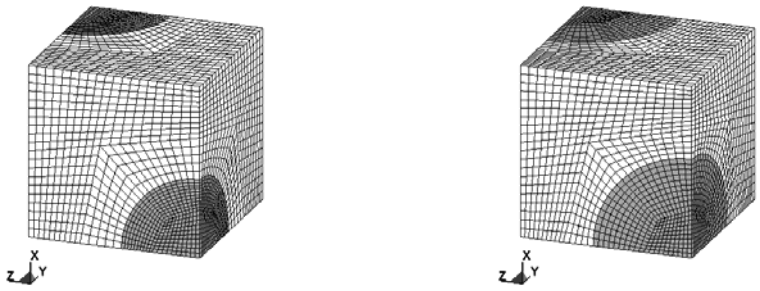

a) b)

Figure 9.5 *Unit cell models representing a staggered array of spherical particles with particle volume fractions of a) $\omega = 0.1$ and b) $\omega = 0.2$.*

9.3 MATERIAL MODEL

The material of the PVC matrix was modelled as linear elastic-plastic with a strain hardening effect being characteristic for the response of neat PVC. The simple elasto-plastic *MAT_024 material model in LS-DYNA with a pre-defined stress-strain response was used [10]. The matrix yield stress and Young's modulus were respectively σ_T = 50 MPa and E = 2000 MPa. Poisson's ratio was set to ν = 0.3. The shape of the curve after yielding was adapted from stress-strain data from G'Sell et al. [11] valid for pure PVC. The curve was shifted to fit the applied yield stress of 50 MPa. The stress-train curve can be seen in Figure 9.6. The calcium carbonate particles were modelled as elastic with the properties E = 35000 MPa and ν = 0.2 [12]. The stress-strain curve of the mineral filled test specimen PVC-8 from Chapter 6 is also included in Figure 9.6 for comparison.

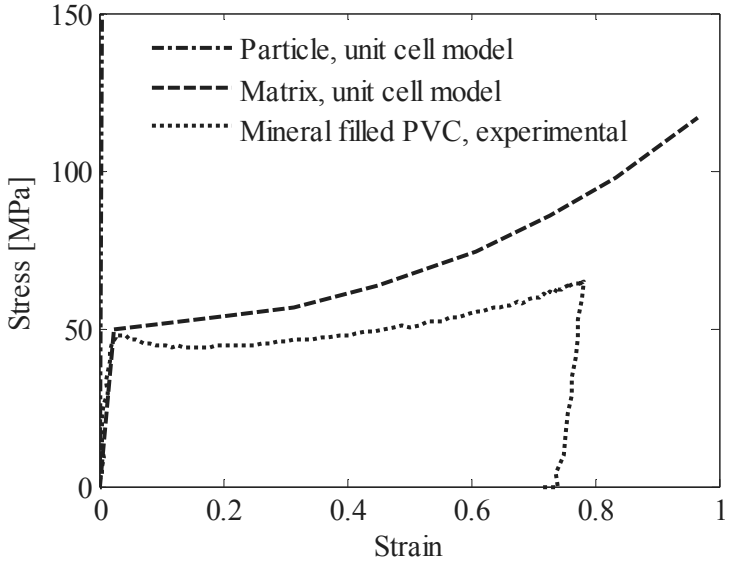

Figure 9.6 *Stress-strain relationships for the components of the unit cell model and also for experimental test specimen PVC-8 from Chapter 6.*

9.4 CONTACT FORMULATION

Debonding of particles was implemented through the contact-automatic-surface-to-surface-tiebreak formulation, which was used with failure law option 2 in LS-DYNA [10]. This means that tying of the nodes breaks when the normal stress σ_n and the shear stress σ_s meet the following criterion:

$$\left(\frac{\langle \sigma_n \rangle}{\sigma_{n,crit}}\right)^2 + \left(\frac{\langle \sigma_s \rangle}{\sigma_{s,crit}}\right)^2 \geq 1 \tag{9.5}$$

The critical normal stress $\sigma_{n,crit}$ and the critical shear stress $\sigma_{s,crit}$ were assumed to be equal, i.e. $\sigma_{n,crit} = \sigma_{s,crit}$. In order to study how the voids are formed around particles without any bonding to the matrix the critical stresses were as one case set to zero. Different matrix-particle interface strengths were modelled by setting the critical stress to 40 MPa, 50 MPa, 60 MPa and 500 MPa. The critical stress of 500 MPa is a value higher than what would occur in the simulation. It is set unrealistically high in order to study how the response would be for a perfectly bonded material. In addition, simulations without any matrix-particle interface strength were carried out in order to study the effect of unbounded particles.

9.5 BOUNDARY CONDITIONS

Boundary prescribed motion was defined for the side of the unit cell cube facing the positive *x*-direction. All nodes on this side, see Figure 9.7 a), were restricted to move equally in the *x*-direction. The nodes of two other sides, one facing the positive *y*-direction and one facing the positive *z*-direction, see Figure 9.7 b), were constrained to planar movement. The remaining three orthogonal faces, facing the negative *x*-, *y*- and *z*-directions, were constrained against translations in the direction they were facing [7]. These planes are addressed in Figure 9.7 c).

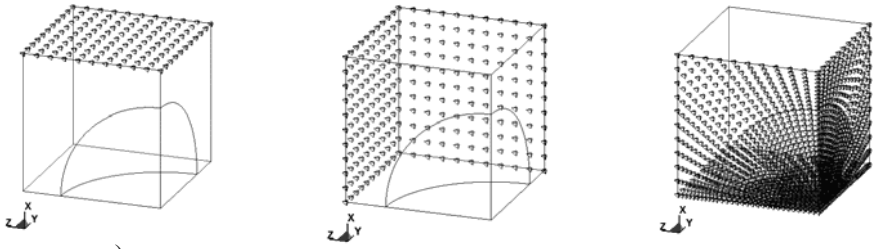

Figure 9.7 *Boundary conditions. a) The displacement is applied in x-direction to nodes on one side of the unit cell. b) The nodes on the two sides of the unit cell constrained to planar movement. c) The nodes on three of the sides of the unit cell constrained against out-of-plane motions.*

9.6 RESULTS

In order to express the joint behaviour of the unit cells, the terms macroscopic stress and macroscopic strain are used. They differ in general from the local stresses and strains within a unit cell. The macroscopic stress for each unit cell cube is a "macroscopic Cauchy stress" calculated by dividing the force acting through the cross section of the unit cell by the area of the cross section at the corresponding time step. The macroscopic strains are calculated as the logarithmic strains computed from the lengths of the edges of the cube. Macroscopic stress-strain curves of the different unit cells containing particles of $\omega = 0.1$ are presented in Figure 9.8. Figure 9.9 shows the same for a particle fraction of $\omega = 0.2$.

The response is dependent on the volume fraction, shape and arrangement of the particles, but some generalities are observed for all unit cell models. The unit cells representing particles without any bonding between the particles and the matrix show the softest behaviour. The other models have higher initial stiffness. The bonded particles carry load and therefore add stiffness to the unit cell. When the tiebreak criterion is fulfilled for the first node, the total stiffness of the unit cells instantly decreases and they tend to act more like the unit cells without bonding strength. Some of the unit cell models show a drop in the stress-strain curve. These drops are more sudden for the cubical than for the spherical particles, and they are greater for the highest volume fraction. A possible explanation for the sudden drops, observed in e.g. Figure 9.9 c), is that a large number of nodes break simultaneously. The unit cell models representing perfectly bonded particles show, naturally, the stiffest behaviour in all cases.

It is common to define the first local stress maximum of the stress-strain curve as the yield stress for polymers. This can be adapted to the macroscopic stress-strain curves for the unit cell models plotted in Figure 9.8 and Figure 9.9. By comparing the macroscopic responses from the unit cell models with the response of the material used to model the PVC matrix, see Figure 9.6, it can be seen that the response is different in the polymer-particle composite. The yield stress of the matrix was set to 50 MPa. Still, it can be seen in Figure 9.8 and Figure 9.9 that the peak stress is somewhat lower in the unit cell models with low or intermediate interface strengths. On the other hand, perfectly bonded particles increase the yield stress of the composite material. This tendency is stronger for the highest particle volume fraction.

If we leave the perfectly bonded particles out of the picture, it can be seen that the strain rehardening is independent on the particle-matrix bonding. It is determined by the geometry of the unit cell, and it is barely stronger for the lowest particle volume fractions. It is more pronounced for spherical particles than for cubical. Also the stacked array seems to increase the rehardening effect. This may be explained by how the particles affect the flow of the matrix, but one should keep in mind that the macroscopic Cauchy stress is also coupled with the volume change of the unit cells.

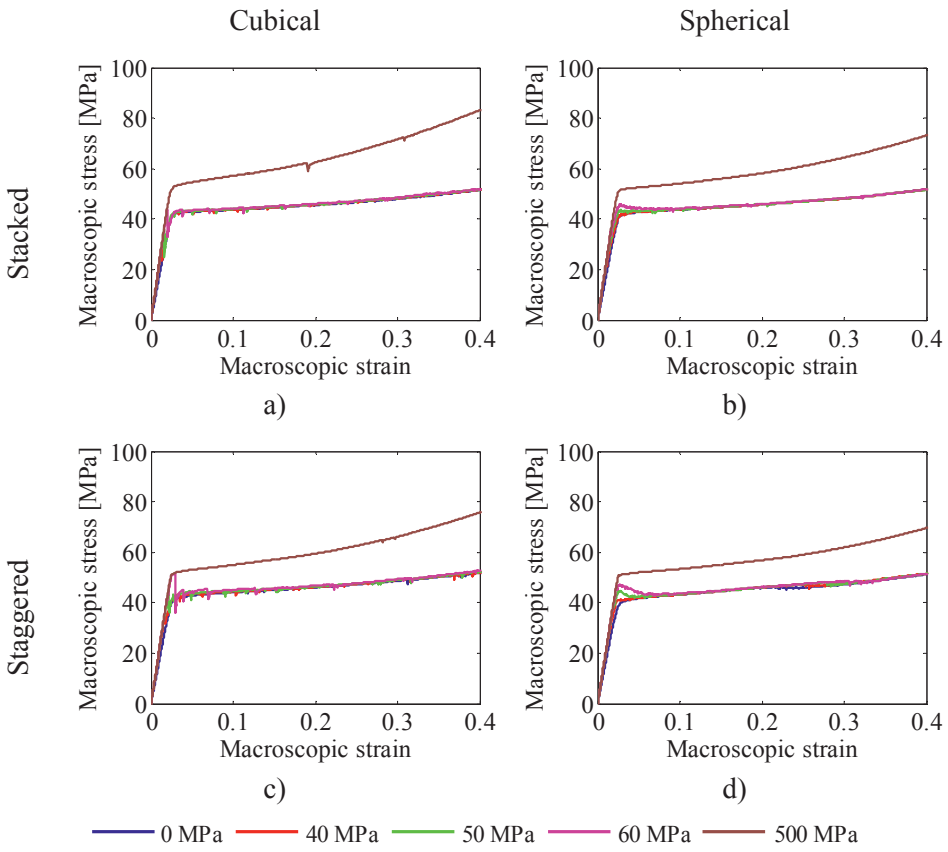

Figure 9.8 *Macroscopic stress-strain curves for the unit cell models with particle volume fraction $\omega = 0.1$. a) Cubical particles in a stacked array. b) Spherical particles in a stacked array. c) Cubical particles in a staggered array. d) Spherical particles in a staggered array.*

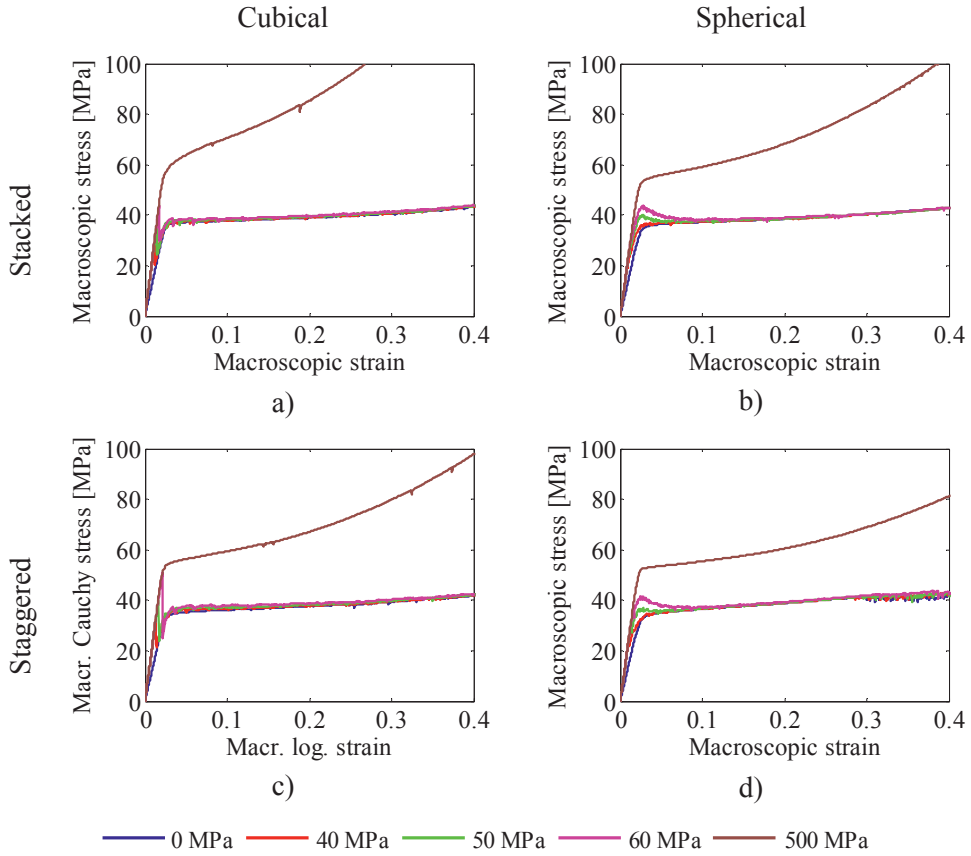

Figure 9.9 *Macroscopic stress-strain curves for the unit cell models with particle volume fraction $\omega = 0.2$. a) Cubical particles in a stacked array. b) Spherical particles in a stacked array. c) Cubical particles in a staggered array. d) Spherical particles in a staggered array.*

Contour plots of equivalent plastic strain and pressure, as provided by LS-DYNA, from a selection of unit cell models are displayed in Figure 9.10 to Figure 9.14. In these plots the particles are blanked. Thus, the plots address the surface of the matrix material adjacent to the particle. Further, the unit cells are mirrored four times in order to give a better visualization of the strain and stress fields in the matrix around the void.

Plasticity in the matrix can occur locally around the particle before the macroscopic yield stress is reached. This can be seen in the sub-figure a) in Figure 9.11, Figure 9.12 and Figure 9.13, which all are plotted just before reaching the maximum of the macroscopic stress-strain curve. Sub-figure c) in the same figures shows that only local plasticity is observed also some time after the stress peak is passed.

Both the unbonded and the bonded particles induce localization of plastic strain in the unit cell models. Plasticity sets in at equator for the spherical particles not bonded to the matrix, see Figure 9.10. Particles with stronger particle-matrix interface strengths, which are shown in Figure 9.11 to Figure 9.14, initiate plastic strain somewhat closer to the pole. The cubical particles initiate plastic strain in the matrix around the sharp edge of the particle.

There seems to be a gradual debonding process of the spherical particles. Debonding always starts at the pole of the particle. It is initiated due to high normal stress. As the deformation proceeds a "debonding zone" moves towards equator and the failure becomes more characterized by shear. As the particles debond from the matrix, a relocation of negative pressure (stress triaxiality) happens. The maximum negative pressure is located around the equator of the unbonded particles, see Figure 9.10. A zone of maximum negative pressure moves from the pole towards the equator of the bonded particles in Figure 9.11, Figure 9.12 and Figure 9.13.

The cubical particles, see Figure 14, experience a more sudden debonding; their two planes orthogonal to the loading direction lose their contact with the matrix almost simultaneously. The four other surfaces of the cube fail in shear subsequently.

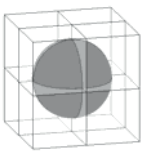

$\omega = 0.2$

$\sigma_{n,crit} = \sigma_{s,crit} = 0$ MPa

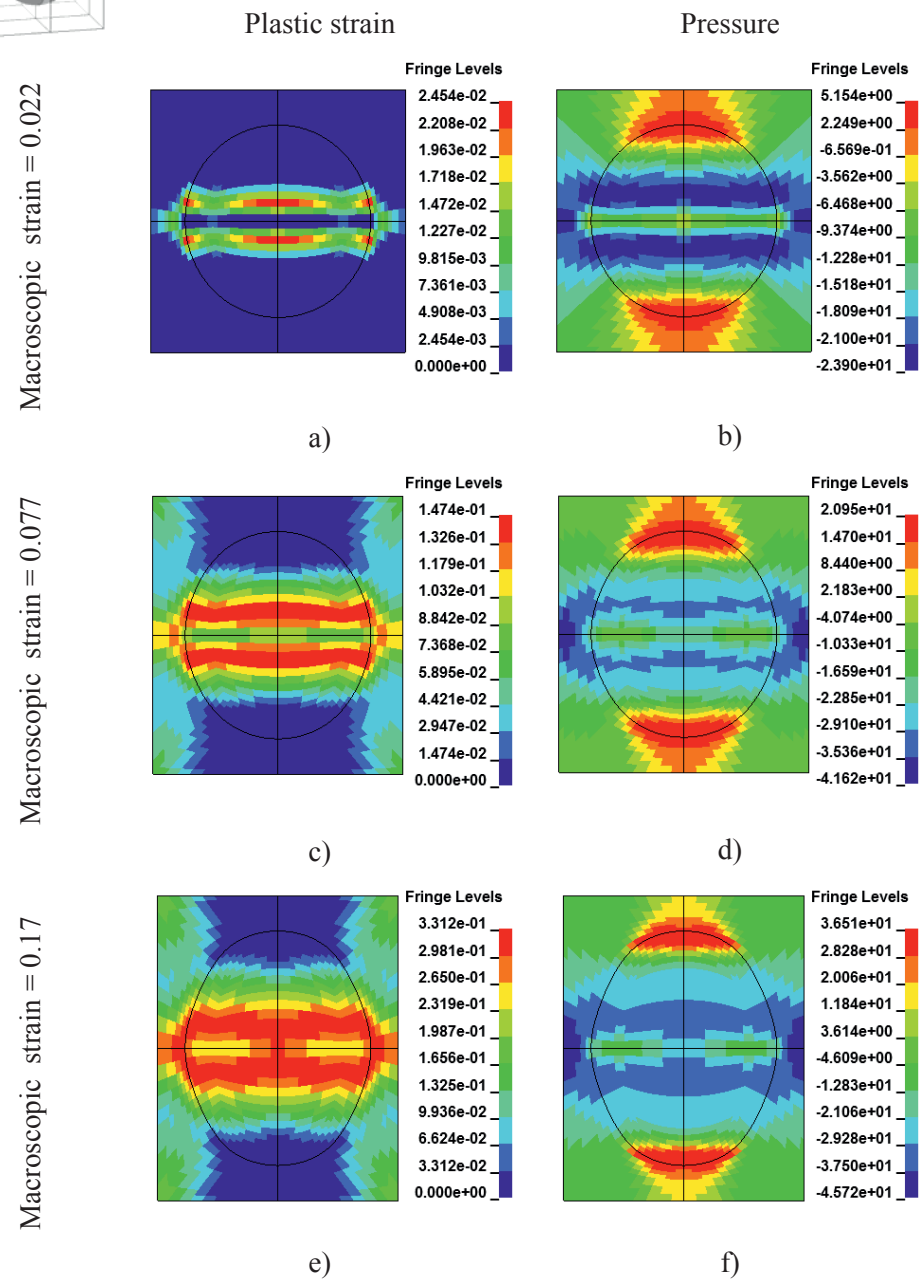

Figure 9.10 *Contour plots of plastic strain and pressure in the matrix around spherical particles organized in a stacked array without any particle-matrix interface strength. The particle volume fraction is $\omega = 0.2$. The unit cell is mirrored four times to better show the result.*

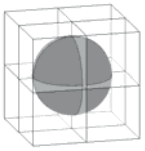

$\omega = 0.2$

$\sigma_{n,crit} = \sigma_{s,crit} = 60$ MPa

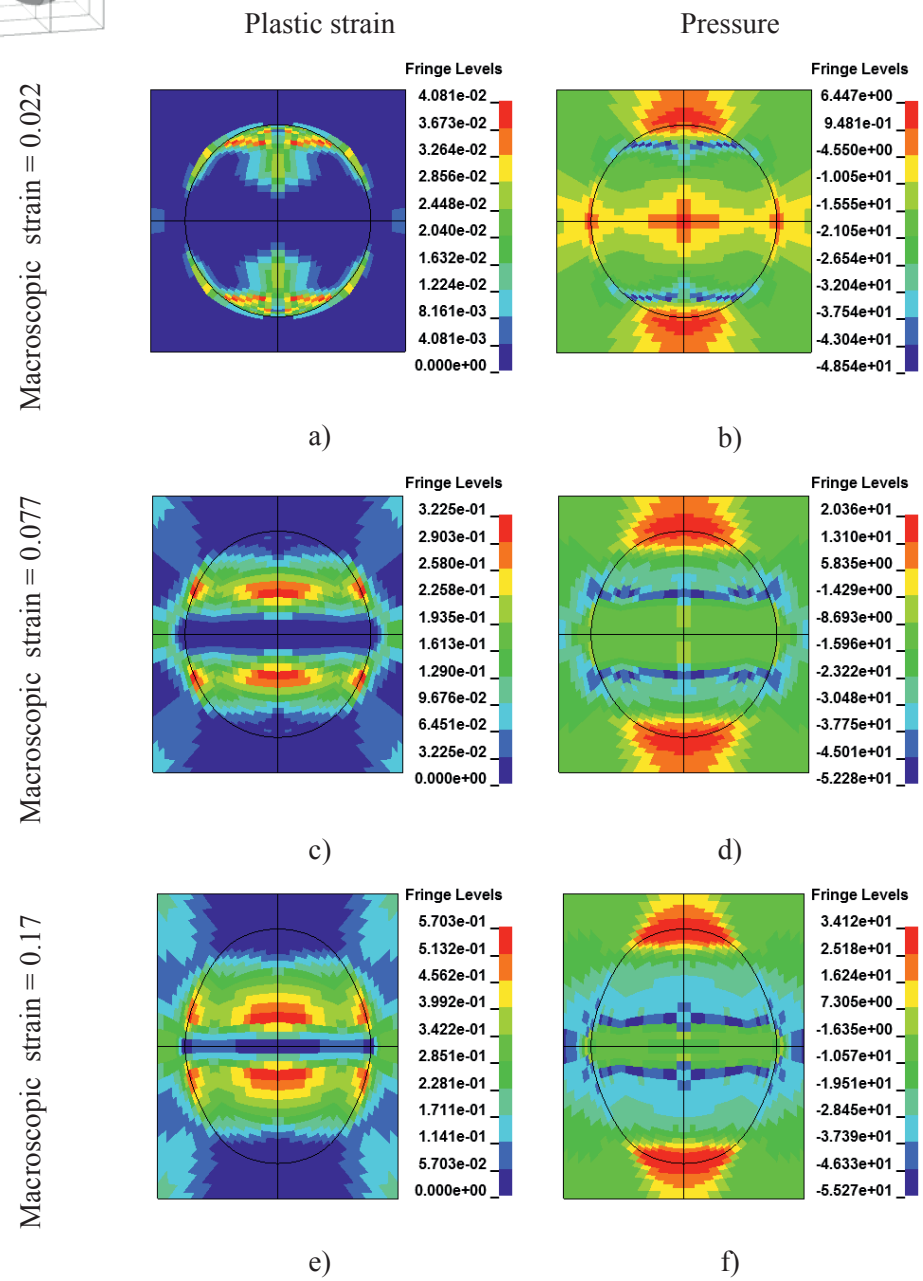

Figure 9.11 *Contour plots of plastic strain and pressure in the matrix around spherical particles organized in a stacked array with particle-matrix interface strength of 60 MPa. The particle volume fraction is $\omega = 0.2$. The unit cell is mirrored four times to better show the result.*

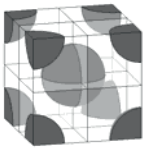

$\omega = 0.2$

$\sigma_{n,crit} = \sigma_{s,crit} = 60$ MPa

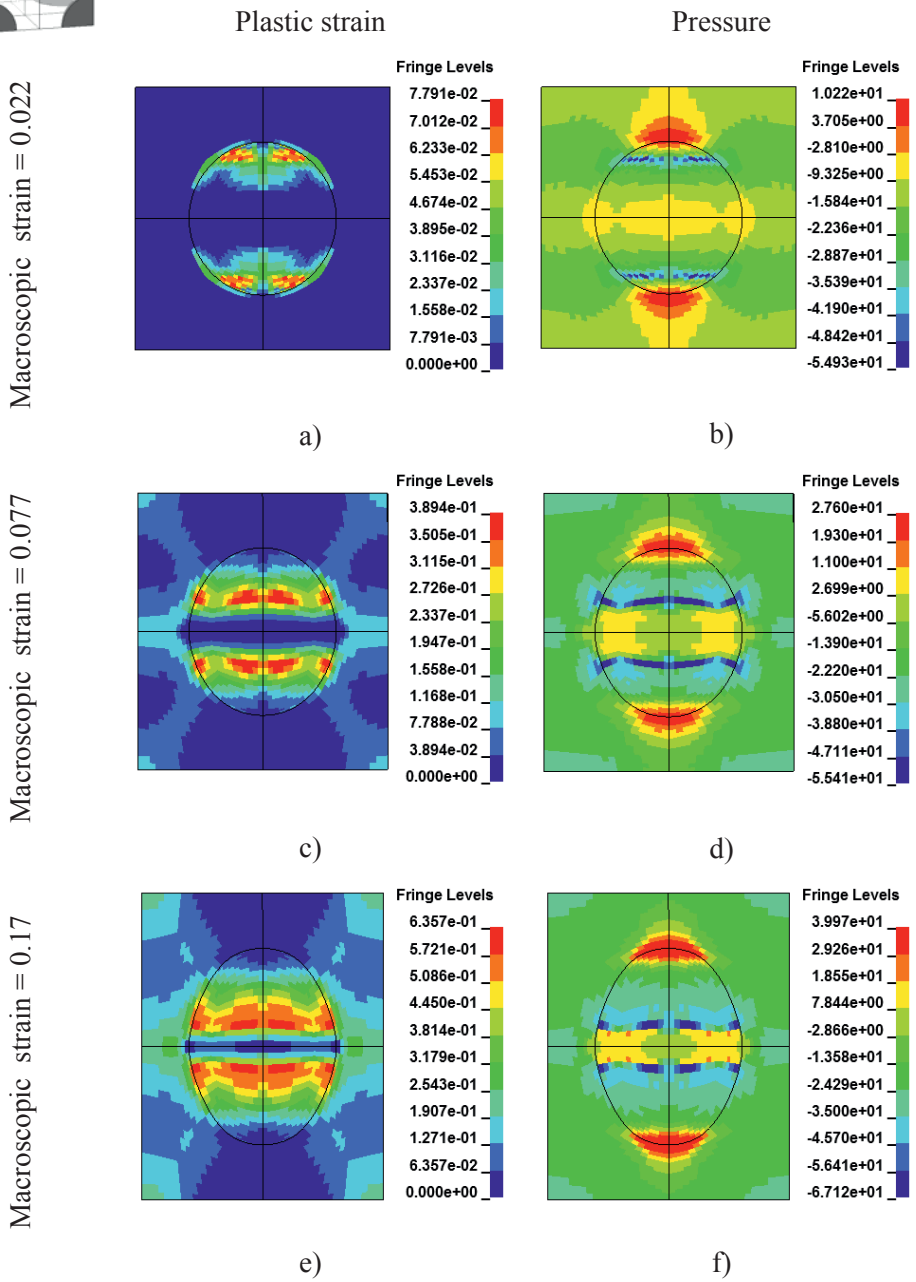

Figure 9.12 *Contour plots of plastic strain and pressure in the matrix around spherical particles organized in a staggered array with particle-matrix interface strength of 60 MPa. The particle volume fraction is $\omega = 0.2$. The unit cell is mirrored four times to better show the result.*

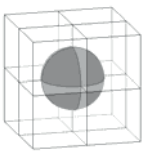

$\omega = 0.1$

$\sigma_{n,crit} = \sigma_{s,crit} = 60$ MPa

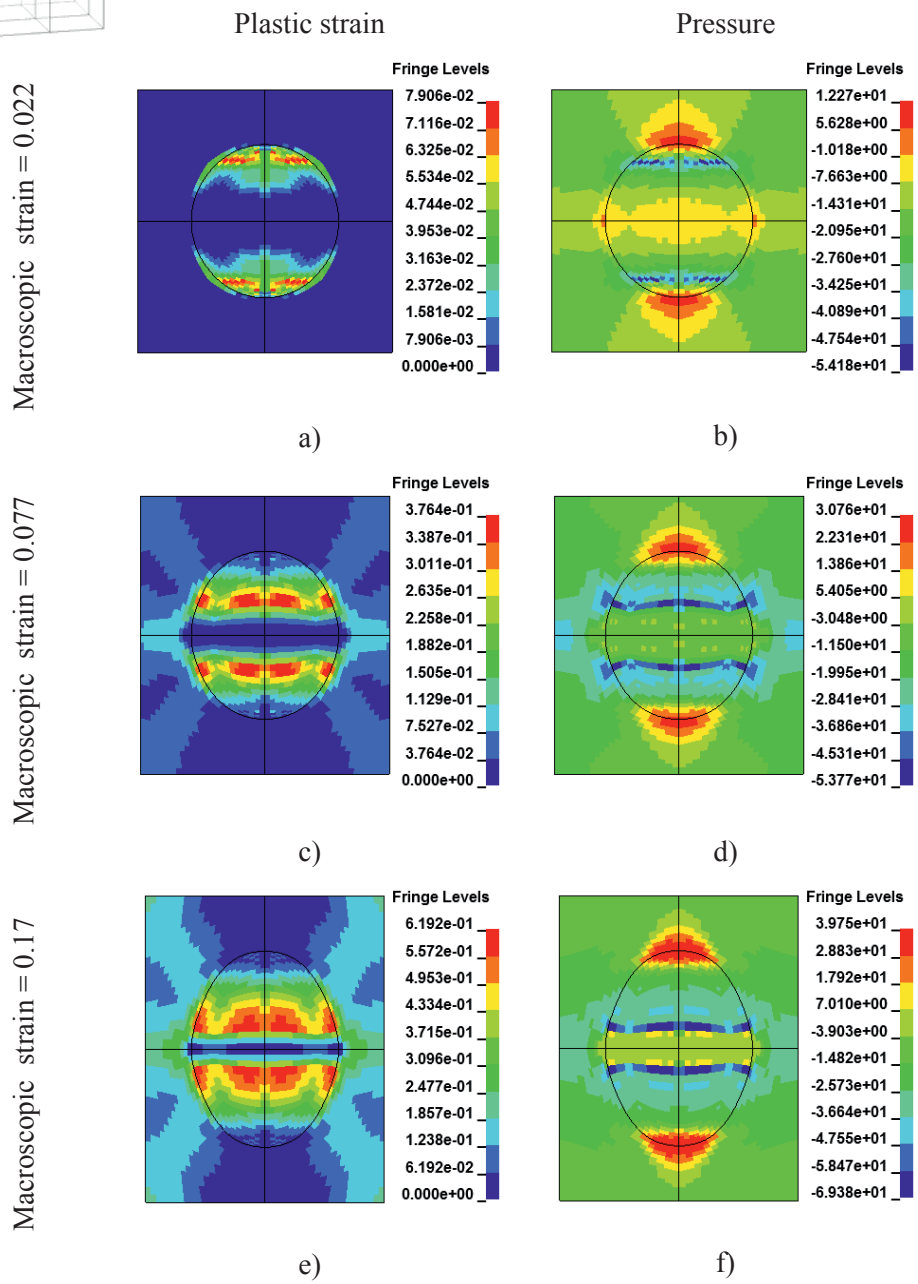

Figure 9.13 *Contour plots of plastic strain and pressure in the matrix around spherical particles organized in a stacked array with particle-matrix interface strength of 60 MPa. The particle volume fraction is $\omega = 0.1$. The unit cell is mirrored four times to better show the result.*

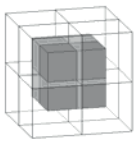

$\omega = 0.2$

$\sigma_{n,crit} = \sigma_{s,crit} = 60$ MPa

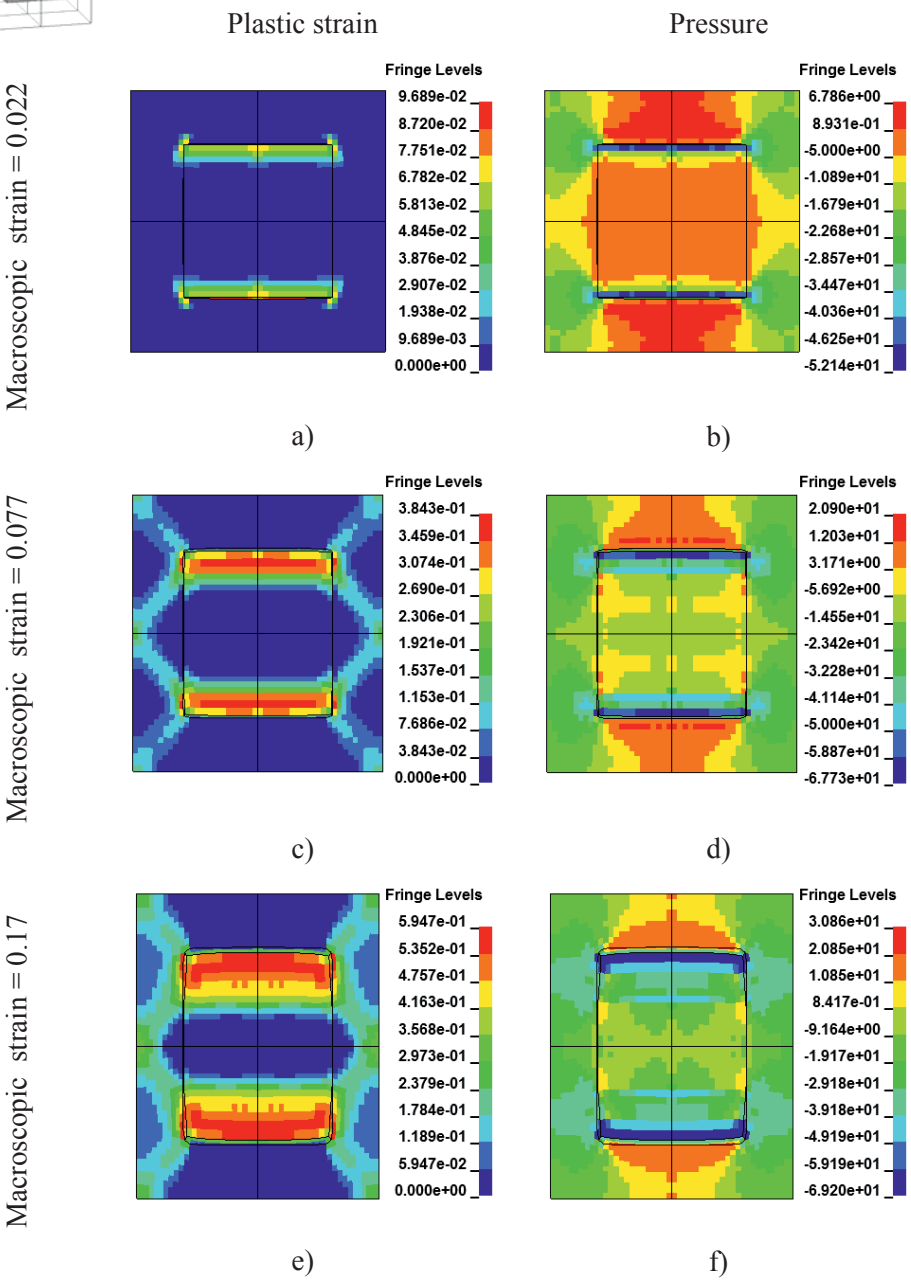

Figure 9.14 *Contour plots of plastic strain and pressure in the matrix around cubical particles organized in a stacked array with particle-matrix interface strength of 60 MPa. The particle volume fraction is $\omega = 0.2$. The unit cell is mirrored four times to better show the result.*

Figure 9.15 shows the void growth around a spherical particle with volume fraction of $\omega = 0.2$ in a stacked array. This unit cell model represented in this picture was modelled without any interface strength between the particle and the matrix. The other unit cells with initially debonded particles showed similar behaviour. Void growth around a cubical particle is displayed in Figure 9.16. Also this figure represents a unit cell with particle volume fraction of $\omega = 0.2$, a staggered array and no particle-matrix interface strength. Both Figure 9.15 and Figure 9.16 clearly show how voids grow around the particles. The void growth leads to increase of volume strain on the macroscale also in the plastic regime.

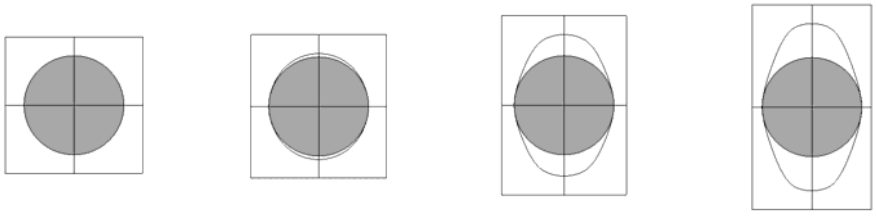

a) b) c) d)

Figure 9.15 *Outline of void growth around a spherical particle of $\omega = 0.2$ in a staggered array without any interface strength to the matrix at different macroscopic logarithmic strains: a) 0, b) 0.049, c) 0.27 and, d) 0.41.*

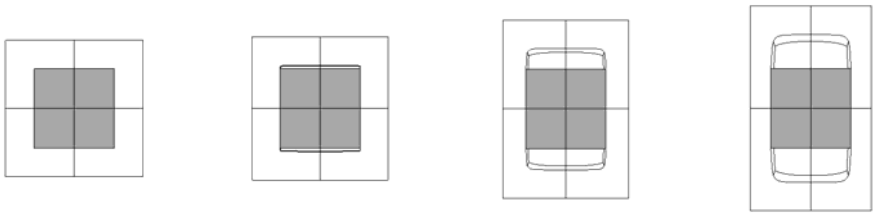

a) b) c) d)

Figure 9.16 *Outline of void growth around a cubical particle of $\omega = 0.2$ in a staggered array without any interface strength to the matrix at different macroscopic logarithmic strains: a) 0, b) 0.04, c) 0.27, and d) 0.41.*

The macroscopic volume strains from the unit cell simulations are plotted in Figure 9.17 and Figure 9.18 representing particle volume fractions $\omega = 0.1$ and $\omega = 0.2$, respectively. Note that towards the end of the deformations some penetration is

observed in the numerical simulations causing the volume strain to decline. The highest content of particles leads to the highest volume strains. Also the cubical particle shape and the staggered arrangement seem to cause most macroscopic dilation. These figures further suggest that the increase of particle volume fraction from $\omega = 0.1$ to $\omega = 0.2$ affects the void growth around cubical particles more than the spherical ones.

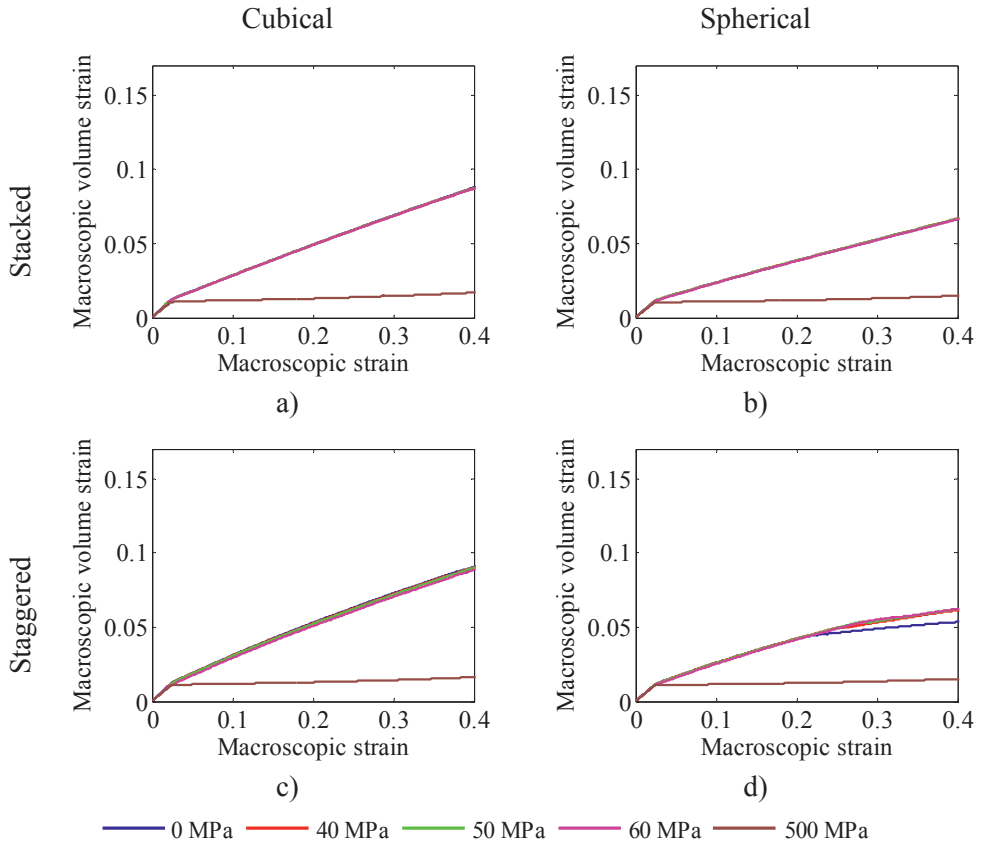

Figure 9.17 *Macroscopic volume strain for the unit cell models with particle volume fraction $\omega = 0.1$. a) Cubical particles in a stacked array. b) Spherical particles in a stacked array. c) Cubical particles in a staggered array. d) Spherical particles in a staggered array.*

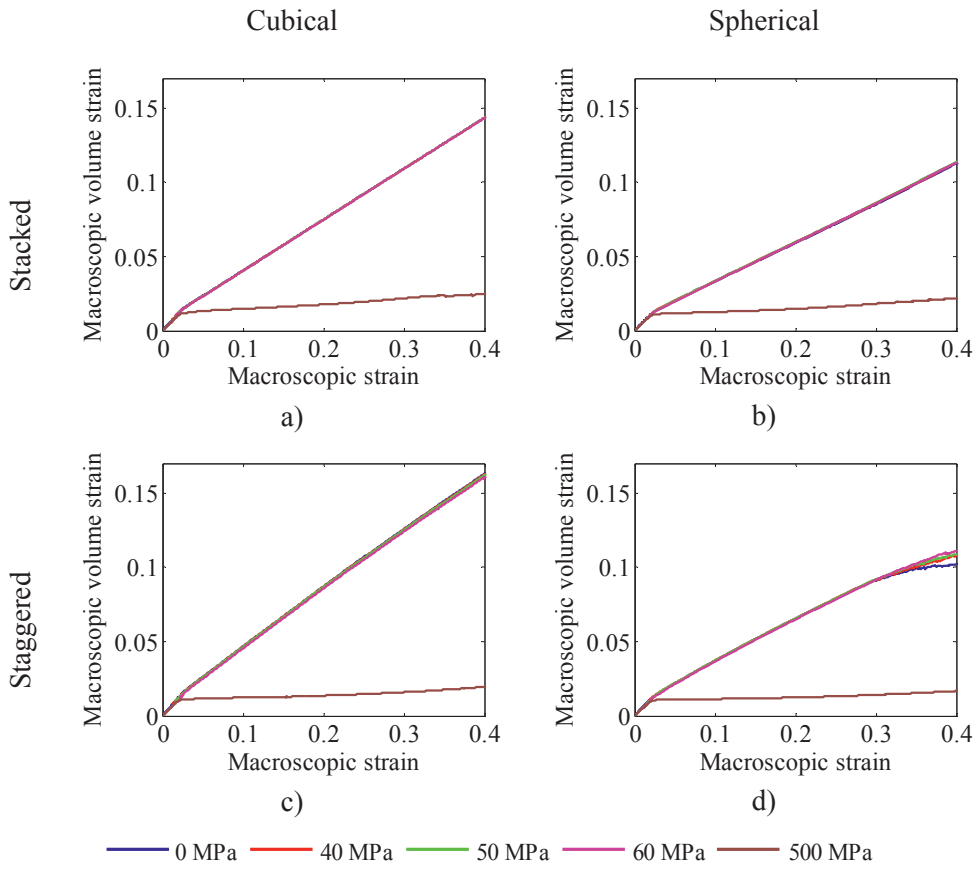

Figure 9.18 *Macroscopic volume strain for the unit cell models with particle volume fraction $\omega = 0.2$. a) Cubical particles in a stacked array. b) Spherical particles in a stacked array. c) Cubical particles in a staggered array. d) Spherical particles in a staggered array.*

Figure 9.19 and Figure 9.20 display the volume change in terms of the retraction ratio $\rho = -\varepsilon_2 / \varepsilon_1$. This quotient corresponds to Poisson's ratio in the elastic domain. It provides an alternative representation of the dilation process.

Voids are growing around the unbonded particles from the very beginning of the deformation, therefore the retraction ratio for these models initially have a low value. On the contrary, no voids are allowed to form around the perfectly bonded particles. The initial value of ρ lies in between the elastic Poisson's ratios for the matrix and the particles. At the onset of yielding, the retraction ratio increases radically since the only contribution then is from the Poisson's ratio of the particles.

For the models with intermediate interface strengths it is seen that when a particle debonds from the matrix, there is a drop in the retraction ratio, i.e. an increase of volume. During plastic deformation there is some increase in the retraction ratio. Owing to the void growth, however, it is still far below 0.5, which corresponds to an isochoric response.

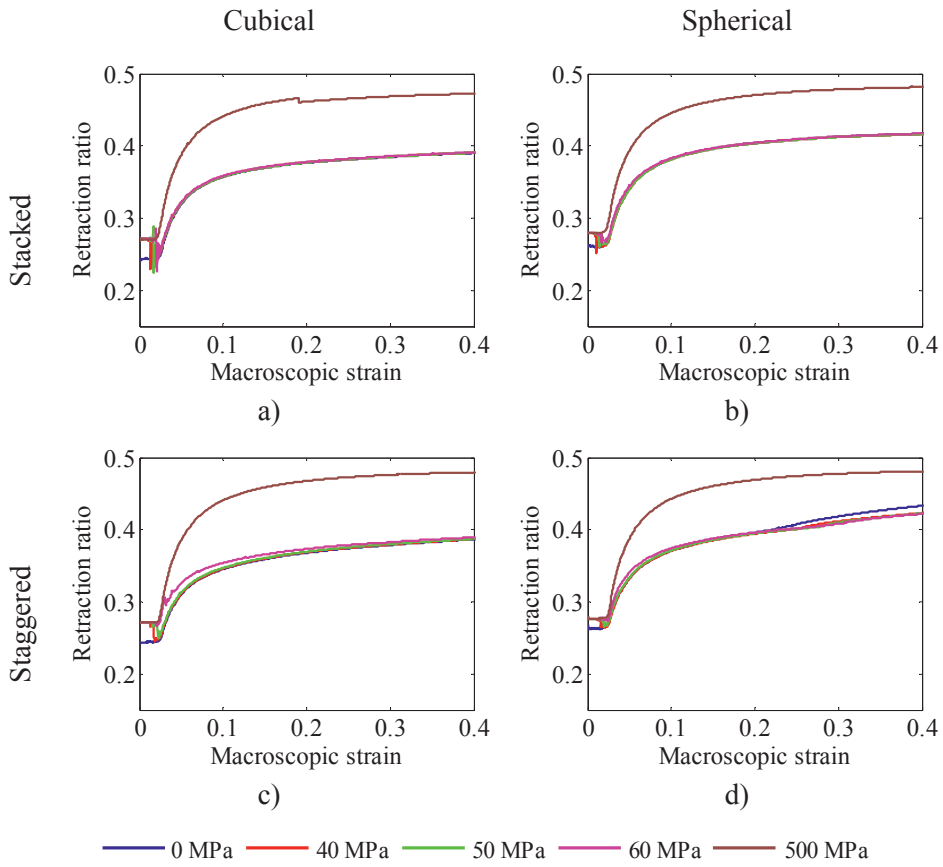

Figure 9.19 *Retraction ratio for the unit cell models with particle volume fraction $\omega = 0.1$. a) Cubical particles in a stacked array. b) Spherical particles in a stacked array. c) Cubical particles in a staggered array. d) Spherical particles in a staggered array.*

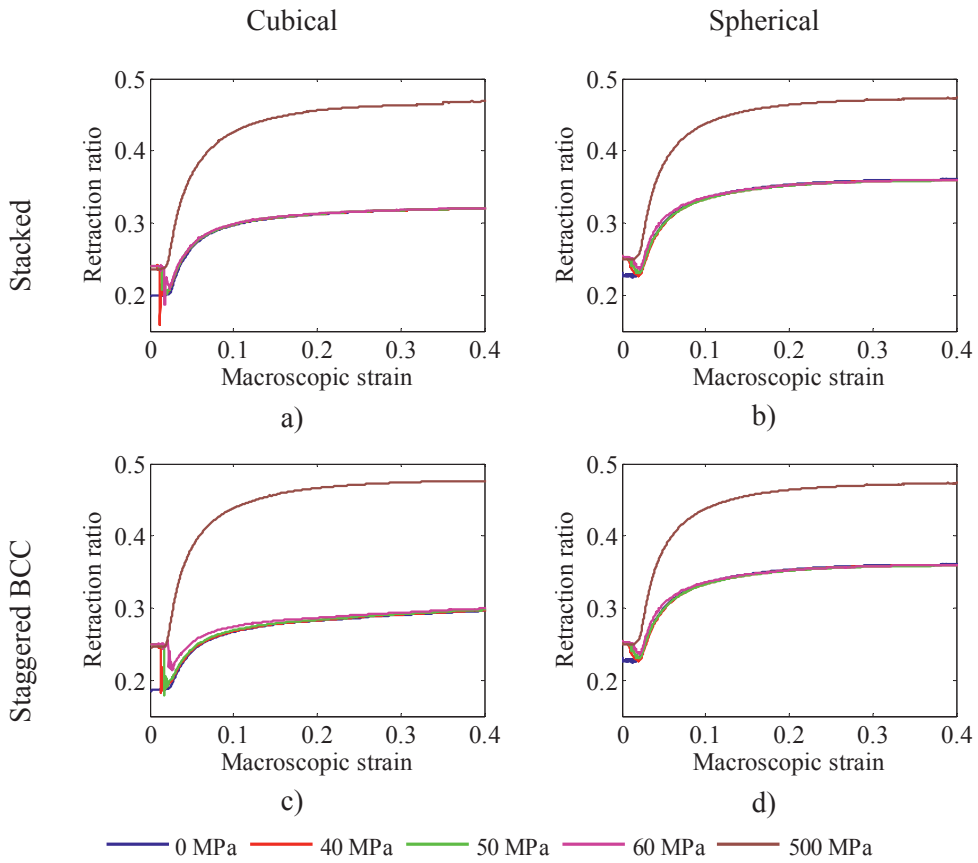

Figure 9.20 *Retraction ratio for the unit cell models with particle volume fraction $\omega = 0.2$. a) Cubical particles in a stacked array. b) Spherical particles in a stacked array. c) Cubical particles in a staggered array. d) Spherical particles in a staggered array.*

Figure 9.21 and Figure 9.22 seek to provide an improved impression of the physics in the debonding process. These figures pay attention to the beginning of the deformation process, and show the macroscopic Cauchy stress together with the retraction ratio.

The initiation of the debonding process can be observed as softening of the stress-strain curve and a decline of the retraction ratio curve. The onset of softening is observed at the same time that LS-DYNA reports activation of the first tiebreak, meaning that the debonding process has begun. This occurs at relatively small strains. It is also seen that when the stress-strain curve passes its local maximum value, the retraction ratio starts to increase.

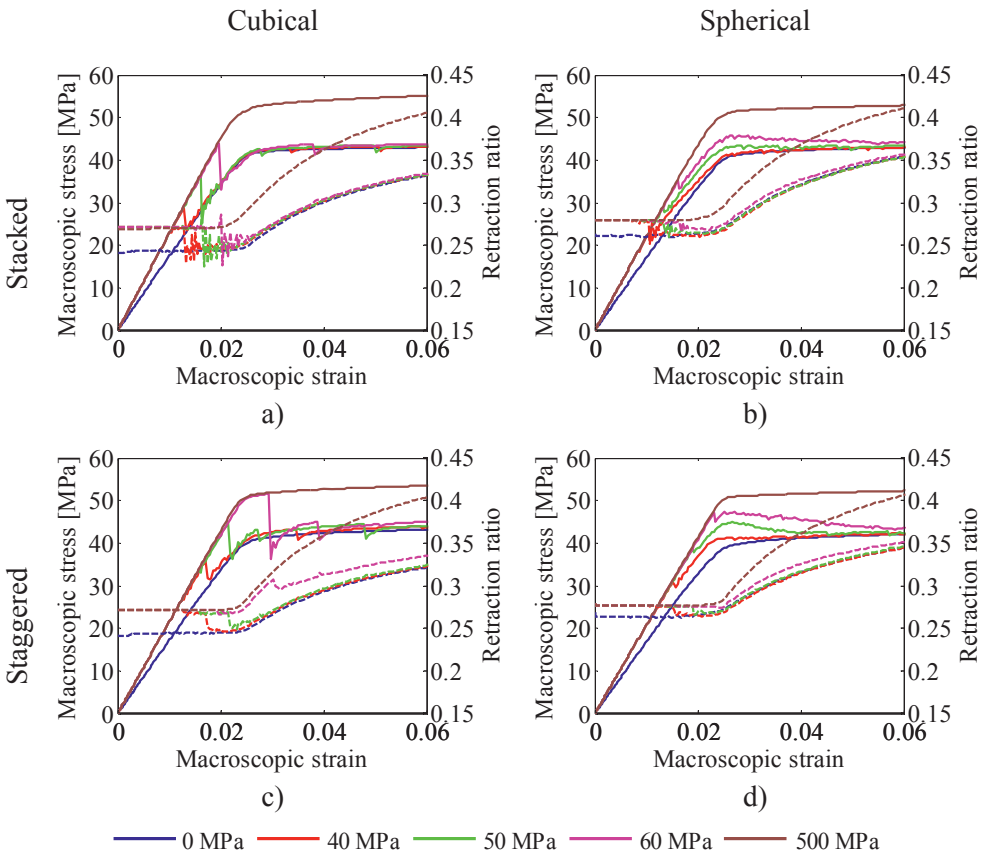

Figure 9.21 *Stress-strain curves (continuous lines) plotted together with retraction ratios (dashed lines) of models of particle volume fraction ω=0.1. a) Cubical particles in a stacked array. b) Spherical particles in a stacked array. c) Cubical particles in a staggered array. d) Spherical particles in a staggered array.*

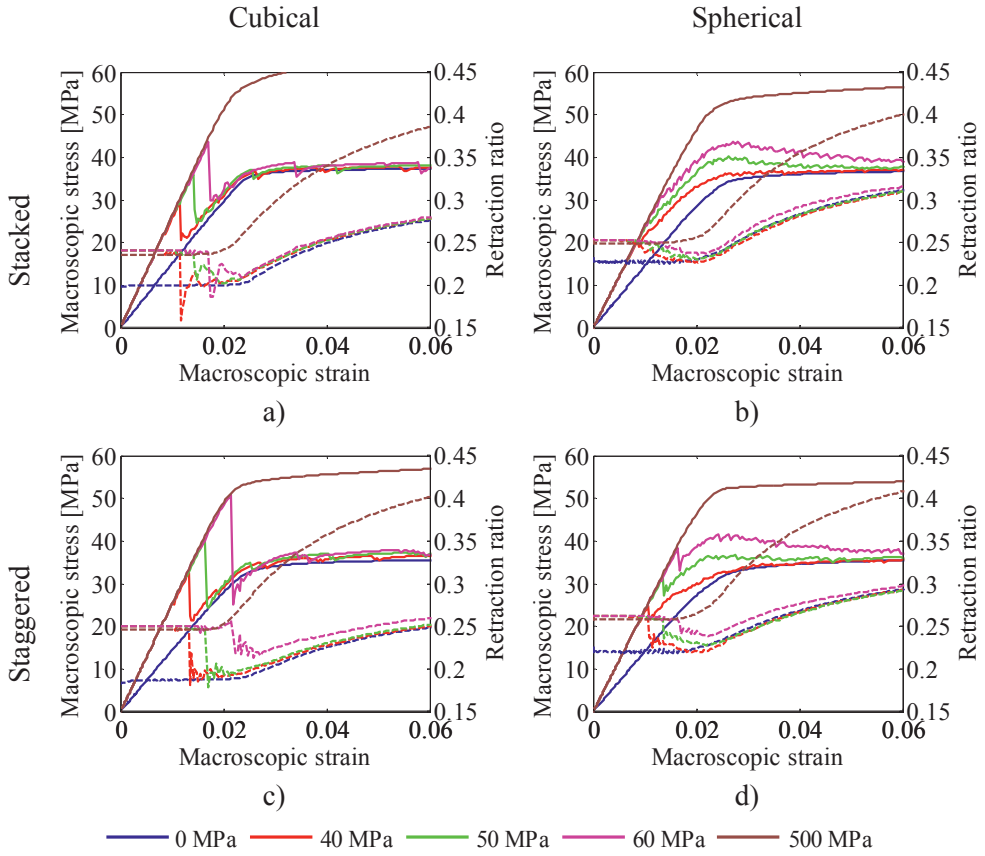

Figure 9.22 *Stress-strain curves (continuous lines) plotted together with retraction ratios (dashed lines) of models of particle volume fraction ω=0.2. a) Cubical particles in a stacked array. b) Spherical particles in a stacked array. c) Cubical particles in a staggered array. d) Spherical particles in a staggered array.*

9.7 DISCUSSION

Despite the simplifications regarding constitutive modelling and geometric representation, several of the characteristics observed in the experimental tests of the mineral filled PVC, see Chapter 6, can also be found in the results from these unit cell simulations. Similar to the PVC in the experiments some of the unit cell models show a rather linear behaviour up to a stress maximum. The stress maximum is, in both cases, followed by a drop and subsequently by a plateau with almost constant stress. Plastic dilation of about the same order is observed both in laboratory tests, as seen in Chapter 6 and in this micromechanical numerical study. Moreover, SEM study of the microstructure of the laboratory test specimens in Chapter 6 and the contour plots of the deformation of the unit cell models, see

Figure 9.10 to Figure 9.14, both conclude that the volume change is related to void growth.

The first softening of the stress-strain curve appears simultaneously with the breaking of the first of the tied nodes in the contact formulation. A similar observation is reported by van Dommelen et al. [9] in their numerical study. This suggests that the softening effect may be a result of particle debonding., also in the laboratory tests.

In many cases, the particle debonds before the macroscopic stress in the unit cell model has reached 50 MPa, i.e. the yield stress of the matrix material. Thus, the composite material has a lower yield stress than in the matrix material. This is seen from comparing the macroscopic stress-strain curves from the unit cell models in Figure 9.8 and Figure 9.9 with the stress-strain curve used to model the PVC matrix in Figure 9.6. Moreover it is seen that presence of particles that debond from the matrix reduces the macroscopic strain hardening effect of the composite. The reduction of strain hardening seems to increase with the particle volume fraction.

Comparison of the results from unit cells containing 10% and 20% particles shows that a higher content of particles increases the initial stiffness of all the unit cells containing bonded particles. At the same time, the highest fraction of particles decreases the stiffness for unit cells with unbonded particles. The stress plateaus observed after debonding are at a lower stress level for the unit cell models with high particle volume fraction. Hence, the load drop appears more dramatic.

The cubical particles seem to provoke a sudden debonding compared to the spherical particles. They also seem to induce more plastic dilation. Also particles organized in a staggered array seem to promote marginally higher dilation than particles in a stacked array. This might be because the voids in the staggered array are organized in such way that they can grow easier without influence from the neighbouring particles. The staggered arrangement causes a larger distance between the particles, a property pointed out to be important for the deformation [1, 8].

The decreasing tendency of the retraction ratio ρ in the beginning of the deformation is assumed to be an effect of debonding and void growth. When the particle in the model is completely debonded, the retraction ratio is not further reduced. The local minimum value in the retraction ratio plots occurs at a lower strain than observed in the experiments reported in Chapter 6. In the unit cell models discussed in this chapter the minimum value of the retraction ratio occurs at the onset of macroscopic yielding while it in the laboratory tests is observed some

time after macroscopic yielding. An important difference between the numerical and the laboratory tests is that in the numerical unit cell model, the particle geometry and arrangement is crudely idealized by a part of a particle. When this part of the particle has debonded, the whole debonding process is over. The retraction ratio of the real composite is in the experiment measured for a volume containing a lot of particles of different sizes and shapes dispersed randomly through the material. As a consequence, the debonding process in the real material can be in progress over a longer period of time.

It is seen from the contour plots in Figure 9.10 to Figure 9.14 that even though the macroscopic strain level is relatively low, comparably high local plastic strains develop between the particles.

Figure 9.10 to Figure 9.14 also reveal that the stress field of the matrix is highly triaxial. It shows that even if the applied load is uniaxial, a triaxial stress field rises on the microscale. The PVC composite in this study has a pressure sensitive behaviour, see Chapter 2.8. We do not know whether the pressure sensitivity is affected by the presence of particles, or if it is a material property of the matrix material only. Therefore, the pressure sensitivity of the matrix was omitted in this study.

The constitutive behaviour of the matrix material is very simplified in this unit cell study. PVC is known to be a material sensitive to strain rate. In the unit cell models, the flow around the particles is not uniform. Some locations in the material are deformed faster than others. This might affect the results. Also, the matrix enclosing the particles may have another morphology and different mechanical behaviour than the rest of the matrix. Van Dommelen el al. [9] included such an effect in terms of local anisotropy in their RVE model representing a semicrystalline polymer with stiff particles. In this study it is not taken into account.

Smit et al. [13] studied the mechanical response of a polycarbonate (PC) matrix possessing stress softening constitutive response containing voids in regular and irregular arrays. They showed that while voids organized in a regular pattern caused a stress softening effect also for the macroscopic level, the stress softening disappeared in the more complex unit cell representing voids in an irregular array. Even though the fundamentals of the study performed by Smit et al. [13] are very different from ours, and the results can therefore not be directly transferred, it is worth to note how the arrangement can alter the macroscopic response. In particular, it should be noted that the periodic arrangements of particles in this study induce layers of yielded and easier deformable material in a regular pattern that is unrealistic for a real composite.

9.8 CONCLUDING REMARKS

- Despite crude idealizations, several of the mechanical characteristics observed in experimental tests are observed in the results from the numerical study.

- The numerical simulations result in macroscopic dilation as a result of void growth. The dilation in the unit cell model is in the same order as measured in uniaxial tension of mineral filled PVC in Chapter 6.

- Stress softening is observed even though none of the materials in the composite is modelled with such behaviour. The stress softening is related to loss of material strength in the composite due to debonding of particles.

- Matrix-particle debonding in the numerical model leads to the presence of a peak stress in the macroscopic stress-strain curve. The local maximum of the stress-strain curve observed in laboratory tests may also be imposed by debonding of particles.

REFERENCES

[1] S. Socrate, M.C. Boyce. Micromechanics of toughened polycarbonate. *Journal of the Mechanics and Physics of Solids*, **48** (2000), 233-273.

[2] T. Seelig, E. van der Giessen. Localized plastic deformation in ternary polymer blends. *International Journal of Solids and Structures*, **39** (2002), 3505-3522.

[3] K.G.W. Pijnenburg, E. van der Giessen. Macroscopic yield in cavitated polymer blends. *International Journal of Solids and Structures*, **38** (2001), 3575-3598.

[4] A.C. Steenbrink, E. van der Giessen, P.D. Wu. Void growth in glassy polymers. *Journal of the Mechanics and Physics of Solids*, **45** (1997), 405-437.

[5] V. Delhaye. Behaviour and modelling of polymers for crash applications. Doctoral thesis, Department of Structural Engineering, NTNU, (2010).

[6] A.C. Steenbrink, E. van der Giessen. On cavitation, post-cavitation and yield in amorphous polymer–rubber blends. *Journal of the Mechanics and Physics of Solids*, **47** (1999), 843-876.

[7] P. Hempel, A. Hillenberg, T. Seelig. Micromechanical modeling of talc particle reinforced thermoplastic polymers. *Proceedings in Applied Mathematics and Mechanics (PAMM)*, **10** (2010), 293-294.

[8] I. Kemal, A. Whittle, R. Burford, T. Vodenitcharova, M. Hoffman. Toughening of unmodified polyvinylchloride through the addition of nanoparticulate calcium carbonate. *Polymer*, **50** (2009), 4066-4079.

[9] J.A.W. van Dommelen, W.A.M. Brekelmans, F.P.T. Baaijens. A numerical investigation of the potential of rubber and mineral particles for toughening of semicrystalline polymers. *Computational Materials Science*, **27** (2003), 480-492.

[10] LS-DYNA. LS-DYNA Keyword User's Manual. Version 971, Livermore Software Technology Corporation (LSTC), 2007.

[11] C. G'Sell, J.M. Hiver, A. Dahoun, A. Souahi. Video-controlled tensile testing of polymers and metals beyond the necking point. *Journal of Materials Science*, **27** (1992), 5031-5039.

[12] P.H.T. Vollenberg, D. Heikens. The mechanical properties of chalk-filled polypropylene: a preliminary investigation. *Journal of Materials Science*, **25** (1990), 3089-3095.

[13] R.J.M. Smit, W.A.M. Brekelmans, H.E.H. Meijer. Prediction of the large-strain mechanical response of heterogeneous polymer systems: local and global deformation behaviour of a representative volume element of voided polycarbonate. *Journal of the Mechanics and Physics of Solids*, **47** (1999), 201-221.

CHAPTER 10

NUMERICAL SIMULATIONS OF THE BEHAVIOUR OF THERMOPLASTICS

In order to carry out realistic numerical simulations of the behaviour of polymer components, a constitutive model that captures the main deformation features is required. Yet, a material model for industrial use has to be "user friendly" without too demanding calibration procedures. This chapter presents a constitutive model for polymer materials proposed by Polanco-Loria et al. [1]. The model is intended for industrial use, involving large scale finite element analysis of polymer components undergoing large deformations. This chapter also addresses identification of material parameters from the uniaxial tension and compression tests of the 5 mm plates of PVC and HDPE presented in Chapter 3 and Chapter 4.

10.1 INTRODUCTION

The deformation of thermoplastic polymers commonly involves large elastic and plastic deformations. Their mechanical response is in general sensitive to strain rate and temperature. Polymers are often regarded as pressure sensitive materials; a higher yield strength in compression than in tension is commonly observed. Another feature is that the volume changes during plastic deformation [2-6]. Moreover, some polymers have a stress softening behaviour after the yield limit, while others experience monotonic hardening [6, 7]. These are some characteristics a material model for thermoplastics should allow for. Based on the original idea of Haward and Thackray [8], Polanco-Loria et al. [1] presented a constitutive model separating the response in two parts describing the intermolecular resistance and the molecular network resistance. The constitutive model includes the pressure dependent Raghava yield criterion [9, 10].

A procedure for determination of the parameters of the constitutive model has been developed and performed by Hovden [11]. Hovden determined the parameters for the 10 mm thick extruded plates of PVC and HDPE. According to the producer, the plates of the two thicknesses, 10 mm and 5 mm, are made of the same materials. However, experimental tests showed some minor difference in the response between the plates. Therefore, a new determination of the material parameters for the 5 mm thick plates is required, calling for some extra material tests. The material tests used for the parameter identification were presented in Chapter 3 and Chapter 4.

10.2 CONSTITUTIVE MODEL FOR THERMOPLASTICS

The hyperelastic-viscoplastic material model presented by Polanco-Loria et al. [1] consists of two parts coupled in parallel. Part A represents an intermolecular barrier to deformation while Part B represents the network stretching. An outline of the model is shown in Figure 10.1.

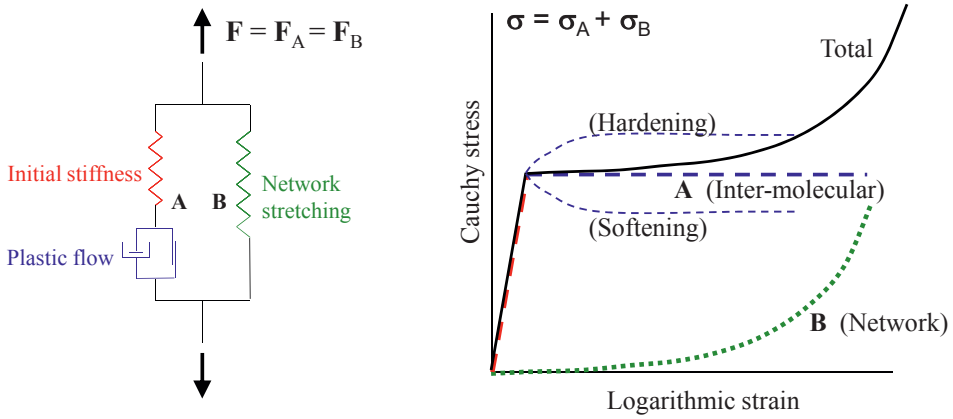

Figure 10.1 *a) Rheological representation of the constitutive model with inter-molecular (A) and network (B) contributions, and b) stress contributions from Part A and Part B.*

The main kinematic variable in the model is the deformation gradient $\mathbf{F}$. It is equal for Part A and Part B: $\mathbf{F} = \mathbf{F}_A = \mathbf{F}_B$. This means also the volume change, the determinant of the deformation gradient, is the same for the two parts:

$J_A = J_B = J = \det \mathbf{F}$. The total Cauchy stress $\boldsymbol{\sigma}$ is taken as the sum of the stress contributions from the two parts

$$\boldsymbol{\sigma} = \boldsymbol{\sigma}_A + \boldsymbol{\sigma}_B \tag{10.1}$$

Part A describes a hyperelastic-viscoplastic response due to intermolecular resistance. A multiplicative split is used to decompose the deformation gradient of Part A into elastic and plastic components: $\mathbf{F}_A = \mathbf{F}_A^e \cdot \mathbf{F}_A^p$. The decomposition produces three configurations: the reference configuration Ω_0, the virtual, intermediate configuration, $\bar{\Omega}_A$, and the current configuration Ω. An illustration of the kinematics is given in Figure 10.2.

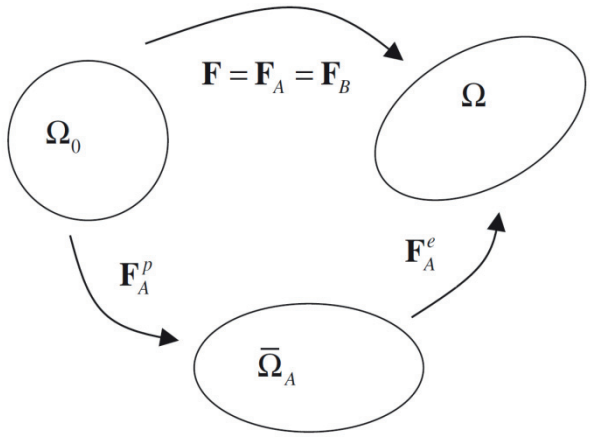

Figure 10.2 *Conceptual illustration of the kinematics of the constitutive model. It shows the decomposition of the deformation gradient* $\mathbf{F}$ *in the reference configuration* Ω_0*, the intermediate configuration* $\bar{\Omega}_A$ *and the current configuration is* Ω *[1].*

The intermediate configuration, defined by the plastic part of the deformation gradient, $\mathbf{F}_A^p$, is invariant to the rigid body rotations of the current configuration. The evolution of the intermediate configuration is defined by the differential equation $\dot{\mathbf{F}}_A^p = \bar{\mathbf{L}}_A^p \cdot \mathbf{F}_A^p$, where $\bar{\mathbf{L}}_A^p$ is the plastic velocity gradient with respect to the intermediate configuration.

A Neo-Hookean model is used to allow for large elastic deformations

$$\boldsymbol{\tau}_A = \lambda_0 \ln J_A^e \mathbf{I} + \mu_0 [\mathbf{B}_A^e - \mathbf{I}] \tag{10.2}$$

where $\boldsymbol{\tau}_A = J_A^e \boldsymbol{\sigma}_A$ is the Kirchhoff stress, $J_A^e = \det \mathbf{F}_A^e$ is the elastic part of the Jacobian, $\mathbf{I}$ is the second-order unit tensor, and $\mathbf{B}_A^e = \mathbf{F}_A^e \cdot (\mathbf{F}_A^e)^T$ is the elastic left Cauchy-Green deformation tensor. The Lamé constants λ_0 and μ_0 are used to define the elastic response. They can also be expressed by Young's modulus E and Poisson's ratio ν

$$E = \frac{\mu_0 (3\lambda_0 + 2\mu_0)}{\lambda_0 + \mu_0}, \qquad \nu = \frac{\lambda_0}{2(\lambda_0 + 2\mu_0)} \tag{10.3}$$

The viscoplastic contribution of Part A is computed on the intermediate configuration, applying the Mandel stress tensor $\bar{\boldsymbol{\Sigma}}_A$. The relationships between the Kirchhoff and Mandel stress tensors read $\boldsymbol{\tau}_A = (\mathbf{F}_A^e)^{-T} \cdot \bar{\boldsymbol{\Sigma}}_A \cdot (\mathbf{F}_A^e)^T$ and $\bar{\boldsymbol{\Sigma}}_A = (\mathbf{F}_A^e)^T \cdot \boldsymbol{\tau}_A \cdot (\mathbf{F}_A^e)^{-T}$. Note that the Mandel stress tensor is symmetric due to the assumed isotropy of the material. The yield criterion is formulated as $f_A = \bar{\sigma}_A - \sigma_T - R = 0$. The Raghava equivalent stress $\bar{\sigma}_A$ is used to express pressure dependency [9]

$$\bar{\sigma}_A = \frac{(\alpha - 1) I_{1A} + \sqrt{(\alpha - 1)^2 I_{1A}^2 + 12 \alpha J_{2A}}}{2\alpha} \tag{10.4}$$

where $I_{1A} = \operatorname{tr} \bar{\boldsymbol{\Sigma}}_A$ and $J_{2A} = \frac{1}{2} \bar{\boldsymbol{\Sigma}}_A^{dev} : \bar{\boldsymbol{\Sigma}}_A^{dev}$ are invariants of respectively the Mandel stress tensor and the deviatoric part. The deviatoric part of the Mandel stress is defined by $\bar{\boldsymbol{\Sigma}}_A^{dev} = \bar{\boldsymbol{\Sigma}}_A - \frac{1}{3} \operatorname{tr}(\bar{\boldsymbol{\Sigma}}_A) \cdot \mathbf{I}$.

The parameter $\alpha = \sigma_C / \sigma_T$ in Equation (10.4) represents the ratio between the yield stresses in compression and tension. These two stress data provide sufficient information to define the shape of the yield surface. By setting $\alpha = 1$ we get the von Mises yield surface as a special case of the Raghava function. Further, the isotropic strain hardening or softening R of Part A, see Figure 10.1 b), is a function of the accumulated plastic strain $\bar{\varepsilon}_A^p$, and it is controlled by the saturation stress σ_S and the hardening/softening parameter H , viz.

$$R(\bar{\varepsilon}_A^p) = (\sigma_S - \sigma_T)\left[1 - \exp(-H \bar{\varepsilon}_A^p)\right] \tag{10.5}$$

A non-associated viscoplastic flow rule is assumed to define the plastic velocity gradient on the intermediate configuration as

$$\bar{\mathbf{L}}_A^p = \dot{\bar{\varepsilon}}_A^p \frac{\partial g_A}{\partial \bar{\boldsymbol{\Sigma}}_A} \tag{10.6}$$

where the plastic potential g_A is defined in the form

$$g_A = \frac{(\beta-1)I_{1A} + \sqrt{(\beta-1)^2 I_{1A}^2 + 12\beta J_{2A}}}{2\beta} \geq 0 \tag{10.7}$$

Here, β is the plastic dilation parameter, determining the increase of volume during plastic flow.

The equivalent plastic strain rate $\dot{\bar{\varepsilon}}_A^p$ of Equation (10.6) is defined by the constitutive relation

$$\dot{\bar{\varepsilon}}_A^p = \begin{cases} 0 & \text{if } f_A \leq 0 \\ \dot{\varepsilon}_{0A}\left\{\exp\left[\frac{1}{C}\left(\frac{\bar{\sigma}_A}{\sigma_T + R} - 1\right)\right] - 1\right\} & \text{if } f_A > 0 \end{cases} \tag{10.8}$$

In this expression, two rate-sensitivity parameters, $\dot{\varepsilon}_0$ and C, are introduced.

Part B of the material model describes a hyperelastic entropic resistance originally proposed by Arruda and Boyce [12]

$$\boldsymbol{\sigma}_B = \frac{C_R}{3J_B}\frac{\bar{\lambda}_L}{\bar{\lambda}}\mathcal{L}^{-1}\left(\frac{\bar{\lambda}}{\bar{\lambda}_L}\right)(\mathbf{B}_B^* - \bar{\lambda}^2\mathbf{I}) \tag{10.9}$$

where C_R is the initial elastic modulus of Part B, $\bar{\lambda}_L$ is the locking stretch, $\mathcal{L}^{-1}$ is the inverse function of the Langevin function which is defined as $\mathcal{L}(x) = \coth x - 1/x$. The Jacobian J_B is $J_B = \det \mathbf{F}_B$ (recall that $\mathbf{F} = \mathbf{F}_B$). The average total stretch ratio $\bar{\lambda}$ is calculated as

$$\bar{\lambda} = \sqrt{\frac{1}{3}\mathrm{tr}\left(\mathbf{B}_B^*\right)} \tag{10.10}$$

where $\mathbf{B}_B^* = \mathbf{F}_B^* \cdot (\mathbf{F}_B^*)^{\mathrm{T}}$ is the distortional left Cauchy-Green deformation tensor, and $\mathbf{F}_B^* = J_B^{-1/3}\,\mathbf{F}_B$ denotes the distortional part of $\mathbf{F}_B$.

The model involves 11 coefficients to be determined from uniaxial tension and compression tests. The parameters are listed in Table 10.1. Neither thermal effects or a fracture criterion is incorporated in the model. For further details about the model it is referred to Polanco-Loria et al. [1].

Table 10.1 *Material parameters.*

E	Young's modulus [MPa]
v	Poisson's ratio
σ_T	Yield stress in uniaxial tension [MPa]
σ_s	Saturation stress [MPa]
α	Pressure sensitivity parameter
β	Plastic dilation parameter
$\dot{\varepsilon}_{0A}$	Reference strain rate [s^{-1}]
C	Strain rate dependency
H	Hardening/softening parameter
C_R	Initial elastic modulus of Part B [MPa]
$\overline{\lambda}_L$	Locking stretch

10.3 PARAMETER IDENTIFICATION

As already mentioned, the parameters of the 5 mm plates of PVC and HDPE have to be identified. To limit the extent of the identification process the Poisson's ratio v, the pressure sensitivity α, the plastic dilation parameter β and the strain rate dependency C are assumed to be the same as for the 10 mm thick plates and as determined by Hovden [11]. Therefore one tensile test and one compression test of

each material are sufficient to determine the remaining parameters: Young's modulus E, the yield stress σ_T, the saturation stress σ_S, the ramping parameter H of the isotropic hardening/softening function, the reference strain rate $\dot{\varepsilon}_{0A}$, the initial elastic modulus of Part B C_R and the locking stretch $\overline{\lambda}_L$. The tensile and compression tests presented in Chapter 3 and Chapter 4 are used as a basis for the parameter identification.

Starting with Part A, the Young's modulus E for both materials is defined as the initial slope of the stress-strain curve. Since the stress state of Part A is affected by strain rate and also the stress of Part B, the yield stress σ_T and the saturation stress σ_S cannot be taken directly from the stress-strain curves in Chapter 3. Therefore a preliminary yield stress σ_{T0} and a preliminary saturation stress σ_{S0} are determined first. The preliminary values, denoted with a sub-script '0', represent the stress at the reference strain rate $\dot{\varepsilon}_{0A}$ without any correction from the stress contribution of Part B. The preliminary yield stress σ_{T0} for PVC is taken as the first local maximum of the stress-strain curve. The HDPE material does not show any obvious maximum point. Therefore, the 0.2% offset from the initial slope is used to define σ_{T0}. Further, the local stress minimum on the true stress-strain curve for PVC is taken as a preliminary saturation stress, σ_{S0}. Since HDPE have no softening, the Considère construction [13] is used for determining σ_{S0} for this material.

The reference strain rate $\dot{\varepsilon}_{0A}$ represents the local strain rate present in the sample when the stress approaches σ_{T0}. It is for both materials set equal to the slope of the strain-time curve, determined by digital image correlation, at the instant where the stress is equal to σ_{T0}.

At onset of plasticity the hardening/softening term in Equation (10.5) is $R = 0$. Equation (10.8) can then be re-arranged into

$$\overline{\sigma}_A = \sigma_T \left\{ 1 + C \ln\left(\frac{\dot{\overline{\varepsilon}}_A^p}{\dot{\varepsilon}_{0A}} + 1 \right) \right\} \tag{10.11}$$

Disregarding the contribution from Part B, the preliminary yield stress σ_{T0} measured in the material test is equal to the Raghava equivalent stress $\overline{\sigma}_A$ at the reference strain rate $\dot{\varepsilon}_{0A}$. In other words $\overline{\sigma}_A = \sigma_{T0}$ when $\dot{\varepsilon}_{0A} = \dot{\overline{\varepsilon}}_A^p$. This means that, at the reference strain rate, Equation (10.11) can be expressed as

$$\sigma_T = \frac{\sigma_{T0}}{1 + C\ln(2)} \tag{10.12}$$

Now the yield stress σ_T at a fictitious strain rate equal to zero can be found. Also the saturation stress for the hypothetical case of zero strain rate can be found from Equation (10.11) employing the strain rate present at σ_{S0}. Subsequently, σ_T and σ_S also have to be adjusted by the stress contribution of Part B.

The ramping parameter H controls the stress evolution towards the saturation stress. It defines the slope between σ_T and σ_S, see Equation (10.5)

According to Equation (10.5) the exact saturation stress will only be approached, never fully reached. Defining a target plastic strain ε_S^p that is equal to the plastic strain at the saturation stress and demanding a 95% attainment of the saturation can be a first step in the determination of H. In other words, we require an amount of softening R equal to 95% of the difference between σ_S and σ_T.

$$R(\varepsilon_S^p) = 0.95(\sigma_S - \sigma_T) \tag{10.13}$$

Combining Equation (10.5) and Equation (10.13) H can then be determined from

$$1 - \exp(-H\varepsilon_S^p) = 0.05 \tag{10.14}$$

The result is

$$H = -\frac{\ln(0.05)}{\varepsilon_S^p} \tag{10.15}$$

Turning the attention to Part B, it is first convenient to isolate the Part B stress from the stress strain curve obtained in the laboratory test. Equation (10.9) produces a deviatoric stress state with the transverse stresses $\sigma_{B2} = \sigma_{B3} = -\frac{1}{2}\sigma_{B1}$ even for uniaxial deformation [11]. However, in uniaxial tension the total transverse stress should be zero, i.e $\sigma_{A2} + \sigma_{B2} = 0$ .The transverse stresses in Part B must thus be counteracted by Part A

$$\sigma_{A2} = \sigma_{A3} = -\sigma_{B2} = \frac{1}{2}\sigma_{B1} \tag{10.16}$$

This again leads to a change in σ_{A1}, which in next turn affects the Raghava equivalent stress $\bar{\sigma}_A$ of Equation (10.4). In the elastic regime, the counteracting stress from Part B is neglected. Taking the yield criterion into account in the plastic regime, Hovden [11] expressed the stress in Part A as

$$\sigma_{A1} = \frac{\bar{\sigma}}{k_1} + \frac{1}{2}\sigma_{B1}\frac{k_2}{k_1} \tag{10.17}$$

where k_1 and k_2 are functions of α

$$k_1 = \frac{1}{\sqrt{\alpha}} + \frac{\alpha - 1}{2\alpha}, \qquad k_2 = \frac{1}{\sqrt{\alpha}} - \frac{\alpha - 1}{\alpha} \tag{10.18}$$

Hovden further assumed $\bar{\sigma}$ in Equation (10.17) to be defined by the previously identified parameters. This stress can be denoted σ_A^{par}. The observed stress σ^{test} in the uniaxial tension test can then be expressed as the sum of the longitudinal Part A and Part B stresses [11]

$$\sigma^{test} = \sigma_{A1} + \sigma_{B1} = \frac{\sigma_A^{par}}{k_1} + \sigma_{B1}\left(1 + \frac{k_2}{2k_1}\right) \tag{10.19}$$

From Equation (10.19) the Part B stress can be isolated and employed for determination of the Part B parameters [11]

$$\sigma_{B1} = \left(\frac{2k_1}{2k_1 + k_2}\right)\left(\sigma^{test} - \frac{\sigma_A^{par}}{k_1}\right) \tag{10.20}$$

There is no analytical expression of the inverse Langevin function of Part B. An approximation proposed by Padé [14] reads

$$\mathcal{L}^{-1}(x) \cong x\frac{3 - x^2}{1 - x^2} \tag{10.21}$$

By using Equation (10.21) and assuming a uniaxial stress state and transverse isotropy, the longitudinal stress σ_{B1} of Part B can be expressed by the initial stiffness C_R of Part B and the locking stretch $\bar{\lambda}_L$ [11].

$$\sigma_{B1} = \frac{2}{9}J^{-\frac{5}{3}}C_R \cdot \frac{3\bar{\lambda}_L^2 - \bar{\lambda}^2}{\bar{\lambda}_L^2 - \bar{\lambda}^2}\left(\lambda_1^2 + \lambda_2^2\right) \tag{10.22}$$

In this expression J is the Jacobian determinant $J = \det(\mathbf{F})$ and λ_1 and λ_2 are the stretch ratios in the longitudinal and transverse directions respectively. The effective distortional stretch is $\bar{\lambda} = \sqrt{\frac{1}{3} J^{-\frac{2}{3}} (\lambda_1^2 + 2\lambda_2^2)}$.

The locking stretch $\bar{\lambda}_L$ can also be expressed by a locking strain ε_L [11]

$$\bar{\lambda}_L = \sqrt{\frac{1}{3}\left[\exp\left(\frac{4}{3}\varepsilon_L (1+\rho) \right) + 2\exp\left(-\frac{2}{3}\varepsilon_L (1+\rho) \right) \right]} \qquad (10.23)$$

The retraction ratio ρ represents the average value of the ratio between longitudinal and transverse strain $-\varepsilon_2 / \varepsilon_1$ in the plastic domain. The locking strain ε_L represents the upper limit strain of the progressive strain hardening of the polymer. It is not straightforward to determine. However, from examination of the stress-strain curves a trial value of ε_L can be found. Then, by Equation (10.23) also a trial value for $\bar{\lambda}_L$ is found. The retraction ratios found by Hovden [11] of ρ = 0.32 and ρ = 0.47 are used in turn for PVC and HDPE. Applying the trial values, both C_R and $\bar{\lambda}_L$ are found by curve fitting.

10.4 THE MATERIAL PARAMETERS

The material parameters determined for the 5 mm plates of mineral filled PVC are listed in Table 10.2 while the parameters for 5 mm plates of HDPE are given in Table 10.3. Both tables present all 11 material parameters for each material, including those found by Hovden [11].

Table 10.2 *Material parameters for 5 mm thick extruded plates of mineral filled PVC.*

E [MPa]	ν	$\dot{\varepsilon}_{0A}$ [s^{-1}]	C	σ_T [MPa]	C_R [MPa]
1800	0.3	0.00100	0.0700	47.3	4.40
$\bar{\lambda}_L$	α	β	σ_S [MPa]	H	
1.87	1.3	1.27	38.0	16.0	

Table 10.3 *Material parameters for 5 mm thick extruded plates of HDPE.*

E [MPa]	ν	$\dot{\varepsilon}_{0A}$ [s^{-1}]	C	σ_T [MPa]	C_R [MPa]
450	0.4	0.00045	0.1080	12.1	1.20
$\overline{\lambda}_L$	α	β	σ_S [MPa]	H	
3.00	1.0	1.04	19.0	24.0	

The material parameters found by Hovden [11] for the 10 mm plates of mineral filled PVC and HDPE are listed in Table 10.4 and Table 10.5.

Table 10.4 *Material parameters for 10 mm thick extruded plates of mineral filled PVC. The parameters are determined by Hovden [11].*

E [MPa]	ν	$\dot{\varepsilon}_{0A}$ [s^{-1}]	C	σ_T [MPa]	C_R [MPa]
3000	0.3	0.00100	0.0700	46.8	5.50
$\overline{\lambda}_L$	α	β	σ_S [MPa]	H	
1.92	1.3	1.27	37.8	15.0	

Table 10.5 *Material parameters for 10 mm thick extruded plates of HDPE. The parameters are determined by Hovden [11].*

E [MPa]	ν	$\dot{\varepsilon}_{0A}$ [s^{-1}]	C	σ_T [MPa]	C_R [MPa]
800	0.4	0.00070	0.1080	13.0	1.74
$\overline{\lambda}_L$	α	β	σ_S [MPa]	H	
7.75	1.0	1.04	23.9	39.6	

The pressure sensitivity α and the plastic dilation parameter β determined for materials in the 10 mm plates are chosen also for the 5 mm plates. The Raghava functions defined by α and β are plotted in Figure 10.3 and Figure 10.4. Figure 10.3 shows the yield surface f_A and the flow potential g_A of PVC and HDPE in a stress space defined by the stress invariants I_1 and J_2. Figure 10.4 represents the same functions, but in a principal stress space normalized with respect to σ_T. It is clearly seen that PVC requires a higher stress to reach the yield limit in

compression than in tension. This is not the case for HDPE. Also in the plastic potential there is a clear difference between the two materials. During plastic deformation, this leads to different responses of PVC and HDPE because the gradients of the potential functions do not have the same directions in stress space.

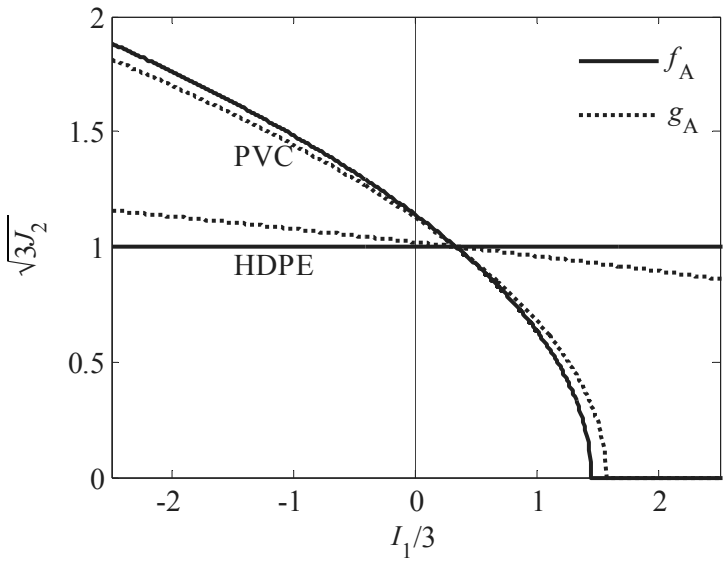

Figure 10.3 *Raghava yield function* f_A *(solid lines) and potential function* g_A *(dotted lines) for PVC and HDPE in the stress space defined by the invariants.*

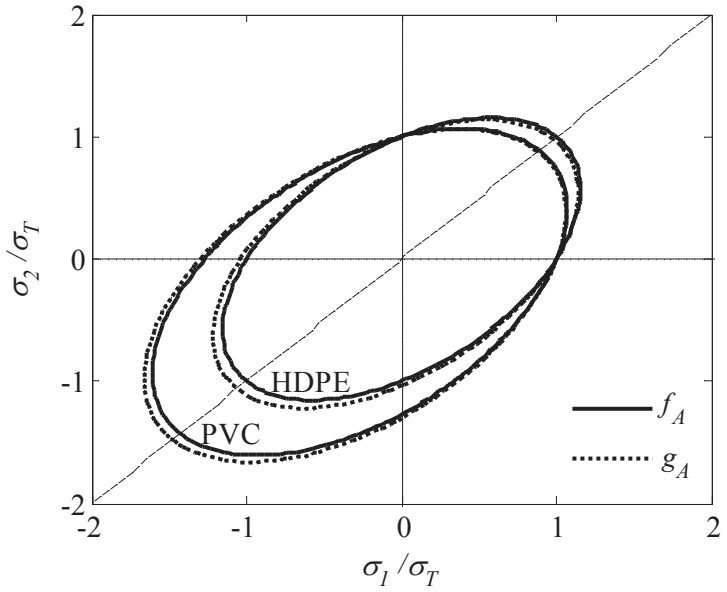

Figure 10.4 *Raghava yield function f_A (solid lines) and potential function g_A (dotted lines) for PVC and HDPE in a normalized principal stress space.*

10.5 DISCUSSION

A constitutive model for thermoplastics [1] has been introduced. The material parameters of the model can be found from uniaxial tension and compression tests. Some of the parameters for the 5 mm plates of PVC and HDPE have been identified in this chapter. The remaining parameters are taken from Hovden [11] . By comparing the stress-strain curves from the tension tests in Chapter 3 with the stress-strain curves from the compression tests in Chapter 4, this was done in figure 4.11, it is seen that the pressure sensitivity coefficients determined by Hovden [11], i.e. α = 1.3 for PVC and α = 1.0 for HDPE, fit the two materials well.

The plastic flow is determined from the gradient of the flow potential g_A . From the flow potentials plotted in Figure 10.3, it is seen that also for stress states of compression, the direction of the gradient indicates positive volume change. However, recall from Chapter 4 that the determination of volume change in the compression samples is rather uncertain. New and better compression tests should be performed before drawing any conclusions of the accuracy of the prediction of volume strain in compression.

The calibration method presented herein involves some trial and error when the curve fitting was used to find the parameters of Part B. Also, since the choice of material parameters of Part A affects the parameters of Part B, some iterations of correcting of the parameters of both parts had to be carried out. Different choices in the parameter identification process can lead to different combinations that produce similar results.

Another source of error in the calibration is that a uniaxial stress state is assumed. The experimental results used for the calibration are not representing a true uniaxial stress state since necking occurred during testing. However, the effect of this stress triaxiality is assumed to be of minor importance.

Delhaye [15] proposed a similar analytical procedure of parameter identification as done by Hovden [11]. An alternative method is by inverse modelling. Such a method has been applied by Polanco-Loria et al. [16].

REFERENCES

[1] M. Polanco-Loria, A.H. Clausen, T. Berstad, O.S. Hopperstad. Constitutive model for thermoplastics with structural applications. *International Journal of Impact Engineering*, **37** (2010), 1207-1219.

[2] F. Grytten, H. Daiyan, M. Polanco-Loria, S. Dumoulin. Use of digital image correlation to measure large-strain tensile properties of ductile thermoplastics. *Polymer Testing*, **28** (2009), 653-660.

[3] J. Mohanraj, D.C. Barton, I.M. Ward, A. Dahoun, J.M. Hiver, C. G'Sell. Plastic deformation and damage of polyoxymethylene in the large strain range at elevated temperatures. *Polymer*, **47** (2006), 5852-5861.

[4] V. Delhaye, A.H. Clausen, F. Moussy, O.S. Hopperstad, R. Othman. Mechanical response and microstructure investigation of a mineral and rubber modified polypropylene. *Polymer Testing*, **29** (2010), 793-802.

[5] V. Delhaye, A.H. Clausen, F. Moussy, R. Othman, O.S. Hopperstad. Influence of stress state and strain rate on the behaviour of a rubber-particle reinforced polypropylene. *International Journal of Impact Engineering*, **38** (2011), 208-218.

[6] R.T. Moura, A.H. Clausen, E. Fagerholt, M. Alves, M. Langseth. Impact on HDPE and PVC plates - Experimental tests and numerical simulations. *International Journal of Impact Engineering*, **37** (2010), 580-598.

[7] C. G'Sell, J.M. Hiver, A. Dahoun, A. Souahi. Video-controlled tensile testing of polymers and metals beyond the necking point. *Journal of Materials Science*, **27** (1992), 5031-5039.

[8] R.N. Haward, G. Thackray. The Use of a Mathematical Model to Describe Isothermal Stress-Strain Curves in Glassy Thermoplastics. *Proceedings of the Royal Society of London. Series A, Mathematical and Physical Sciences*, **302** (1968), 453-472.

[9] R. Raghava, R.M. Caddell, G.S.Y. Yeh. The macroscopic yield behaviour of polymers. *Journal of Materials Science*, **8** (1973), 225-232.

[10] R.S. Raghava, R.M. Caddell. Macroscopic yield criterion for crystalline polymers. *International Journal of Mechanical Sciences*, **15** (1973), 967-974.

[11] M.T. Hovden. Test and numerical simulations of polymer components. Master thesis, Department of Structural Engineering, NTNU, (2010).

[12] E.M. Arruda, M.C. Boyce. A three-dimensional constitutive model for the large stretch behavior of rubber elastic materials. *Journal of the Mechanics and Physics of Solids*, **41** (1993), 389-412.

[13] N.G. McCrum, C.B. Bucknall, C.P. Buckley. *Principles of polymer engineering.* Oxford University Press, Oxford (1997).

[14] A. Cohen. A Padé approximant to the inverse Langevin function. *Rheologica Acta*, **30** (1991), 270-273.

[15] V. Delhaye. Behaviour and modelling of polymers for crash applications. Doctoral thesis, Department of Structural Engineering, NTNU, (2010).

[16] M. Polanco-Loria, H. Daiyan, F. Grytten. Material parameters identification: An inverse modeling methodology applicable for thermoplastic materials. *Polymer Engineering & Science*, **52** (2012), 438-448.

CHAPTER 11

NUMERICAL SIMULATIONS OF UNIAXIAL TENSION AND COMPRESSION TESTS

The material parameters determined in Chapter 10 for the 5mm thick plates of PVC and HDPE are verified by employing the parameters on meshes of simple uniaxial tension and compression test specimens. In other words, it is checked whether the laboratory tests used for the parameter identification could be reproduced by numerical simulations.

11.1 INTRODUCTION

The constitutive model described in Chapter 10 has been confirmed to predict the behaviour of uniaxial tension and compression tests of polymer materials in a good way [1, 2]. The uniaxial deformation of specimens cut out from 10 mm thick sheets of mineral filled PVC and HDPE was predicted by numerical simulations by Hovden [1] by employing the material parameters determined for these materials, listed in Table 10.4 and Table 10.5. Delhaye [2] also achieved good results when using the same constitutive model, though with different material parameters, in the prediction of uniaxial response of particle-reinforced polypropylene. This chapter aims to check whether the material parameters for the 5 mm plates of PVC and HDPE, determined in Chapter 10, can reproduce the response of the uniaxial tensile tests from Chapter 3 and the uniaxial compression tests in Chapter 4.

11.2 UNIAXIAL TENSION TESTS

11.2.1 MESH

The finite element model of the uniaxial tensile specimen is shown in Figure 11.1. It was created to represent the tensile specimens used in the experimental tests presented in Chapter 3. The left and the right ends were modelled as rigid bodies. The mesh consists of 5 elements over the thickness, 12 elements in the width direction and 52 elements along the gauge part. Eight node solid elements with reduced integration [3] were used in the numerical simulations. To avoid unphysical energies from hourglass modes, a stiffness based hourglass control was employed. Mass scaling by a factor of 10^3 was used in the simulations in order to reduce the computation time. The elements marked in grey in Figure 11.1 were modelled as rigid material. After the simulations it was checked that the kinetic energy and the hourglass energy was much less than 1% of the total energy in the simulation.

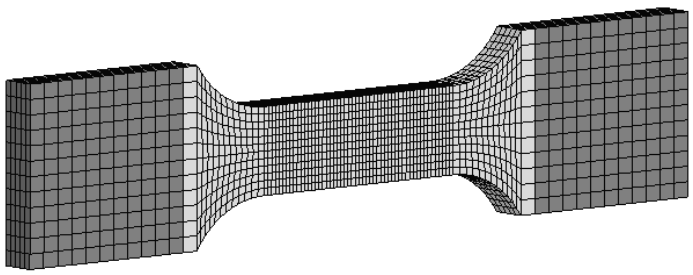

Figure 11.1 *Finite element mesh of the uniaxial tensile specimen.*

11.2.2 MATERIAL MODEL

The constitutive model proposed by Polanco-Loria et al. [4], as presented in Chapter 10 was employed for the materials. The parameters, determined from the response of 5 mm thick extruded sheets of mineral filled PVC and HDPE, are listed in Table 10.2 and Table 10.3.

11.2.3 BOUNDARY CONDITIONS

A motion corresponding to $3.3 \cdot 10^{-2}$ mm/s was applied to the right part of the finite element mesh modelled as a rigid body. This motion gives the same strain rate as in the experiments. The rigid body at the opposite end of the specimen was fixed.

11.2.4 RESULTS

The force-displacement relationships from the numerical simulations are compared with results from experiments in Figure 11.2. The solid lines represent numerical results while the dashed lines represent the results from the laboratory tests. The numerical simulation captures the initial stiffness and the peak force for PVC. The softening, however, occurs more sudden in the laboratory test than in the numerical simulation. Regarding the HDPE, the initial stiffness is somewhat softer in the experimental test than what is predicted by the simulation. The peak force is well captured also for the HPDE. During cold-drawing of HDPE there is some increase in the force level predicted by the numerical model while that from the experiment remains constant.

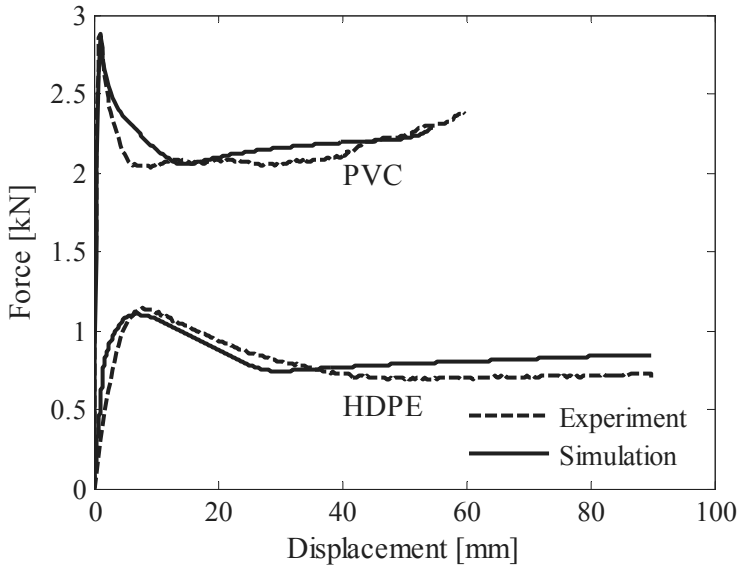

Figure 11.2 *Force-displacement curves from finite element simulations and experimental tests.*

11.3 UNIAXIAL COMPRESSION TESTS

11.3.1 MESH

The mesh of the compression test coupon is seen in Figure 11.3. It was modelled by 20 elements over the diameter and 40 elements over the height. Eight node solid elements with selectively reduced integration [5] were used to carry out the simulations. The cylindrical specimens tested in Chapter 4 differed somewhat from the drawing in Figure 4.1. The meshes were defined according to the actual geometry of the test specimens as listed in Table 11.1. The compression platens were modelled as rigid bodies employing shell elements. Mass scaling by a factor of 10^3 was used also for the compression tests without causing high levels of kinetic energy or penetration problems. After the simulations it was checked that the kinetic energy was much less than 1% of the total energy in the simulation.

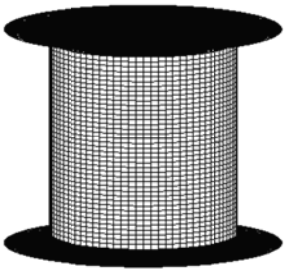

Figure 11.3 *Finite element mesh of the compression coupon between the compression platens.*

Table 11.1 *Height and diameter measures for the compression test coupons.*

	Nominal height	Nominal diameter
PVC coupon	5.09 mm	4.76 mm
HDPE coupon	5.04 mm	4.86 mm

11.3.2 MATERIAL MODEL

Again, the constitutive model [4] presented in Chapter 10 with parameters determined for the 5 mm sheets of PVC and HDPE was employed. The material parameters are listed in Table 10.2 and Table 10.3.

11.3.3 BOUNDARY CONDITIONS

A velocity corresponding to $5 \cdot 10^{-3}$ mm/s was applied the upper compression platen while the lower platen was fixed. This was to recreate the deformation imposed to the test coupon in the test. The contact formulation contact-automatic-one-way-surface-to-surface in LS-DYNA [3] was used to model the contact between the compression platens and the test specimen. Static and dynamic friction coefficients μ of 0.1, 0.05 and 0.01 were used in the contact formulation between the platens and the test coupon. After the simulations it was checked that the sliding energy remained positive during the simulations.

11.3.4 RESULTS

The force-displacement curves from the numerical simulations of PVC are compared with results from experiments in Figure 11.4. The initial response is reasonable well predicted. However, the post-yield response is overestimated.

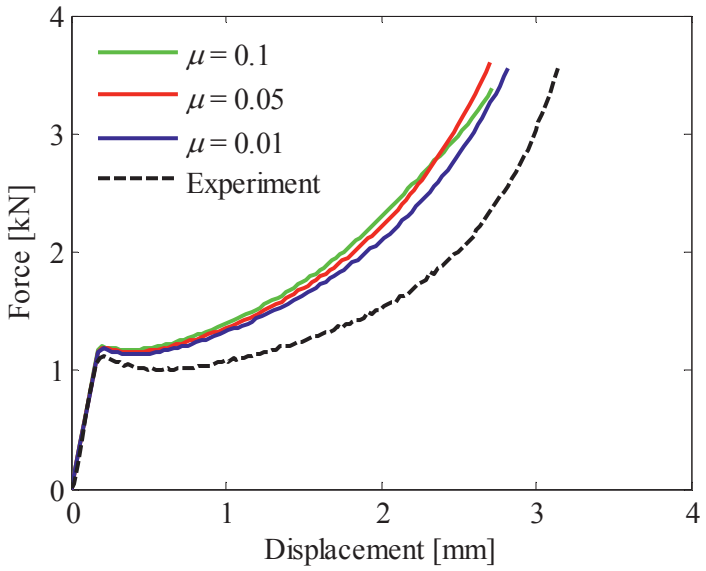

Figure 11.4 *Force-displacement curves from finite element simulations and experimental test of PVC in compression.*

Figure 11.5 shows the force-displacement curves from the HDPE simulations together with the response from the experimental test. The initial response is well captured by the numerical model. For large deformations there is some deviation.

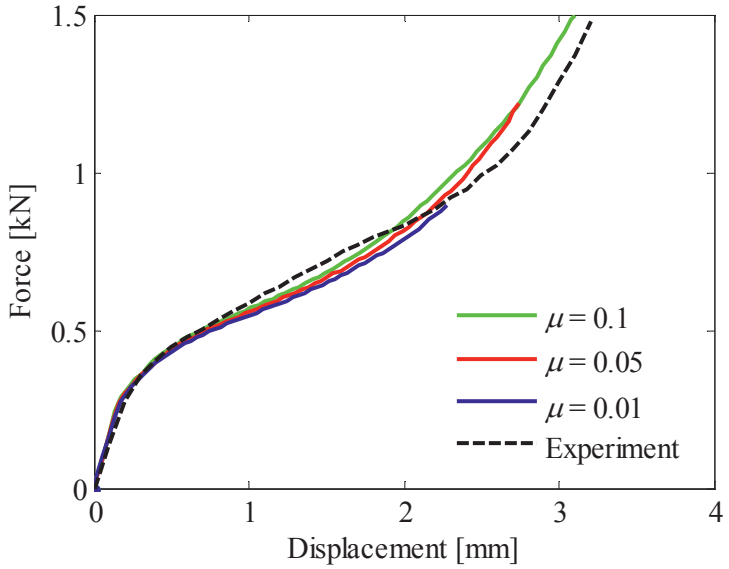

Figure 11.5 *Force-displacement curves from finite element simulations and experimental tests of HDPE in compression.*

11.4 Discussion

The constitutive model [6] is well capable of predicting the main features of the response in uniaxial tension of both the mineral filled PVC and the HDPE. This can be seen in Figure 11.2. Also in compression, the response of HDPE is well described. For PVC, the initial response is reasonably well captured. However, we see a clear overestimation of the force in the plastic domain.

The mineral filled PVC is modelled with a plastic dilation coefficient of $\beta = 1.27$. This gives the plastic flow potential shown in Figure 10.3. The predicted flow direction is normal to the plastic potential function. From the figure it is seen that in any case, also in compression, the constitutive model predicts positive volume change. To check whether the overestimation of the force level in the compression of PVC, see Figure 11.4, was related to incorrect dilation, additional simulations were carried out with $\beta = 1$. This eliminates any volume change in the numerical model. The results from these simulations are plotted in Figure 11.6. Although the

post-yield response is better reproduced in Figure 11.6 than in Figure 11.4, it is still somewhat overestimated.

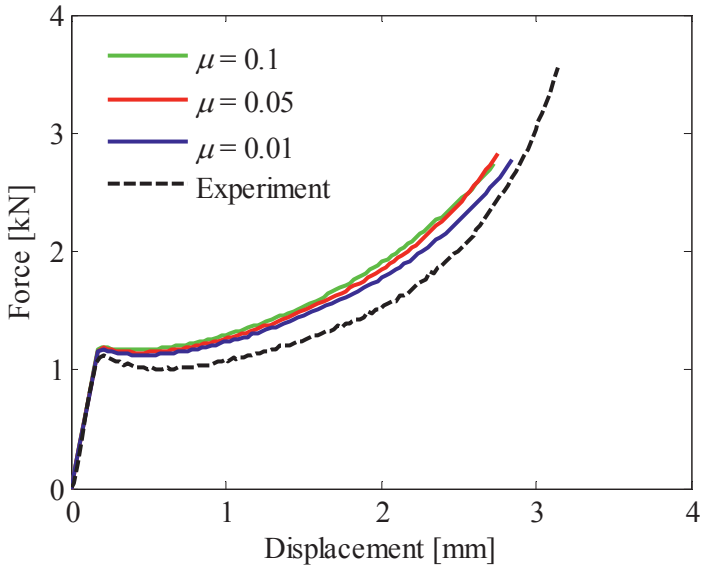

Figure 11.6 *Force-displacement curves from numerical simulations of compression of PVC without plastic dilation, i.e. $\beta = 1$.*

The shape of the stress-strain curve in the numerical model is determined from tension. In Chapter 4 it was observed that the stress-strain curve for compression exhibited a larger stress drop than what occurs in the stress-strain curve for tension. To check whether this was caused by the geometrical conditions, from the barrelling due to friction between the test coupon and the compression platens, Cauchy stress – logarithmic strain curves were computed from the numerical results in similar ways as for the test results in Chapter 4. The numerical simulations for PVC without plastic dilation, i.e. $\beta = 1$, were used for this purpose to exclude any effects from artificial volume change. The results plotted in Figure 11.7 show stress-strain curves for PVC modelled with different friction coefficients μ between the test coupon and the compression platen. The numerical model is not able to predict the same stress drop in compression that is observed in experimental test, not even with the higher friction coefficients μ. In fact, the stress-strain curve is almost unaffected by μ.

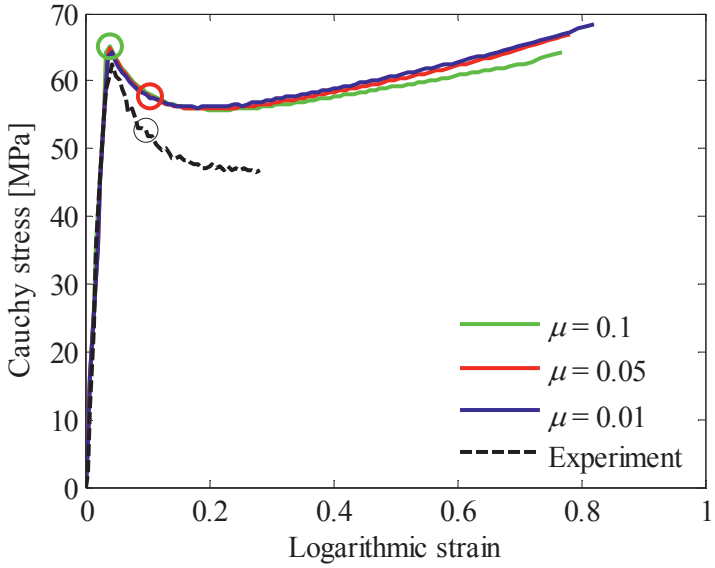

Figure 11.7 *Cauchy stress vs. logarithmic strain from numerical simulations of compression of PVC without plastic dilation, i.e.* $\beta = 1$. *Onset of barrelling is marked by circles.*

The simulations of compression of PVC without any plastic dilation, i.e. $\beta = 1$, were also used to calculate volume strains in the same manner as in the numerical tests in Chapter 4. These volume strains are plotted in Figure 11.8, and they clearly show the necessity of reducing the friction between the test coupon and the compression platens.

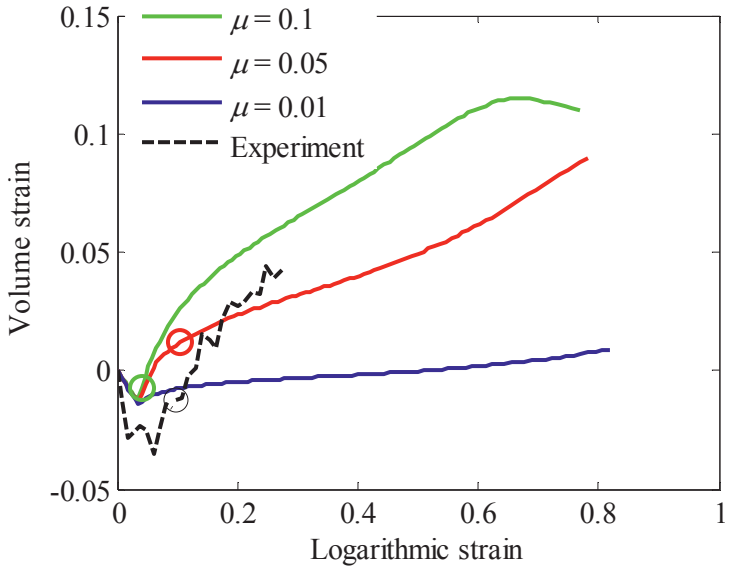

Figure 11.8 *Logarithmic volume strain from numerical simulations of compression of PVC without plastic dilation, i.e. $\beta = 1$. Onset of barrelling is marked by circles.*

11.5 CONCLUDING REMARKS

- The constitutive model with the parameters determined for 5 mm thick plates of mineral filled PVC and HDPE are well able to predict the mechanical response in uniaxial tension.

- The material model is well capable of predicting the initial response in compression tests of the mineral filled PVC and the HDPE. The post-yield behaviour in the mineral filled PVC subjected to compression is somewhat overestimated. In the HDPE, it is better captured.

- The stress softening in compression of PVC is not captured by the numerical model. Eliminating plastic dilation in the constitutive model or reducing friction coefficients does not account for this.

- Numerical simulations of PVC without any plastic dilation shows that the volume increase observed in the compression tests in Chapter 4 might be due to friction between the test coupon and the compression platens.

REFERENCES

[1] M.T. Hovden. Test and numerical simulations of polymer components. Master thesis, Department of Structural Engineering, NTNU, (2010).

[2] V. Delhaye. Behaviour and modelling of polymers for crash applications. Doctoral thesis, Department of Structural Engineering, NTNU, (2010:251).

[3] LS-DYNA. LS-DYNA Keyword User's Manual. Version 971, Livermore Software Technology Corporation (LSTC), 2007.

[4] M. Polanco-Loria, A.H. Clausen, T. Berstad, O.S. Hopperstad. Constitutive model for thermoplastics with structural applications. *International Journal of Impact Engineering*, **37** (2010), 1207-1219.

[5] L. Anand. A constitutive model for compressible elastomeric solids. *Computational Mechanics*, **18** (1996), 339-355.

[6] A.H. Clausen, M.T. Hovden, M. Polanco-Loria, T. Berstad, O.S. Hopperstad. Constitutive model for thermoplastics - Calibration and validation. 19th DYMAT Technical Meeting, Strasbourg, France, (2010).

CHAPTER 12

NUMERICAL SIMULATIONS OF BIAXIAL TENSION TESTS

Numerical simulations of the deformation of biaxial test specimens are carried out to check whether the material parameters determined from uniaxial tension and compression tests are adequate in a more complex stress state. Force-displacement curves and strain fields from the simulations are compared with those from the laboratory tests. Thus, the capability of the constitutive model presented in Chapter 10 is explored through nonlinear finite element analyses of the biaxial tests presented in Chapter 7.

12.1 INTRODUCTION

In Chapter 11 it was shown that the constitutive model described in Chapter 10 was able to represent the force-displacement curves obtained in uniaxial tension and compression tests rather well. This chapter aims to explore whether the material model is able to predict the behaviour observed in a biaxial loading case. The intended use of this particular constitutive model is for simulations of polymeric components for industrial applications. In this perspective, the biaxial tension tests are believed to represent realistic loading cases. The tests in Chapter 7 are therefore applied in this validation study of the constitutive model.

12.2 MESH

The geometry of the mesh, displayed in Figure 12.1, was defined in order to describe the geometry of the biaxial tension test specimens presented in Chapter 7. Two meshes with three and five elements through the thickness were considered for the finite element simulations of equibiaxial loading of cross shaped biaxial test

specimens. The two meshes gave similar results as seen in Figure 12.2. To save computational time, the mesh with three elements through the thickness was used in the further simulations. As seen in Figure 12.1, smaller elements were applied in the areas where large deformations were expected. In total, 12660 solid elements were used to model the deformable part of the sample. Eight node solid elements with reduced integration and a stiffness based hourglass control were used in the simulations. The hourglass energy did not exceed 2% of the total energy during the simulations. Mass scaling of a factor 10^3 was employed to make the simulations run faster. After the simulations it was checked that the kinetic energy was less than 1% of the total energy in the simulations.

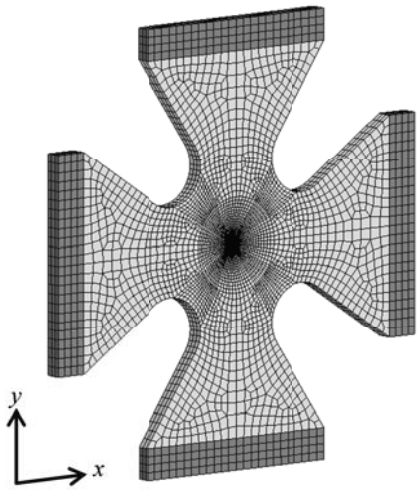

Figure 12.1 *The finite element mesh of the biaxial specimen. The mesh has 3 elements over the thickness. The clamping areas, modelled as rigid bodies, are marked with grey.*

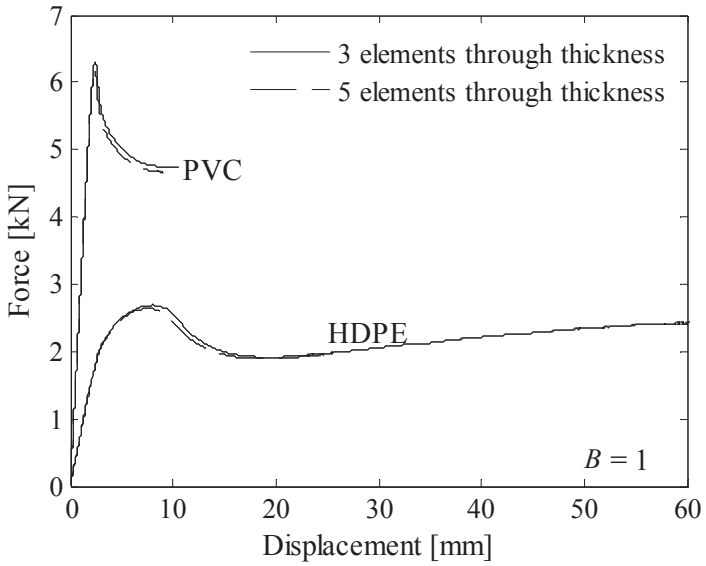

Figure 12.2 *Results from numerical simulations of equibiaxial tension tests employing meshes with three and five elements through the thickness.*

12.3 MATERIAL MODEL

The material model of Polanco-Loria et al. [1], see Chapter 10, has been employed to model the material. The parameters, displayed in Table 10.2 and Table 10.3, were determined from the response of 5 mm thick extruded sheets of the mineral filled PVC and HDPE. Addressing the pressure sensitivity of the yield surface, it should be noted that the mineral filled PVC is modelled with $\alpha = 1.27$ while the HDPE is modelled with $\alpha = 1$. The yield stress of the PVC is in other words pressure sensitive in the material model and the yield stress in HDPE is insensitive to pressure. The four clamping areas of the specimen, addressed in dark grey in Figure 12.1, were idealized as a rigid material.

12.4 BOUNDARY CONDITIONS

Different biaxial extension ratios B were simulated by applying different velocities v_y and v_x to each of the four rigid clamping areas. The biaxial extension ratio is defined as $B = v_y / v_x$. It is the ratio between the deformation velocities v_y and v_x in the *y*- and *x*-directions, i.e. the vertical and the horizontal directions. The

values of v_y and v_x used in the simulation corresponded to the velocities from the laboratory tests, as listed in Table 7.1. The addressed biaxial extension ratios were B = ¼, B = ½, and B = 1. As in the experimental tests v_y varied between the different tests while v_x was fixed. Moreover, one of the numerical models was deformed in uniaxial tension.

12.5 RESULTS

Figure 12.3 shows results from the simulations together with the tests results obtained in Chapter 7 for PVC. Solid lines represent the numerical results while the dotted lines address test results. Figure 12.4 expresses the effect of biaxial loading mode on the force-displacement curve, in other words how the response in the *x*-direction is affected by a change of the deformation in the *y*-direction. The sub-figure a) and b) represent the numerical predictions and the laboratory tests in turn.

It can be seen both from Figure 12.3 a) and from Figure 12.4 that the finite element model underestimates the maximum force for the cross-shaped test specimen of PVC loaded in uniaxial tension. For the biaxial loading cases, the maximum force predicted from the simulation is somewhat higher than the experimental results. The model captures that the maximum force is largest when the extension ratio B is equal to ½ or ¼.

In similar manner as for PVC, numerical and test results for HDPE are displayed in Figure 12.5 and Figure 12.6. Again the solid lines in Figure 12.5 represent the numerical predictions and the dashed lines refer to the test results from Chapter 7. In Figure 12.6, sub-figures a) and b) show numerical and test results in turn. It can be seen from the figures that the numerical model underestimates the maximum force in all load cases of the HDPE specimens. However, it is captured that the specimen loaded with biaxial extension ratio B = ¼ reaches the highest maximum force while the specimen with B = ½ reaches the second highest one. As mentioned in Chapter 7 a hole appeared in the centre of each of the biaxially loaded HDPE test specimens in the laboratory tests after some deformation. The first visual appearances of the holes in the test specimen centres are marked with circles in Figure 12.5 and Figure 12.6 b). These holes were not included in the numerical model. However, at this stage the elements in the centre region of the model were very thin. The rehardening seen in the numerical simulations and not in the laboratory tests might be related to the absent holes.

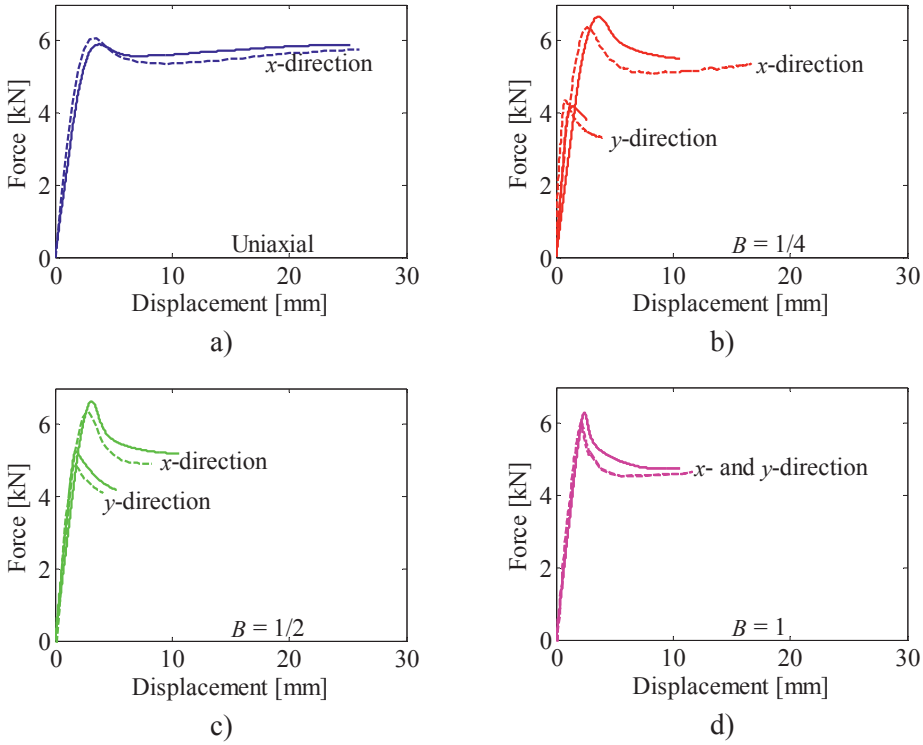

Figure 12.3 *Force-displacement curves for PVC. a) Uniaxial test on biaxial sample. Biaxial tests with b) B = ¼ , c) B = ½ and d) B =1. Solid lines represent results from simulations while the dashed lines represent the results from the tests.*

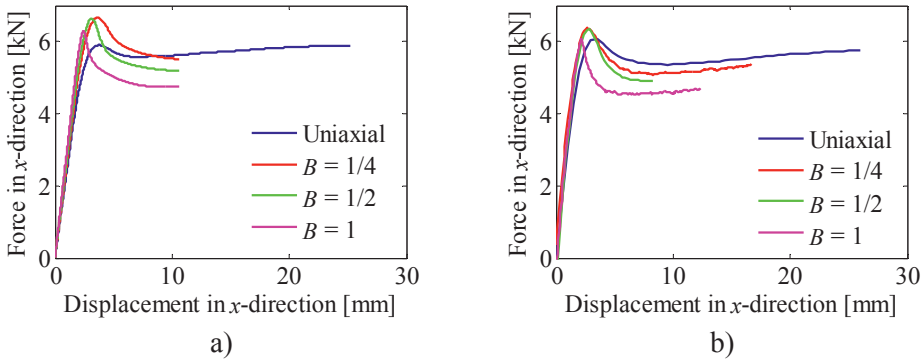

Figure 12.4 *Force-displacement displacement curves in x-direction for biaxial samples of PVC loaded at various extension ratios. a) Numerical simulations. b) Experimental tests.*

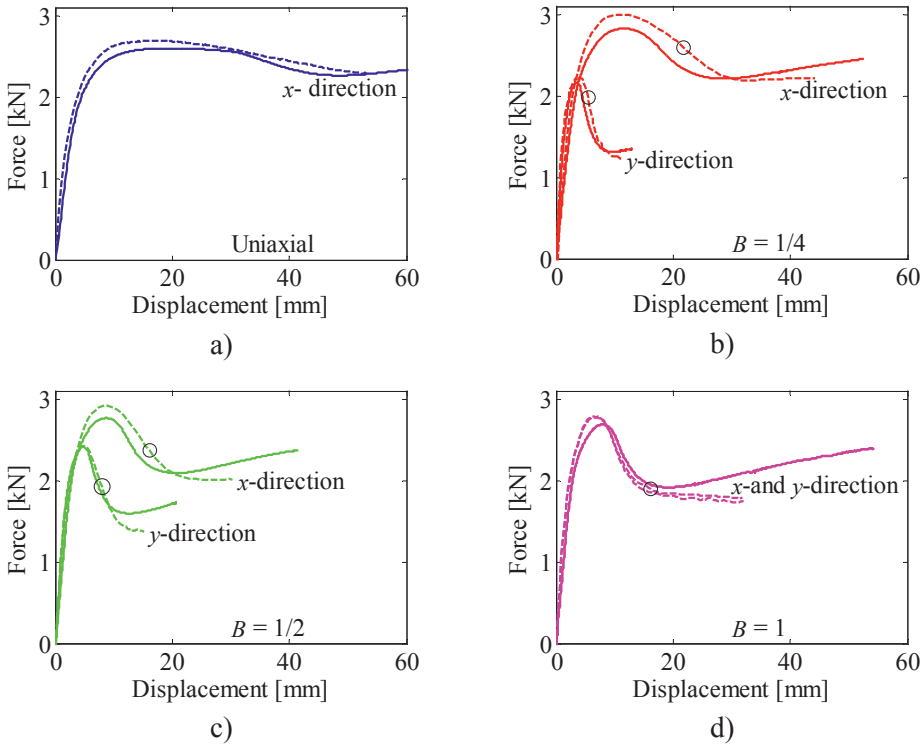

Figure 12.5 *Force-displacement curves for HDPE. a) Uniaxial test on biaxial sample. Biaxial tests with b) B = ¼, c) B = ½ and d) B =1. Solid lines represent results from simulations while the dashed lines represent the results from the tests. The appearances of holes in the tests are marked with circles.*

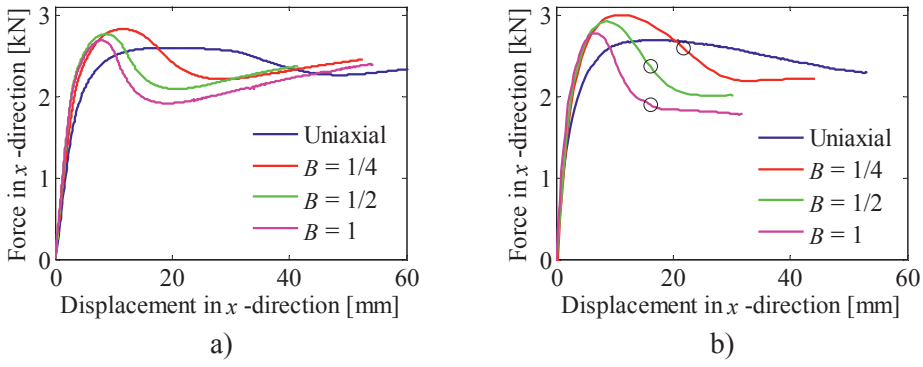

Figure 12.6 *Force-displacement curves in x-direction for biaxial samples of HDPE loaded at various extension ratios. a) Numerical simulations. b) Experimental tests. The appearances of holes in the tests are marked with circles.*

The Green strain fields E_x and E_y from numerical simulation of the PVC specimen loaded in equibiaxial tension, i.e. B = 1, are plotted in Figure 12.7. Similar strain fields, E_x and E_y, from laboratory tests are shown in Figure 12.8. The laboratory test data was obtained by digital image correlation (DIC). The agreement between the numerical predictions and the laboratory tests seem to be good apart from the somewhat stronger strain localization in the centre region of the test specimens seen in sub-figures b) and c). As in the laboratory tests, large deformations in the finite element model lead to strain localization and necking of the X-shaped centre region. The strain levels are captured reasonably well.

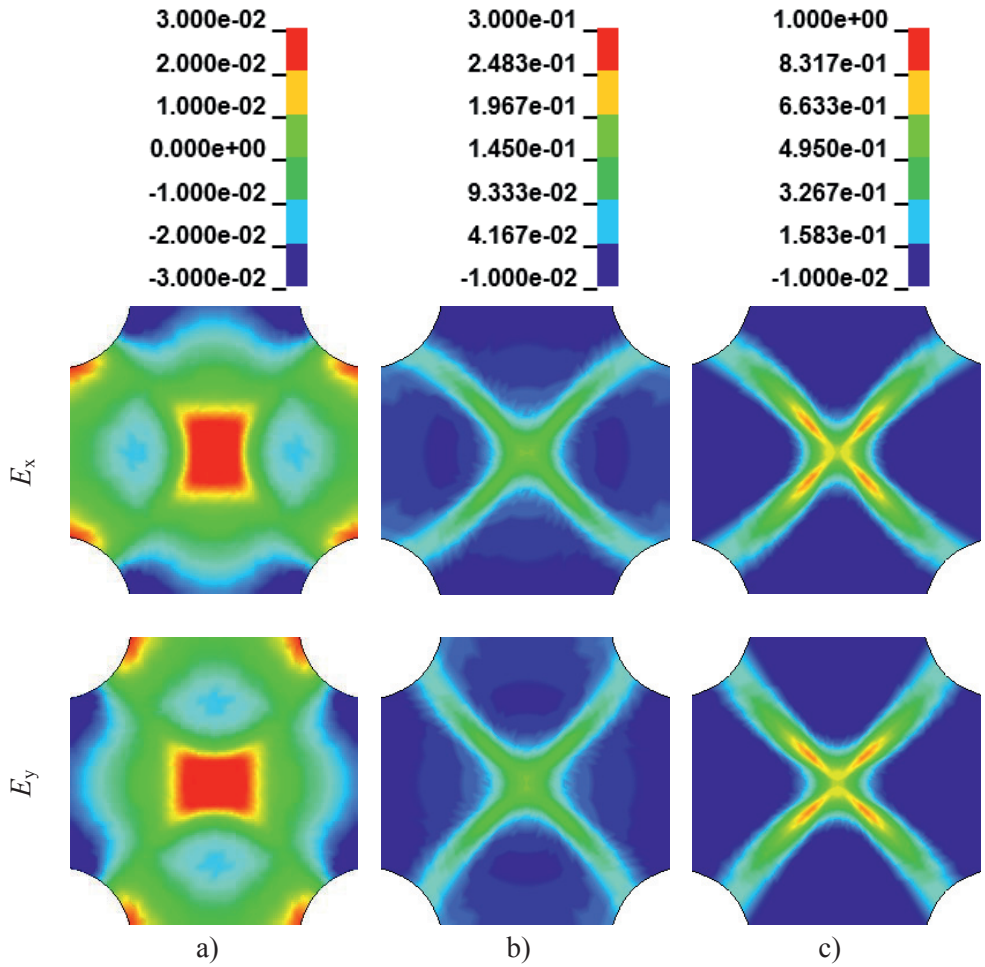

Figure 12.7 *Green strain fields E_x and E_y obtained from numerical simulation of PVC subjected to equibiaxial tension at a) 2.4 mm , b) 3.1 mm and c) 5.9 mm deformation in the x- and y-direction*

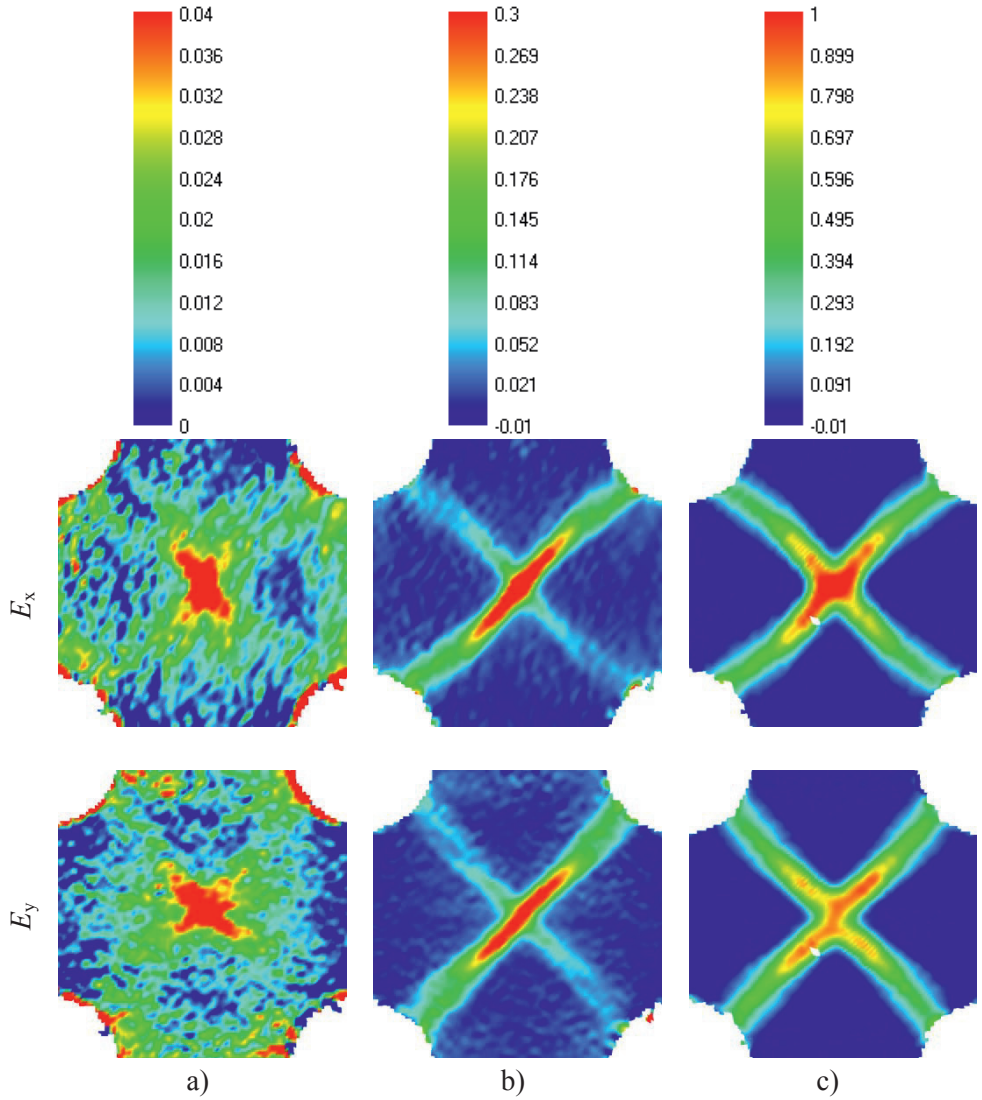

Figure 12.8 *Green strain fields E_x and E_y obtained from test of PVC subjected to equibiaxial extension, i.e. $B = 1$, at a) 2.2 mm b) 3.0 mm and c) 5.7 mm deformation in the x- and y-direction .*

The Green shear strain field E_{xy}, also from the simulation of the biaxial sample with $B = 1$, is plotted in Figure 12.9. Corresponding strain fields from the laboratory test are plotted in Figure 12.10. The shear strains seem to be in the same order in the two figures. Again, the X-shape of the localized zone can be recognized, and the width of this zone is approximately the same in both figures.

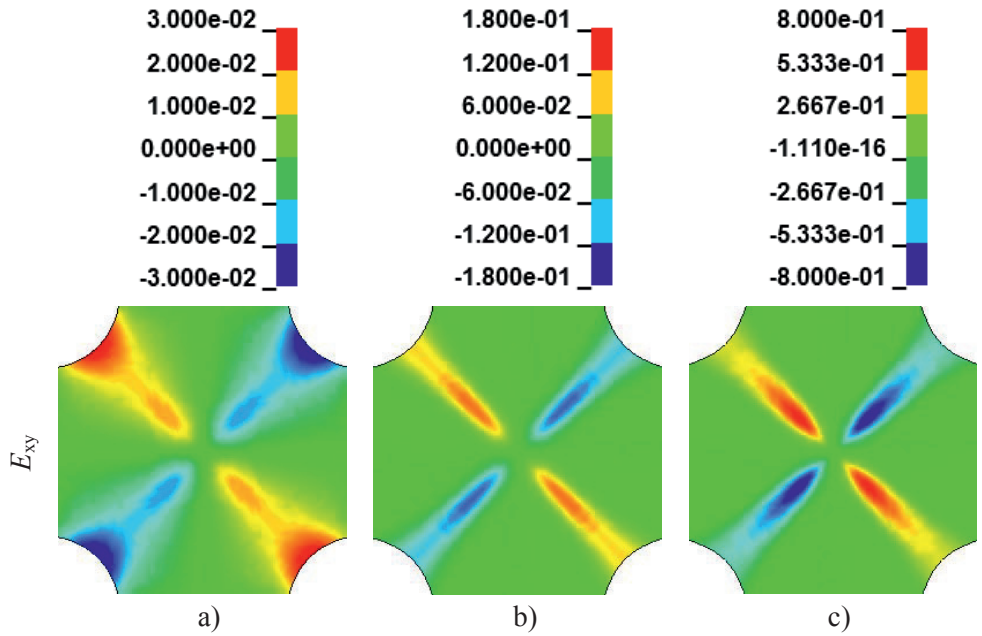

Figure 12.9 *Green shear strain fields* E_{xy} *obtained from numerical simulation of PVC subjected to equibiaxial tension at a) 2.4 mm , b) 3.1 mm and c) 5.9 mm deformation in the x- and y-direction.*

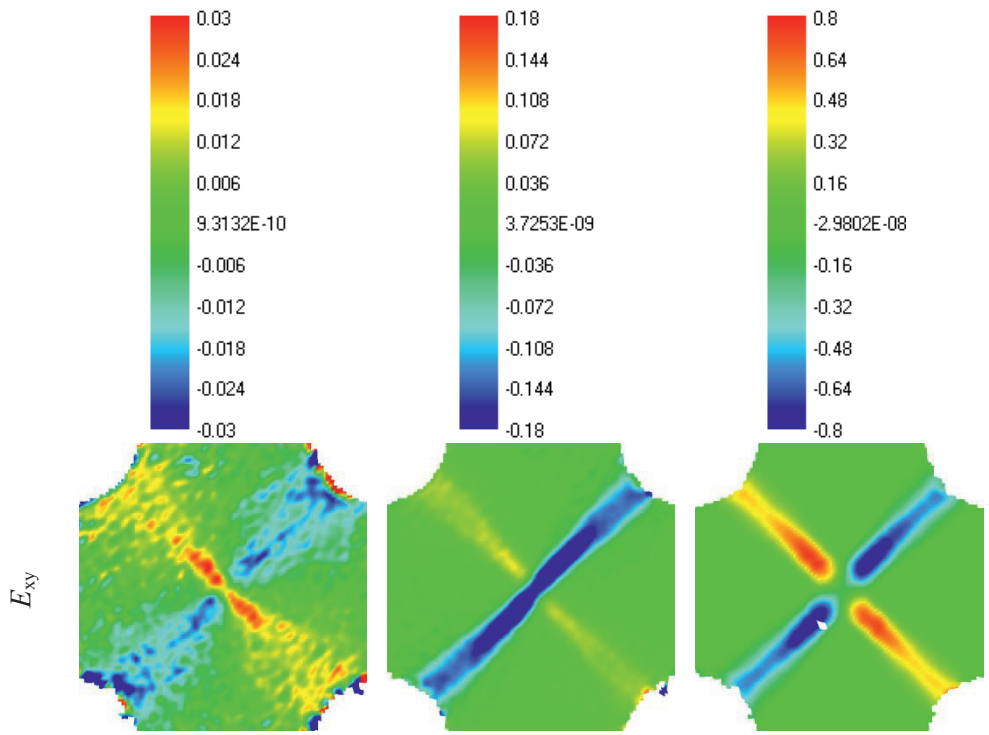

Figure 12.10 *Green shear strain field* E_{xy} *obtained from test of PVC subjected to equibiaxial extension, i.e.* $B = 1$*,at a) 2.2 mm b) 3.0 mm and c) 5.7 mm deformation in the x- and y-direction .*

Figure 12.11 displays the Green strain fields E_x and E_y obtained from numerical simulation of the HDPE specimen loaded with $B = 1$. Strain fields of from the corresponding laboratory test are shown in Figure 12.12. In the numerical model of HDPE as well as in the laboratory tests, the characteristic X-shaped region of strain localization can be recognized. Note that the last strain field of HDPE in Figure 12.11 c) the strain field at 12.5 mm deformation in *x*- and *y*-direction is plotted with a colour bar with a higher span in values than used in the strain field in Figure 12.12. Due to distortion of the speckle pattern, the DIC software could not track the information at all points in the laboratory test specimen. Therefore some information is missing. It can be assumed that the lacking strain values are somewhat higher than indicated by the corresponding colour bar.

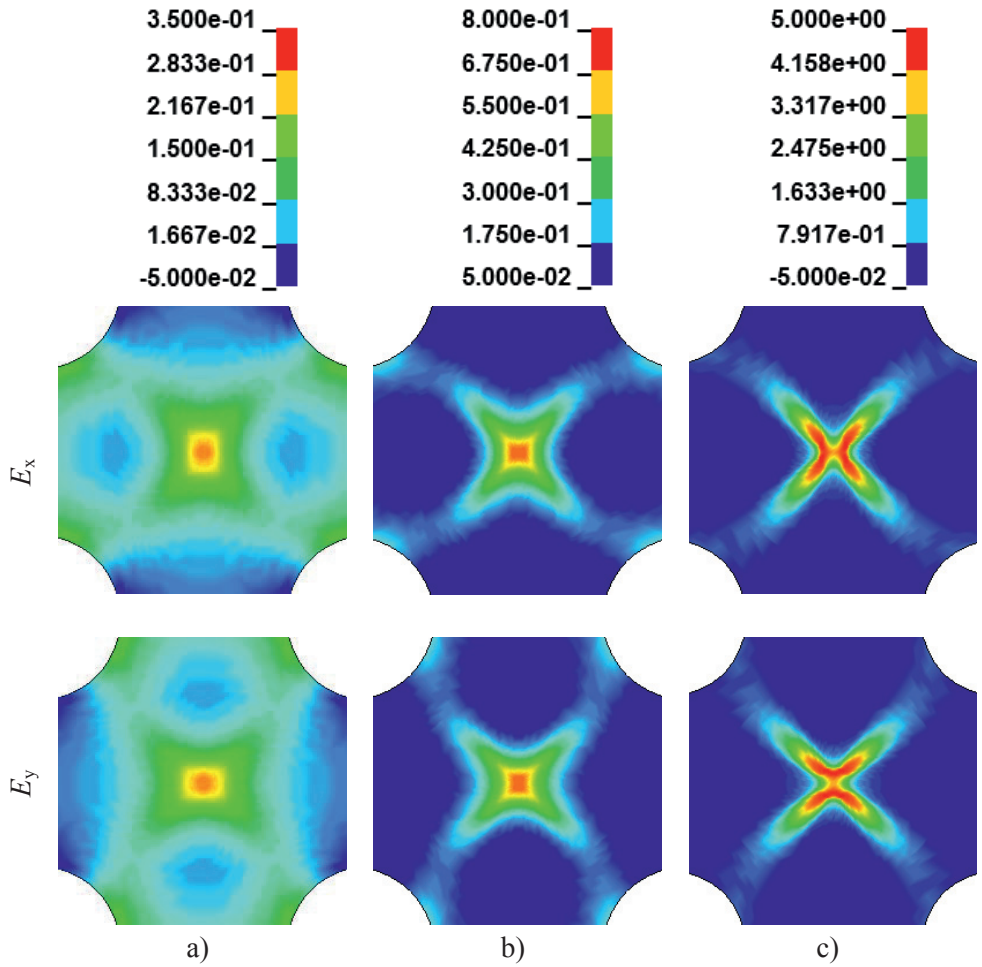

Figure 12.11 *Green strain fields E_x and E_y obtained from numerical simulation of HDPE subjected to equibiaxial tension at a) 7.1 mm, b) 9.3 mm and c) 12.5 mm deformation in the x- and y-direction.*

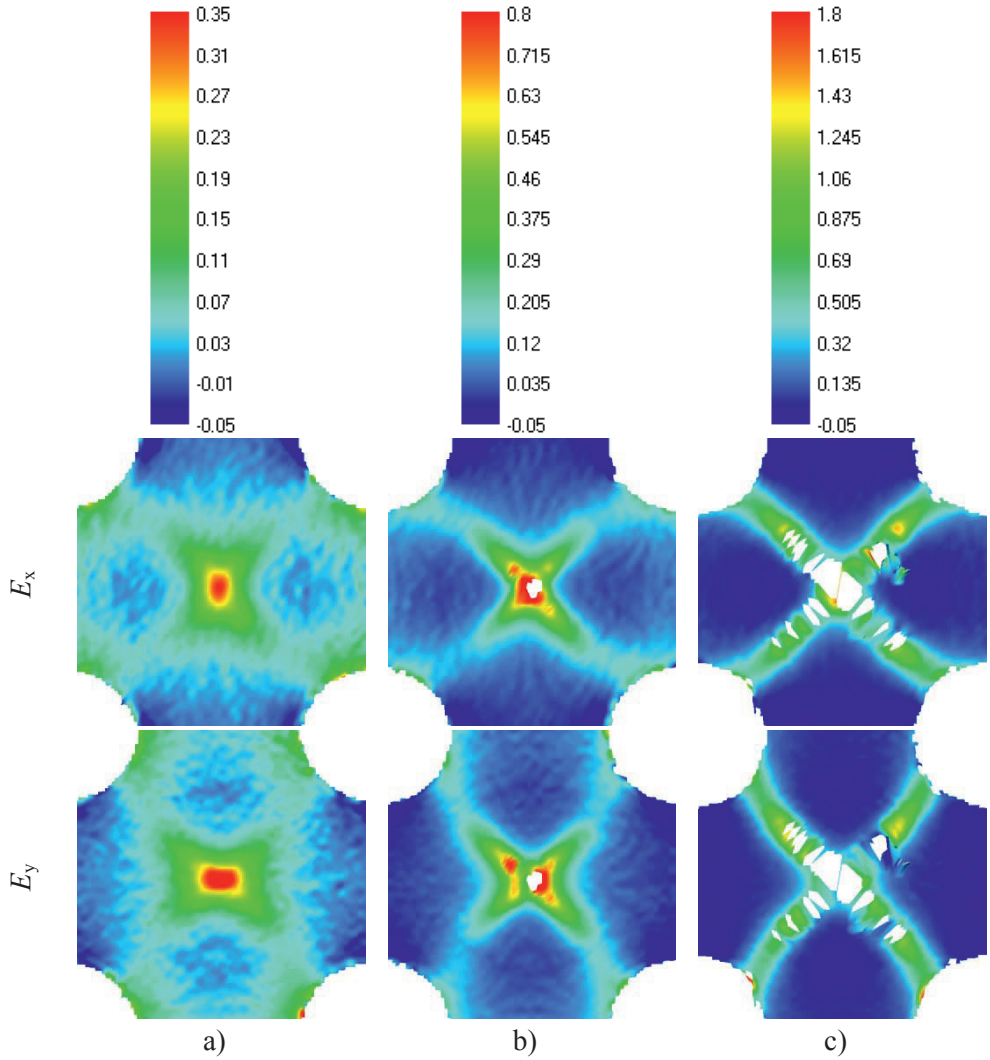

Figure 12.12 *Green strain fields* E_x *and* E_y *obtained from test of HDPE subjected to equibiaxial extension, i.e.* $B = 1$*,at a) 6.8 mm b) 9.0 mm and c) 12.8 mm deformation in the x- and y-direction .*

Figure 12.13 displays the Green strain fields E_{xy} from the numerical simulation of the biaxial HDPE specimen deformed with $B = 1$. The corresponding experimental strain fields are shown in Figure 12.14. There is a good agreement between the two figures. Note that the colour bars in Figure 12.15 c) and Figure 12.16 c) are different.

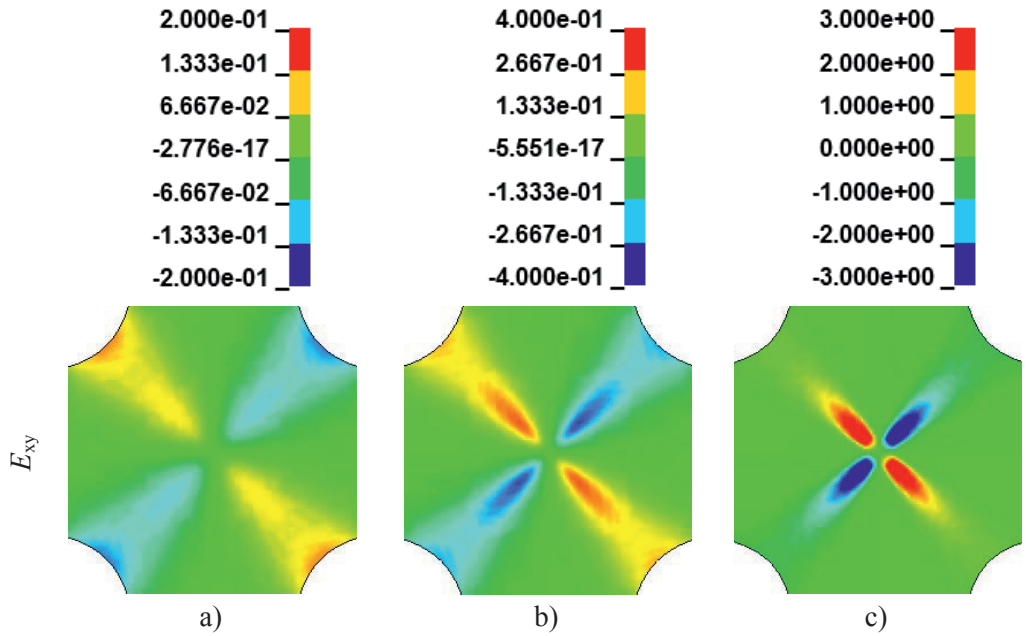

Figure 12.13 *Green strain fields* E_{xy} *obtained from numerical simulation of HDPE subjected to equibiaxial tension at a) 7.1 mm, b) 9.3 mm and c) 12.5 mm deformation in the x- and y-direction.*

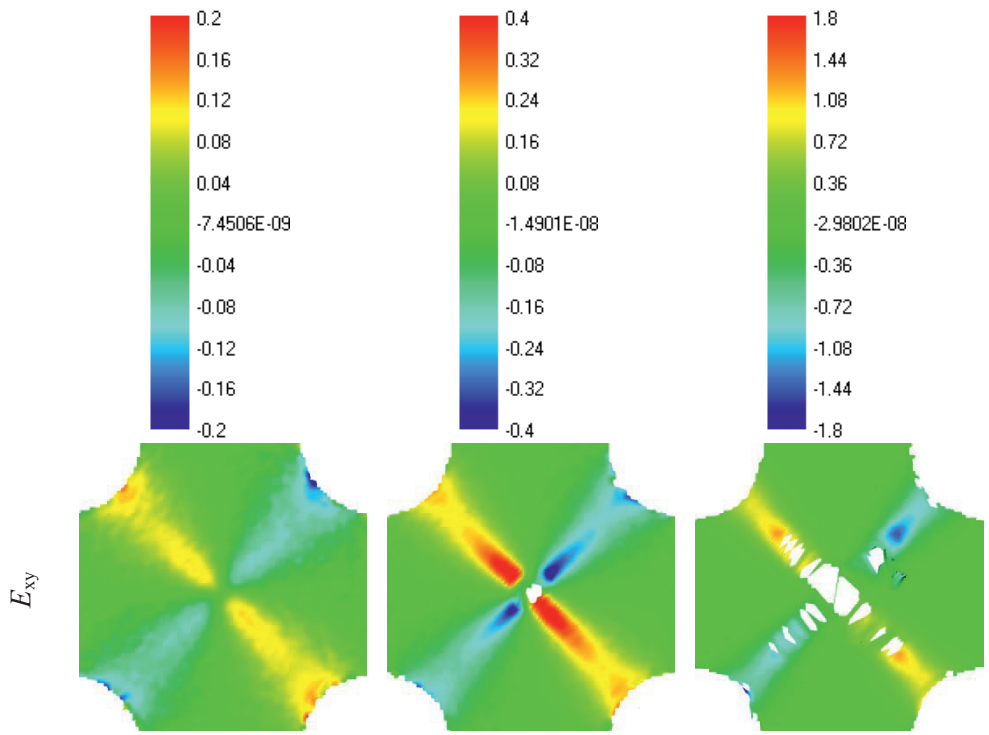

Figure 12.14 *Green shear strain field* E_{xy} *obtained from test of HDPE subjected to equibiaxial extension, i.e.* $B = 1$*, at a) 6.8 mm b) 9.0 mm and c) 12.8 mm deformation in the x- and y-direction .*

The Green strains E_x and E_y taken from the centre point are chosen to represent how the evolution of strains is affected by the biaxial extension ratio B. The shear strains are small at this location, and are therefore not plotted in these figures. Figure 12.15 represents the strains in the PVC specimens. Numerical results are plotted on the left hand side in sub-figure a) and c). For comparison, the test results from Chapter 7 are plotted on the right hand side in sub-figure b) and d). For values of E_x below 1, the numerical and the experimental results are comparable. For larger strains, the deviation is larger. This may be related to the distortion of the speckle pattern in the laboratory test causing difficulties for the DIC-software. An up-turn in E_x is seen at about 3 mm deformation in the x-direction both in the numerical simulations and the laboratory tests. The strains E_y are reasonably well predicted by the numerical simulation. The negative E_y produced in the uniaxial tests, as discussed in Chapter 7, is also captured by the numerical simulations.

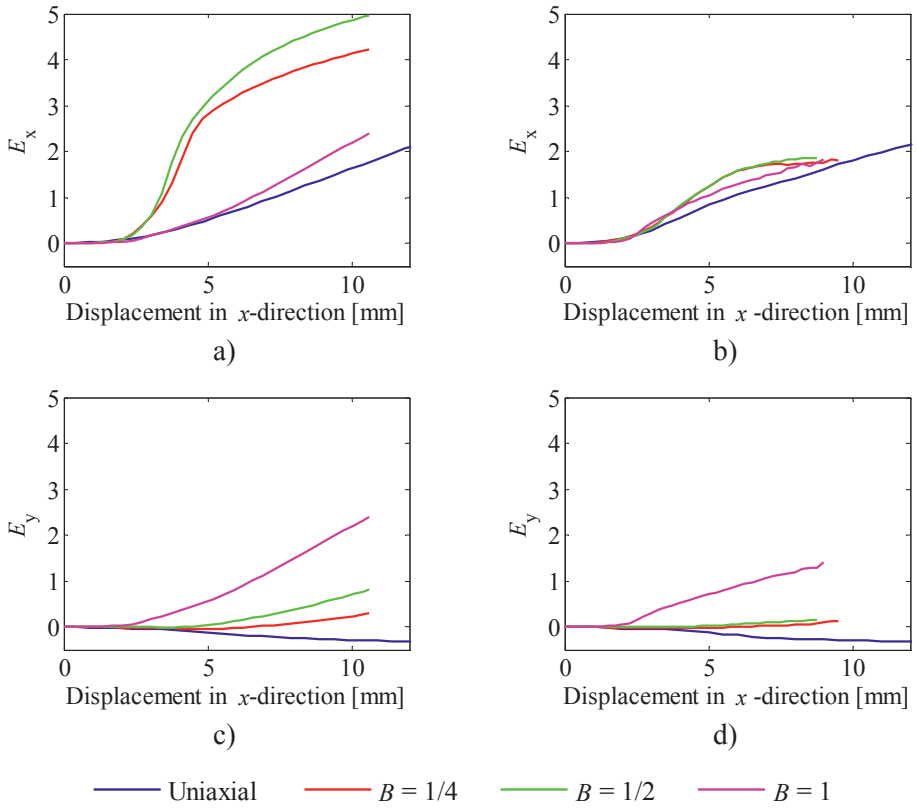

Figure 12.15 *Green strain E_x and E_y taken from the centre point of the biaxial specimens of PVC as function of displacement in x-direction: a) E_x from numerical simulation, b) E_x from the test, c) E_y from numerical simulation and d) E_y from the test.*

Figure 12.16 displays the Green strains E_x and E_y taken from the centre point of the HDPE specimens. Again, numerical results are displayed on left hand side in sub-figures a) and c). The test results from Chapter 7 are displayed on the right hand side in sub-figure b) and d) for comparison. As mentioned before, the DIC-software could not follow the strains for large deformations because of distortion of the speckle pattern. For deformations in the x-direction lower than 8 mm, the strains in the centre point are captured in a relatively good way by the numerical model. Also for the uniaxial deformation of HDPE it is captured that negative E_y is produced. Moreover, in the laboratory tests it was seen that the uniaxially deformed specimens of both PVC and HDPE started to buckle after some deformation. The same could be observed in the numerical models.

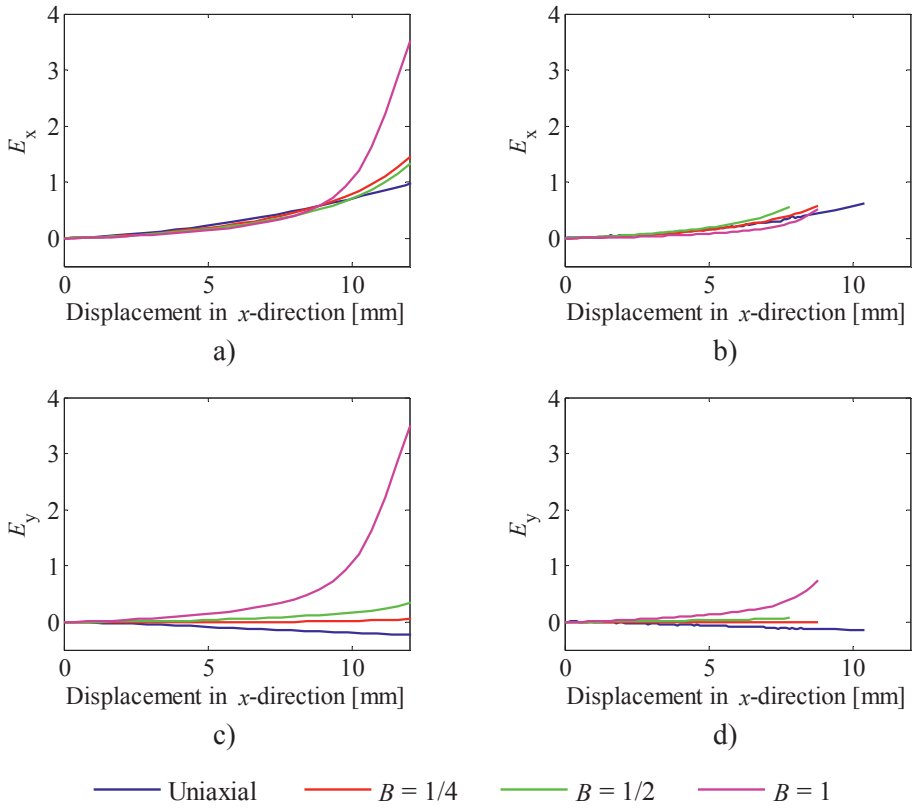

Figure 12.16 *Green strain E_x and E_y taken from the centre point of the biaxial specimens of HDPE as function of displacement in x-direction: a) E_x from numerical simulation, b) E_x from the test, c) E_y from numerical simulation and d) E_y from the test.*

12.6 Discussion

The constitutive model [1] described in Chapter 10 with parameters determined from uniaxial tension and compression tests was employed to predict the mechanical response of PVC and HDPE in biaxial tension. The purpose was to evaluate the material model in a deformation state different from those used as a basis for the parameter identification. The biaxial tests presented in Chapter 7 are relevant for such a validation.

In particular, validation of the pressure-dependent Raghava yield criterion was addressed in this study. In that perspective, the main difference between the two materials is the pressure sensitivity. The mineral filled PVC was modelled with α

= 1.3 in the yield function to incorporate pressure sensitivity of the yield surface. HDPE, on the other hand, was modelled with α = 1.0, which corresponds to the von Mises yield criterion. Another main difference between the two materials is that the PVC exhibits stress softening after reaching the yield stress while HDPE does not. The numerical analyses of the biaxial tests slightly overestimate the force level for PVC, while for HDPE the force level is somewhat lower in the simulations than in the tests. However, the main features of the behaviour observed in the test seem to be captured by the numerical model.

The model predicts that the specimens deformed at B = ½ and B = ¼ reach about the same force level in PVC. With respect to the strain state at the centre point, this prediction is in accordance with the shape of the yield surface employed for this material, see Figure 12.17. According to the yield surface, a higher value of the *x*-direction stress can be obtained in uniaxial tension (corresponding to the horizontal axis) than for equibiaxial tension (corresponding to the dashed line in the figure).

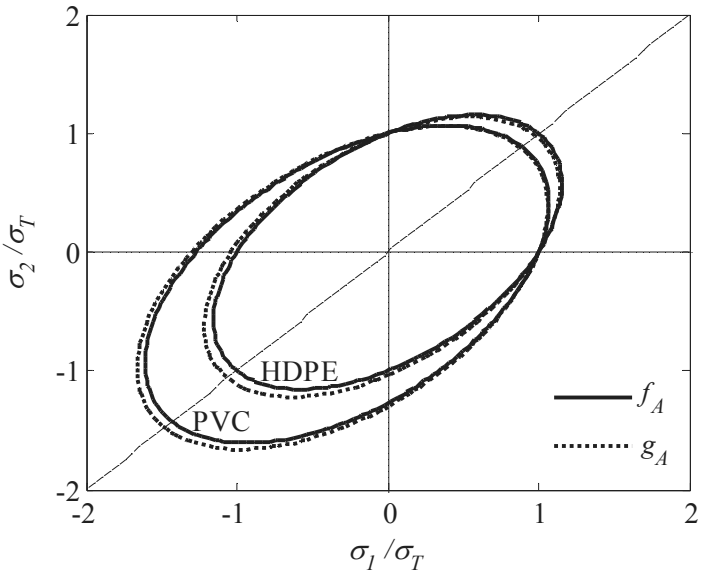

Figure 12.17 *Yield surface f_A and plastic potential g_A, plotted in the principal stress space, employed for the PVC and the HDPE in the numerical model.*

The maximum force in the equibiaxial test of PVC is overestimated by the numerical model. The reason may be that there seem to be some strain localization in the experimental test that is not captured by the numerical simulation. This can be seen by comparing the strain field from the simulations of PVC, see Figure 12.7,

with the strain fields from experimental tests shown in Figure 12.8. By examination of the yield surface used for modelling of PVC, see Figure 12.17, it would be expected that the peak load in uniaxial tension is higher than the one in equibiaxial tension. Due to the transverse compression at the centre of specimen subjected to uniaxial loading, however, the stress state in this specimen is not uniaxial. Thus, the location on the yield surface corresponding to this stress state is not on the *x*-axis of the yield surface in the principal stress space but slightly below. Figure 12.15 shows that at the centre of the specimen, the ratio E_x / E_y at 10 mm deformation can roughly be estimated to –6.3 and –5.9 for the experiments and simulations, respectively. This also suggests that the corresponding stress state is somewhere within the fourth quadrant of the yield surface in the principal stress space. The ultimate rupture of the specimens was not captured in the simulation because no failure criterion was employed in the numerical model.

Figure 12.6 b) shows that there is not much difference in the maximum force level reached in the uniaxial test and the equibiaxial test of HDPE. This is captured well by the numerical model, see Figure 12.6 a). Also for HDPE the intermediate extension ratios result in a larger maximum force in the *x*-direction in the tests as well as in the numerical analyses. In particular, the test deformed at B = ¼ reaches the highest force level both in the test and the analyses. The drawing of the centre region of the HDPE specimens makes the specimens very thin. In the laboratory tests, this thinning leads to creation of holes in the three biaxial tests on HDPE. This hole-growth is not included in the model. However, the elements in the numerical model in this region are extremely thin at this stage. Even though some rehardening is observed in the global response of the numerical simulations, the response is still quite similar to the one observed in the experiments some time after the hole initiation. Compression could be observed also at the centre of the HDPE specimen tested in uniaxial tension, see Figure 12.16. It is seen that the ratio E_x / E_y at 10 mm deformation is around –3.8 for both experiment and simulation. Due to the comprehensive thinning of this section, the load-bearing capacity might be reduced so much that the global response of the specimen is not affected by the transverse compression in the same manner as in the case of PVC. Modelling this particular HDPE with a von Mises yield criterion seems to be in reasonable accordance with the experimental results.

Comparing the strain fields from the simulations of both materials with the strain fields from the tests, see Figure 12.7 to Figure 12.14, it is seen that there is a reasonably good agreement between the experimentally and numerically obtained strain fields. Some information is lost in the strain fields from the laboratory test of HDPE due to large deformations and distortion of the speckle pattern used for digital image correlation. However, the blank spots in the plots indicate that the

local strain values are rather high. This is confirmed in the strain fields obtained from the numerical simulations.

From Figure 12.15 and Figure 12.16 it can be seen that the Green strains at the centre points of the specimens found from the experiments and the numerical simulations are comparable. These plots also show that the model is able to predict the earlier localization of strains for PVC compared with HDPE.

Addressing the post yield behaviour, it can be seen from Figure 12.3 and Figure 12.4 that there is some mismatch between experiments and simulations after onset of yielding in PVC, especially for the uniaxially loaded specimen. In the simulations, the load drop is less pronounced than in the experiments. This might be related to the plastic potential g_A. If the plastic dilation is overestimated, the load drop will be too small.

12.7 CONCLUDING REMARKS

- It is found that the constitutive model proposed by Polanco-Loria et al. [1] is capable of describing the response of the mineral filled PVC and the HDPE in biaxial tension with good accuracy.

- The 11 parameters in the material model determined from uniaxial tension and compression tests are adequate for describing a biaxial load case. This facilitates an industrial use of the model.

REFERENCES

[1] M. Polanco-Loria, A.H. Clausen, T. Berstad, O.S. Hopperstad. Constitutive model for thermoplastics with structural applications. *International Journal of Impact Engineering*, **37** (2010), 1207-1219.

CHAPTER 13

NUMERICAL SIMULATIONS OF AXISYMMETRIC TENSILE BARS WITH NOTCH

This chapter presents results from numerical simulations of the behaviour of the axisymmetric notched tensile bars from Chapter 8. This numerical study is carried out to check whether the constitutive model, employing a Raghava yield surface and flow potential, can predict the response of the polymers under triaxial stress state. In particular, the prediction of yield stress and volume change is discussed.

13.1 INTRODUCTION

The previous chapters have shown that the material model of Polanco-Loria et al. [1] with parameters calibrated from uniaxial tension and compression tests is capable of describing the behaviour of the polymers under uniaxial and biaxial stress states. This chapter is concerned with how the material model represents triaxial stress states. As described in Chapter 8, experimental tests have been performed on axisymmetric notched tensile bars with notches of different sizes. The current chapter employs the material model in numerical simulations of the behaviour of the test specimens to see how well the response is captured. The results from the numerical simulations are compared with the experimental results to check the agreement.

13.2 MESH

Figure 13.1 shows outlines of the five mesh geometries employed in this study. The figure displays the sketches used to create an axisymmetric solid from 2D elements. Four node axisymmetric elements with reduced integration together with

a stiffness based hourglass control were employed to carry out the simulations [2]. Mass scaling of a factor of 10^6 was used to decrease the simulation time. After the simulations it was controlled that the hourglass energy and the kinetic energy were much less than 1% of the total energy. Since large deformations were expected in the notch, this region was defined by smaller elements, as seen in Figure 13.2. Across the minimum cross section 20 elements were used. This corresponds to the distance a_0 in Figure 13.2. The part of the sample located 1 mm to each side of the minimum cross section was divided into 40 elements in the longitudinal direction. This corresponds to the distance L_0 in Figure *13.2* and the distance used for axial strain measurements in the laboratory tests in Chapter 8.

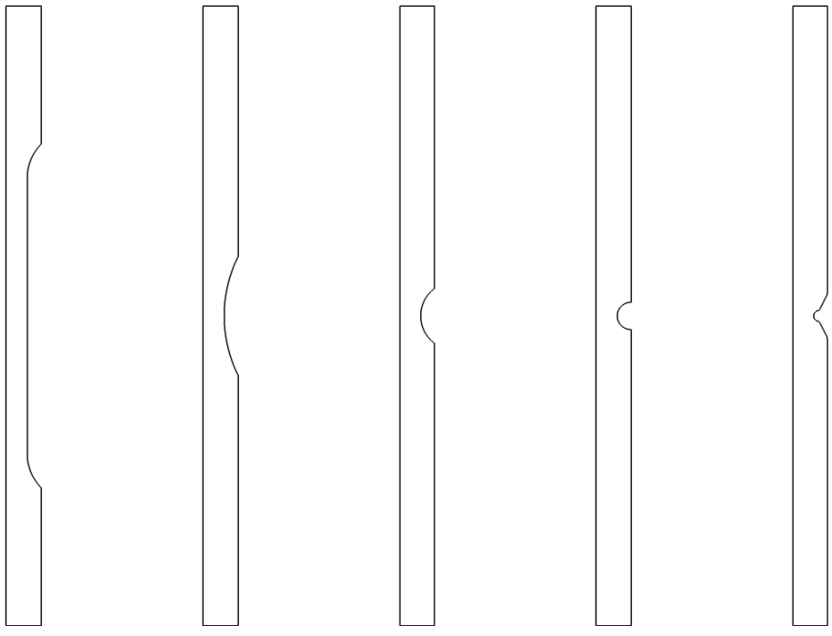

Figure 13.1 *The geometries of a) the smooth test specimen, and test specimens with initial notch radii R_0 equal to b) 20 mm, c) 5 mm, d) 2 mm and e) 0.8 mm.*

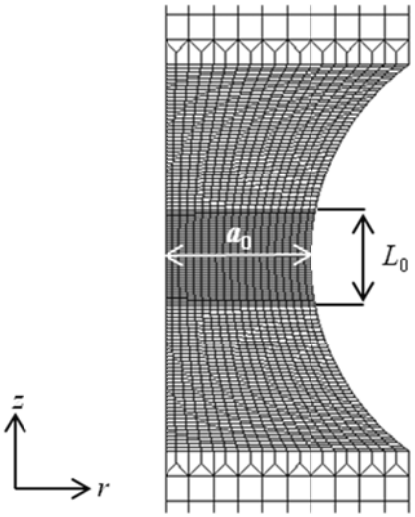

Figure 13.2 *Example of mesh refinement in the notch of an axisymmetric bar with* R_0 *= 5 mm. The height of the area with the finest mesh is* L_0 *= 2 mm.*

13.3 MATERIAL MODEL

The material model of Polanco-Loria et al. [1], see Chapter 10, was used for describing the material behaviour in this study. The material parameters, determined from uniaxial tension and compression tests of the 10 mm sheets of mineral filled PVC and HDPE [3] are given in Table 10.4 and Table 10.5, respectively. Since this study focuses on the onset of yielding and the plastic dilation, it is worth paying attention to the values of the α- and β-parameters. The pressure sensitivity parameter α, defining the shape of the yield surface, introduces pressure sensitivity in PVC by having a value of 1.3. In HDPE pressure sensitivity is excluded by setting α equal to 1.0 and thereby defining a von Mises yield surface. The plastic dilation is given by the shape of the plastic potential, which is controlled by β. For PVC and HDPE β is set to 1.27 and 1.04, respectively. This means that the material model predicts some plastic dilation in both materials. However, for HDPE β is close to unity and therefore the plastic change of volume is minor.

13.4 BOUNDARY CONDITIONS

The nodes facing the positive and negative *z*-direction at each end of the mesh were applied a prescribed motion of 0.02 mm/s in the direction they were facing. When the global displacement in the numerical simulations has passed about 1/3 of the global displacement at fracture in the experiments, the simulations were stopped. Numerical simulations of the specimen that did not fracture were carried out to approximately the same global deformation level as in the experiments.

13.5 POST PROCESSING

With the purpose of comparing the results from the numerical simulations with the results from the experimental tests in Chapter 8, some of the same measures were extracted. These measures were the length L spanning over the root of the notch, the minimum cross section radius a and the global displacement and force. Like in the experimental tests, the initial values of L and a are $L_0 = 2$ mm and $a_0 = 3$ mm. Further average stresses and strains were computed in similar manner as for the experimental tests. Thus, the average axial strain from the simulation was calculated by

$$\bar{\varepsilon}_z = \ln\left(\frac{L}{L_0}\right) \tag{13.1}$$

The average radial strain was calculated from the radius a as

$$\bar{\varepsilon}_r = \ln\left(\frac{a}{a_0}\right) \tag{13.2}$$

The net axial stress was found from dividing the applied force F by the actual cross section area

$$\bar{\sigma}_z = \frac{F}{\pi a^2} \tag{13.3}$$

The plastic deformation gradient $\mathbf{F}^p$ was extracted from the 20 elements defining the minimum cross section. It was used to find the plastic volume strain ε_v^p over the cross section

$$\varepsilon_v^p = \ln\left(\det \mathbf{F}^p\right) \tag{13.4}$$

This made it possible to plot the radial distribution of plastic volume strain ε_v^p for several deformation levels.

Finally, the stress triaxiality ratio σ^*, as defined as in Chapter 8, is

$$\sigma^* = \frac{I_1 / 3}{\sqrt{3J_2}} \tag{13.5}$$

The data required to plot σ^* over the cross section was extracted in terms of pressure, $-I_1 / 3$, and von Mises stress, $\sqrt{3J_2}$, as provided by LS-DYNA from the 20 elements in the minimum cross section.

13.6 RESULTS

In the following, results from the numerical simulations will be presented together with experimental results from Chapter 8. Results from the numerical simulations will be displayed on the left hand side in sub-figures a) and the laboratory test results will be included on the right hand side in sub-figures b).

The force-displacement curves from simulations and laboratory tests are plotted in Figure 13.3 for PVC and Figure 13.4 for HDPE. The response of the smooth PVC specimen and the specimen with R_0 = 20 mm seems to be well captured by the finite element models. For the specimens with smaller notch radius, on the other hand, it is seen that the maximum force level in PVC is overestimated. The PVC specimens from the tests all reach about the same maximum force level. The numerical simulations, on the other hand, predict a higher maximum force for the specimens with smaller notch radius. For the HDPE the numerical model generally overestimates the maximum force. However it is captured that the specimen with smallest notch radius reaches the highest maximum force while the smooth specimen reaches the lowest.

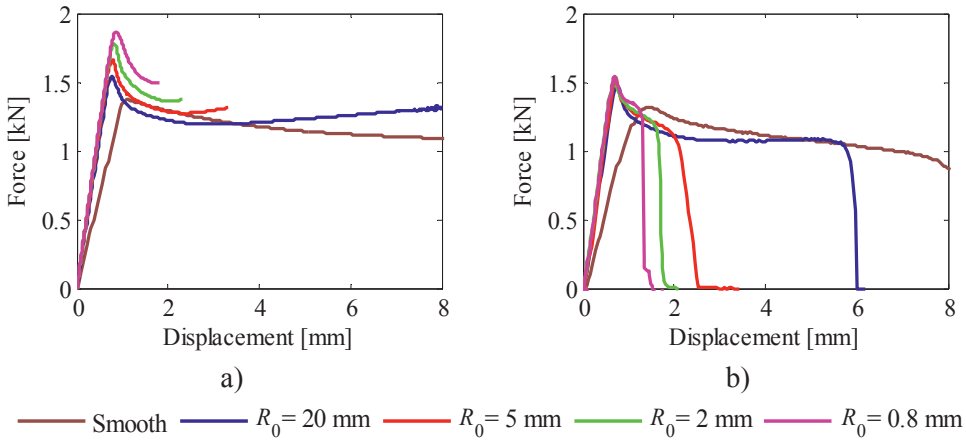

Figure 13.3 *Force-displacement curves for PVC from a) numerical simulations and b) experimental tests.*

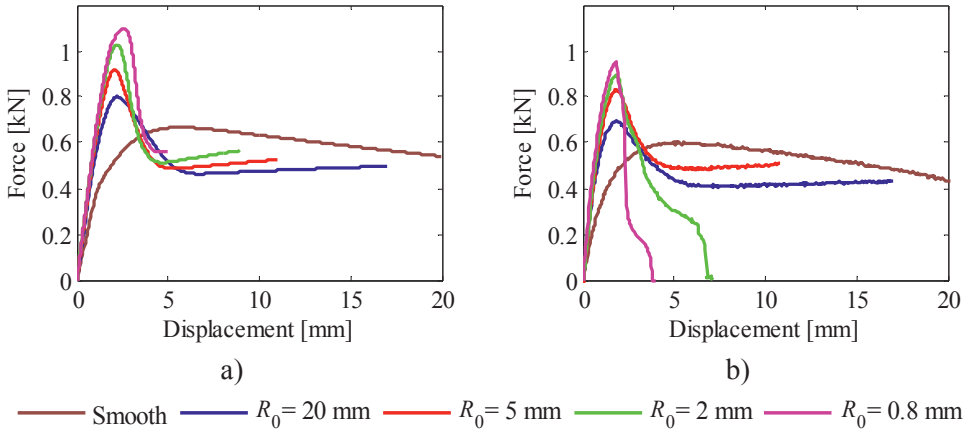

Figure 13.4 *Force-displacement curves for HDPE from a) numerical simulations and b) experimental tests.*

The averaged axial stress and strain was computed from Equation (13.3) and Equation (13.1), respectively. Figure 13.5 presents results for PVC and Figure 13.6 for HDPE.

As for the force-displacement relationships, also the stress-strain curves for PVC specimens with small notch radii are overestimated by the finite element model. According to the simulations, the axial average peak stress increases with reduction

of the notch radius. The experimental test results are different; all notched specimens reach about the same peak stress independent on the notch size.

In the experimental test, the smooth HDPE specimen experienced severe strain localization, maybe due to an uneven lathe surface finish. This strain localization is not captured in the numerical model. Therefore, the local strains in the numerical model ceases at a lower level than in the experiment, even though they had the same global displacement. The response of the HDPE specimen with $R_0 = 20$ mm in Figure 13.6 a) seems to reproduce the experimental observations in sub-figure b) rather well, although both the stress and the strain level are somewhat overestimated. Worse is the response estimation of the two specimens with the smallest notch radii; $R_0 = 2$ mm and $R_0 = 0.8$ mm. Both specimens show a softening behaviour in the experimental test that is not captured by the numerical simulations.

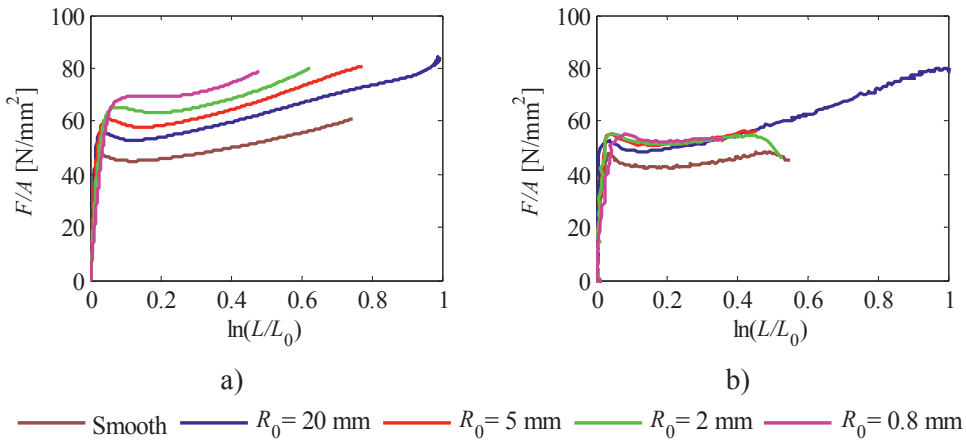

Figure 13.5 *Net axial stress-strain curves for PVC from a) numerical simulations and b) experimental tests.*

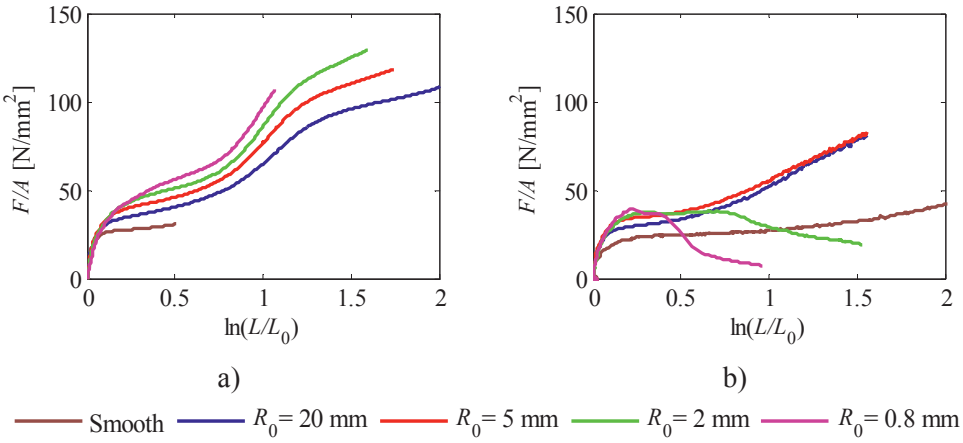

Figure 13.6 *Net axial stress-strain curves for HDPE from a) numerical simulations and b) experimental tests.*

The rates of average axial strain $\dot{\bar{\varepsilon}}_z$ at the state of maximum force in the numerical simulation of each test are presented in Table *13.1* and Table *13.2*.These values for the net strain rate are similar to those found in the experimental tests presented in Chapter 8.

Table 13.1 *Rate of average axial strain at maximum force in simulations of PVC specimens.*

	PVC smooth	PVC-20	PVC-5	PVC-2	PVC-08
$\dot{\bar{\varepsilon}}_Z$ $[s^{-1}]$	0.00096	0.0087	0.015	0.019	0.017

Table 13.2 *Rate of average axial strain at maximum force in simulations of HDPE specimens.*

	HDPE smooth	HDPE-20	HDPE-5	HDPE-2	HDPE-08
$\dot{\bar{\varepsilon}}_Z$ $[s^{-1}]$	0.0091	0.0068	0.010	0.012	0.011

Figure 13.7 and Figure 13.8 display contour plots of the equivalent plastic strain as provided by LS-DYNA in the notch in PVC and HDPE specimens from numerical simulations. The plots are captured at net axial strain levels $\ln(L / L_0)$ similar to the strain levels in the experimental tests displayed in Figure 9 and Figure 10 in Chapter 8. The contour plots have been mirrored about the symmetry axis for better visualization.

From the contour of the specimens it can be seen that some of the main characteristics of the deformation are captured. Both in the numerical simulations and the experimental tests, a local neck in some cases appeared inside the pre-machined neck. Also the cold-drawing seen in the experimental test as elongation of the most central region of the neck can be observed in the numerical results.

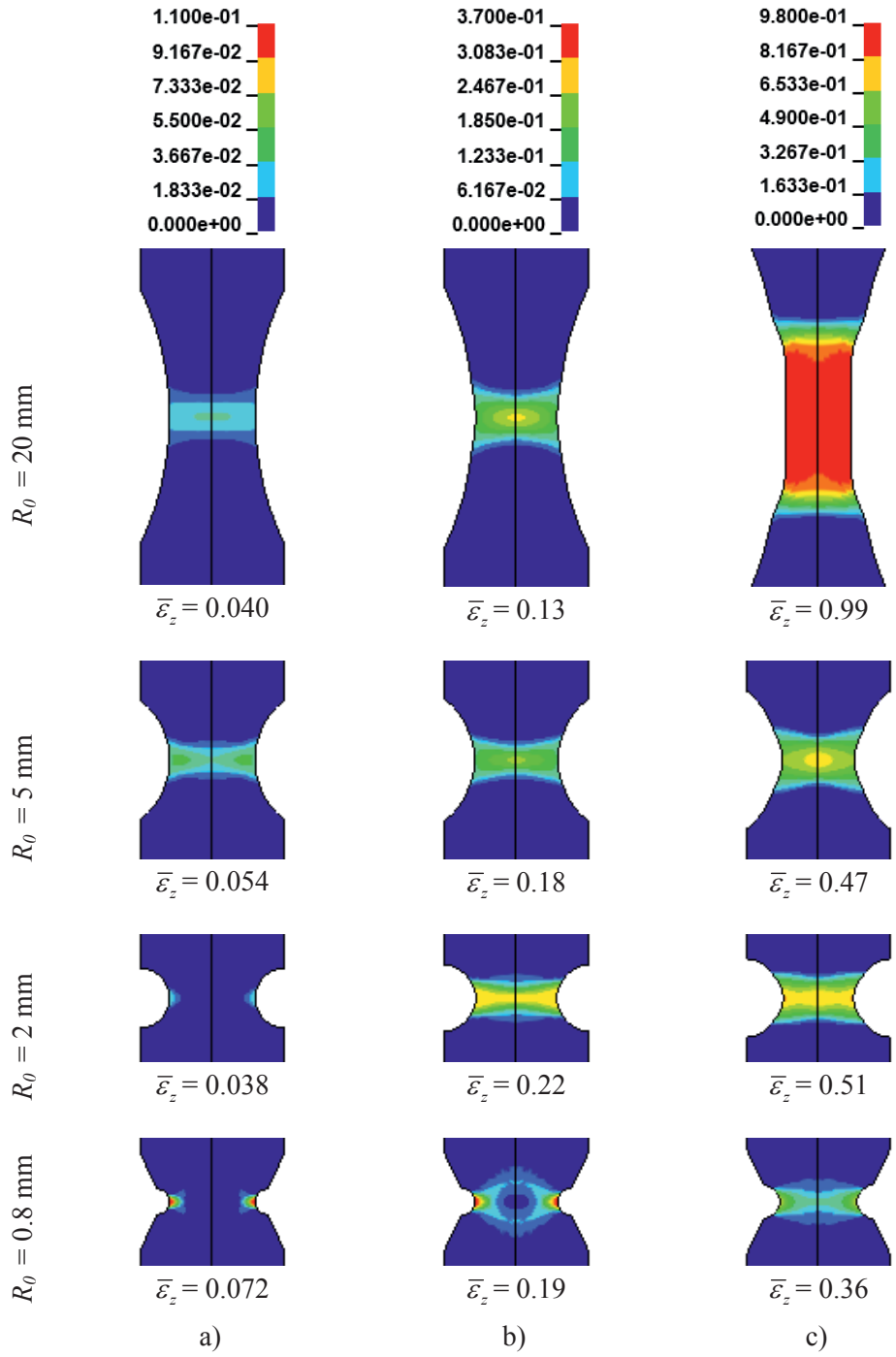

Figure 13.7 *Contour plots of plastic strain from simulations of the PVC specimens. The columns a), b) and c) refer to different deformation levels.*

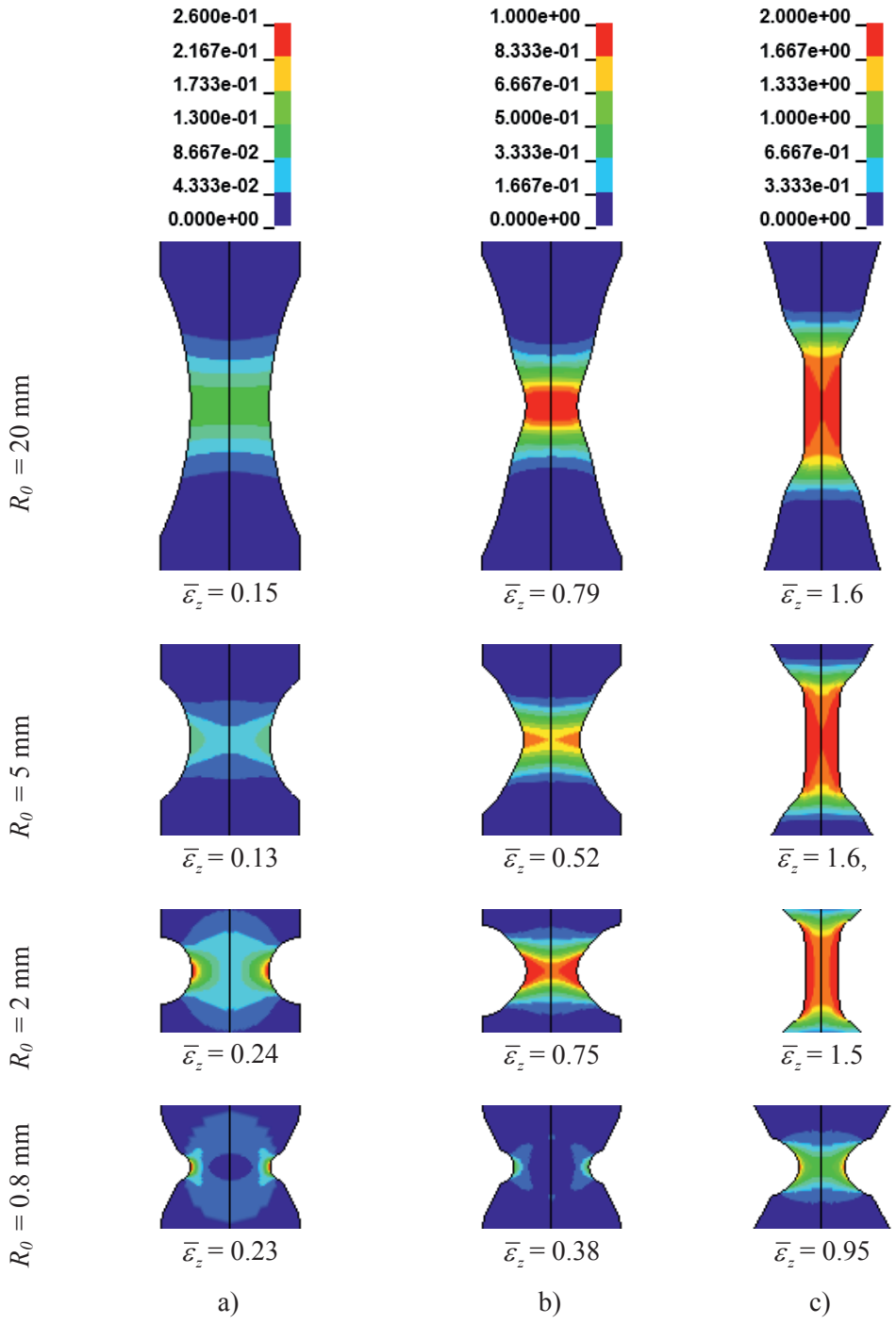

Figure 13.8 *Contour plots of plastic strain from simulations of the HDPE specimens. The columns a), b) and c) refer to different deformation levels.*

The axial force is plotted against the average radial strain from both numerical simulations and experiments in Figure 13.9 and Figure 13.10. These figures provide a more precise representation of the difference between the numerical and the experimental data, since these quantities are more directly comparable. The force is taken directly from the numerical simulations and the tensile testing machine without any kind of conversion. The average radial strain is determined from the radius measured exactly in the minimum cross section of both the numerical models and the test specimens. It becomes clear also here that the material model is better for HDPE than for PVC at predicting the behaviour before localization.

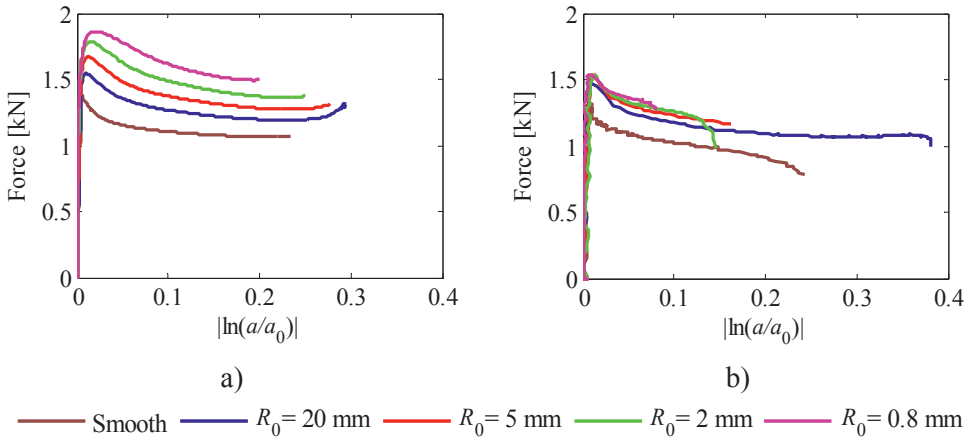

Figure 13.9 *Force against average radial strain for PVC in a) numerical simulations and b) experimental tests.*

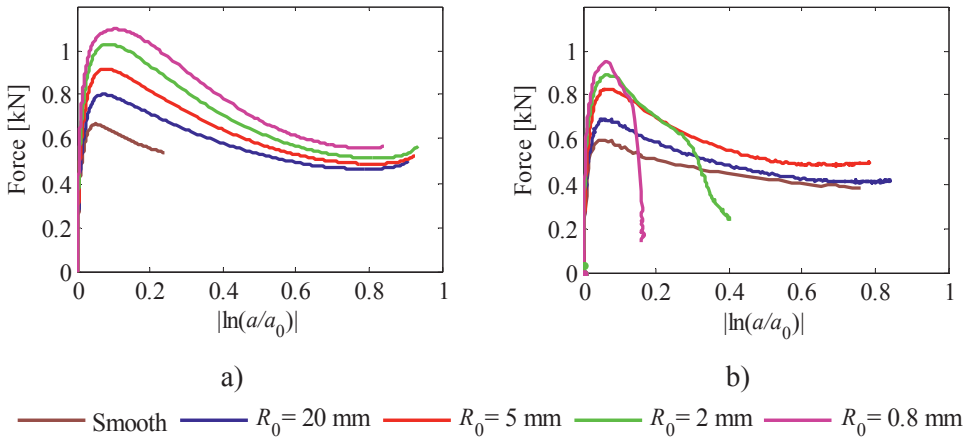

Figure 13.10 *Force against average radial strain for HDPE in a) numerical simulations and b) experimental tests.*

Figure 13.11 and Figure 13.12 show average radial strain against average axial strain. By comparing the contraction of the minimum cross section of the finite element models and the experimental tests, it is seen that the volume change is poorly reproduced by the simulations. The variation in the contraction produced by the different notch geometries is not captured. In general, the finite element model predicts stronger contraction of the minimum cross section than what is observed in the experiments. This means that the estimated increase of volume is too small in the finite element analyses.

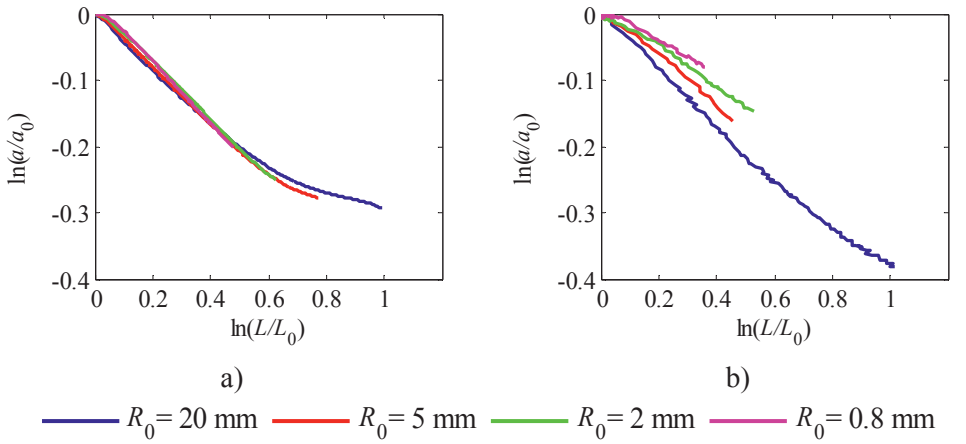

Figure 13.11 *Average radial strain against average axial strain for PVC in a) numerical simulations and b) experimental tests.*

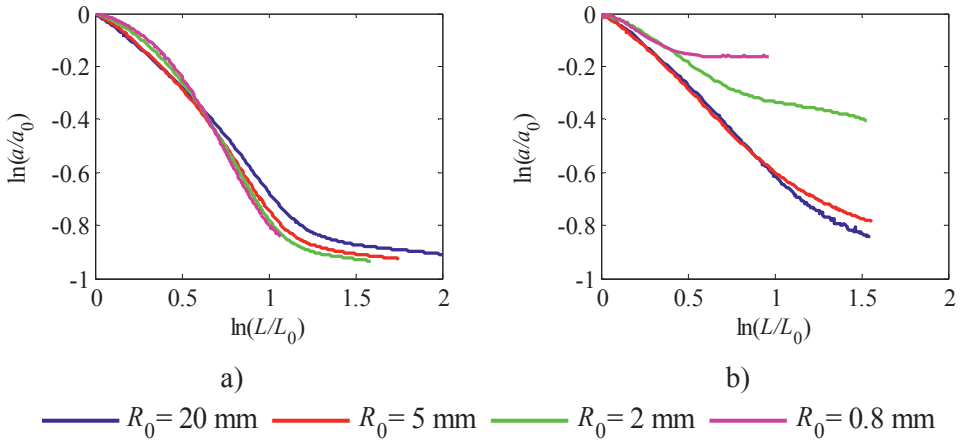

Figure 13.12 *Average radial strain against average axial strain for HDPE in a) numerical simulations and b) experimental tests.*

From the numerical results it is seen that the notch produces heterogeneous stress and strain fields that vary with the notch radius R. In the following, radial distributions of the stress triaxiality ratio σ^* and the plastic volume strain ε_v^p for each of the materials and geometries are presented. The stress triaxiality factor was found according to Equation (13.5) employing the hydrostatic stress $I_1/3$ and the equivalent von Mises stress $\sqrt{3J_2}$ taken directly from LS-DYNA. The plastic volume strains ε_v^p was found by Equation (13.4). The results are presented in Figure 13.13 to Figure 13.16 for PVC, while Figure 13.17 to Figure 13.20 display results for HDPE. Each figure includes three lines representing the three deformation levels which were displayed in sub-figures a), b) and c) in Figure 13.7 and Figure 13.8.

Even though the different figures represent different deformation stages, it seems that the stress triaxiality factor varies from case to case and also during deformation. A comparison between the different figures shows that specimens with largest R_0 have the lowest σ^*. By comparing the deformation levels represented within each figure, it is seen that as the model of the specimen is deformed a small neck is formed inside the pre-machined notch causing a reduction of R. Consequently, the value of σ^* increases in the centre of the specimen. During further deformation R increases again, and σ^* is reduced.

For all specimens, except those with the smallest notch, both the stress triaxiality σ^* and the plastic volume strain ε_v^p have their largest value in the centre of the specimen. In the specimens with R_0 = 0.8 mm the maximum values occur closer to the root of the notch.

In the numerical simulations, the plastic dilation parameter is β = 1.27 for PVC and β = 1.04 for PVC. As a result, the volume strain in the simulations of PVC is in general higher than in the simulations of HDPE even though the level of average axial strain $\bar{\varepsilon}_z$ is higher in HDPE.

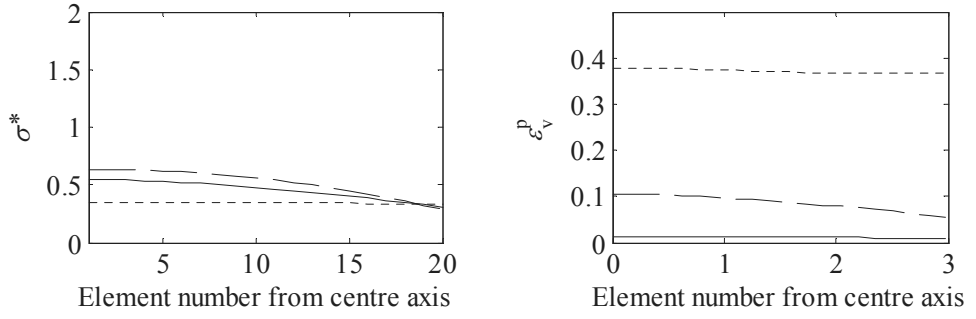

Figure 13.13 *Radial distribution of a) stress triaxiality ratio and b) plastic volume strain in the minimum cross section of PVC model with R_0 = 20 mm. The solid lines represent $\bar{\varepsilon}_z$ = 0.040, the dashed lines $\bar{\varepsilon}_z$ =0.13 and the dotted lines $\bar{\varepsilon}_z$ =0.99.*

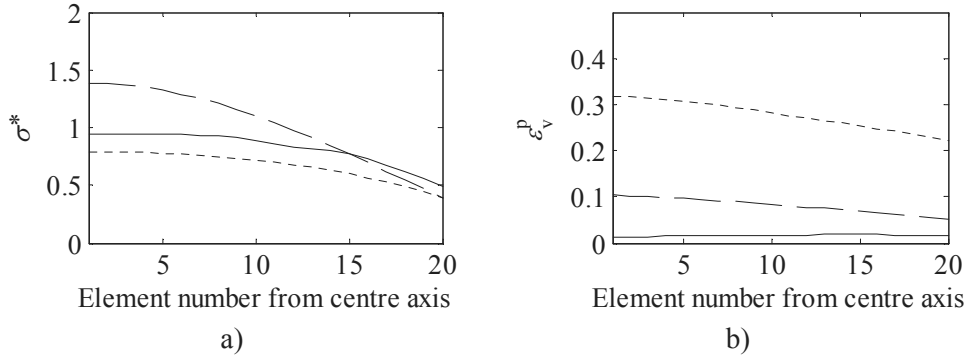

Figure 13.14 *Radial distribution of a) stress triaxiality ratio and b) plastic volume strain in the minimum cross section of PVC model with R_0 = 5 mm. The solid lines represent $\bar{\varepsilon}_z$ = 0.054, the dashed lines $\bar{\varepsilon}_z$ =0.18 and the dotted lines $\bar{\varepsilon}_z$ =0.47.*

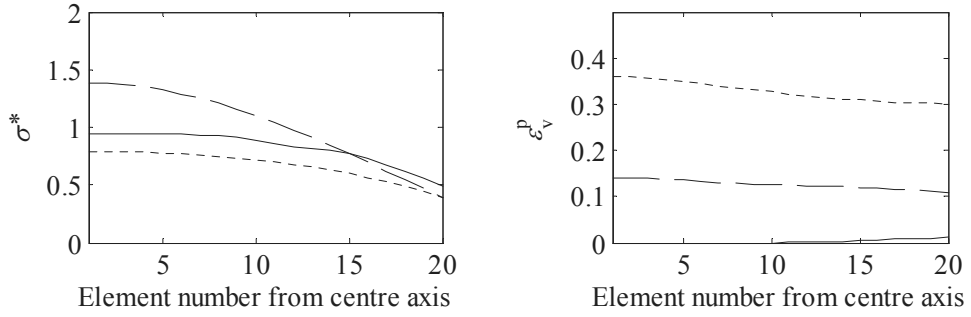

Figure 13.15 *Radial distribution of a) stress triaxiality ratio and b) plastic volume strain in the minimum cross section of PVC model with* R_0 *= 2 mm. The solid lines represent* $\bar{\varepsilon}_z$ *= 0.038, the dashed lines* $\bar{\varepsilon}_z$ *=0.18 and the dotted lines* $\bar{\varepsilon}_z$ *=0.47.*

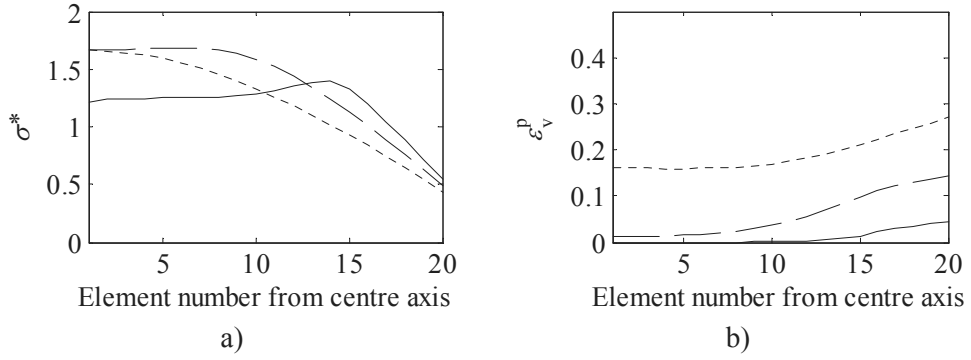

Figure 13.16 *Radial distribution of a) stress triaxiality ratio and b) plastic volume strain in the minimum cross section of PVC model with* R_0 *= 0.8 mm. The solid lines represent* $\bar{\varepsilon}_z$ *= 0.054, the dashed lines* $\bar{\varepsilon}_z$ *=0.18 and the dotted lines* $\bar{\varepsilon}_z$ *=0.47.*

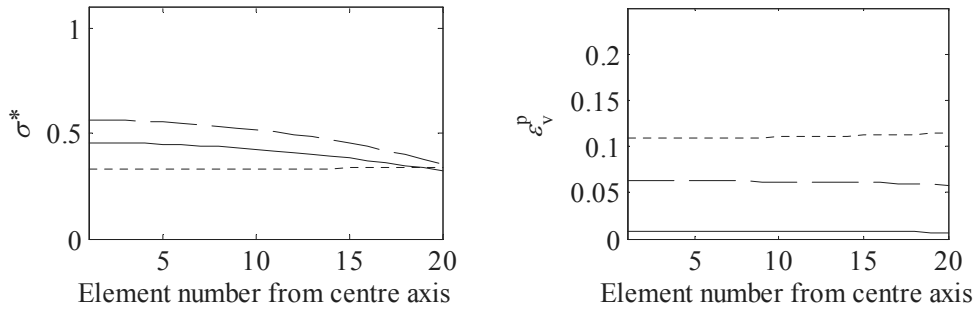

Figure 13.17 *Radial distribution of a) stress triaxiality ratio and b) plastic volume strain in the minimum cross section of HDPE model with* R_0 *= 20 mm. The solid lines represent* $\bar{\varepsilon}_z$ *= 0.15, the dashed lines* $\bar{\varepsilon}_z$ *=0.79 and the dotted lines* $\bar{\varepsilon}_z$ *=1.6.*

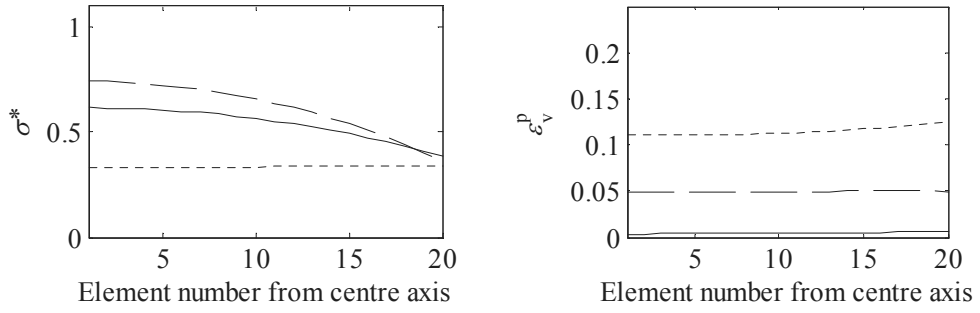

Figure 13.18 *Radial distribution of a) stress triaxiality ratio and b) plastic volume strain in the minimum cross section of HDPE model with* R_0 *= 5 mm. The solid lines represent* $\bar{\varepsilon}_z$ *= 0.13, the dashed lines* $\bar{\varepsilon}_z$ *=0.52 and the dotted lines* $\bar{\varepsilon}_z$ *=1.6.*

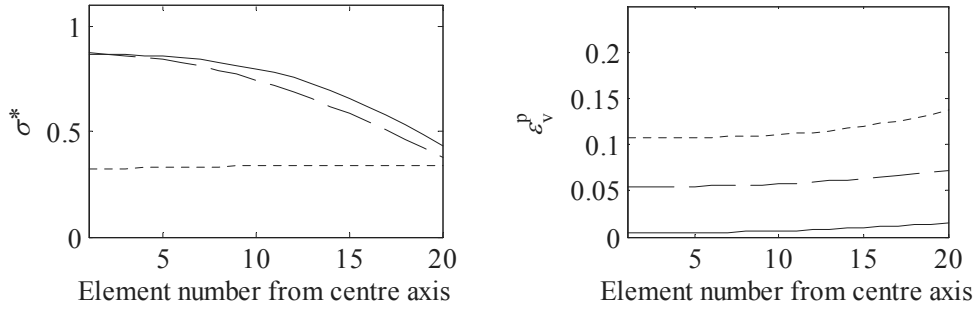

Figure 13.19 *Radial distribution of a) stress triaxiality ratio and b) plastic volume strain in the minimum cross section of HDPE model with* R_0 *= 2 mm. The solid lines represent* $\bar{\varepsilon}_z$ *= 0.24, the dashed lines* $\bar{\varepsilon}_z$ *=0.75 and the dotted lines* $\bar{\varepsilon}_z$ *=1.5.*

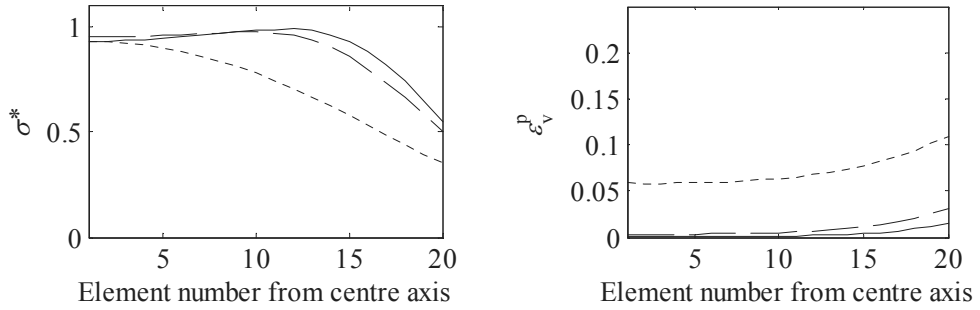

Figure 13.20 *Radial distribution of a) stress triaxiality ratio and b) plastic volume strain in the minimum cross section of HDPE model with* R_0 *= 0.8 mm. The solid lines represent* $\bar{\varepsilon}_z$ *= 0.23, the dashed lines* $\bar{\varepsilon}_z$ *=0.38 and the dotted lines* $\bar{\varepsilon}_z$ *=0.95.*

The stress state in the numerical simulations is plotted as sectors in the principal stress space $I_1/3 - \sqrt{3J_2}$ in Figure 13.21. The figure addresses the deformation state depicted in Figure 13.7 a) and Figure 13.8 a) which approximately corresponds to state at peak force. The sectors between the solid lines describe the stress state in PVC while the dashed lines represent the HDPE. Included in Figure 13.7 are also the yield functions employed to model PVC and HDPE. The figure gives an indication of what range of the yield surface that is relevant in this study. In the experimental test, only the average value of one of the stress components is measured, namely the average axial stress $\bar{\sigma}_z$. Without knowledge about the two

other stress components the yield stress from the experiments cannot be included in the figure.

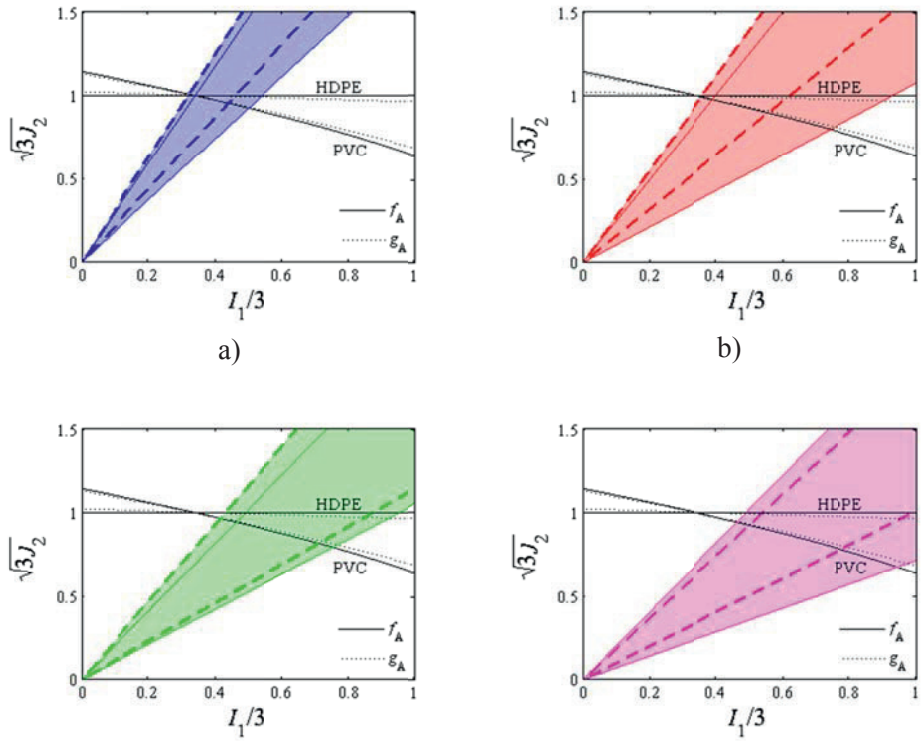

Figure 13.21 *The yield function f_A and flow potential g_A for PVC and HDPE together with sectors representing the approximate stress states present in the minimum cross section of each model at onset of plasticity in both materials. The values for PVC lie within the coloured solid lines, while the values for HDPE lies within the coloured dashed lines.*

13.7 DISCUSSION

Employing the material model of Polanco-Loria et al. [1], the deformation of axisymmetric notched tensile bars was studied numerically. The results from the simulations were compared with the experimental results presented in Chapter 8. The stress triaxiality factor σ^* in the axisymmetric notched tensile bars is shown to increase with the reduction of notch radius R, see Figure 13.13 to Figure 13.20.

The numerical simulations predict an increase in maximum average axial stress for specimens with higher triaxialities, see Figure 13.5 a) and Figure 13.6 a). This is not in accordance with the results from the experiments presented in the corresponding sub-figures b). It seems that a pressure sensitivity parameter of $\alpha =$ 1.3 for PVC does not reduce the yield stress in the constitutive model sufficiently. For HDPE, the choice of $\alpha = 1$ seems to fit better. However, in both materials the stress triaxiality that increases with decreasing notch radius R appears to introduce some damage effect that is not captured in the constitutive model. For the PVC the damage might affect the value of obtained maximum force, while for HDPE it becomes important after the maximum force level is reached. Also Figure 13.9 and Figure 13.10, representing the axial force plotted against average radial strain, support the impression that there might be some damage in the experiments that is not taken into account in the numerical simulations.

To check whether the differences observed in the maximum force level might be related so strain rate, the net strain rate $\dot{\bar{\varepsilon}}_z$ at the point of maximum force was found for the numerical simulation of each test. The values presented in Table *13.1* and Table *13.2* are similar to those found in the experimental tests, as seen in Chapter 8. Therefore, the mismatch in the maximum force level can probably not be ascribed to differences in strain rate.

The experimental tests show that the plastic dilation increases with the stress triaxiality in both materials. This is not well captured in the numerical simulations, as seen from the contraction of the minimum cross section plotted in terms of radial strain in Figure 13.11 and Figure 13.12.

The material model used in the simulations [1] employs the pressure dependent Raghava yield criterion. It is a function of the first principal stress invariant I_1 and the second deviatoric stress invariant J_2, where the shape is controlled by the pressure dependency parameter α. Since the stress triaxiality σ^* is the ratio between the two invariants it serves as an indication of the location on the yield surface. For PVC, modelled with $\alpha = 1.3$, a stress state of high triaxiality reduces

the yield stress measured in terms of the peak of average axial stress $\bar{\sigma}_z$. For HDPE with $\alpha = 1$, the value of I_1 does not affect yielding.

In Chapter 6 it was suggested that the peak stress in the mineral filled PVC can be interpreted as a "matrix - particle debonding stress" rather than a "yield stress of the PVC matrix". Micrographs of HDPE reveal that also this material contains some amount of particles, although it is much less than the PVC. In this perspective it is possible to imagine that a high triaxial stress state stimulates the process of particle debonding. Moreover, such a stress state most probably enhances the void growth around the debonded particles. Therefore, the numerical results might have been better by using a yield criterion and a plastic potential with blunter shape in the domain of hydrostatic tension. Then the yield stress would have been lower for higher stress triaxialities. Also, the gradient of the plastic potential would produce higher volume strains.

For the modelling of the mineral filled PVC material, a softening function was employed by using that $\sigma_T > \sigma_S$. This softening can be interpreted as the reduction of strength in the material due to damage. It might have been an interesting modification of the material model to control, or just scale, the softening by the volumetric strain instead of the equivalent plastic strain. However, this would not affect the prediction of the yield stress, i.e. the debonding stress, only the subsequent behaviour.

Another approach of modelling the behaviour of these materials subjected to triaxial stress could have been to use a material model based on the mechanisms of void growth. Boisot et al. [4] report good numerical results from employing a modified Gurson-Needleman-Tvergaard model on axisymmetric notched specimens of polyamide 11 with an initial porosity of 1%. Especially when it comes to peak stress, stress softening and the stress plateau, they state that their results are in good agreement with experimental data. However, such a material model requires a more complicated calibration process including determination of the initial porosity. The model is therefore considered as less attractive for industrial applications.

13.8 CONCLUDING REMARKS

- In the experimental tests there seem to be some increasing damage with stress triaxiality that affects the volume change and the maximum force level. This is not captured by the numerical simulations.

REFERENCES

[1] M. Polanco-Loria, A.H. Clausen, T. Berstad, O.S. Hopperstad. Constitutive model for thermoplastics with structural applications. *International Journal of Impact Engineering*, **37** (2010), 1207-1219.

[2] LS-DYNA. LS-DYNA Keyword User's Manual. Version 971, Livermore Software Technology Corporation (LSTC), 2007.

[3] M.T. Hovden. Test and numerical simulations of polymer components. Master thesis, Department of Structural Engineering, NTNU, (2010).

[4] G. Boisot, L. Laiarinandrasana, J. Besson, C. Fond, G. Hochstetter. Experimental investigations and modeling of volume change induced by void growth in polyamide 11. *International Journal of Solids and Structures*, **48** (2011), 2642-2654.

CHAPTER 14

DISCUSSION, CONCLUSIONS AND SUGGESTIONS FOR FURTHER WORK

14.1 DISCUSSION

Experimental and numerical studies of the large-deformation behaviour of thermoplastics have been addressed in this thesis. The work is a part of a more comprehensive research project about constitutive modelling of thermoplastics for industrial applications.

Within the framework of the polymer research project, two types of thermoplastic polymers, a PVC and a HDPE, are addressed. These two materials were chosen because they are fundamentally different. The PVC is an amorphous polymer filled with mineral fillers by a volume fraction of about 0.2. The HDPE is semicrystalline and contains much less particle fillers.

Through the research project, the behaviour in uniaxial tension and compression has already been well studied and reported for the PVC and the HDPE [1, 2]. The two materials have different mechanical behaviour. The Young's modulus and the yield stress for the PVC are somewhat higher than for the HDPE. From tension and compression tests it has been found that the yield stress of PVC is pressure sensitive, while that of HDPE is not. Moreover, the PVC dilates markedly during uniaxial tension, while the dilation in the HDPE is almost zero. After the onset of yielding a stress drop is observed on the stress-strain curve of the PVC. The HDPE has no such stress drop. Even though the fundamental behaviour of the two materials is well known, little has been done to study the behaviour at more complex stress states. Furthermore, the mechanisms behind the deformation have been paid little attention to.

The research group has proposed a constitutive model for thermoplastics for industrial applications [3]. In this monograph, the capabilities and the limitations of this constitutive model at different stress states have been explored. Moreover, the mechanisms behind the deformation characteristics, that are not yet fully understood, have been studied.

It was considered relevant to check how the constitutive model, with parameters determined from uniaxial tension and compression tests, was applicable for other stress states. To serve as validation, biaxial tension tests of specimens of the PVC and the HDPE were carried out, as described in Chapter 7. These tests produced a complex biaxial stress state in the centre part of the samples without any distortion from contact or friction. Numerical simulations of the behaviour, presented in Chapter 12, show that the constitutive model is well capable of predicting the maximum level of the force-displacement curves from the experiments. Thus, the pressure sensitivity of the onset of yield in the biaxial test specimens is captured by the model. Moreover, the strain fields produced in the numerical simulations seem to be comparable with those from the laboratory tests. The capability of the constitutive model was also checked for triaxial stress states in Chapter 13. This was done through numerical simulations of the tests on axisymmetric tensile bars with notch reported in Chapter 8. At high stress triaxialities there seem to be some damage in the tests that is not captured by the constitutive model. The numerical model overestimates the yield stress in the PVC at high stress triaxialities. For HDPE the result is somewhat better. However, the volume change observed in both materials at high stress triaxialities is not well captured by the numerical model. To sum up, it can be concluded that the constitutive model works well for biaxial tension while it is less accurate for higher triaxialities. Since polymer components are often injection moulded into components with maximum wall thickness up to 3 mm, it can be argued that the biaxial load case is more relevant. However, it is important to know that the constitutive model can have some limitations at highly triaxial stress states.

By employing various experimental test setups and different measurement techniques the deformation mechanisms of the PVC and HDPE have been investigated. In Chapter 5, addressing loading, storage and reloading of uniaxial tension specimens, it was found that the shape of the initial stress-strain curve of HDPE is recalled during the second loading cycle. Moreover, the volume change remains close to zero. The response of PVC, on the other hand, is softer and the stress-softening effect vanishes during the second loading cycle. This result, together with the observed plastic dilation and the stress whitening, was interpreted as a sign of damage occurring in the material. The damage in PVC was investigated on a microscopic level in Chapter 6. It was concluded that debonding of mineral particles and subsequent void growth are two damage mechanisms in

the PVC. This means that the damage cannot be determined by volume strains alone. At a certain stress level, the particles detach from the matrix, and the material consequently loses 20% of its load carrying cross section. It was further suggested that the stress softening effect in the PVC could be a consequence of damage. Damage and void growth was also investigated in a numerical study of the matrix-particle interaction by the use of unit cell models in Chapter 9. The numerical simulations confirmed that debonding and void growth can cause volume changes and a stress-drop similar to what is seen in laboratory tests of the PVC. In the unit cell study, the macroscopic peak stress of the composite was lower than the yield stress of the matrix material. This means that the peak stress observed in laboratory test of PVC might be related to debonding of particles. The unit cell study confirmed that the subsequent stress drop may be related to the loss of strength due to debonding. However, the peak stress and stress drop observed in compression call for further investigation. In fact, the stress drop is more intense in compression than in tension. The reason for this observation remains to be explained.

It is shown in Chapter 8 that the volume change in both the PVC and the HDPE increase with the degree of triaxiality in the stress state. From investigation of fractured specimens, it was concluded that void growth had been a comprehensive mechanism in both materials.

14.2 Conclusions

Biaxial tension test has been proposed as a validation for the constitutive model. Further validation has been carried out on simulations of axisymmetric tensile bars with notch. It can be concluded that:

- The constitutive model is well capable of describing the behaviour of the PVC and the HDPE in biaxial tension.
- The numerical model does not capture the behaviour of PVC or HDPE at high stress triaxialities. This may be related to the enhancement of damage in the material at high stress triaxialities.

Several material test setups for investigation of the large-deformation behaviour of polymers have been presented. From the test results, it can be concluded that:

- Damage mechanisms observed in uniaxial tension of the PVC are debonding of mineral particles and void growth. These mechanisms lead to

volume change. The damage may also contribute to the stress drop on the stress-strain curve of the material.

- Void growth is a damage mechanism both in the PVC and the HDPE at high stress triaxialities. The volume change in both materials increases with the stress triaxiality. Fracture surfaces of the axisymmetric test specimens with notch further suggest that void growth and coalescence are factors determining the fracture.

14.3 SUGGESTIONS FOR FURTHER WORK

The damage mechanisms in the PVC have been identified as debonding of mineral particles and subsequent growth of voids. Thus, it seems reasonable to assume that the particle content is a determining factor for the void growth. It is tempting to suggest including the particle volume fraction as a parameter in a constitutive model. However, the particle volume fraction can be hard to determine. Material parameters that cannot be determined from stress and strain measurements are undesirable in a constitutive model for industrial applications. It may therefore be relevant to include a failure criterion simply based on a critical volume strain in the existing constitutive model. Another, more comprehensive, suggestion is to employ a flow potential formulated to consider porous materials, like the Gurson model or similar.

Turning attention to experimental work, it is recommended to carry out new compression tests. An attempt should be made to reduce the friction between the specimen and the compression platen, for instance by using some PTFE-film. Moreover, the volume change during deformation should be investigated in more depth. Addressing the stress-drop, it would have been interesting to study compressed specimens in a scanning electron microscope (SEM) to see whether any signs of damage could be observed on the microscopic level. Simulations of unit-cell models in compression could also be carried out at the same time to study the matrix-particle interaction. In addition, loading and reloading in compression could be performed to investigate the effect of a second load cycle on the peak stress.

It would have been interesting to study the effect of the mineral particles closer. For instance, the matrix-particle interaction in other materials than PVC can be studied. As a start, a SEM study of the deformation of HDPE can be performed. Moreover, it is suggested to employ specimens made of the same type of polymer but with different volume fractions of particles added. Comparison of stress-strain

curves in tension and compression, as well as volume strain curves, might give deeper insight in how the particles affect the mechanical response. In particular, it would be interesting to see how different particle volume fractions affect the damage.

Another relevant topic concerning material modelling of thermoplastics for industrial applications is the material behaviour at various temperatures and at higher strain rates. At other temperatures or at higher strain rates, the debonding and void growth may act differently.

REFERENCES

[1] M.T. Hovden. Test and numerical simulations of polymer components. Master thesis, Department of Structural Engineering, NTNU, (2010).

[2] R.T. Moura, A.H. Clausen, E. Fagerholt, M. Alves, M. Langseth. Impact on HDPE and PVC plates - Experimental tests and numerical simulations. *International Journal of Impact Engineering*, **37** (2010), 580-598.

[3] M. Polanco-Loria, A.H. Clausen, T. Berstad, O.S. Hopperstad. Constitutive model for thermoplastics with structural applications. *International Journal of Impact Engineering*, **37** (2010), 1207-1219.

DEPARTMENT OF STRUCTURAL ENGINEERING
NORWEGIAN UNIVERSITY OF SCIENCE AND TECHNOLOGY

N–7491 TRONDHEIM, NORWAY
Telephone: +47 73 59 47 00 Telefax: +47 73 59 47 01

"Reliability Analysis of Structural Systems using Nonlinear Finite Element Methods",
C. A. Holm, 1990:23, ISBN 82-7119-178-0.

"Uniform Stratified Flow Interaction with a Submerged Horizontal Cylinder",
Ø. Arntsen, 1990:32, ISBN 82-7119-188-8.

"Large Displacement Analysis of Flexible and Rigid Systems Considering Displacement-Dependent Loads and Nonlinear Constraints",
K. M. Mathisen, 1990:33, ISBN 82-7119-189-6.

"Solid Mechanics and Material Models including Large Deformations",
E. Levold, 1990:56, ISBN 82-7119-214-0, ISSN 0802-3271.

"Inelastic Deformation Capacity of Flexurally-Loaded Aluminium Alloy Structures",
T. Welo, 1990:62, ISBN 82-7119-220-5, ISSN 0802-3271.

"Visualization of Results from Mechanical Engineering Analysis",
K. Aamnes, 1990:63, ISBN 82-7119-221-3, ISSN 0802-3271.

"Object-Oriented Product Modeling for Structural Design",
S. I. Dale, 1991:6, ISBN 82-7119-258-2, ISSN 0802-3271.

"Parallel Techniques for Solving Finite Element Problems on Transputer Networks",
T. H. Hansen, 1991:19, ISBN 82-7119-273-6, ISSN 0802-3271.

"Statistical Description and Estimation of Ocean Drift Ice Environments",
R. Korsnes, 1991:24, ISBN 82-7119-278-7, ISSN 0802-3271.

“Properties of concrete related to fatigue damage: with emphasis on high strength concrete”,
G. Petkovic, 1991:35, ISBN 82-7119-290-6, ISSN 0802-3271.

"Turbidity Current Modelling",
B. Brørs, 1991:38, ISBN 82-7119-293-0, ISSN 0802-3271.

"Zero-Slump Concrete: Rheology, Degree of Compaction and Strength. Effects of Fillers as Part Cement-Replacement",
C. Sørensen, 1992:8, ISBN 82-7119-357-0, ISSN 0802-3271.

"Nonlinear Analysis of Reinforced Concrete Structures Exposed to Transient Loading",
K. V. Høiseth, 1992:15, ISBN 82-7119-364-3, ISSN 0802-3271.

"Finite Element Formulations and Solution Algorithms for Buckling and Collapse Analysis of Thin Shells",
R. O. Bjærum, 1992:30, ISBN 82-7119-380-5, ISSN 0802-3271.

"Response Statistics of Nonlinear Dynamic Systems",
J. M. Johnsen, 1992:42, ISBN 82-7119-393-7, ISSN 0802-3271.

"Digital Models in Engineering. A Study on why and how engineers build and operate digital models for decisison support",
J. Høyte, 1992:75, ISBN 82-7119-429-1, ISSN 0802-3271.

"Sparse Solution of Finite Element Equations",
A. C. Damhaug, 1992:76, ISBN 82-7119-430-5, ISSN 0802-3271.

"Some Aspects of Floating Ice Related to Sea Surface Operations in the Barents Sea",
S. Løset, 1992:95, ISBN 82-7119-452-6, ISSN 0802-3271.

"Modelling of Cyclic Plasticity with Application to Steel and Aluminium Structures",
O. S. Hopperstad, 1993:7, ISBN 82-7119-461-5, ISSN 0802-3271.

"The Free Formulation: Linear Theory and Extensions with Applications to Tetrahedral Elements
with Rotational Freedoms",
G. Skeie, 1993:17, ISBN 82-7119-472-0, ISSN 0802-3271.

"Høyfast betongs motstand mot piggdekkslitasje. Analyse av resultater fra prøving i Veisliter'n",
T. Tveter, 1993:62, ISBN 82-7119-522-0, ISSN 0802-3271.

"A Nonlinear Finite Element Based on Free Formulation Theory for Analysis of Sandwich Structures",
O. Aamlid, 1993:72, ISBN 82-7119-534-4, ISSN 0802-3271.

"The Effect of Curing Temperature and Silica Fume on Chloride Migration and Pore Structure of High Strength Concrete",
C. J. Hauck, 1993:90, ISBN 82-7119-553-0, ISSN 0802-3271.

"Failure of Concrete under Compressive Strain Gradients",
G. Markeset, 1993:110, ISBN 82-7119-575-1, ISSN 0802-3271.
"An experimental study of internal tidal amphidromes in Vestfjorden",
J. H. Nilsen, 1994:39, ISBN 82-7119-640-5, ISSN 0802-3271.

"Structural analysis of oil wells with emphasis on conductor design",
H. Larsen, 1994:46, ISBN 82-7119-648-0, ISSN 0802-3271.

"Adaptive methods for non-linear finite element analysis of shell structures",
K. M. Okstad, 1994:66, ISBN 82-7119-670-7, ISSN 0802-3271.

"On constitutive modelling in nonlinear analysis of concrete structures",
O. Fyrileiv, 1994:115, ISBN 82-7119-725-8, ISSN 0802-3271.

"Fluctuating wind load and response of a line-like engineering structure with emphasis on motion-induced wind forces",
J. Bogunovic Jakobsen, 1995:62, ISBN 82-7119-809-2, ISSN 0802-3271.

"An experimental study of beam-columns subjected to combined torsion, bending and axial actions",
A. Aalberg, 1995:66, ISBN 82-7119-813-0, ISSN 0802-3271.

"Scaling and cracking in unsealed freeze/thaw testing of Portland cement and silica fume concretes",
S. Jacobsen, 1995:101, ISBN 82-7119-851-3, ISSN 0802-3271.

"Damping of water waves by submerged vegetation. A case study of laminaria hyperborea",
A. M. Dubi, 1995:108, ISBN 82-7119-859-9, ISSN 0802-3271.

"The dynamics of a slope current in the Barents Sea",
Sheng Li, 1995:109, ISBN 82-7119-860-2, ISSN 0802-3271.

"Modellering av delmaterialenes betydning for betongens konsistens",
Ernst Mørtsell, 1996:12, ISBN 82-7119-894-7, ISSN 0802-3271.

"Bending of thin-walled aluminium extrusions",
Birgit Søvik Opheim, 1996:60, ISBN 82-7119-947-1, ISSN 0802-3271.

"Material modelling of aluminium for crashworthiness analysis",
Torodd Berstad, 1996:89, ISBN 82-7119-980-3, ISSN 0802-3271.

"Estimation of structural parameters from response measurements on submerged floating tunnels",
Rolf Magne Larssen, 1996:119, ISBN 82-471-0014-2, ISSN 0802-3271.

“Numerical modelling of plain and reinforced concrete by damage mechanics”,
Mario A. Polanco-Loria, 1997:20, ISBN 82-471-0049-5, ISSN 0802-3271.

“Nonlinear random vibrations - numerical analysis by path integration methods”,
Vibeke Moe, 1997:26, ISBN 82-471-0056-8, ISSN 0802-3271.

“Numerical prediction of vortex-induced vibration by the finite element method”,
Joar Martin Dalheim, 1997:63, ISBN 82-471-0096-7, ISSN 0802-3271.

“Time domain calculations of buffeting response for wind sensitive structures”,
Ketil Aas-Jakobsen, 1997:148, ISBN 82-471-0189-0, ISSN 0802-3271.

"A numerical study of flow about fixed and flexibly mounted circular cylinders",
Trond Stokka Meling, 1998:48, ISBN 82-471-0244-7, ISSN 0802-3271.

“Estimation of chloride penetration into concrete bridges in coastal areas”,
Per Egil Steen, 1998:89, ISBN 82-471-0290-0, ISSN 0802-3271.

“Stress-resultant material models for reinforced concrete plates and shells”,
Jan Arve Øverli, 1998:95, ISBN 82-471-0297-8, ISSN 0802-3271.

“Chloride binding in concrete. Effect of surrounding environment and concrete composition”,
Claus Kenneth Larsen, 1998:101, ISBN 82-471-0337-0, ISSN 0802-3271.

“Rotational capacity of aluminium alloy beams”,
Lars A. Moen, 1999:1, ISBN 82-471-0365-6, ISSN 0802-3271.

“Stretch Bending of Aluminium Extrusions”,
Arild H. Clausen, 1999:29, ISBN 82-471-0396-6, ISSN 0802-3271.

“Aluminium and Steel Beams under Concentrated Loading”,
Tore Tryland, 1999:30, ISBN 82-471-0397-4, ISSN 0802-3271.

"Engineering Models of Elastoplasticity and Fracture for Aluminium Alloys",
Odd-Geir Lademo, 1999:39, ISBN 82-471-0406-7, ISSN 0802-3271.

"Kapasitet og duktilitet av dybelforbindelser i trekonstruksjoner",
Jan Siem, 1999:46, ISBN 82-471-0414-8, ISSN 0802-3271.

“Etablering av distribuert ingeniørarbeid; Teknologiske og organisatoriske erfaringer fra en norsk ingeniørbedrift”,
Lars Line, 1999:52, ISBN 82-471-0420-2, ISSN 0802-3271.

“Estimation of Earthquake-Induced Response”,
Símon Ólafsson, 1999:73, ISBN 82-471-0443-1, ISSN 0802-3271.

“Coastal Concrete Bridges: Moisture State, Chloride Permeability and Aging Effects”
Ragnhild Holen Relling, 1999:74, ISBN 82-471-0445-8, ISSN 0802-3271.

”Capacity Assessment of Titanium Pipes Subjected to Bending and External Pressure”,
Arve Bjørset, 1999:100, ISBN 82-471-0473-3, ISSN 0802-3271.

“Validation of Numerical Collapse Behaviour of Thin-Walled Corrugated Panels”,
Håvar Ilstad, 1999:101, ISBN 82-471-0474-1, ISSN 0802-3271.

“Strength and Ductility of Welded Structures in Aluminium Alloys”,
Miroslaw Matusiak, 1999:113, ISBN 82-471-0487-3, ISSN 0802-3271.

“Thermal Dilation and Autogenous Deformation as Driving Forces to Self-Induced Stresses in High Performance Concrete”,
Øyvind Bjøntegaard, 1999:121, ISBN 82-7984-002-8, ISSN 0802-3271.

“Some Aspects of Ski Base Sliding Friction and Ski Base Structure”,
Dag Anders Moldestad, 1999:137, ISBN 82-7984-019-2, ISSN 0802-3271.

"Electrode reactions and corrosion resistance for steel in mortar and concrete",
Roy Antonsen, 2000:10, ISBN 82-7984-030-3, ISSN 0802-3271.

"Hydro-Physical Conditions in Kelp Forests and the Effect on Wave Damping and Dune Erosion. A case study on Laminaria Hyperborea",
Stig Magnar Løvås, 2000:28, ISBN 82-7984-050-8, ISSN 0802-3271.

"Random Vibration and the Path Integral Method",
Christian Skaug, 2000:39, ISBN 82-7984-061-3, ISSN 0802-3271.

"Buckling and geometrical nonlinear beam-type analyses of timber structures",
Trond Even Eggen, 2000:56, ISBN 82-7984-081-8, ISSN 0802-3271.

”Structural Crashworthiness of Aluminium Foam-Based Components”,
Arve Grønsund Hanssen, 2000:76, ISBN 82-7984-102-4, ISSN 0809-103X.

“Measurements and simulations of the consolidation in first-year sea ice ridges, and some aspects of mechanical behaviour”,
Knut V. Høyland, 2000:94, ISBN 82-7984-121-0, ISSN 0809-103X.

”Kinematics in Regular and Irregular Waves based on a Lagrangian Formulation”,
Svein Helge Gjøsund, 2000-86, ISBN 82-7984-112-1, ISSN 0809-103X.

”Self-Induced Cracking Problems in Hardening Concrete Structures”,
Daniela Bosnjak, 2000-121, ISBN 82-7984-151-2, ISSN 0809-103X.

"Ballistic Penetration and Perforation of Steel Plates",
Tore Børvik, 2000:124, ISBN 82-7984-154-7, ISSN 0809-103X.

"Freeze-Thaw resistance of Concrete. Effect of: Curing Conditions, Moisture Exchange and Materials",
Terje Finnerup Rønning, 2001:14, ISBN 82-7984-165-2, ISSN 0809-103X

"Structural behaviour of post tensioned concrete structures. Flat slab. Slabs on ground",
Steinar Trygstad, 2001:52, ISBN 82-471-5314-9, ISSN 0809-103X.

"Slipforming of Vertical Concrete Structures. Friction between concrete and slipform panel",
Kjell Tore Fosså, 2001:61, ISBN 82-471-5325-4, ISSN 0809-103X.

"Some numerical methods for the simulation of laminar and turbulent incompressible flows",
Jens Holmen, 2002:6, ISBN 82-471-5396-3, ISSN 0809-103X.

“Improved Fatigue Performance of Threaded Drillstring Connections by Cold Rolling”,
Steinar Kristoffersen, 2002:11, ISBN: 82-421-5402-1, ISSN 0809-103X.

"Deformations in Concrete Cantilever Bridges: Observations and Theoretical Modelling",
Peter F. Takâcs, 2002:23, ISBN 82-471-5415-3, ISSN 0809-103X.

"Stiffened aluminium plates subjected to impact loading",
Hilde Giæver Hildrum, 2002:69, ISBN 82-471-5467-6, ISSN 0809-103X.

"Full- and model scale study of wind effects on a medium-rise building in a built up area",
Jónas Thór Snæbjørnsson, 2002:95, ISBN82-471-5495-1, ISSN 0809-103X.

“Evaluation of Concepts for Loading of Hydrocarbons in Ice-infested water”,
Arnor Jensen, 2002:114, ISBN 82-417-5506-0, ISSN 0809-103X.

”Numerical and Physical Modelling of Oil Spreading in Broken Ice”,
Janne K. Økland Gjøsteen, 2002:130, ISBN 82-471-5523-0, ISSN 0809-103X.

”Diagnosis and protection of corroding steel in concrete”,
Franz Pruckner, 20002:140, ISBN 82-471-5555-4, ISSN 0809-103X.

“Tensile and Compressive Creep of Young Concrete: Testing and Modelling”,
Dawood Atrushi, 2003:17, ISBN 82-471-5565-6, ISSN 0809-103X.

“Rheology of Particle Suspensions. Fresh Concrete, Mortar and Cement Paste with Various Types of Lignosulfonates”,
Jon Elvar Wallevik, 2003:18, ISBN 82-471-5566-4, ISSN 0809-103X.

“Oblique Loading of Aluminium Crash Components”,
Aase Reyes, 2003:15, ISBN 82-471-5562-1, ISSN 0809-103X.

“Utilization of Ethiopian Natural Pozzolans”,
Surafel Ketema Desta, 2003:26, ISSN 82-471-5574-5, ISSN:0809-103X.

“Behaviour and strength prediction of reinforced concrete structures with discontinuity regions”, Helge Brå, 2004:11, ISBN 82-471-6222-9, ISSN 1503-8181.

“High-strength steel plates subjected to projectile impact. An experimental and numerical study”, Sumita Dey, 2004:38, ISBN 82-471-6282-2 (printed version), ISBN 82-471-6281-4 (electronic version), ISSN 1503-8181.

“Alkali-reactive and inert fillers in concrete. Rheology of fresh mixtures and expansive reactions.”
Bård M. Pedersen, 2004:92, ISBN 82-471-6401-9 (printed version), ISBN 82-471-6400-0 (electronic version), ISSN 1503-8181.

“On the Shear Capacity of Steel Girders with Large Web Openings”.
Nils Christian Hagen, 2005:9 ISBN 82-471-6878-2 (printed version), ISBN 82-471-6877-4 (electronic version), ISSN 1503-8181.

”Behaviour of aluminium extrusions subjected to axial loading”.
Østen Jensen, 2005:7, ISBN 82-471-6873-1 (printed version), ISBN 82-471-6872-3 (electronic version), ISSN 1503-8181.

”Thermal Aspects of corrosion of Steel in Concrete”.
Jan-Magnus Østvik, 2005:5, ISBN 82-471-6869-3 (printed version), ISBN 82-471-6868 (electronic version), ISSN 1503-8181.

”Mechanical and adaptive behaviour of bone in relation to hip replacement.” A study of bone remodelling and bone grafting.
Sébastien Muller, 2005:34, ISBN 82-471-6933-9 (printed version), ISBN 82-471-6932-0 (electronic version), ISSN 1503-8181.

“Analysis of geometrical nonlinearities with applications to timber structures”.
Lars Wollebæk, 2005:74, ISBN 82-471-7050-5 (printed version), ISBN 82-471-7019-1 (electronic version), ISSN 1503-8181.

“Pedestrian induced lateral vibrations of slender footbridges”,
Anders Rönnquist, 2005:102, ISBN 82-471-7082-5 (printed version), ISBN 82-471-7081-7 (electronic version), ISSN 1503-8181.

“Initial Strength Development of Fly Ash and Limestone Blended Cements at Various Temperatures Predicted by Ultrasonic Pulse Velocity”,
Tom Ivar Fredvik, 2005:112, ISBN 82-471-7105-8 (printed version), ISBN 82-471-7103-1 (electronic version), ISSN 1503-8181.

“Behaviour and modelling of thin-walled cast components”,
Cato Dørum, 2005:128, ISBN 82-471-7140-6 (printed version), ISBN 82-471-7139-2 (electronic version), ISSN 1503-8181.

“Behaviour and modelling of selfpiercing riveted connections”,
Raffaele Porcaro, 2005:165, ISBN 82-471-7219-4 (printed version), ISBN 82-471-7218-6 (electronic version), ISSN 1503-8181.

”Behaviour and Modelling og Aluminium Plates subjected to Compressive Load”,
Lars Rønning, 2005:154, ISBN 82-471-7169-1 (printed version), ISBN 82-471-7195-3 (electronic version), ISSN 1503-8181.

”Bumper beam-longitudinal system subjected to offset impact loading”,
Satyanarayana Kokkula, 2005:193, ISBN 82-471-7280-1 (printed version), ISBN 82-471-7279-8 (electronic version), ISSN 1503-8181.

“Control of Chloride Penetration into Concrete Structures at Early Age”,
Guofei Liu, 2006:46, ISBN 82-471-7838-9 (printed version), ISBN 82-471-7837-0 (electronic version), ISSN 1503-8181.

“Modelling of Welded Thin-Walled Aluminium Structures”,
Ting Wang, 2006:78, ISBN 82-471-7907-5 (printed version), ISBN 82-471-7906-7 (electronic version), ISSN 1503-8181.

”Time-variant reliability of dynamic systems by importance sampling and probabilistic analysis of ice loads”,
Anna Ivanova Olsen, 2006:139, ISBN 82-471-8041-3 (printed version), ISBN 82-471-8040-5 (electronic version), ISSN 1503-8181.

“Fatigue life prediction of an aluminium alloy automotive component using finite element analysis of surface topography”.
Sigmund Kyrre Ås, 2006:25, ISBN 82-471-7791-9 (printed version), ISBN 82-471-7791-9 (electronic version), ISSN 1503-8181.

”Constitutive models of elastoplasticity and fracture for aluminium alloys under strain path change”,
Dasharatha Achani, 2006:76, ISBN 82-471-7903-2 (printed version), ISBN 82-471-7902-4 (electronic version), ISSN 1503-8181.

“Simulations of 2D dynamic brittle fracture by the Element-free Galerkin method and linear fracture mechanics”,
Tommy Karlsson, 2006:125, ISBN 82-471-8011-1 (printed version), ISBN 82-471-8010-3 (electronic version), ISSN 1503-8181.

“Penetration and Perforation of Granite Targets by Hard Projectiles”,
Chong Chiang Seah, 2006:188, ISBN 82-471-8150-9 (printed version), ISBN 82-471-8149-5 (electronic version), ISSN 1503-8181.

“Deformations, strain capacity and cracking of concrete in plastic and early hardening phases”,
Tor Arne Hammer, 2007:234, ISBN 978-82-471-5191-4 (printed version), ISBN 978-82-471-5207-2 (electronic version), ISSN 1503-8181.

“Crashworthiness of dual-phase high-strength steel: Material and Component behaviour”, Venkatapathi Tarigopula, 2007:230, ISBN 82-471-5076-4 (printed version), ISBN 82-471-5093-1 (electronic version), ISSN 1503-8181.

“Fibre reinforcement in load carrying concrete structures”,
Åse Lyslo Døssland, 2008:50, ISBN 978-82-471-6910-0 (printed version), ISBN 978-82-471-6924-7 (electronic version), ISSN 1503-8181.

“Low-velocity penetration of aluminium plates”,
Frode Grytten, 2008:46, ISBN 978-82-471-6826-4 (printed version), ISBN 978-82-471-6843-1 (electronic version), ISSN 1503-8181.

“Robustness studies of structures subjected to large deformations”,
Ørjan Fyllingen, 2008:24, ISBN 978-82-471-6339-9 (printed version), ISBN 978-82-471-6342-9 (electronic version), ISSN 1503-8181.

“Constitutive modelling of morsellised bone”,
Knut Birger Lunde, 2008:92, ISBN 978-82-471-7829-4 (printed version), ISBN 978-82-471-7832-4 (electronic version), ISSN 1503-8181.

“Experimental Investigations of Wind Loading on a Suspension Bridge Girder”,
Bjørn Isaksen, 2008:131, ISBN 978-82-471-8656-5 (printed version), ISBN 978-82-471-8673-2 (electronic version), ISSN 1503-8181.

"Cracking Risk of Concrete Structures in The Hardening Phase",
Guomin Ji, 2008:198, ISBN 978-82-471-1079-9 (printed version), ISBN 978-82-471-1080-5 (electronic version), ISSN 1503-8181.

"Modelling and numerical analysis of the porcine and human mitral apparatus",
Victorien Emile Prot, 2008:249, ISBN 978-82-471-1192-5 (printed version), ISBN 978-82-471-1193-2 (electronic version), ISSN 1503-8181.

"Strength analysis of net structures",
Heidi Moe, 2009:48, ISBN 978-82-471-1468-1 (printed version), ISBN 978-82-471-1469-8 (electronic version), ISSN1503-8181.

"Numerical analysis of ductile fracture in surface cracked shells",
Espen Berg, 2009:80, ISBN 978-82-471-1537-4 (printed version), ISBN 978-82-471-1538-1 (electronic version), ISSN 1503-8181.

"Subject specific finite element analysis of bone – for evaluation of the healing of a leg lengthening and evaluation of femoral stem design",
Sune Hansborg Pettersen, 2009:99, ISBN 978-82-471-1579-4 (printed version), ISBN 978-82-471-1580-0 (electronic version), ISSN 1503-8181.

"Evaluation of fracture parameters for notched multi-layered structures",
Lingyun Shang, 2009:137, ISBN 978-82-471-1662-3 (printed version), ISBN 978-82-471-1663-0 (electronic version), ISSN 1503-8181.

"Modelling of Dynamic Material Behaviour and Fracture of Aluminium Alloys for Structural Applications"
Yan Chen, 2009:69, ISBN 978-82-471-1515-2 (printed version), ISBN 978-82 471-1516-9 (electronic version), ISSN 1503-8181.

"Nanomechanics of polymer and composite particles"
Jianying He 2009:213, ISBN 978-82-471-1828-3 (printed version), ISBN 978-82-471-1829-0 (electronic version), ISSN 1503-8181.

"Mechanical properties of clear wood from Norway spruce"
Kristian Berbom Dahl 2009:250, ISBN 978-82-471-1911-2 (printed version) ISBN 978-82-471-1912-9 (electronic version), ISSN 1503-8181.

"Modeling of the degradation of TiB_2 mechanical properties by residual stresses and liquid Al penetration along grain boundaries"
Micol Pezzotta 2009:254, ISBN 978-82-471-1923-5 (printed version) ISBN 978-82-471-1924-2 (electronic version) ISSN 1503-8181.

"Effect of welding residual stress on fracture"
Xiabo Ren 2010:77, ISBN 978-82-471-2115-3 (printed version) ISBN 978-82-471-2116-0 (electronic version), ISSN 1503-8181.

“Pan-based carbon fiber as anode material in cathodic protection system for concrete structures”
Mahdi Chini 2010:122, ISBN 978-82-471-2210-5 (printed version) ISBN 978-82-471-2213-6 (electronic version), ISSN 1503-8181.

“Structural Behaviour of deteriorated and retrofitted concrete structures”
Irina Vasililjeva Sæther 2010:171, ISBN 978-82-471-2315-7 (printed version) ISBN 978-82-471-2316-4 (electronic version) ISSN 1503-8181.

“Prediction of local snow loads on roofs”
Vivian Meløysund 2010:247, ISBN 978-82-471-2490-1 (printed version) ISBN 978-82-471-2491-8 (electronic version) ISSN 1503-8181.

“Behaviour and modelling of polymers for crash applications”
Virgile Delhaye 2010:251, ISBN 978-82-471-2501-4 (printed version) ISBN 978-82-471-2502-1 (electronic version) ISSN 1503-8181.
“Blended cement with reducted CO_2 emission – Utilizing the Fly Ash-Limestone Synergy”,
Klaartje De Weerdt 2011:32, ISBN 978-82-471-2584-7 (printed version) ISBN 978-82-471-2584-4 (electronic version) ISSN 1503-8181.

“Chloride induced reinforcement corrosion in concrete” Concept of critical chloride content – methods and mechanisms.
Ueli Angst 2011:113, ISBN 978-82-471-2769-9 (printed version) ISBN 978-82-471-2763-6 (electronic version) ISSN 1503-8181.

“A thermo-electric-Mechanical study of the carbon anode and contact interface for Energy savings in the production of aluminium”.
Dag Herman Andersen 2011:157, ISBN 978-82-471-2859-6 (printed version) ISBN 978-82-471-2860-2 (electronic version) ISSN 1503-8181.

“Structural Capacity of Anchorage Ties in Masonry Veneer Walls Subjected to Earthquake”. The implications of Eurocode 8 and Eurocode 6 on a typical Norwegain veneer wall.
Ahmed Mohamed Yousry Hamed 2011:181, ISBN 978-82-471-2911-1 (printed version) ISBN 978-82-471-2912-8 (electronic ver.) ISSN 1503-8181.

“Work-hardening behaviour in age-hardenable Al-Zn-Mg(-Cu) alloys”.
Ida Westermann , 2011:247, ISBN 978-82-471-3056-8 (printed ver.) ISBN 978-82-471-3057-5 (electronic ver.) ISSN 1503-8181.

“Behaviour and modelling of selfpiercing riveted connections using aluminium rivets”. Nguyen-Hieu Hoang, 2011:266, ISBN 978-82-471-3097-1 (printed ver.) ISBN 978-82-471-3099-5 (electronic ver.) ISSN 1503-8181.

“Fibre reinforced concrete”.
Sindre Sandbakk, 2011:297, ISBN 978-82-471-3167-1 (printed ver.) ISBN 978-82-471-3168-8 (electronic ver) ISSN 1503:8181.

“Dynamic behaviour of cablesupported bridges subjected to strong natural wind”.
Ole Andre Øiseth, 2011:315, ISBN 978-82-471-3209-8 (printed ver.) ISBN 978-82-471-3210-4 (electronic ver.) ISSN 1503-8181.

“Constitutive modeling of solargrade silicon materials”
Julien Cochard, 2011:307, ISBN 978-82-471-3189-3 (printed ver). ISBN 978-82-471-3190-9 (electronic ver.) ISSN 1503-8181.

“Constitutive behavior and fracture of shape memory alloys”
Jim Stian Olsen, 2012:57, ISBN 978-82-471-3382-8 (printed ver.) ISBN 978-82-471-3383-5 (electronic ver.) ISSN 1503-8181.

“Field measurements in mechanical testing using close-range photogrammetry and digital image analysis”
Egil Fagerholt, 2012:95, ISBN 978-82-471-3466-5 (printed ver.) ISBN 978-82-471-3467-2 (electronic ver.) ISSN 1503-8181.

“Towards a better under standing of the ultimate behaviour of lightweight aggregate concrete in compression and bending”,
Håvard Nedrelid, 2012:123, ISBN 978-82-471-3527-3 (printed ver.) ISBN 978-82-471-3528-0 (electronic ver.) ISSN 1503-8181.

“Numerical simulations of blood flow in the left side of the heart”
Sigrid Kaarstad Dahl, 2012:135, ISBN 978-82-471-3553-2 (printed ver.) ISBN 978-82-471-3555-6 (electronic ver.) ISSN 1503-8181.

“Biomechanical aspects of distraction osteogensis”
Valentina La Russa, 2012:250, ISBN 978-82-471-3807-6 (printed ver.) ISBN 978-82-471-3808-3 (electronic ver.) ISSN 1503-8181.

“Ductile fracture in dual-phase steel. Theoretical, experimental and numerical study”
Gaute Gruben, 2012:257, ISBN 978-82-471-3822-9 (printed ver.) ISBN 978-82-471-3823-6 (electronic ver.) ISSN 1503-8181.

“Damping in Timber Structures”
Nathalie Labonnote, 2012:263, ISBN 978-82-471-3836-6 (printed ver.) ISBN 978-82-471-3837-3 (electronic ver.) ISSN 1503-8181.

“Biomechanical modeling of fetal veins: The umbilical vein and ductus venosus bifurcation”
Paul Roger Leinan, 2012:299, ISBN 978-82-471-3915-8 (printed ver.) ISBN 978-82-471-3916-5 (electronic ver.) ISSN 1503-8181.